CITY UNIVERSITY
LONDON

Optical aberrations in ametropic eyes and their change with corneal refractive surgery

Thesis submitted by Lourdes Llorente

To aspire to the Degree of Ph.D. in Optometry and Visual Science

At City University

From the Department of Optometry & Visual Science

April 2009

A mis padres y a mis hermanos y hermanas.

To Neil.

"To suppose that the eye with all its inimitable contrivances for adjusting the focus to different distances, for admitting different amounts of light, and for the correction of spherical and chromatic aberration, could have been formed by natural selection, seems, I freely confess, absurd in the highest degree (…). Reason tells me, that if numerous gradations from a simple and imperfect eye to one complex and perfect can be shown to exist, each grade being useful to its possessor, as is certainly the case; if further, the eye ever varies and the variations be inherited, as is likewise certainly the case; and if such variations should be useful to any animal under changing conditions of life, then the difficulty of believing that a perfect and complex eye could be formed by natural selection, though insuperable by our imagination, should not be considered as subversive of the theory." – *Charles Darwin, On the Origin of Species (1859).*

"For the eye has every possible defect that can be found in an optical instrument, and even some which are peculiar to itself; but they are all so counteracted, that the inexactness of the image which results from their presence very little exceeds, under ordinary conditions of illumination, the limits which are set to the delicacy of sensation by the dimensions of the retinal cones. But as soon as we make our observations under somewhat changed conditions, we become aware of the chromatic aberration, the astigmatism, the blind spots, the venous shadows, the imperfect transparency of the media, and all the other defects of which I have spoken. The adaptation of the eye to its function is, therefore, most complete, and is seen in the very limits which are set to its defects. Here the result which may be reached by innumerable generations working under the Darwinian law of inheritance, coincides with what the wisest Wisdom may have devised beforehand. A sensible man will not cut firewood with a razor, and so we may assume that each step in the elaboration of the eye must have made the organ more vulnerable and more slow in its development." – *Hermann von Helmholtz, Popular scientific lectures (1885)*

CONTENTS

LIST OF TABLES

LIST OF ILLUSTRATIONS

ACKNOWLEDGEMENTS

I would like to thank those who, during all these years, have helped me in one or another way with their help and support.

First, I must thank my supervisors for their support during this thesis. This odyssey would have not started without Susana Marcos's suggestion and encouragement to could use my lab work to complete a good thesis. From her I learnt not only about science but also about how to do things right. Luis Díaz-Santana did not hesitate to offer his experience and support from London, giving me the possibility to get a PhD degree. John Barbur was there whenever his experience in academic procedures was necessary. Thank you all.

I would like to thank the Comunidad Autónoma de Madrid (CAM) and the European Social Fund because the fellowship they awarded me (1999-2001) allowed me to confirm that I like doing research.

Some people have contributed more directly to part of the work presented here even if their names do not appear in the corresponding chapter: Esther Moreno-Barriuso contributed in the myopic LASIK measurements and the early stages of the infrared-green comparison; Sergio Barbero participated in the measurements of Chapters 3 and 4; Guadalupe Rodríguez and Raúl Martín from IOBA organised and carried out the optometric measurements of the LASIK patients (Chapter 7); Agustin Mayo, also from IOBA, advised me about the statistics of polarisation (Chapter 3), and Laura Barrios about the statistics of calibrations (Chapter 2), sampling patterns (Chapter 5) and ametropic eyes (Chapter 6); C. Dainty and the Photonics Optics Group at Imperial College allowed L. Díaz-Santana the use and modifications of the HS wavefront sensor utilised in Chapter 4 and Y. Tsang from City University helped during the experimental sessions in London; Alberto de Castro and Noemi Carranza helped me with Gaussian fitting algorithms, and Javier Portilla, Carlos Dorronsoro and Rafael Redondo helped me with the image processing of the passive eye tracking on Chapter 2. I would also like to thank all those who volunteered for being subjects in the different studies. This thesis would not exist without you.

Being in David Williams' lab in Rochester was a great opportunity which I really enjoyed. I would like to thank the organisers of the CVS undergraduate summer fellowship, and specially David Williams for giving me this opportunity. I would also like to thank the people I could interact with then, and specially Jason, Stacey, Nathan, Li Chen, and Debbie Shannon&Co. for their help.

I would like to thank Luis Díaz-Santana for the opportunity to spend some time in his adaptive optics lab. Thanks to Carolina, Franzisca, Brice, Cristiano and specially Marisa and for their help in London, and to Julien for his invaluable help in the lab. Thanks also to the staff for their help with the bureaucracy, and specially Steve Bunting for his help and patience.

Thanks to people from IOBA (especially Guadalupe, María, Isabel Vicky, Bety, Tomás, Raúl, Jesús) for being always so helpful.

Thank you also to my workmates: Esther, for teaching me so much in my first months in the lab; Sergio, for your help all these years in so many things; Patricia and Elena, for sharing basement and measurement sessions in the tough times, for your help and encouragement until the end, and for bearing me in the worst moments. Dani, thanks for sharing your knowledge about human nature, and about conics fitting. Carlos, thanks for your effort to make the LRT2 system

work, for your enthusiasm and for the times you have supported me. Sergio thanks for your help, trying to explain me all those hardcore optics. Enrique and Alfonso, for your help in the lab and for trying to make me more positive. It might work from now on. Requejo, I really learnt a lot from you. Damian, thanks for devoting your spare time selflessly to help me. Alberto, thanks for your help from Gaussian fitting to measurements, for your patience and for interesting discussions. Lucie thank you for so much: for your help and patience, for your hard work, for cheering me up and teaching me so much…and for discovering me the Tariquet!!. Laura, thank you for being always ready to help and for sharing your happiness with everyone. Thanks to you both for being the other two Ls and for your permanent smiles. Saro, it was great to have you in the lab, and to keep in touch since, thanks for your support. Thanks also to Ainara and Vincenzo for being so supportive, good listeners and patient, to Noemí for being the helpful specialist in Word templates and for learning court procedures with me, among other things, and Ana, Vali, Sylvain, Héctor, Amelia, Raul, Oscar, Víctor, Dani, Sara, Michela, Andrés (bambino!), Jesús (mozo!), Alex, Isi, David, Elena, Jeremie, Marcial, Lorena, Lidia, Cristian, Jose A., Vincenzo G, Jan, Portilla, and of course Matts (and Esther), José Luis, Belén, Erwin & Robin, Mª Ángeles…

Thanks to all the colleagues that, during all these years, have helped me in one or other way. Thanks to Steve Burns for processing the sampling patterns data almost in real time from the other side of the ocean and for his advices.

Thanks to all the staff of Instituto de Óptica in Madrid: Chary, Encarnita y Eloy por resolver tanto con paciencia y una sonrisa; a Sole, Encarnita, Yali, Eduardo y Mari Paz por la paciencia con el flujo de pacientes. Paquita, muchas gracias por tu cariño. Gracias Benito por tu ayuda en el taller. Marisa, Mª Luisa, Sole, Cecilia gracias por mantener todo limpio y ordenado con una sonrisa. Belén, Chema y demás gente de mantenimiento, gracias por solucionar las cosas casi al momento. Mª Jesús muchas gracias por tu eficiencia y tu amabilidad a cargo del almacén. Armando, muchas gracias por tu ayuda todos estos años especialmente por resucitar al LRT2 tantas veces, junto con Gema y Carlos. Carlos, gracias por tu ayuda tantas veces tan paciente y eficientemente. Gracias Vicente y Pepe Granados por vuestra ayuda cada vez que la he pedido.

No habría podido llegar aquí sin los que me habéis ayudado con mis problemas de salud. Gracias a todos, y especialmente a Alicia Hernán, Eduardo Zamorano, Yolanda Plata y Sofía (Fisyos).

Muchas gracias por vuestra paciencia a todos los que habéis sufrido mi estrés o mis desapariciones en las peores épocas, sobre todo a Silvia y a Mari Paz por su infinita paciencia y cariño, y a Rebeca y Ana por soportar mis peores momentos en casa. Especialmente quiero dar las gracias a mi madre porque gracias a su "el no ya lo tienes" he llegado a hacer cosas de las que nunca me hubiera imaginado capaz. Por su comprensión, por su apoyo constante y por enseñarme que uno tiene que vivir según sus reglas aunque juegue en desventaja, si quiere ser feliz. Sin ella hoy no estaría aquí…en todos los sentidos. A mi padre, por las veces que me ha apoyado pese a no entender por qué trabajaba tanto en algo que ni me aseguraba un futuro ni me sacaría de pobre, por mantenerme con los pies en la tierra. Ambos me han enseñado a trabajar duro y hacer las cosas bien hechas. A César, Javi, Marta y Ana, por las veces que han tenido paciencia conmigo y las que me han hecho reír cuando estaba a punto de llorar. Eso no tiene precio, y no lo consigue cualquiera. To Neil…he knows why.

Declaration

I grant powers of discretion to the University Librarian to allow this thesis to be copied in whole or in part without further reference to me. This permission covers only single copies made for study purposes, subject to normal conditions of acknowledgement.

Abstract

In this thesis the laser ray tracing (LRT) technique for measurement of ocular aberrations has been implemented, validated and applied, in conjunction with complementary techniques, to the study of ocular aberrations in human eyes. In particular, we studied optical aberrations in myopic and hyperopic eyes and the optical changes induced by refractive surgery for myopia and hyperopia.

We have studied the impact of the optimisation of some experimental parameters on the estimation of the wave aberration. We demonstrated that although the polarisation state and wavelength of the illumination light affected the intensity patterns of the images obtained using reflectometric aberrometry (LRT and Hartmann Shack sensor), these changes did not affect the estimation of aberrations. We also showed that the difference in the defocus term (focus shift) due to the use of different wavelengths is in agreement with the Longitudinal Chromatic Aberration of the Indiana Chromatic Eye Model for average normal eyes, although intersubject variability is not negligible. In addition, we studied experimentally the influence of the geometrical distribution and density of the pupil sampling on the estimation of aberrations using artificial and normal human eyes, and performed numerical simulations to extend our results to "abnormal"eyes. We found that the spatial distribution of the samples can be more important than the number of samples, for both our measured as well as our simulated "abnormal" eyes. Experimentally, we did not find large differences across patterns except, as expected, for undersampled patterns.

We found that hyperopic eyes tended to have more positive asphericity and greater total and corneal spherical aberration than myopic eyes, as well as greater 3rd and higher order aberrations. Although we found no significant differences between groups in terms of internal aberrations, internal spherical aberration showed a significant age-related shift toward less negative values in the hyperopic group. We also assessed the impact of the LASIK corneal surgery, a popular surgical technique for correction of refractive errors, on the optical quality for both myopic and hyperopic standard techniques. Third and higher order ocular and anterior corneal aberrations increased with the surgery. Ocular and corneal spherical aberration changed towards more positive values with myopic LASIK, and towards more negative values with hyperopic LASIK. Changes in internal spherical aberration were of opposite sign than those induced in corneal spherical aberration. Changes induced by hyperopic LASIK were larger than those induced by myopic LASIK for a similar attempted correction.

KEY FOR SYMBOLS AND ABBREVIATIONS

2D	two dimensional
3D	three dimensional
A49	Albrecht pattern with 49 samples
AL	Axial Length
AL/CR	Axial Length to Corneal Radius ratio
ANOVA	Analysis of Variance
CCD	Coupled Charge Device
Cn	Circular pattern with n samples
CPP	Conjugate Pupil Plane
CR	Corneal Radius
CRT	Cathode Ray Tube
CSF	Contrast Sensitivity Function
D	Dioptres
DF	Dichroic Filter
FA	Field Aperture
FB	Focusing Block
GRIN	Gradient Index
HCA	Hierarchical cluster analysis
He-Ne	Helium Neon
Hn	Hexagonal pattern with n samples
HOA	3rd and Higher Order Aberrations (excluding piston, tilts, defocus and astigmatism)
HS	Hartmann-Shack
i.e.	id est, this is
IR	Infrared
J49	Jacobi pattern with 49 samples
λ	Wavelength
L	lens
L49	Legendre pattern with 49 samples

LASIK	Laser Assisted In situ Keratomileusis
LCA	Longitudinal Chromatic Aberration
LED	Light Emitting Diode
LP	Linear Polariser
LRT	Laser Ray Tracing
LRT1	1st generation laser ray tracing device
LRT2	2nd generation laser ray tracing device
μm	microns
MPE	Maximum Permitted Exposure
mrad	milliradians
MTF	Modulation Transfer Function
nm	nanometres
^{o}	degrees
OCT	Optical Coherence Tomography
PCBS	Polarising Cubic Beam Splitter
PRK	PhotoRefractive Keratectomy
PSF	Point-Spread Function
Q	Asphericity
QWP	Quarter Wave Plate
R	Radius of curvature
RMS	Root Mean Square wavefront error
Rn	Rectangular pattern with n samples
RPE	Retinal Pigment Epithelium
SA	Spherical Aberration
SE	Refractive error Spherical Equivalent
SF	Spatial Filter
SRR	Spatially Resolved Refractometre
std	standard deviation
TCA	Transverse Chromatic Aberration
vs	Versus, compared to

Chapter 1

INTRODUCTION

The human eye shows such a brilliant design "with all its inimitable contrivances for adjusting the focus to different distances, for admitting different amounts of light, and for the correction of spherical and chromatic aberration" (Darwin, 1859) that it was one of the weak points of Darwin's evolution theory. The eye, paradoxically, has eventually turned into one of the confirmations of Darwin's theory (Land and Nilsson, 2002, Nilsson and Arendt, 2008). Helmholtz, aware of the fact that the optics of the eye were far from perfect, also recognized that the eye was so adapted to its function that its limits were set to its defects (Helmholtz, 1885).

Since Helmholtz's times, technology has advanced to the point of introducing ocular aberrations measurement in clinical environments or making corneal laser refractive surgery an extended alternative for refractive error correction. Knowledge on the aetiology of refractive errors of the eye as well as structural differences across refractive groups has also advanced in the last century. Whereas the exact mechanisms that lead the eye to become ametropic remain unknown, the retinal image is known to have a role in this mechanism (Wallman, 1993, Wildsoet, 1997, Wallman and Winawer, 2004). The aim of this work is to study ametropia in humans, as well as to assess the outcomes of a correction method such as

corneal refractive surgery, using an optical approach, i.e., measurement of ocular aberrations using the laser ray tracing technique (LRT). Additionally, a study of the effect on the estimation of aberrations of different parameters that can be optimised for measurements under particular conditions, such as natural accommodation, is included in this thesis. As an external student, I have carried out this experimental work at Instituto de Óptica (Consejo Superior de Investigaciones Científicas) in Madrid (Spain).

In this introductory chapter a description of the eye is first presented. A short review of the history of aberrometry will follow where the different existing techniques to measure ocular aberrations will be described. Then, the advantages of applying aberrometry to the study of myopia and to assess refractive surgery as a correction method for ametropic eyes will be pointed out. An introduction of the aspects related to aberrometry that will be treated in this thesis will follow: the effect of the interactions of polarisation and wavelength of the light used in the measurement as well as the sampling pattern used to sample the pupil in the estimation of wavefront aberration. Finally, a review of ametropia and the emmetropisation process, followed by a short revision of corneal refractive surgery will complete this chapter.

1.1.- THE HUMAN EYE

Figure 1.1 shows a cross-section of the eye (horizontal section), where it is evident the roughly circular shape of the ocular globe. The axial length of an average adult is approximately 24 mm. The eye is an image forming device, where the cornea and the lens are the optical elements that form a focused image of the outer world on the retina. The refractive power of the eye is about 60 D (Atchison and Smith, 2000).

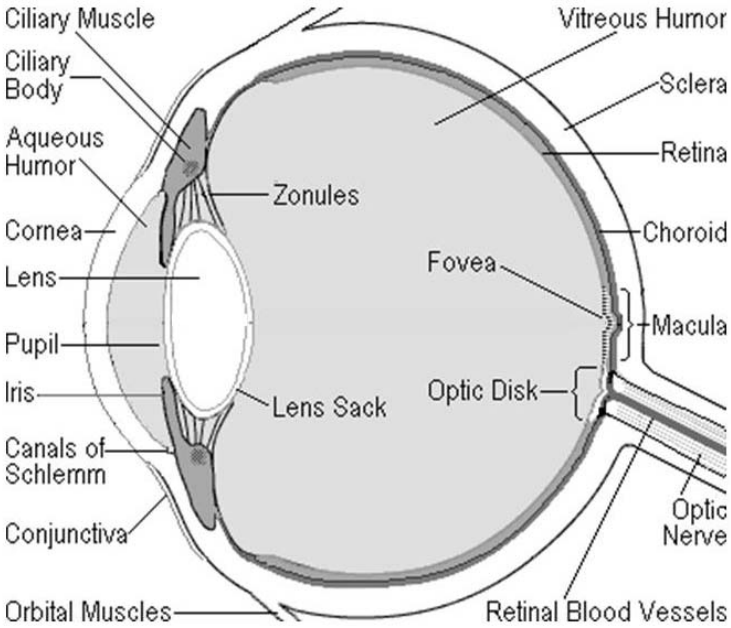

Figure 1.1. Cross-section of the eye (horizontal section) showing the main elements of the eye. Image obtained from http://www.99main.com/~charlief/Blindness.htm

1.1.1.- CORNEA

The cornea contributes about two-thirds of the power of the relaxed eye (~42 D) (Atchison and Smith, 2000), with anterior and posterior paraxial powers of about +49 D and – 6D, respectively (Charman, 1991b). It forms a meniscus which is thinner in the centre (~500 μm) than at the edge (~700 μm), with a refractive index of 1.376 (depending on wavelength and temperature at which it is measured).

Histologically, the cornea can be divided in 5 layers (see Figure 1.2) (Atchison and Smith, 2000): the *epithelium*, in direct contact with the tear film, acts as a barrier against water (to keep corneal transparency) and toxic substances; *Bowman's membrane*, consisting mainly on randomly arranged collagen fibrils; the *stroma*, comprising 90% on the corneal thickness; *Descemet's membrane*, basement membrane of the endothelial cells; and the *endothelium*, consisting on a single layer of hexagonal cells that tile the posterior corneal surface and regulate the corneal hydration in

order to keep transparency. Although the tear film and each corneal layer have their own refractive index (Barbero, 2006), a mean value is usually used (n=1.376) (Atchison and Smith, 2000). The optical inhomogeneity of the cornea contributes to the scattering of light that makes it susceptible to be observed in optical section using a slit-lamp or optical coherence tomography (OCT). Of special optical interest is the stroma, and particularly the way the constituent collagen fibres are arranged, which leads to birefringence (see section 1.2.5.1.-) and is crucial to keep corneal transparency, and the mechanical structure of the cornea. The fibres are arranged in approximately regular lattices called lamellae, which are stacked layer upon layer and run from limbus to limbus parallel to the corneal surface, frequently interweaving (Komai and Ushiki, 1991). The orientation of the lamellae is not completely random, but there exists a preferential direction, usually nasal downwards, although there is intersubject variability.

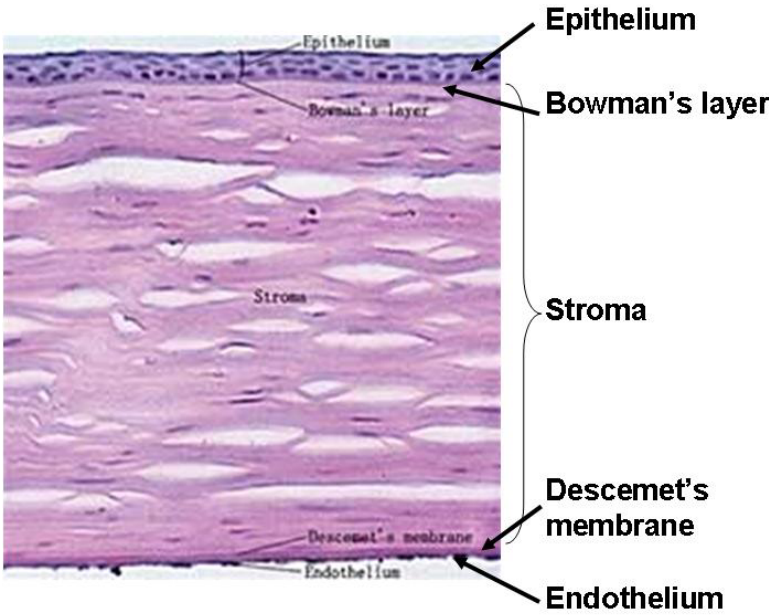

Figure 1.2. Histological section of the cornea showing the different layers. Image from (Yu et al., 2006).

Anatomically, the cornea is oval, its vertical and horizontal diameters being about 12 and 11 mm, respectively. It is continued by the sclera, a dense whitish fibrous layer that gives structure to the eye and that backscatters light strongly (Atchison and Smith, 2000). The cornea is covered by the tear film that, with a thickness of 4-7 μm (Atchison and Smith, 2000), has the optical function of maintaining a smooth optical surface. The anterior corneal surface usually presents different radius at vertical and horizontal meridians (toricity), which produces astigmatism. Generally, in young eyes, the vertical meridian is steeper than the horizontal one, although this tendency reverses with age (Atchison and Smith, 2000). The contour of the anterior cornea can be approximated to a conicoid with rotational symmetry about the z-axis (Kiely et al., 1982), defined by a radius of curvature (CR) and asphericity (Q), which specifies the form of the conicoid. Thus, for Q>0, the conicoid is an oblate ellipsoid (major axis parallel to the y-axis), for Q=0 a sphere, or for -1<Q<0 a prolate ellipsoid (major axis along the z-axis) (Figure 1.3). Kiely et al found human corneas to be prolate ellipsoids, i.e., the cornea flattens towards the periphery, with mean CR and Q being 7.72 ± 0.27 mm and -0.26 ± 0.18. This asphericity is not enough to compensate for corneal spherical aberration, which is usually positive. Corneas that have suffered LASIK for myopic correction typically present an oblate shape, which results in an increased spherical aberration (see Chapter 7).

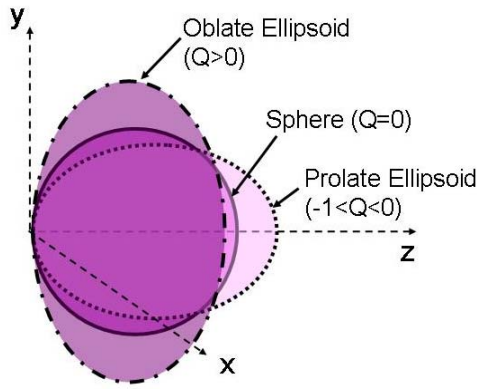

Figure 1.3. Diagram showing the shape of cross-sections of a prolate and an oblate ellipsoids compared to a sphere, according to their asphericity (Q) value.

The posterior corneal surface has a smaller importance in optical terms than the anterior surface due to the smaller index difference in the cornea-aqueous humour interface. In addition, due to the strong influence of the anterior surface, it has been more difficult to measure. Dubbelman et al. (2006) measured the shape of anterior and posterior aging cornea using a Scheimpflug camera (Brown, 1972) and found that the posterior corneal surface had an average radius of 6.53 ± 0.25 mm, the vertical meridian being steeper than the horizontal one, same as for the anterior surface. They also reported that the posterior astigmatism was twice that of the anterior surface. Their posterior Q values varied significantly between meridians, the mean value across the eyes they measured being 0.48 ± 0.26. With age, the Q of both, anterior and posterior surfaces changed significantly, producing a peripheral thinning.

1.1.2.- CRYSTALLINE LENS

The lens has the shape of a biconvex lens (see Figure 1.4). Different parts can be distinguished (Atchison and Smith, 2000). The lens *capsule* or *sack*, which is a transparent elastic membrane, is attached to the ciliary body by the zonules (see Figure 1.1), and plays an important role in accommodation. Contraction of the ciliary muscle within the ciliary body decreases the tension of the zonules, allowing the lens to take up a more curved shape. This leads to changes in the curvature and index distribution that increase the power of the lens, and therefore of the whole eye to allow focusing near objects. The *lens epithelium* extends from the anterior pole to the equator and it is responsible for the continuous growth of the lens throughout life with new epithelial cells forming at the equator. These cells elongate wrapping the older *fibres*, under the capsule and the epithelium, meeting at the sutures of the lens, originating its characteristic "onion-like" layered structure. The older fibres lose their nuclei and other intracellular organelles, forming a stratified structure of fibre membranes and interstitial cytoplasm (Bettelheim, 1975). The older more central fibres

are squeezed by the younger peripheral ones and have a smaller water content, determining the *nucleus of the lens*, which is less elastic and shows the highest refractive index (about 1.41) (Charman, 1991b). The continuous growth of the nucleus and loss of elasticity is thought to be one of the factors involved on the gradual loss of accommodation with age that leads to presbyopia (complete loss of accommodation) that may occur from 35-40 years. The more peripheral fibres form the *cortex*, which presents the smallest refractive index in the lens (about 1.38). Therefore, the lens has a gradient-index (GRIN), which is thought, together with aspheric surfaces, to reduce spherical aberration. For some purposes, an equivalent refractive index (1.42) is used.

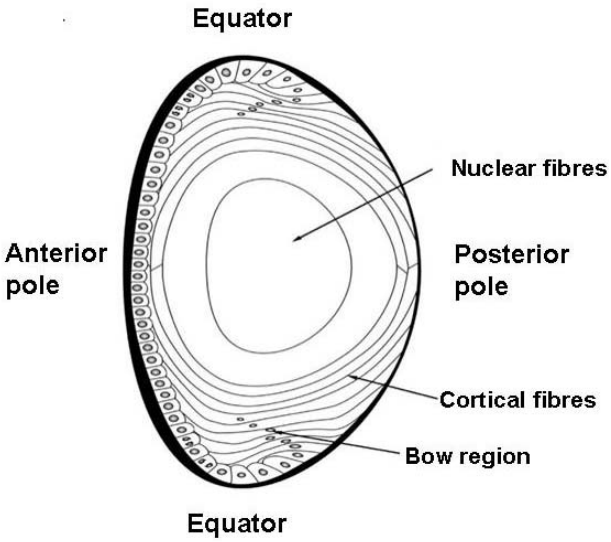

Figure 1.4. Diagram showing a cross-section of the crystalline lens, from (Gupta et al., 2004).

Average (± standard deviation) values of the geometrical parameters of the lens for emmetropic eyes can be found in (Atchison et al., 2008). Reported data for anterior lens radius are 10.32 ± 1.41 mm and 10.53 ± 1.40 mm for males and females, respectively, and for posterior lens radius -6.77 ± 0.78 mm and -6.95 ± 0.91 mm for males and females, respectively, all obtained from Purkinje images. Lens central thickness reported values are

4.19 ± 0.47 mm and 4.13 ± 0.40 mm, for males and females, respectively, obtained from ultrasonography. Lens diameter reported values from magnetic resonance imaging (MRI) are 9.21 ± 0.26 mm and 9.31 ± 0.37 mm for males and females, respectively. The reported values of the lens power, obtained from Purkinje images are 23.36 ± 2.09 D and 24.48 ± 2.40 D for males and females, respectively.

1.1.3.- CHAMBERS OF THE EYE

The eye is divided into three chambers: vitreous, anterior and posterior chambers. Anterior and posterior chambers are limited by posterior corneal surface and the iris, and the iris and the crystalline lens anterior surface, respectively (see Figure 1.1). Both chambers are connected by the pupil and filled by the aqueous humour, a transparent liquid with a refractive index about 1.337, very similar to that of the cornea. The aqueous humour is produced in the ciliary processes, at the posterior chamber, and drained at the irido-corneal angle at the anterior chamber. Therefore, it is constantly moving from the posterior to the anterior chamber through the pupil. Under normal conditions it is quite homogenous and does not scatter much light. The vitreous chamber, limited by the posterior surface of the lens and the retina, is the largest chamber in the eye. It is filled by the vitreous body, a transparent gel that fills the vitreous chamber and helps to maintain the structure of the eye. The vitreous body is quite homogeneous and clear, although with age it tends to liquefy and present refractive irregularities (Charman, 1991b).

1.1.4.- UVEA

The uvea is the pigmented vascular layer that lies between the corneoscleral layer and the retina. It consists, from back to front of the eye, of the choroids, the ciliary body and the iris. The iris acts as a variable aperture stop, which controls the amount of light entering the eye and the retinal image quality through its influence on diffraction, aberration and

depth of focus (Charman, 1991b). It can change from about 2 mm to 8 mm in young eyes, but its maximum aperture decreases at old age (miosis). The aperture is called the pupil, and can be artificially dilated (mydriasis) with chemical substances called mydriatics, such as tropicamide. The ciliary body is involved in the accommodation process (see section 1.1.2.-) as well as the production of the aqueous humor (see section 1.1.3.-). The choroid lies behind the retina and due to its high vascularisation and melanin content (Atchison and Smith, 2000) it strongly absorbs short wavelengths and back-scatters long wavelengths (Delori and Pfibsen, 1989).

1.1.5.- RETINA

The retina is the light sensitive tissue located at the eye fundus, and connected with the brain through the optical fascicle. The position of the retina in the unaccommodated eye in relation to the focused image projected by the cornea and the lens determines the refractive state of the eye. If the retina is in front of the image, the eye will be hyperopic, and conversely, if it is behind the image, the eye will be myopic. Histologically, it is composed of several cellular and pigmented layers and a nerve fibre layer (see Figure 1.5) that faces the vitreous body and forms the optical fascicle (also called nerve) (see Figure 1.1). Light reaches the retina at the inner limiting membrane, where there is some specular reflection (Atchison and Smith, 2000). The six layers between this and the photoreceptors are highly transparent. The radial arrangement of the fibres in the nerve fibre layer has some effect on polarised light (see Section 1.2.5.1.-). The photoreceptors are the light sensitive cells and are in contact with the retinal pigment epithelium (RPE). Light has to go through the rest of the retinal layers to reach them. There are two kinds of photoreceptors: rods, which are sensitive to low-level light, and the cones, which are wavelength sensitive and are classified as L, M and S depending on whether they are sensitive to long, medium or short wavelengths of the

visible spectrum, respectively. Photoreceptors have wave-guiding properties (Enoch and Lakshminarayanan, 1991). This implies that only light entering each photoreceptor with a particular angle will be guided through it and hence perceived. This also implies that light reflected by the photoreceptors (light in the visible range of the spectrum) will also be guided as opposed to scattered. This will be discussed in section 1.2.5.2.- and Chapter 4. The retinal pigment epithelium (RPE), which is in contact with the choroid, receives this name due to its high content of melanin. Therefore the RPE presents a strong absorption and scatter by melanin granules, although some light passes through it and enters the choroid (Atchison and Smith, 2000). The RPE is involved in the phagocytosis of the outer segment of photoreceptor cells. The residual of this process, a molecule called lipofuscin, accumulates throughout life and has the property of being fluorescent (Delori et al., 1995) (see Chapter 3).

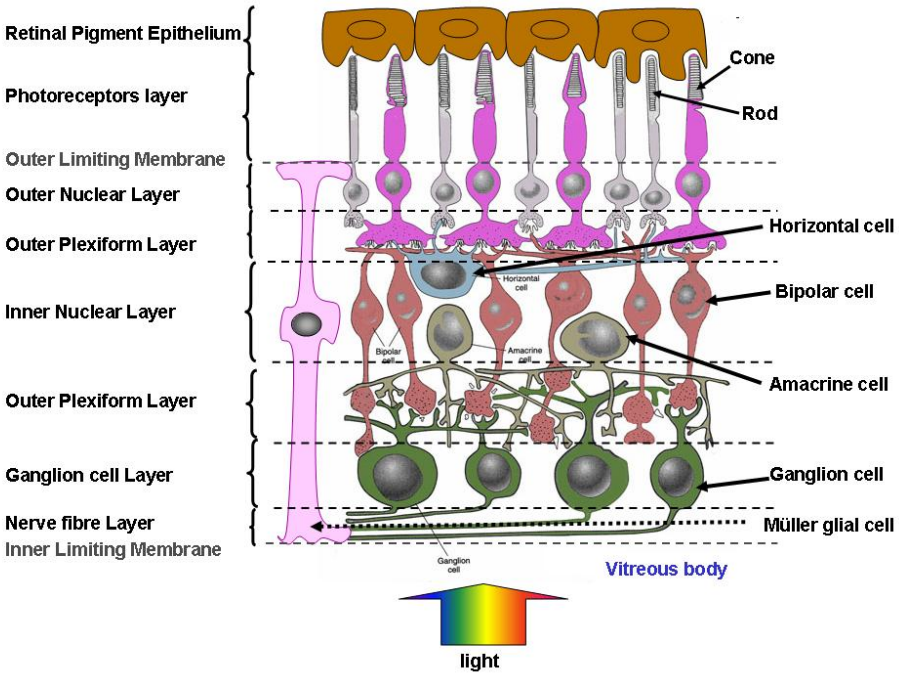

Figure 1.5. Diagram showing the different layers of the vertebrate retina (modified from http://www.skidmore.edu/~hfoley/images/Retina.jpg).

Anatomically, two important structures in the retina can be distinguished, the fovea and the optic disk. The fovea (Atchison and Smith, 2000), where cones predominate (no rods exist at its centre), is 1.5

mm wide, and its centre is about 5º from the optical axis (see Section 1.1.6.-). From an optical point of view, the fovea presents an area where the optical aberrations do not change significantly, the *isoplanatic patch*, with a reported diameter of about 0.80 ± 010º (Bedggood et al., 2008). The optic disk (Atchison and Smith, 2000) is approximately 5º horizontally by 7º vertically. With its centre located approximately 15º nasally and 1.5º upwards from the fovea, it is the region where vascular supply enters the eye and the optic fascicle leaves the eye. Therefore there are no photoreceptors in this region, and because of that the corresponding region in the visual field is called *blind spot*.

1.1.6.- AXIS OF THE EYE

The eye is not a centred, rotationally symmetric optical system: the curvature centres of the ocular surfaces as well as the fovea do not lie in a single common axis (Atchison and Smith, 2000). Because of this, different axes are defined for the eye. The *optical axis* of the eye is defined as the line joining the centres of curvature of the anterior cornea and the posterior lens surfaces. The *line of sight* is the line joining the fixation point and the centre of the entrance pupil of the eye, and is the reference that will be used for the ocular aberrations maps (see section 1.2.1.-). The keratometric axis is that used in keratometers or corneal topographers and contains the centre of curvature of the anterior cornea, usually intercepting the line of sight at the fixation point.

1.2.- ABERROMETRY

1.2.1.- OPTICAL ABERRATIONS

There are different methods to specify the image quality yielded by an optical system. The approach usually applied to describe the optical performance of the eye, is in terms of the wave aberration (see Figure 1.6). The wave aberration, W(x,y), describes the distortions of the wavefront as

it goes through an optical system. A mathematical description of the electromagnetic waves can be found in Born and Wolf (1993). The wavefront is the surface containing the points of a wave on the same phase, which are orthogonal to the corresponding ray pencils. Therefore, if an aberrations-free optical system forms a perfect point image, all the imaging rays will intersect this point to form the image, or equivalently, all the imaging wavefronts will be spherical, centred on the image point. Under these conditions the optical system will be estigmatic and tehe image of a point source will be a point. However, when the optical system is aberrated there is no longer a point focus: the rays will not intersect on a single point, and the wavefronts will no longer be spherical. When the system forms a perfect image focused at infinity, the rays will be parallel, and the wavefronts will be planes (spheres of infinite radius). Thus, the aberration can be described in terms of the distance that each point of the wavefront departs from the ideal sphere at the exit pupil (Charman, 1991b). Wave aberration can be represented in a wave aberration map as shown in Figure 1.6, where the colour indicates the distance between the wavefront and the reference sphere, and the lines join points at equal distance. Therefore, optical aberrations can be represented as: wave aberration (departure of the wavefront from the ideal wavefront, as measured at the exit pupil), transverse aberration (departure of a ray from its ideal position at the image plane), or longitudinal aberration (departure of the intersection of a ray with the optical axis from its ideal position) (Atchison and Smith, 2000).

Optical aberrations can be divided in chromatic and monochromatic (geometrical) aberrations. Chromatic aberrations are a consequence of the dispersion (variation of refractive index with wavelength) of the refractive media of an optical system. There are two types of chromatic aberrations. The *longitudinal* chromatic aberration (LCA) is produced because different wavelengths are focused at different image planes, and can be quantified as the variation in power with wavelength. The *transverse* chromatic

aberration (TCA) is produced when obliquely incident rays are focused at different transverse positions within the image plane.

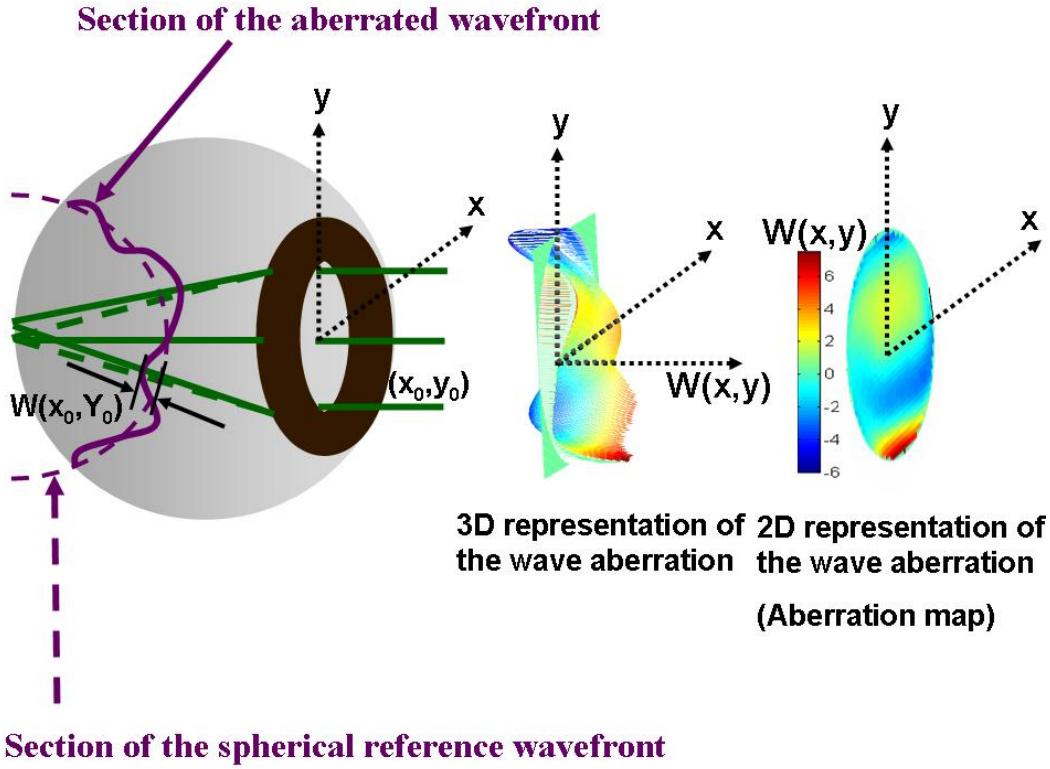

Figure 1.6. Schematic representation of the wave aberration. Wave aberration values (distances between the distorted aberrated wanefront and the spherical reference) can be represented as z-coordinate referred to the pupil plane (three-dimensional representation) or can be represented as a colour gradation (Aberration map).

Monochromatic aberrations are those present when only one wavelength is considered, and arise from the geometry, irregularities, tilts and decentrations of the components of the optical system. The magnitude of the geometrical aberrations increases with the diameter of the exit pupil considered. Seidel (Seidel, 1856) named in 1856 the seven primary aberrations, which include, apart from the chromatic aberrations, five monochromatic aberrations: Astigmatism, Spherical aberration, Coma, Field Curvature and Distortion. In the presence of any of the first three aberrations, the optical system will not be able to image a point source as a point, and the resulting image will be blurred, degrading the retinal image. When astigmatism is present, parallel rays are focused down to two mutually perpendicular focal lines at different positions (see Figure

1.7 A). Astigmatism is usually due to lack of symmetry of at least one surface, usually the anterior cornea in the eye (Atchison and Smith, 2000). Positive (negative) spherical aberration is present when parallel non-paraxial rays do not intersect at the paraxial focus, but in front or behind it (see Figure 1.7 B). The further the ray is from the optical axis, the greater this effect will be. Spherical aberration (SA) is rotationally symmetric and depends on the radius of curvature (R) and on the asphericiy (Q) of the optical surfaces (SA decreases when R increases and increases with Q). In a rotationally symmetric system, coma is an off-axis aberration, where rays departing from an off-axis point reach the image plane at different points (see Figure 1.7 C). In the eye, coma-like aberrations present at the fovea are the result of the lack of symmetry of the optical elements around an optical axis (Atchison and Smith, 2000). Field curvature and distortion are also off-axis aberrations. In both cases a source point is imaged as a point, but the position will be different from that predicted from paraxial optics: when field of curvature is present the point will be imaged in front of (for systems with components of positive power such as the eye) or behind the paraxial focal plane, and when distortion is present, the point is formed in the paraxial image plane but further away (positive distortion) or closer (negative distortion) to the optical axis than expected (Atchison and Smith, 2000).

Piston, tilt and defocus are not considered Seidel aberrations, although tilt and defocus have the same dependence with pupil coordinates as distortion and field of curvature, respectively. Piston is the mean value of the wavefront across the pupil of an optical system, and tilt quantises the average slope of the wavefront in X and Y directions (Malacara, 1992). Defocus occurs when parallel rays (paraxial and not paraxial) converge in front of (positive defocus) or behind (negative defocus) the paraxial focus. Although not considered a Seidel aberration, defocus is considered a low order aberration when the wave aberration is described in terms of a polynomial series.

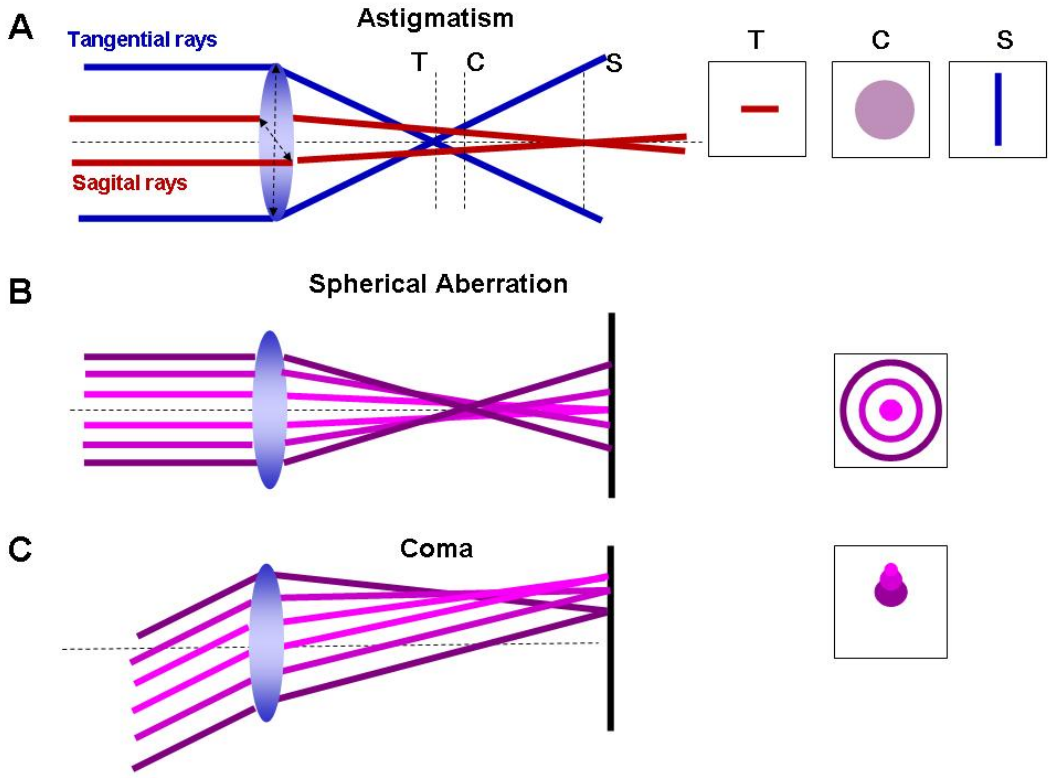

Figure 1.7. Illustration of those Seidel aberrations which prevent optical systems from forming a point image from a point object: astigmatism (A), spherical aberration (B) and coma (C). T, S, and C stand for the image planes corresponding to tangential rays, sagital rays and circle of minimum confusion.

Apart from the optical aberrations, other retinal image quality criteria are commonly used, such as the point-spread fuction (PSF) and the Modulation Transfer Function (MTF). The PSF is the illuminance distribution of a point source of light in the image, and its shape depends on diffraction, defocus, aberrations and scatter. The PSF produced by the optical aberrations is proportional to the Fourier transform of the wave aberration function. The MTF quantifies how each spatial frequency is transferred by an optical system by measuring the amplitude of the output (image) for each spatial frequency in relation to an input (object) of known amplitude (de Valois and de Valois, 1988). The MTF can be calculated as the magnitude of the autocorrelation of the wave aberration function (Atchison and Smith, 2000). The quality of the visual system depends not only on optical factors, but on neural factors such as sizes and spacing of

retinal cells, the degree of spatial summation at the different levels from the retina to the visual cortex and higher level processing (Atchison and Smith, 2000). The Contrast Sensitivity Function (CSF) measures the contrast required by an observer for the detection of each of different spatial frequencies, and is expressed as the reciprocal of the contrast required for detection (de Valois and de Valois, 1988). It hence includes optical as well as neural factors. The MTF and the reciprocal of the CSF are therefore closely associated (Atchison and Smith, 2000).

1.2.2.- ESTIMATION OF ABERRATIONS

The wave aberration of a general optical system can be described mathematically by a polynomial series. Although some other polynomial series have been proposed (Howland and Howland, 1977), Zernike polynomial (Born and Wolf, 1993) expansion has become the standard for representing ocular wave aberration data, since they present some advantages for this purpose: 1) they are defined over the unit circle, and aberrations are usually referred to circular pupils; and 2) some terms can be easily related to Seidel aberrations (Born and Wolf, 1993). Therefore, a wave aberration can be described as a summation of Zernike polynomial functions weighted by the so-called Zernike coefficients, which indicate the magnitude of each particular aberration present:

$$W(X,Y) \approx \sum_{n} \sum_{m} C_n^m Z_n^m (X,Y) \qquad (1.1)$$

where $W(X,Y)$ is the wave aberration phase in microns as a function of cartesian coordinates, C_n^m and $Z_n^m(X,Y)$ are the Zernike coefficient in microns and Zernike polynomial (dimensionless), respectively, as a function of cartesian coordinates, corresponding to the radial order n and the meridional frequency m (see Figure 1.8). The Optical Society of America established a set of recommendations regarding sign, normalisation and ordering that will be followed

throughout this work (Thibos et al., 2000). A mathematical definition of the Zernike polynomials according to these recommendations can also be found in the same reference. Following this convention, W>0 means the wavefront is phase-advanced relative to the chief ray. Figure 1.8 shows the three-dimensional representation of the Zernike polynomials up to 6th order with the corresponding names and notation. As can be observed fro the figure, terms with meridional frequency zero are rotationally symmetric. The Root Mean Square wavefront error (RMS), defined as "the root square of the sum of the squares of the optical path differences as measured from a best-fit reference spherical wavefront over the total wavefront area"(Fischer et al., 2007), is typically used as a global metric for the optical quality.

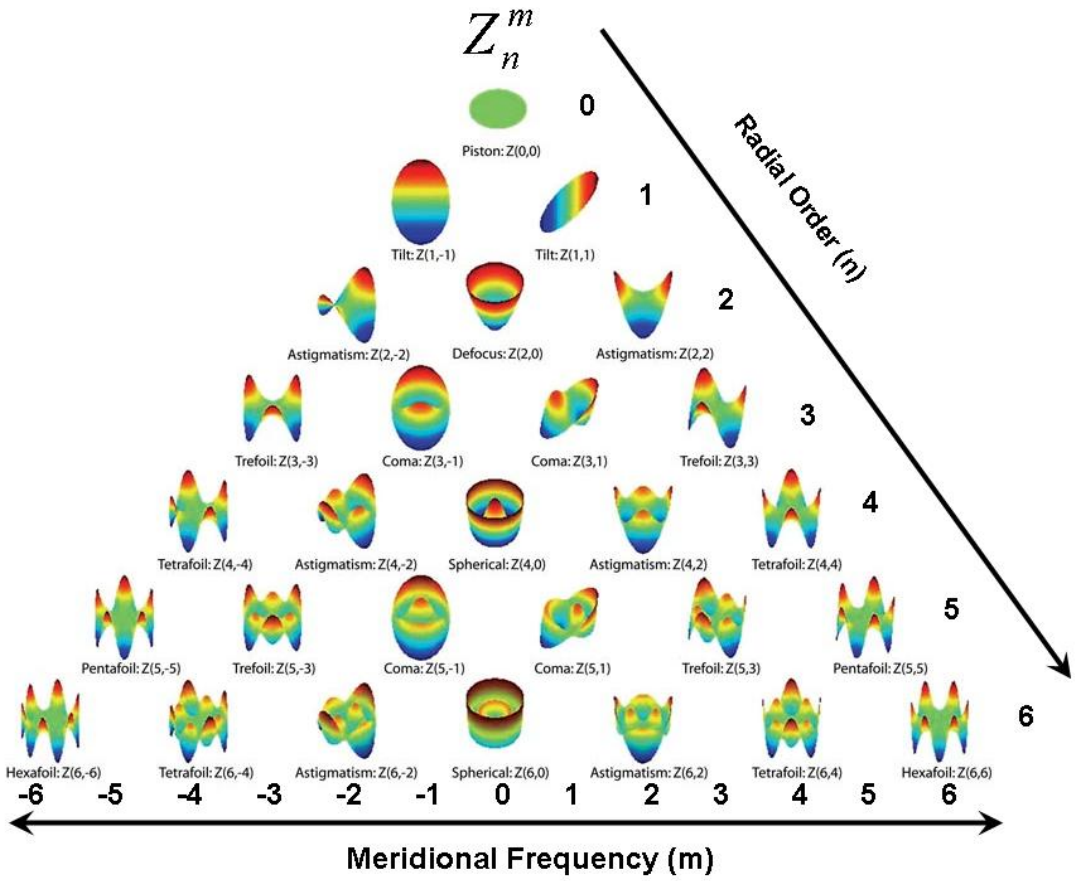

Figure 1.8. Representation of the Zernike base functions. Each row in the pyramid corresponds to a radial order of the polynomial, and each column to a meridional frequency. Positive and negative frequencies indicate harmonics in cosine and sine phase, respectively. Negative frequency astigmatism and n-foil terms are usually denominated "oblique" astigmatism or n-foil. Positive and negative frequency coma terms are usually denominated as horizontal or vertical coma, respectively. Although each mode can be assigned a single reference number, a double-script notation which designates each basis function according to its order (subscript) and frequency (superscript) is commonly used (Thibos et al., 2000).

Most methods of estimation of the wave aberration are based on local sampling of the pupil and measurement of the local wave aberration slope. The local slope (partial derivatives) of the wavefront is proportional to the ray aberration (Born and Wolf, 1993):

$$\Delta x' = \frac{1}{R_p}\frac{\partial W(\bar{\xi},\bar{\eta})}{\partial \bar{\xi}}; \quad \Delta y' = \frac{1}{R_p}\frac{\partial W(\bar{\xi},\bar{\eta})}{\partial \bar{\eta}} \qquad (1.2)$$

where $\bar{\xi} = \xi / R_p$, $\bar{\eta} = \eta / R_p$ are dimensionless canonical pupil coordinates and R_p is the pupil radius (Moreno-Barriuso et al., 2001a). The wave aberration is reconstructed by integrating the slopes of an array of beams intersecting the eye's entrance (or exit in some cases) pupil (Howland, 2000). This reconstruction can be local (Southwell, 1980), modal (Cubalchini, 1979, Rimmer, 1974, Fried, 1977, Herrmann, 1981) (or a mixture of both), if the estimate is a phase value on a local area or a coefficient of an aperture function (Southwell, 1980). Usually, in any case a least-square estimation is used for phase reconstruction. Some questions to consider when selecting the reconstruction model are the compatibility with the sampling geometry of the sensor, the reconstruction algorithm complexity (convergence problems, computation speed requirements), and the propagation error. The most widely used method in ocular aberrometry is a modal reconstruction that is based on the expansion of the derivatives of wave aberration as a linear combination of a set of base functions (most frequently the derivatives of Zernike polynomial expansion), and a subsequent least-squares fit of the expansion coefficients to the measured gradients (Rios et al., 1997). Southwell (Southwell, 1980) found that modal estimation was superior to zonal estimation in terms of noise propagation, particularly when only a fixed number of modes were of interest, and that modal estimation was computationally easier and faster. These advantages enhanced as the number of samples increased. Regarding the compatibility with the geometry of the sensor, some geometries not currently being used might be better adapted to the

geometry of Zernike functions (see Section1.2.5.3.-). This topic will be addressed in Chapter 5 of this thesis.

1.2.3.- HISTORY AND TYPES OF ABERROMETERS

The history of aberrometry dates back to 1619 when Scheiner (Scheiner, 1619 in Biedermann, 2002) invented a disk with a central and a peripheral pinhole that was placed in front of the eye of a subject, so that an imperfect eye would form two retinal images when looking at a distant point light source. Helmholtz (1821-1894) was one of the pioneers who extensively investigated the structure of the human eye, including its aberrations. He foresaw that human ocular aberrations were significant enough to degrade the retinal image (Helmholtz, 1885). Around the same time, in 1894, Tscherning (Tscherning, 1894 in Biedermann, 2002) built what he called "an aberroscope" to measure human eye aberrations, consisting on a grid superimposed on a 5-diopter lens so that the image of the grid was shadowed on the subject's retina when viewing a distant point light source through the "aberroscope". Aberrations were estimated from the distortions of the grid. In 1900 Hartmann (Hartmann, 1900 in Biedermann, 2002) used Scheiner's idea to measure aberrations in mirrors and lenses, using an opaque screen perforated with numerous holes, which is commonly referred to as wavefront sensor. Independently Smirnov (Smirnov, 1961), in 1961 had the idea of sequentially rotating Scheiner's disk in order to sample the whole pupil. One year before B. Howland (Howland, 1968) had invented the crossed cylinder aberroscope, a modification of Tscherning's one that used a crossed cylinders lens, that he used to study aberrations in camera lenses. It was not until a few years later that it was applied to measure aberrations of the human eye subjectively (Howland and Howland, 1976), with the subject drawing the perceived distorted grid. In 1984, Walsh et al. (1984) turned Howland's aberroscope into an objective method by photographing the image of the grid on the retina. In 1971 Shack and Platt (Shack and Platt, 1971)

improved Hartmann's screen by using an array of microlenses (or lenslets) instead of the perforations to analyse the wavefront coming out of the optical system to study. The array of microlenses is called a Hartmann-Shack (HS) wavefront sensor, and it is composed of a number of microlenses with the same focal length, arranged in a known geometry. A diagram of the working principle of a HS is shown in Figure 1.9. In this technique (Liang et al., 1994), a point source is created in the object space, at the fovea. Light from the eye reaching each lenslet is brought to a focus in the focal plane of the lens array. When an ideal plane wave reaches the sensor, the image obtained in its focal plane reproduces the geometry of the sensor, given that each spot is located on the optical axis of the corresponding lenslet. The pattern of spots in this image will be used as a reference. When an aberrated wavefront is measured, the image spot produced by each lenslet shifts with respect to the corresponding point in the reference a distance proportional to the local phase distortion (transverse aberration). The HS sensor was first applied in astronomy. It was in 1994 when it was adapted by Liang et al (Liang et al., 1994) in Heidelberg for measuring aberrations of the eye, and a couple of years later it was developed in Rochester and integrated in an adaptive optics flood illumination fundus camera to image the human eye retina with unprecedented resolution by removing the eye aberrations using a deformable mirror (Miller et al., 1996). In this thesis a HS sensor has been used to measure ocular aberrations in Chapters 3 and 4.

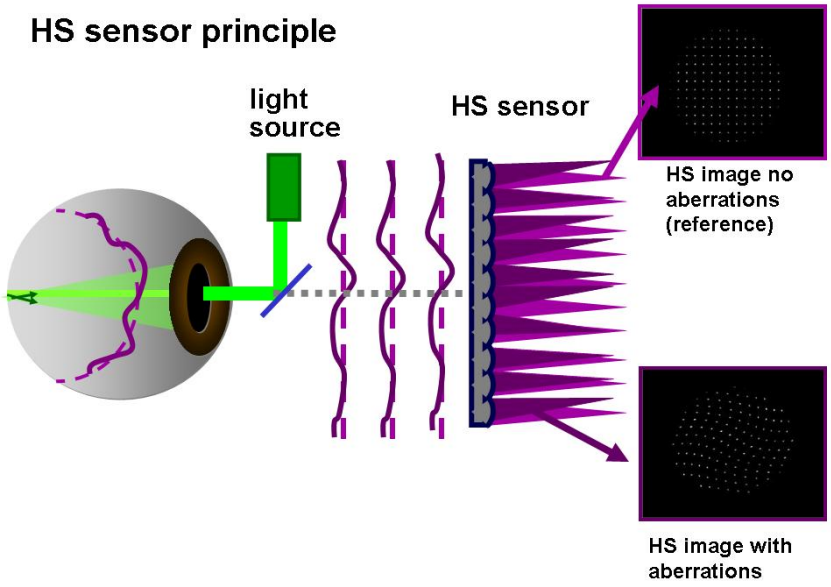

Figure 1.9. Diagram of the working principle of Hartmann-Shack (SH) sensor. A point source at the retina emits spherical wavefronts which are distorted by the eye aberrations. Each lenslet will sample a portion of the wavefront on a different phase, and will form a point image away from its focal point a distance proportional to the phase distortion. Modified from original by S. Marcos.

Some years later, the Ray Tracing technique (LRT) (Navarro and Losada, 1997, Molebny et al., 1997) was applied to measure ocular aberrations. This technique, which has been used throughout this thesis will be more extensively described in Chapter 2, section 2.2. A diagram of the working principle of LRT is shown in Figure 1.10. Collimated laser pencils are sequentially delivered through different pupil positions, so that each pencil will be deviated an angle proportional to the local wave aberration, and will impact at a foveal location away from that of the reference central ray (transverse aberration). The joint plot of the impacts corresponding to the rays entering through different pupil locations is a spot diagram. There is a psychophysical version of the ray tracing, the Spatially Resolved Refractometer (SRR), where the ray aberration at each pupil point is computed as the angle that the subject has to tilt the incoming beam in order to visualize the ray centred on the retina (Webb et al., 1992, He et al., 1998). Some aberrometers measure the ray aberration on the retina or image space ("ingoing" techniques), i.e., they measure the deviation of the rays as they enter the eye. This is the case of the LRT, SRR or Tscherning's type aberrometer (Seiler et al., 2000) previously described.

In other aberrometers, aberrations are measured in the object space ("outgoing" techniques), i.e., as the light exit the eyes. This is the case of the Hartmann-Shack technique. Table 1.1 compares the different aberrometry techniques according to some of their features.

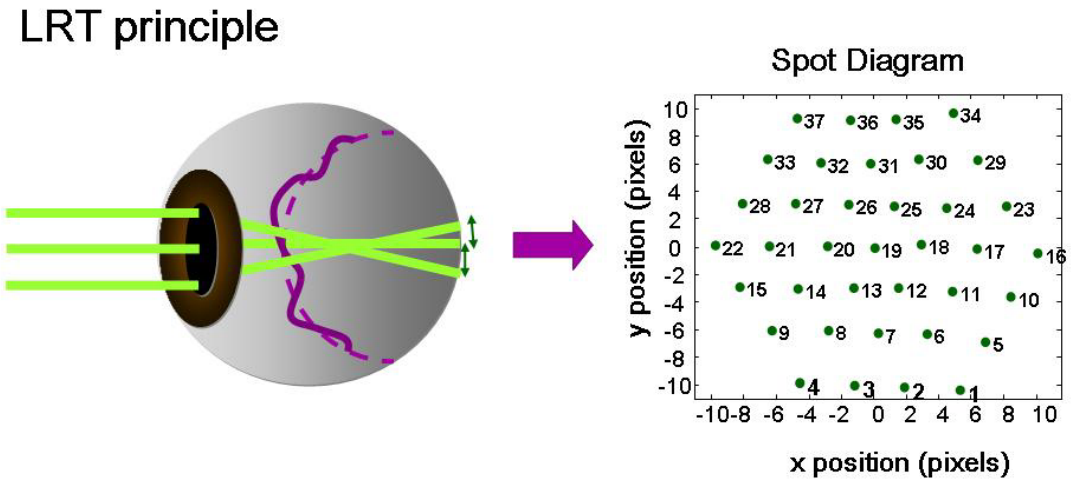

Figure 1.10. Schematic diagram showing the working principle of Laser Ray Tracing (LRT): parallel rays sequentially delivered through different pupil positions deviate an angle proportional to the wave aberration will impact at a different foveal location. A spot diagram can be represented by plotting jointly the impacts sequentially collected for all the pupil locations. Modified from an original diagram by S. Marcos.

COMPARISON	HS	Tscherning	LRT	SRR
Method type	Objective	Objective	Objective	Psychophysic-al
Configuration	Parallel	Parallel	Sequential	Sequential
Flexibility	"Rigid" configuration	"Rigid" configuration	Configurable sampling pattern	Configurable sampling pattern
Measurement Step	Measurement in 2nd step ("outgoing")	Measurement in 1st step ("ingoing")	Measurement in 1st step ("ingoing")	Measurement in 1st step (only) ("ingoing")
Pixels per centroid Range	Few pixels	Few pixels	Whole sensor	Whole sensor
Test size on retina	Foveal	Extensive	Foveal	Foveal
Measurement time range	milliseconds	milliseconds	seconds	minutes

Table 1.1. Comparison of the features of the different techniques to estimate ocular aberrations from transverse aberrations.

In this work, the LRT technique to measure ocular aberrations has been mainly used. This technique has a large dynamic range and can measure largely degraded eyes given that, since images are captured sequentially, the entire CCD sensor is available for each aerial image. This makes LRT well-suited to study eyes with optical quality varying widely in magnitude in a wide range, as will be explained in section 1.2.6.-. The flexibility in its configuration has allowed us to carry out experiments that would have been more challenging with other techniques, such as the work described in Chapter 5. Finally, this objective method allows shorter measuring times compared to its psychophysical counterpart (SRR).

1.2.4.- OPTICAL ABERRATIONS OF THE HUMAN EYE

Ever since Helmholtz foresaw that the eye, far away from being a perfect optical system, presented even more optical aberrations than the optical instruments at the time (Helmholtz, 1885), the measurement of aberrations has advanced to the point that there exist several studies characterising the aberrations of the general population and aberrometers have become available in the clinical practice. In this section a description of the characteristics of the aberrations pattern which are common among the normal population is presented. An overview of current knowledge of the aberrations of the entire eye will be presented, followed by the aberrations of the cornea and finally discuss the interaction of corneal and internal aberrations to yield the overall ocular aberrations pattern.

1.2.4.1.- Ocular Aberrations

Early studies on the ocular (total) aberrations of the human eyes (Von Bahr, 1945, Van Heel, 1946, Ivanoff, 1953, Smirnov, 1961, Van der Brink, 1962, Jenkins, 1963, Howland and Howland, 1976, Howland and Howland, 1977) already reported a large variation of the magnitude and distribution of the aberrations among individuals, which has been confirmed by later studies including a larger number of eyes. In addition,

optical aberrations are known to change with age (see below), be related to the refractive group of the eye (see section 1.3.1.-) and depend on the pupil size. However, some general conclusions across the population can be extracted.

1) The defocus Zernike term, followed by both astigmatic terms (second Zernike order), are the main contributors to the total RMS (Porter et al., 2001, Castejon-Mochon et al., 2002, Thibos et al., 2002, Cheng et al., 2004);

2) In general, for each subject, the magnitude of the aberrations decreases as the Zernike order increases (Porter et al., 2001, Castejon-Mochon et al., 2002, Thibos et al., 2002, Cheng et al., 2004), with terms beyond fourth Zernike order being practically zero (Castejon-Mochon et al., 2002, Cheng et al., 2004). Fourth order SA (Z_4^0) has been reported to be larger in magnitude than the previous third order terms (Porter et al., 2001, Castejon-Mochon et al., 2002, Thibos et al., 2002). However, some studies also report third order aberrations (coma and trefoil) to dominate the HOA pattern of normal eyes (Howland, 2002, Applegate et al., 2007).

3) The average value of each term across the population is zero, except for 4th order SA (Z_4^0), which has been found to be significantly positive across subjects, with reported values including, for example, 0.037 μm (6 mm pupil) (Plainis and Pallikaris, 2006), 0.065±0.083 μm (5 mm pupil) (Cheng et al., 2004), 0.128±0.096 μm (6 mm pupil) (Salmon and de Pol, 2006) and 0.138 μm (5.7mm pupil) (Porter et al., 2001). These values depend on characteristics of the studied population such as age and refractive error. However, Plainis et al. reported that also oblique trefoil (Z_3^{-3}) was significantly different from zero with an average value of -0.062 μm. Data reported by Salmon and de Pol (2006) support this finding (they report a mean value of 0.11 μm), and include vertical coma (Z_3^{-1}), with a mean value of 0.14 μm, among the most prominent Zernike terms.

4) The aberrations of the eye seem to be related in such a way that the overall optical quality of the eye was optimised (McLellan et al., 2006). This feature was not found for corneal aberrations or for randomly generated sets of aberrations with the same RMSs as the measured eyes.

5) The reported average RMS for HOA in a large young normal population is 0.22 μm (5 mm pupil) (Cheng et al., 2004), 0.26 μm (6 mm pupil)) (Plainis and Pallikaris, 2006) and 0.33 μm (6 mm pupil) (Salmon and de Pol, 2006).

6)A bilateral symmetry in the aberration patterns corresponding to both eyes of the same subject has been reported (Castejon-Mochon et al., 2002, Marcos and Burns, 2000, Plainis and Pallikaris, 2006, Thibos et al., 2002, Porter et al., 2001, Kelly et al., 2004). Aberration patterns from both eyes present a mirror symmetry, which is confirmed by negative correlations found between left and right eyes for most of the Zernike coefficients corresponding to asymmetric Zernike functions such as coma and astigmatism (Porter et al., 2001). The highest correlation between Zernike terms was found for defocus, followed by SA and astigmatic terms (Porter et al., 2001, Castejon-Mochon et al., 2002).

Ocular aberrations have been reported to increase with age (Applegate et al., 2007, Artal et al., 2002, Mclellan et al., 2001, Calver et al., 1999) for a fixed pupil diameter, and in particular, the RMS for HOA has been found to increase significantly (McLellan). A change in SA with age towards positive values, attributed to a loss of the compensation between the cornea and the crystalline lens (Artal et al., 2001, He et al., 2003, Mclellan et al., 2001, Smith et al., 2001, El Hage and Berny, 1973, Radhakrishnan and Charman, 2007, Millodot and Sivak, 1979), has also been found. Salmon et al. (2006) found a gradual increase of SA with age, although the wide variability they found indicated the influence of other factors than age. Recent studies in emmetropic eyes (Atchison et al., 2008, Plainis and Pallikaris, 2006) did not confirm this change, suggesting that

interactions between age and refraction might have influenced the results of previous studies. Third order aberrations have also been reported to increase with age (Mclellan et al., 2001), particularly horizontal coma (Z_3^1) (Atchison et al., 2008, Salmon and de Pol, 2006). Salmon et al. (2006) also found correlations for terms Z_3^{-1}, Z_4^2 and Z_4^4. McLellan et al. found a strong significant positive correlation between 5th and higher order aberrations RMS and age, and Salmon et al. found significant correlations for 3rd, 4th, 5th and 6th RMSs.

1.2.4.2.- Corneal Aberrations

Given that the cornea contributes about two-thirds of the power of the relaxed eye (Atchison and Smith, 2000), it has a great influence in the ocular aberrations. Currently, the most extended way to estimate anterior corneal aberrations is from the elevation maps obtained from a corneal topographer in combination with ray tracing through the optical surface defined by these maps (Applegate et al., 1996, Barbero et al., 2002b, Guirao and Artal, 2000). Similarly to ocular aberrations, corneal aberrations have been reported to vary widely among the population (Guirao et al., 2000, Wang et al., 2003b), and apparently corneal aberrations also present some bilateral symmetry (Wang et al., 2003b, Lombardo et al., 2006). The anterior cornea presents with-the-rule astigmatism (vertical meridian steeper), which generally reverses with age into against-the-rule, and positive SA. Wang et al. (2003b) reported average values of 0.280 ± 0.086 μm, 0.248 ± 0.135 μm and 0.479 ± 0.124 μm for SA, coma and HOA, respectively for a population ranging from 20 to 79 years old (mean age was 50 years). In terms of aging, anterior corneal aberrations have been reported to increase moderately with age (Oshika et al., 1999a, Guirao et al., 2000, Atchison et al., 2008). Particularly, third order coma has been found to increase with age (Oshika et al., 1999a, Guirao et al., 2000). However, Atchison et al. only found a significant increase in the 6th order

terms, apart from HOA. The reason might be the interaction between age and refraction previously commented.

The posterior corneal surface has a smaller effect on HOA of the eye (Dubbelman et al., 2007), due to the small index difference between the cornea and the aqueous humour (Atchison and Smith, 2000). Using a distortion corrected Scheimpflug camera (Brown, 1972), Dubbelmann et al. (2006) found a compensation of 31% of the anterior corneal astigmatism by the posterior cornea. Using the same technique, Sicam et al. (2006) found that SA of the posterior cornea is negative in young eyes and becomes positive with age, disrupting the compensation of the positive SA of the anterior cornea. Dubbelman et al. (2007) also found a coma compensation of 3.5% between both corneal surfaces, that disappeared with age.

1.2.4.3.- Internal Aberrations: interaction between total and corneal aberrations

Internal aberrations can be estimated from the subtraction of anterior corneal aberrations from ocular (total) aberrations, and include the aberrations of the lens and the posterior cornea (as the humours are not believed to play a significant role in terms of aberrations). Knowledge of the relative contribution of the cornea and the lens to the ocular wave aberration is important for both, basic study of the human eye and clinical applications, as will be shown in Chapters 6 and 7, respectively.

The existing compensation of the positive corneal SA by the negative SA of the lens has been reported since the 70's (El Hage and Berny, 1973, Millodot and Sivak, 1979), and has been confirmed since, using different techniques (Tomlinson et al., 1993, Smith et al., 2001, Artal and Guirao, 1998, Artal et al., 2001, Barbero et al., 2002a, Kelly et al., 2004). This compensation had also been reported for astigmatism (Le Grand and El Hage, 1980, Artal et al., 2001, Kelly et al., 2004) and is quite well known in clinical practice. The development of tecniques to measure the aberrations

has allowed the initial studies on astigmatism and SA compensation to be expanded to other aberrations. Artal et al. (2001) found compensation in both astigmatism Zernike terms, SA, oblique trefoil and coma. Kelly et al. (2004) confirmed Artal's findings for horizontal/vertical astigmatism (Z_2^2), horizontal coma (Z_3^1) and SA (Z_4^0), but they did not find compensation for oblique trefoil (Z_3^{-3}) or oblique astigmatism (Z_2^{-2}), maybe because only 10% of their sample had oblique astigmatism axes. Two different mechanisms have been suggested for this compensation (Artal et al., 2001, Barbero et al., 2002a, Kelly et al., 2004): a passive geometric mechanism resulting from the evolution and genetically programmed, responsible for the compensation of SA, for which the pattern is similar across the population (positive corneal/negative lens SA); and a fine-tuning active process that would take place during the development of the eye (similar to the emmetropisation process for the defocus that will be addressed in section 1.3.-), responsible of the compensation of those aberrations which pattern is more randomly distributed across the population, such as coma and astigmatism. Some years later, Artal et al. (2006) found that eyes with larger misalignments between the fovea and the optical axis, and therefore likely to have larger amounts of coma, had larger coma compensation. He suggested that the passive geometric evolutionary mechanism responsible for SA compensation could also be responsible for coma compensation. Corneal/internal compensation of horizontal coma has also been reported in patients with aspheric intraocular lenses implanted (Marcos et al., 2008), supporting that the mechanism is geometric.

The increased optical aberrations (see section 1.2.4.1.-) present in the old years has been attributed to the loss of this compensation with age, reported for SA. Changes in the crystalline lens seem to be responsible for this balance disruption, as the corneal aberrations have been found to remain fairly constant (Smith et al., 2001).

1.2.5.- *ABERRATION MEASUREMENT IN PATIENTS: INFLUENCE OF THE MEASUREMENT LIGHT AND SAMPLING PATTERN*

The generalised use of aberrometry in clinics has brought some additional needs such as speed in the measurement and comfort for the patient. In applications such as adaptive optics, speed in the data processing is crucial in order to achieve real time correction. Acquisition times can be reduced by reducing the number of samples in sequential aberrometers, or the exposure times. Using infrared (IR) wavelength (more reflected by the eye fundus than visible light (Delori and Pfibsen, 1989)), or polarisation configurations that maximise light reflected on the photoreceptors layer (Lopez-Gil and Artal., 1997) can help to avoid stray light or unwanted reflections in the image, optimising processing time. The latter can also be minimised by decreasing the number of samples. However, given that some aberrometry techniques use light reflected back from the retina, the interaction of the light with the different retinal layers can influence the measured aberration pattern. In addition, changes in the number and distribution of samples can also influence the accuracy in the estimation of aberrations.

1.2.5.1.- *Polarisation State of the measurement light*

Polarisation is a property of transverse waves that describes the behaviour of the electric field vector $\vec{E}$ as the wave propagates (see Figure 1.11). When $\vec{E}$ rotates uniformly through 2π radians over one wave period, the wave is said to be elliptically polarised, since the end point of $\vec{E}$ will describe within each wave period what is called a *polarisation ellipse* (Born and Wolf, 1993) perpendicular to the direction of propagation (Figure 1.11 C). If the modulus of $\vec{E}$ is constant in time, then the elliptic polarisation will degenerate into circular polarisation (Figure 1.11 B). This happens when the phase difference between the orthogonal components of $\vec{E}$, φ, is an odd multiple of $\pi/2$. When $\vec{E}$ vibrates always on the same plane, the

wave is said to be linearly polarised (δ is 0 or a positive multiple of π) (Figure 1.11 A).

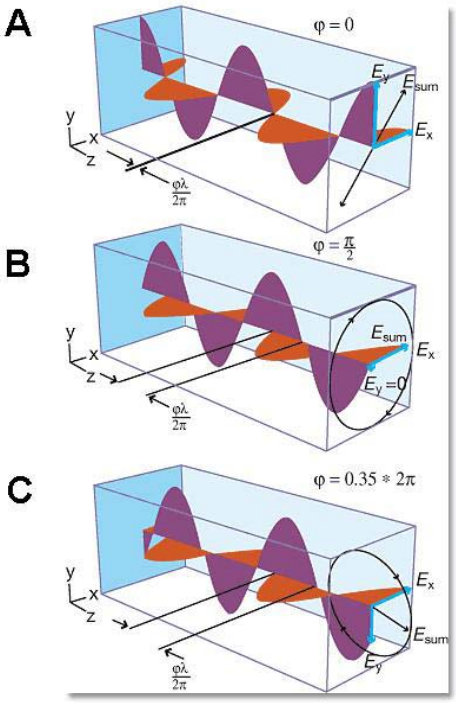

Figure 1.11. Diagrams showing different states of polarisation depending on the behaviour of electric field vector $\vec{E}$: linear polarisation (A), circular polarisation (B) and elliptical polarisation (C). φ indicates the phase difference between the x and y components of $\vec{E}$. Image obtained from http://spie.org/x17069.xml?ArticleID=x17069

There are different ways in which matter interacts with polarised light as it travels through it. The interaction of most importance in the human eye is the retardation due to birefringence. Birefringence results from the existence of two or three different refractive indices in the same material, depending on whether it is uniaxial or biaxial. When light enters a birefringent material, the incident beam is split in two different beams that travel at different speeds (depending on the refraction index they find) and therefore a phase shift will be produced between both components (retardation). When linearly polarised light goes through a birefringent material the phase shift will produce elliptically polarised

light. If the phase shift is $\pi/2$ (quarter wave plate) the resulting beam will be circularly polarised. Dichroism consists on the selective absorption of light by a material, depending on the propagation direction, and that results in partial polarisation of the light. It is present in the fovea together with birefringence (Van Blokland, 1985).

The cornea, the crystalline lens and the retina interact with polarised light (Van Blokland, 1986, Bueno, 1999, Bour, 1991), producing mainly retardation (Figure 1.12 A). The cornea is the optical element of the eye that most affects polarised light. Corneal epithelium and endothelium (see Figure 1.2) can be considered optically anisotropic. However, the stroma (see section 1.1.1.-), accounting for 90% of corneal thickness, shows birefringence. Although the intrinsic birefringence of the cylindrical collagen fibrils is cancelled out as a consequence of the different orientations of the lattices (Van Blokland and Verhelst, 1987), each lamella shows form birefringence due to the arrangement of the collagen fibrils and can be considered as a retarding plate, with its fast axis aligned with the axis of the collagen fibrils (Farrell et al., 1999). Because there exists a preferential direction in the orientation of the lamellae, usually nasal downwards, the cornea behaves as a biaxial crystal (Van Blokland and Verhelst, 1987), i.e., optically anisotropic in three directions, with the fastest axis lying along the normal to the corneal surface and the slowest axis, parallel to the corneal surface lying usually along the nasal downwards direction (from 10^o to 30^o from the horizontal). The retardation measured for human corneas varies between 30^o to 90^o, and increases from the centre to the periphery (Bueno and Jaronski, 2001, Jaronski and Kasprzak, 2003, Gotzinger et al., 2004, Van Blokland and Verhelst, 1987) and in depth (Gotzinger et al., 2004, Van Blokland and Verhelst, 1987). The birefringent structure of the cornea can be seen when the cornea is placed between two crossed polarisers: a typical polarisation cross pattern appears as seen in Figure 1.12 B. The crystalline lens would be expected to show form birefringence due to the structure of the cortex

(Bour, 1991), consisting on a stratified structure of fibre membranes and interstitial cytoplasm (Bettelheim, 1975) arranged like the layers of an onion (See section 1.1.2.-). It also exhibits intrinsic birefringence, probably induced by a regular arrangement of water-insoluble proteins that form the cytoskeletal bodies of its fibre cells (Philipson et al., 1975). However, the contribution of the crystalline lens to the birefringence of the eye is almost negligible, given that intrinsic and form birefringence values are similar in magnitude and of opposed signs, and therefore they cancel each other (Bettelheim, 1975). The retina has been reported to be dichroic as well as birefringent (Bueno, 1999, Hocheimer and Kues, 1982, Naylor and Stanworth, 1954) apparently due to the orientation of the molecules of macular pigment (intrinsic) and the Henle fibres layer (form). A minor contribution from the external segment of the cones to both intrinsic and form birefringence has also been suggested. However, the retardation and the dichroism in the central fovea are quite small.

A mean retardation of 70^{o}, which varied across the pupil, was found experimentally with double-pass ellipsometric measurements (λ=514 nm) of the polarization properties of ocular structures (Van Blokland, 1986). This shift will produce an average phase difference of $\lambda/5$ when changing the polarization of the incident light and/or analyser in the imaging channel in imaging aberrometers. Some HS set-ups described in the literature (Liang et al., 1994) use polarised light in order to avoid corneal reflexes that would make the data processing difficult. The use of polarizers in the illumination and detection channels affects the intensity of the raw data (aerial retinal images captured on a CCD camera). Changes in the polarization state of light passing through the eye produce different intensity patterns after the light passes through an analyzer. These changes of intensity have a large impact on the point-spread-function (PSF) estimates obtained by using a double-pass arrangement that incorporates a polarizing channel and an analyzer channel (Bueno and Artal, 1999). As opposed to the conventional double-pass technique,

the aerial images recorded in LRT or HS systems are used only to compute the centroid of several intensity patterns. However, relative differences in intensity in the core and tails of the retinal image or differences in shape could result in changes in the estimation of the centroid and have an impact on the wave aberration estimate. A previous study (Prieto et al., 2001) using a SRR showed no difference in the wave aberration measured with different states of polarization of the illuminating channel. The possible effect of the polarisation state of the incident and collected light in objective aberrometers (LRT and HS) will be studied in Chapter 3 of this thesis.

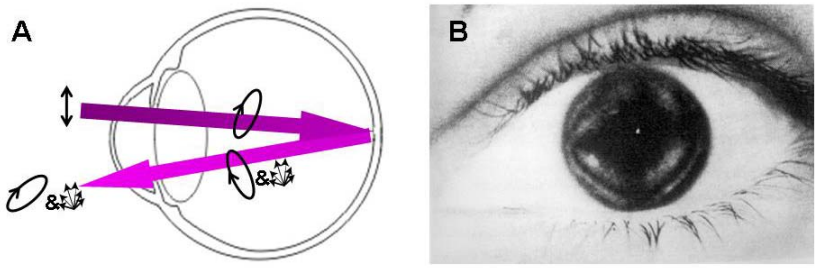

Figure 1.12. Polarisation effects in the eye. (A) Schematic diagram showing the changes that linearly polarised light suffers when it double passes the eye. The corneal and the lens, due to their birefringence, change the light to elliptically polarised. Scattering at the eye fundus produces additional retardation and partial depolarisation. The cornea and the lens introduce additional retardation to the remaining polarised light. Modified from (Van Blokland, 1986). (B) .The corneal polarisation cross. Image from (Cope et al., 1978)

1.2.5.2.- Measurement LightWavelength

Most of the currently available wavefront sensing techniques use IR illumination, due to its advantages over visible light. It is more comfortable for the patient because the human eye is less sensitive to IR (Wyszecki and Stiles, 1982); the safety limits for retinal exposure to light are larger in IR range, so more intensities can be applied to the eye (ANSI, 2000); pupil dilation is not strictly required; the retina reflects a higher percentage of the incident light compared with shorter wavelengths (Delori and Burns, 1996); and backscatter by the anterior optics is reduced

(Van Den Berg, 1997). Dynamic measurement (Hofer et al., 2001b, Fernandez et al., 2001) of aberrations is then possible using IR illumination with natural accommodation because mydriasis (and its associated cycloplegic effects, such as paralysation of accomodation) is not necessary. However, given that the visual function takes place under visible light conditions, data from visible light are desirable. For direct comparison between optical measurements (estimated from the wave aberration) and visual performance verification of the equivalence between results obtained with IR light and with visible light is needed. This is particularly important if the measured wave aberration is planned to be used to guide ablation in refractive surgery procedures (see section 1.4.1.-), where the aim is to improve the patient's visual performance. Knowledge of the defocus shift between IR and visible wavelengths is essential if the results are to be used to predict refraction.

It has been reported (Delori and Burns, 1996) that visible light is more likely to be reflected by the photoreceptor outer segments which behave as waveguides (Enoch and Lakshminarayanan, 1991, Marcos and Burns, 1999) whereas near IR light is reflected more by deeper layers RPE and choroid, which backscatter longer wavelengths (Delori and Pfibsen, 1989) (see sections 1.1.4.- and 1.1.5.-). It is also known that the estimation of defocus is affected by the retinal layer in which the light is reflected for the measurement (Howland, 1991). Refraction estimates from retinoscopy are systematically more hyperopic than those from subjective refraction (Safir et al., 1971) and this effect is attributed to the light from the retinoscope reflecting on a retinal layer in front of the photoreceptors (Glickstein and Millodot, 1970). In addition, the longitudinal chromatic aberration (LCA) based on reflectometric double-pass measurements (Rynders et al., 1998, Charman and Jennings, 1976) has been reported to be lower than conventional psychophysical estimates. These findings suggest that reflections at different retinal layers, as well as differences in reflectance and scattering across wavelengths may affect the estimation of

ocular aberrations. They also open the question whether the focus difference can be explained by the LCA and therefore be reasonably predictable across subjects. These questions will be addressed in the study presented in the Chapter 4 of this thesis.

1.2.5.3.- Pupil Sampling Pattern

The actual sampling pattern and density of sampling sub-apertures differ across aberrometers. The lenslets in HS wave aberration sensor are typically arranged in either a fixed rectangular or hexagonal configuration, and the number of samples range from around 50 to more than 15,000 spots within the dilated pupil. Ray tracing aberrometers (such as the LRT or SRR), on the other hand, sample the pupil sequentially and can use a variable sampling configuration. However, given the sequential nature of these devices, high sampling densities are not typically used, to reduce measuring times.

In the case of HS sensor increasing the number of lenslets, and therefore the sampling density, involves: 1) smaller lenslet diameters, which implies a decrease in the amount of light captured by each lenslet and an increase the size of the diffraction-limited spots; 2) greater number of spots, and therefore compromising the dynamic range of the device, as well as an increase of the processing time and potentially decrease the reproducibility, due to the lower signal strengths. In addition, increasing the number of samples may not decrease the variance of the estimates of the wave aberration (Cubalchini, 1979) nor the aliasing error (Soloviev and Vdovin, 2005). For sequential aberrometers, the determination of a sampling pattern with the minimum sampling density providing accurate results is a matter of practical importance, as it decreases measurement time.

The question of the minimum number of samples necessary is of general interest to better understand the trade-offs between aberrometers, but in addition, to study the influence of the sampling pattern will be

useful to determine whether there are sampling patterns that are better adapted to typical ocular aberrations, or particular sampling patterns optimized for measurement under specific conditions. Rectangular and hexagonal distributions are geometries typically used in Harmann-Shack sensors (Liang et al., 1994, Thibos et al., 1999, Porter et al., 2001, Fernandez and Artal, 2008) or sequential aberrometers (He et al., 1998, Moreno-Barriuso et al., 2001b, Dorronsoro et al., 2003b). However, circular sampling geometries might be more adequate for modal estimation using Zernike coefficients (see section 1.2.2.-), given the circular nature of these functions. Additionally, circular geometry might be more adequate to measure eyes with multifocal contact or intraocular lenses with concentric geometries (Martin and Roorda, 2003, Bennett, 2008). Also, some geometries could be more adequate for specific sampling patterns and need smaller number of samples to accurately retrieve the wave aberration than other geometries.

The first studies on wavefront estimates date from 1979, when Cubalchini (Cubalchini, 1979) was the first to study the modal estimation of the wave aberration from derivative measurements using a least squares method. He concluded that modal estimates of the wavefront obtained using this method, which is almost a standard today in the aberrometry community in combination with the Zernike polynomial series (Rios et al., 1997), were sensitive to the number of samples and their geometry. The problem of the optimal sampling pattern has been investigated theoretically, from both, analytical (Diaz-Santana et al., 2005, Soloviev and Vdovin, 2005) and numerical simulation (He et al., 1998, Burns and Marcos, 2000, Burns et al., 2003) approaches. The findings by previous theoretical studies, described in more depth in chapter 5, section 5.2, can be summarised as follows:

1) Number of samples: errors can be minimised by using the minimum number of samples necessary to estimate a fixed number of

Zernike terms (Cubalchini, 1979), and extracting the coefficients corresponding to the maximum complete order possible (He et al., 1998).

2) Spatial distribution of the samples on the pupil: Samples should be taken as far from the centre of the aperture as possible in order to minimise the variance of higher order Zernike terms (McLellan et al., 2006, Applegate et al., 2002, Cubalchini, 1979).

3) Sampling sub-aperture: a sampling aperture size so that the measured extent of the pupil is practically covered minimises the fit error, and the error arising from using the value of the slope at the centre of such large sampling sub-apertures has a small overall effect (He et al., 1998). Using the average slope across the sub-aperture instead of using a point estimator for the derivative at the centre of the aperture decreases modal aliasing (Burns et al., 2003).

4) Sampling patterns (density and distribution): The number of samples and geometry influences modal estimates of the wave aberration by least squares (Cubalchini, 1979). Non-regular distributions seem to perform better in terms of error minimising in presence of sampling noise than regular patterns, such as rectangular or hexagonal grids of similar density (Burns et al., 2003, Diaz-Santana et al., 2005, Soloviev and Vdovin, 2005). Cubatures have been suggested as an example of non-regular sampling schemes (Burns et al., 2003, Rios et al., 1997), and particularly Albrecht cubatures (Bará et al., 1996) have been found to be a good candidate for modal wave aberration reconstruction due to its circular geometry, and greater density in the periphery (Rios et al., 1997). Recent theoretical studies Diaz-Santana et al. (2005) found that the optimal pattern depends on the statistics of the aberration to be measured and the system error, and therefore there is no universal optimal pattern.

The determination of a sampling pattern with the minimum sampling density that provides accurate estimates for the ocular aberrations to be measured is of practical importance for sequential

aberrometers, since it would decrease measurement time, and of general interest to better understand the trade-offs between aberrometers. It is also useful to determine whether there are sampling patterns that are better adapted to typical ocular aberrations, or particular sampling patterns optimized for measurement under specific conditions. Although interesting conclusions have been reached from previous theoretical studies, the applicability to human eyes should be tested experimentally. This question will be addressed in Chapter 5.

1.2.6.- APPLICATIONS

Aberrometry has been used to study many different eye-related issues. Some examples are: 1) Ocular aberrations as a function of accommodation (Atchison et al., 1995, He et al., 2000, Hofer et al., 2001a, Plainis et al., 2005) and aging (Calver et al., 1999, Oshika et al., 1999a, Guirao et al., 2000, Mclellan et al., 2001); 2) the study of ametropic eyes (Charman, 2005, Paquin et al., 2002, Radhakrishnan and Charman, 2007, Collins et al., 1995); 3) the assessment of refractive correction techniques such as refractive surgery (Seiler et al., 2000, Moreno-Barriuso et al., 2001b), cataract surgery (Guirao et al., 2002, Barbero, 2003) or contact lenses (Hong et al., 2001, Martin and Roorda, 2003, Dorronsoro et al., 2003a); 4) the correction of ocular aberrations to visualize the eye fundus (Liang et al., 1997, Roorda et al., 2002, Burns et al., 2002). In this work aberrometry has been applied to the study of the ametropic eye (myopic and hyperopic eyes), and to the assessment the LASIK corneal surgery as a technique to correct refractive error.

A study of ametropia from an aberrometric approach can contribute to different interesting aspects of research in this topic: 1) Combined measurements of biometry and aberrometry in the same eyes will allow identification of geometrical features leading to given optical properties. 2) Given that the development of myopia and hyperopia are likely substantially different, a comparison between biometry and aberrations in

myopic versus hyperopic eyes may give clues into the development of ametropias. In addition, it has been shown that degraded retinal image quality might lead to elongation of the eye and therefore to myopia, raising the question whether degradation imposed by increased ocular aberrations might lead to development of myopia or increased aberrations in myopic eyes can be a consequence of the structural differences of the myopic ocular components. 3) Knowledge of the optical properties of ametropic eyes (i.e. typical corneal shapes, internal aberrations, etc…) will help in the customisation of correction methods, such as refractive surgery or contact lenses.

On the other hand, aberrometry has shown to be a useful tool to assess objectively the outcomes of Refractive Surgery. Information from both, corneal topography and ocular aberrometry before and after the surgery will also allow: 1) to assess the role of the crystalline lens aberrations in the surgical outcome; 2) to evaluate the changes on the posterior corneal surface and therefore potential role of biomechanical factors; 3) to identify factors related to aberration induction; 4) to understand individual surgical outcomes. 5) to understand better the corneal biomechanics, and to optimise ablation patterns.

1.3.- AMETROPIA AND EMMETROPISATION

Ametropia can be defined from the optical point of view as the refractive condition in which best focus for distant objects is not located on the retina of the unaccommodated eye. When best focus is in front of the retina, the eye is said to be myopic, and when it is behind the retina, the eye is hyperopic (see Figure 1.13). Therefore, the image will be perceived as blurred unless the eyes are corrected by refractive means, or in the case of hyperopic eyes, the eye accommodates to bring the image to the retina.

Whereas there is a considerable variation of ocular biometric

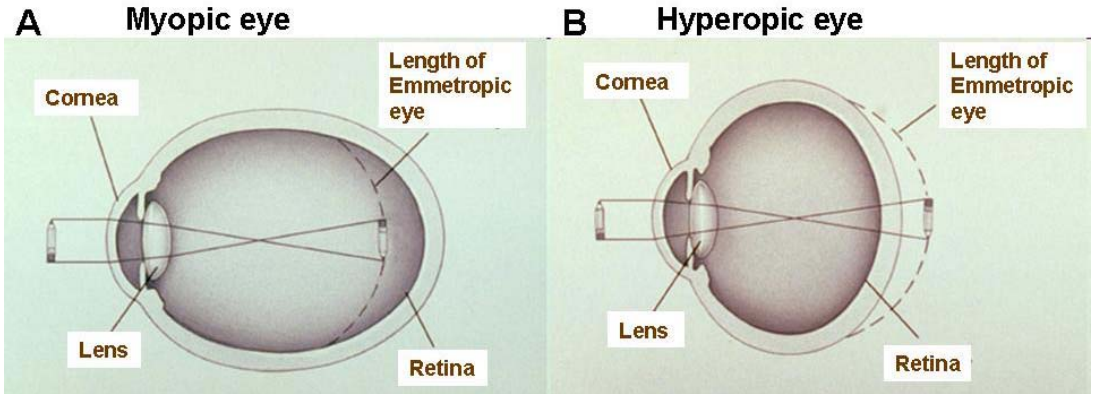

Figure 1.13. Cross-section of ametropic eyes. (A) myopic eye, and (B) hyperopic eye). The main differential feature is the axial length, longer in the myopic eye and shorter in the hyperopic eye, compared to the emmetropic eye, which is used as a refference. Modified from http://www.drsheingorn.com/CSlasik1.htm

parameters (surface curvatures, distances between components and axial length), each of which following approximately normal distributions (Sorsby et al., 1957, Sorsby et al., 1981, Stenström, 1946 in Charman, 1991b), there is a marked excess of refractions around emmetropia in the population not expectable from a random combination of these parameters. This implies some degree of correlation between the different ocular parameters, which agrees with the observations in the population (Young and Leary, 1991). Straub (1909) called emmetropisation the process that guides the ocular development towards emmetropia (the absence of refractive errors) by adjusting its axial length to the optical power of the

eye, although van Alphen (van Alphen, 1961) owns the credit for the development of the concept (Young and Leary, 1991). The key feature in his theory is that the retinal image quality is continuously monitored at the retinal level, any error signal producing adjustments in axial length. This mechanism has been shown to be visually guided (Wallman, 1993, Wildsoet, 1997, Wallman and Winawer, 2004). Studies using experimental animal eye models show that developing eyes are able to change their structural components (mainly axial length) in order to compensate for the refractive error induced by ophthalmic lenses (Wallman and Winawer, 2004, Schmid and Wildsoet, 1997, Smith and Hung, 1999, Schaeffel and Diether, 1999). In addition, corneal (Gee and Tabbara, 1988) and lens opacities, which make difficult that the retina receives a clear image (Rasooly and BenEzra, 1988), induce excessive eye elongation in infants. While ametropia can be regarded as a failure in the emmetropisation process, the exact cause for the disruption in the eye growth coordination remains unknown. However, the prevalence of myopia related to parental history of myopia seems to point out inheritance has a role in myopia development, and environmental factors related to visual experience (near work, accommodative errors, retinal defocus) seem to be also involved (Gilmartin, 2004, Weale, 2003).

While hyperopia has been usually less studied than myopia because of its smaller prevalence in developed countries, relatively stability and difficulties to measure in young hyperopes (Strang et al., 1998), myopia has attracted even more attention in the last decades. The association of myopia to a greater risk of ocular pathologies, has turned it into an important public health issue (Saw, 2003), specially in Asia and other developed and developing countries where the prevalence has increased in the last decades (Saw, 2003) (Figure 1.14). Prevalence rates are strongly associated to age and genetics (parental myopia, ethnicity) and environmental (near work, school achievement, nutrition) factors: rural areas tend to have a smaller prevalence of myopia than urban areas (Ip et

al., 2008, Saw, 2003), and in terms of ethnicity, high prevalence rates of myopia are found in Chinese and Japanese populations (Saw, 2003). Figure 1.14 shows myopia prevalence and progression in different populations of the world, where the geographical differences are evident in spite of the differences in protocols among studies (Gilmartin, 2004). Most humans are born hyperopic (Wallman and Winawer, 2004), and during the first three years of life (Sorsby et al., 1961) the cornea and the lens have to compensate about 20 D for a 5 mm increase in axial length (AL), adult dimensions being approximately reached at 2 years of age (Gilmartin, 2004). A juvenile phase comes then, between 3 and 13 years of age, where the refractive compensation decreases to about 3 D for about 1 mm increase in AL. Although coordinated biological growth of the eye ceases around 15 years of age, for an important proportion of myopes myopia starts as late as in their early twenties (Gilmartin, 2004).

The significant correlations found between AL and refractive errors points AL out as a major contributor to the refractive state of the eye. In addition, the role of AL in determining the structure of the ocular globe

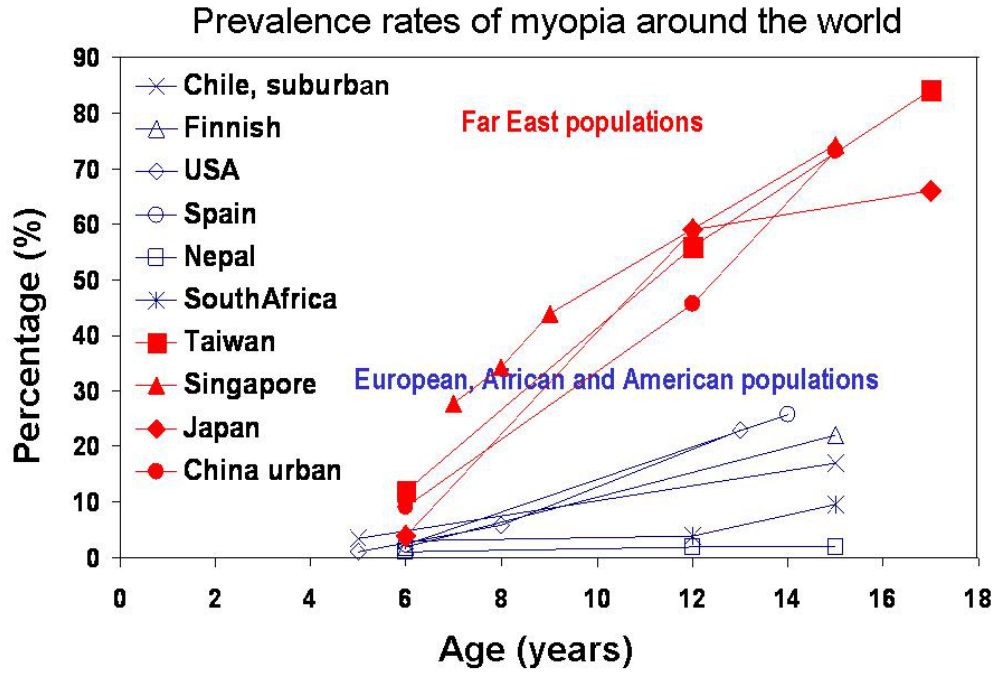

Figure 1.14. Prevalence rates (%) of myopia around the world as a function of age, from (García de la Cera, 2008).

(Sorsby et al., 1961), added to the fact that retinal neurons can be stimulated by hyperopic defocus to release growth factors to enhance scleral growth, thus resulting in an increase of AL (Schaeffel et al., 2003), confirms this as the main variable in the emmetropisation process. This is also supported by the fact that AL has been found to be significantly larger in myopic and smaller in hyperopic eyes than in emmetropic eyes (Strang et al., 1998, Carney et al., 1997, Mainstone et al., 1998, Grosvenor and Scott, 1994). In general, the myopic eye described by the literature (bearing in mind that not all studies agree) is larger than hyperopic or emmetropic eyes in all three dimensions, with a prolate shape (Cheng et al., 1992, Atchison et al., 2004), i.e., more elongated in the axial than in the horizontal and vertical directions (see section 1.1.1.-), apparently due to the constraints imposed by the orbit of the eye (Atchison et al., 2004). This elongation seems to take place at the posterior segment, given that deeper vitreous chambers have been reported for these eyes than for emmetropes (Goss et al., 1997, McBrien and Adams, 1997, Bullimore et al., 1992, Grosvenor and Scott, 1991). Myopic eyes corneas tend to be steeper (smaller anterior CR) than those of hyperopic eyes (Grosvenor and Goss, 1998, Carney et al., 1997, Sheridan and Douthwaite, 1989), and more oblate, i.e., less negative Q values (See section 1.1.1.-) (Carney et al., 1997, Horner et al., 2000, Budak et al., 1999). The crystalline lens power has been reported to be lower in myopic than in emmetropic eyes (Garner et al., 1992, Goss et al., 1997, Weale, 2003), and the anterior chamber deeper in myopic (and emmetropic) eyes than in hyperopic eyes (Weale, 2003).

These structural differences between hyperopic and myopic eyes are likely to determine differences in the optical quality of these eyes. On the other hand, since the emmetropisation process is visually guided, differences in the optical quality of some eyes, and consequent differences in imposed retinal degradation, might play a role in the development of myopia or hyperopia. Knowledge of optical aberrations in the different refractive groups will contribute to develop better correction strategies for

these eyes, but additionally might give some information on the development of ametropia.

1.3.1.- AMETROPIA AND OPTICAL ABERRATIONS

There are not many studies comparing optical aberrations (see section 1.2.4.-) across refractive groups, and the results are somewhat controversial. While some authors did not find a correlation between aberrations and refractive error (Porter et al., 2001, Cheng et al., 2003), or differences in the amount of aberrations across refractive groups (Cheng et al., 2003), other authors reported higher amounts of aberrations in myopes when compared to emmetropes (Collins et al., 1995, He et al., 2002, Paquin et al., 2002, Marcos et al., 2002a). For the SA specifically, some authors find a significant correlation with myopic error (Collins et al., 1995); or significant differences across high myopes with respect to low myopes, emetropes or hyperopes (Carkeet et al., 2002) while others did not find a significant correlation between SA and a wide range of myopia (Marcos et al., 2002a).

Given that optical aberrations degrade the retinal image quality, and a sharp image is required for proper emmetropisation, a deeper knowledge on the aberration pattern of the ametropic eye, and its relationship with the geometrical structure of the optical components will help to understand possible cause-effect relationships between optical aberrations of the eye and myopia. These effects have been debated both in humans (Thorn et al., 2003) and animal models (de la Cera et al., 2006, Kisilak et al., 2002, Smith, 1998).

1.4.- LASIK AS A CORRECTION OF REFRACTIVE ERRORS

Given that the anterior cornea is the ocular surface that contributes most to the refractive state of eye (Atchison and Smith, 2000) and its easy access, it is not surprising that corneal refractive surgery is currently one

of the most popular surgical approaches to correct ametropia. Incisional corneal surgery first attempts date from 1885 (Sakimoto et al., 2006), and the technique evolved through the 1930s and 40s with Sato (Sato, 1942) to the early 80s when Fyodorov (Fyodorov and Durnev, 1979) developed a systematic more predictable radial keratotomy process that he applied to thousands of patients. In the 1960s, Barraquer (Barraquer, 1964, Barraquer, 1967) invented the Keratomileusis, the first lamellar surgical technique. This technique consisted on separating a thin layer of the superficial corneal tissue using a microkeratome, removing a small piece of cornea, changing its curvature using a lathe, and then suturing it back into place. In the 1980s, Trokel et al. (1983) applied an argon-fluoride excimer laser (with an emission wavelength of 193 nm, which breaks carbon molecules at the corneal stroma) directly on the most external layers of bovine corneas, after previous mechanical removal of the outer layer of the cornea (corneal epithelium) thus giving birth to Photorefractive Keratectomy (PRK). A couple of years later, Seiler (Seiler and Wollensak, 1986) applied for the first time the excimer laser to treat a blind eye to treat ametropia, and in 1989 the first PRK surgery on a myopic seeing eye was performed by McDonald et al. (1989). Munnerlyn et al. (1988) calculated the thickness of tissue necessary to be removed to correct myopia and hyperopia, as a function of the distance to the optical axis. Their suggested ablation pattern included the attempted correction, the radius of curvature of the cornea to be treated, the treatment zone diameter and the corneal refractive index as parameters. However, PRK was limited by unpredictability in higher ranges of refractive error and higher risk of corneal haze after surgery (Corbett et al., 1995). In 1990s Pallikaris (Pallikaris et al., 1990) combined these two techniques (Keratomileusis and PRK), creating the Laser Assisted In situ Keratomileusis (LASIK), which has become the most popular refractive surgery technique. In this technique a hinged flap is created in the cornea by means of a microkeratome (Figure 1.15 B and C), and folded back to let

the stroma exposed (Figure 1.15 D). An excimer laser is then used to photoablate the stroma in the corresponding shape, depending on the kind of treatment (Figure 1.15 E and F). Finally the flap is repositioned in its original place without suturing (Figure 1.15 G). The shape ablation pattern depends on the ametropy to be corrected. In myopic treatment, stromal tissue is removed from the centre of the cornea (Figure 1.16 A) so that the curvature of the central cornea is flattened (Figure 1.16 B), and therefore the excessive refractive power of the myopic eye is compensated. In the case of hyperopic correction the laser removes a ring of tissue in the mid-peripheral zone of the corneal stroma (Figure 1.16 C), resulting in a cone-like corneal profile (Figure 1.16 D), which produces an increased corneal refractive power. The ablation profile in these eyes requires a smooth transition zone to prevent an abrupt step and the peripheral edge (Dierick and Missotten, 1996).

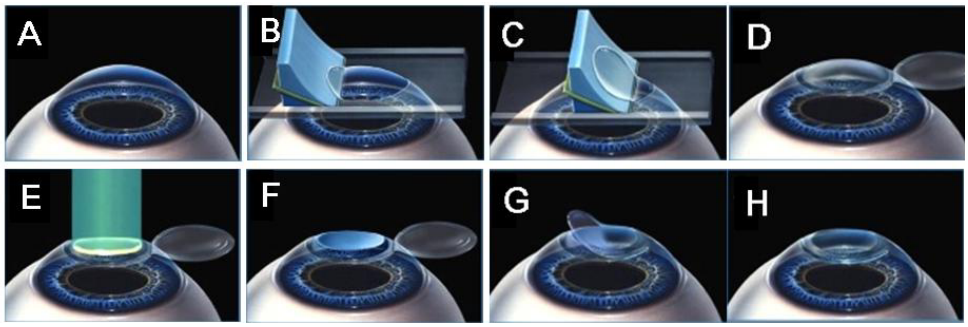

Figure 1.15. LASIK surgical procedure: A hinged flap is created using a microkeratome (B and C), and folded back to let the stroma exposed (D). The stroma is photoablated with an excimer laser in the corresponding shape, depending on the kind of treatment (E and F). Finally the flap is repositioned in its original place without suturing (G and H). http://www.eyeclinicpc.com

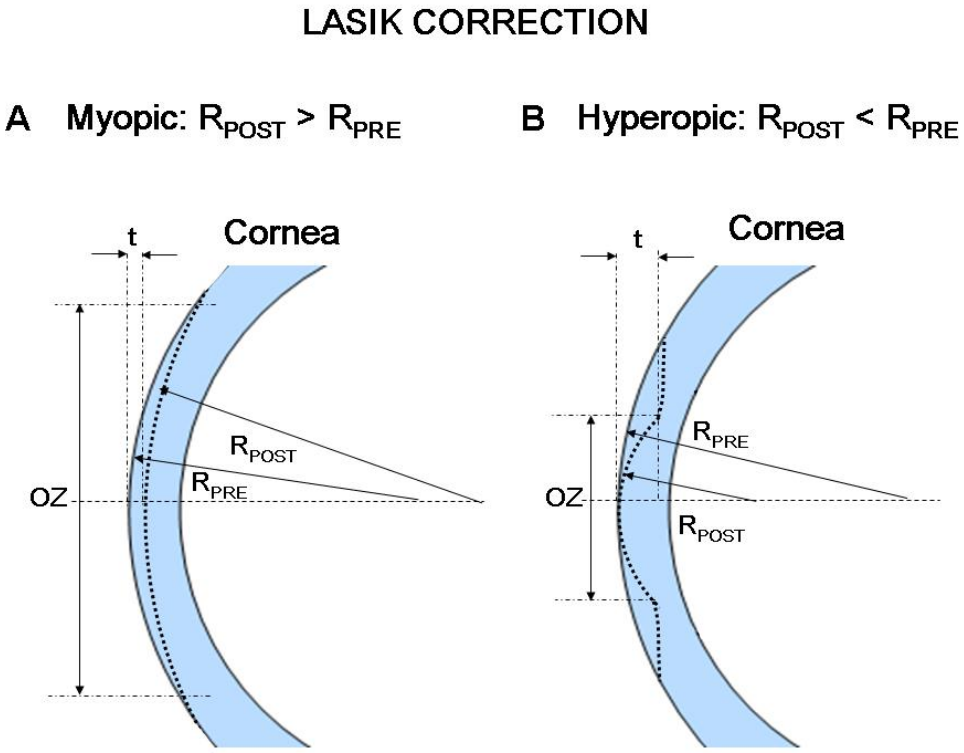

Figure 1.16. Cross-sectional representation of the ablation patterns for myopia and hyperopia correction. In myopic treatment, stromal tissue is removed from the centre of the cornea so that the curvature of the central corneal is flattened (A). In hyperopic correction the laser removes a ring of tissue in the mid-peripheral zone of the corneal stroma, resulting in a cone-like corneal profile (B). RPRE abd RPOST are pre- and post-sugical CR, respectively; OZstands for optical zt is the maximum thickness ablated in the optical zone.After Munnerlyn et al. (1988).

Although the predictability and accuracy in terms of refraction were quite good in PRK and LASIK within the prescription range suitable for each technique, the patients complained of decreased vision and glare in mesopic and scotopic light levels, i.e., night vision problems. This was illustrated by a decrease in low contrast visual acuity and contrast sensitivity (Verdon et al., 1996, Fan-Paul et al., 2002, Montes-Mico and Charman, 2002). This decrease in visual performance was attributed to haze and scars, and to optical aberrations (Seiler et al., 2000). However, glare disability and decrease in contrast sensitivity do not appear to be correlated with the magnitude of haze after PRK (Seiler et al., 2000), whereas patients with clear corneas also reported these problems (Martinez et al., 1998), and moreover, haze is reduced in LASIK. The fact that optical aberrations are more significant for larger pupils (night vision)

suggests that those are the most likely to be responsible for the reduced visual performance. In fact, the decrease in the area under the contrast sensitivity function has been shown to match the decrease in the area under the modulation transfer function obtained from wave aberrations pointing out at the optical aberrations as the main responsible of post-surgical degradation in the visual performance.

The implementation of aberrometry in refractive surgery has meant a turning point in the history of laser refractive surgery since, along with other technological advances including improvements in surgical lasers (such as flying spot lasers), ablation algorithms and eye-tracking (Mrochen, 2001) the measurement of ocular wave aberrations has opened the potential for improved refractive surgery, aiming not only at correcting refractive errors but also to minimise optical aberrations of the eye.

1.4.1.- REFRACTIVE SURGERY AND OPTICAL ABERRATIONS

Objective assessment of the optical changes induced by refractive surgery is important to understand the surgical outcomes and optimise corneal laser ablation patterns. Two approaches have been followed, both to assess and to guide ablation procedures: wavefront aberrations, which describe the aberrations of the ocular optical system (Seiler et al., 2000 , Moreno-Barriuso et al., 2001b, Campbell et al., 1999, Thibos et al., 1999), and corneal topography {Applegate R.A., 1998 #1386; Oshika, 1999 #1677; Oliver, 1997 #710; Oliver, 2001 #1379}, which allows to estimate aberrations of the anterior surface of the cornea as well as geometry data (CR and Q). Given that the ablation takes place at the anterior corneal surface, anterior corneal topography seems a suitable tool to assess the outcomes of the surgery. As mentioned above, high correlations between corneal aberrations (wavefront variance) and visual performance (area under contrast sensitivity function) (Applegate et al., 2000) as well as under pre/post- surgical MTF and CSF ratios (Marcos, 2001) have been

reported. However, it is not clear whether aberrations estimated from corneal topography are a sufficient tool to assess optical outcomes, given that even though refractive surgery takes place on the anterior surface of the cornea, the optical properties of this surface are combined with those of the other ocular surfaces to yield the ocular (total) optical quality. Information from both corneal topography and ocular aberrometry is important in understanding individual surgical outcomes, since information of the influence of other optical components of the eye in combination with the cornea on the overall optical quality can be obtained. It also provides insights into the biomechanical response of the cornea (both the anterior and posterior surfaces) to laser refractive surgery, and therefore changes on the posterior surface of the cornea could be assessed.

Published studies on the change of aberrations with refractive surgery for myopia report an increase of total (Seiler et al., 2000, Moreno-Barriuso et al., 2001b) and corneal (Oshika et al., 1999b, Oliver et al., 1997) HOA (i.e. excluding tilts, defocus and astigmatism), mainly due to an increase of SA towards more positive values, although a significant increase in the coma term was also found. Earlier studies of hyperopic correction with excimer laser also suggest an increase of optical aberrations with the procedure. Oliver et al (Oliver et al., 2001) reported a change with PRK in corneal SA from positive in all cases towards negative values and a significant increase in coma RMS. This change in corneal aberrations was greater than that obtained in their previous study on myopic PRK, and consistent with the change in corneal asphericity towards more negative values reported by Chen et al (Chen et al., 2002). Ma et al. (2004) found the greatest RMS and most negative total and corneal SA in their hyperopic LASIK group when compared to their control eyes group and lensectomy group corrected (with intraocular lens implantation) for hyperopia. Additionally, they found significant differences in the internal SA in the LASIK group.

The reported increase in aberrations after surgery, specifically SAs, has driven the advance of corneal refractive surgery due to its impact on postsurgical visual quality. With the insight gained in recent years, the expectations on wavefront-guided procedures have now changed from eliminating to reducing the natural aberrations of the eye, and to minimise the aberrations induced by the procedure (Padmanabhan et al., 2008, Kim et <al., 2004, Schallhorn et al., 2008, Kim and Chuck, 2008, Zhang et al., 2008, Netto et al., 2006, Mrochen, 2006). Technological advances (high frequency eye-tracking, improved laser delivery systems, flap creation by femtosecond lasers) (Netto et al., 2006) as well as the greater experience of the surgeons with the platforms available and nomogram optimisation may explain the improvement in the outcomes of wavefront-guided surgery in terms of decrease of induced aberrations reported by more recent studies (Kimet al., 2004, Zhang et al., 2008). Theoretical (Anera et al., 2003, Jimenez, 2004a, Jimenez, 2004b, Kwon et al., 2008, Arba-Mosquera and de Ortueta, 2008) and experimental (Dorronsoro et al., 2006) models are being used to identify the different factors that contribute to the induction of the aberrations during the surgery. These different works are being carried out in order to avoid the induction of aberrations by the corneal refractive surgery and they reflect the influence of the experimental work presented in Chapter 6 of this thesis on the evolution of the this field.

1.5.- THESIS SYNOPSIS

The body of this thesis is structured as follows:

In **Chapter 2** a description of the common methods used throughout this thesis is given, specifically the laser ray tracing technique used to measure ocular aberrations in subjects. A description of the setup and the control and processing software follows. Finally, some calibrations of the system are reported.

Chapter 3 presents the study carried out to verify whether the polarisation state of the measurement light used in aberrometry reflectometric techniques (Laser Ray Tracing and Hartmann-Shack) to measure aberrations influences the estimated wavefront. For this purpose, wavefront estimations obtained from different states of light and analyser polarisation are studied as well as the changes in the raw images obtained.

In **Chapter 4** the study performed in order to find out the effect of using IR (786 nm) instead of visible (543 nm) light to measure aberrations using reflectometric techniques is explaned. The consistence between the difference in the defocus term with both wavelengths (focus shift) and the shift due to longitudinal chromatic aberration has also been verified. This has important implications for the computation of the refractive error from aberrations measurements.

In **Chapter 5** the effect of applying different patterns to sample the pupil when measuring ocular aberrations on the wavefront estimates is analysed. For this purpose artificial and human eyes were measured using different sampling distributions and densities on the pupil, and the resulting aberrations were studied. In addition numerical simulations were used to extend the extent of the experimental results to abnormal eyes, such as keratoconic or post-surgical eyes.

Chapter 6 compares optical and biometric properties in two age and refractive error matched groups of myopic and hyperopic eyes, using an optical and geometrical approach. Measurements of anterior corneal and ocular aberrations were performed as well as axial length, and corneal radius and asphericity. The combination of this information gives us an insight on the relationships between the different parameters, as well as the contribution of the crystalline lens to the ocular aberrations.

Chapter 7 presents the application of ocular and corneal aberrometry to assess the changes produced by LASIK surgery in myopic and hyperopic eyes.

Finally, **Chapter 8** summarises the major findings of this work, and presents a discussion on the implications of the results.

Chapter 2

METHODS

In the current chapter the experimental techniques used in this work are described, and specifically, the Laser Ray Tracing (LRT) technique. The contributions of the author of this thesis have been mainly in the processing software (sections 2.2.2.2.- and 2.2.2.3.-), as well as calibrations (section 2.3.-) of the LRT device. Specifically, in this chapter are presented: 1) the general principles of the technique and the optical implementation of LRT used in the lab to measure the aberrations; 2) the software developed to control the device, as well as the software to process the raw images in order to compute the aberrations and to estimate eye movements during the measurement; 3) Different calibrations carried out to get the system ready for measurements; 4) the general protocol followed in the measurement sessions. The first description of the new LRT device, was presented as part of a poster (Dorronsoro et al., 2003b), at the Spanish Optical Society (SEDO) annual meeting (2003), where C. Dorronsoro won a Young Investigator Award as first author of this work, and as a talk at the Spanish Physics Society meeting the same year. The authors of this work were: Carlos Dorronsoro, Elena García de la Cera, Lourdes Llorente, Sergio Barbero and Susana Marcos.

The contribution of the author was: 1) participation on the design and implementation of the device (assistance in placement and alignment

of elements in the setup, in hardware connections and in the installation of drivers); 2) testing and debugging the control software, giving feedback from the measurements and suggesting possible improvements; 3) developing of a new software for computing ocular aberrations from the retinal images using some routines from the previous device; 4) automating the software to compute eye movements from the pupil images; 5) calibration of the setup. An statistician advised most of the statistics used in this chapter.

2.1.- MEASUREMENT OF OCULAR ABERRATIONS: THE LASER RAY TRACING TECHNIQUE.

As mentioned in Chapter 1, there are different techniques to measure ocular aberrations. Most of the experimental measurements of aberrations in this thesis were performed using Laser Ray Tracing (LRT) technique. This technique was chosen for its advantages versus other techniques such as Hartmann Shack (HS) (see Chapter 1): greater dynamic range, which allowed to measure highly aberrated eyes without complications (see Chapter 7), and flexibility in the configuration of the sampling pattern (see Chapter 5).

The LRT technique was first applied to measure ocular aberrations in human eyes in 1997 (Navarro and Losada, 1997, Molebny et al., 1997). A deeper description of the method can be found at Moreno-Barriuso's thesis (Moreno-Barriuso, 2000). This is a double pass technique, since light is delivered into the eye and the reflection from the retina is captured on a CCD camera (see Figure 2.1). In the first pass the pupil of the eye is sequentially sampled with laser pencils parallel to the optical axis. Each ray is deflected at a specific angle α depending on the slope of the wavefront at that particular point of the pupil plane (defined by the optical characteristics of the surfaces it goes through), and therefore will impact the retina at a specific point. In an aberration-free system, all rays

superimpose on the same retinal location. However, when optical aberrations are present the rays hit the retina at different positions. In the second pass the light is reflected off the retina, exiting the eye through the whole pupil, and forming an aerial image of the double-pass (or rather one-and-a-half-pass (Navarro and Losada, 1995)) point spread function (PSF) on a plane conjugated with the retina, but displaced an angle α away from the reference (chief ray, entering the eye through the pupil centre). This angle α is proportional to the slope of the wavefront at the point where the incoming beam entered the eye. This image is collected by a high resolution cooled CCD camera. Although in this second pass the aberrations of the eye affect the PSF, its position relative to the reference is not affected (as long as the PSF is contained within the isoplanatic area of the retina). Therefore, the angles are preserved, and the ray (transverse) aberration can be computed from the distance between the position (centroid) of the aerial image corresponding to each pupil location, and that corresponding to the aerial image for the reference ray (chief ray). The sampled pupil size is defined by the diameter of the sampling pattern projected on the pupil, and therefore, can be controlled by software (as long as the eye pupil is at least of the programmed diameter).

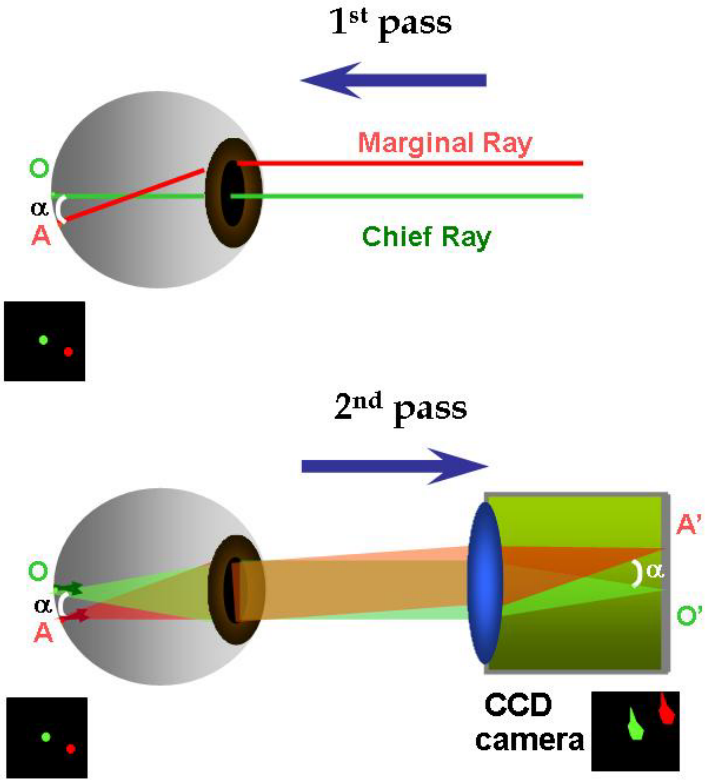

Figure 2.1. Laser Ray Tracing Technique.

In the 1st pass (top) rays are deviated due to the aberrations, in the 2nd pass (bottom) light reflected off the retina exits the eye through the whole pupil and is recorded by a CCD camera. O and A indicate the position where the chief and marginal rays strike the retina, respectively, separated an angle α. O' and A' indicate the position (centroids) of the aerial images corresponding to the chief and marginal rays, respectively, collected by the CCD camera. These are separated an angle α in the CCD. Modified from original diagram by S. Marcos and E. Moreno.

The wavefront phase is estimated by modal (Cubalchini, 1979) fitting of the directional derivatives of the wave aberration (transverse ray aberration) to the derivatives of the Zernike polynomials, using a standard least squares procedure. This approach has been chosen instead of zonal (Southwell, 1980) fitting due to the advantages previously mentioned (see Chapter 1, section 1.2.2) and because it is the standard in the visual optics field. A seventh-order Zernike polynomial expansion has been used in this thesis, unless indicated otehrwise. A representation of the Zernike functions can be seen in Figure 1.8, Chapter 1. In addition to Zernike polynomials, the Root Mean Square (RMS) wavefront error will also be used as a global metric for the optical quality. RMS is computed directly from the Zernike coefficients, using the following approximation:

$$RMS = \sqrt{\sum_{n,m} \left(Z_n^m\right)^2} \qquad (2.1),$$

where Z_n^m is the Zernike coefficient corresponding to the order *n* and frequency *m*. This approximation is considered valid, given that terms beyond 7th order can be considered negligible for human ocular aberrations(Porter et al., 2001, Castejon-Mochon et al., 2002, Thibos et al., 2002).

2.2.- THE LASER RAY TRACING DEVICE.

Two different LRT devices, both built at the Instituto de Óptica, Madrid (Spain), were used to measure ocular aberrations in this work. The first device (LRT1) was built by Esther Moreno during her doctorate research (Moreno-Barriuso, 2000, Moreno-Barriuso and Navarro, 2000, Moreno-Barriuso et al., 2001a, Moreno-Barriuso et al., 2001b) and was validated by comparison with other aberration measurement techniques, such as HS and the SRR (Moreno-Barriuso and Navarro, 2000, Moreno-Barriuso et al., 2001a). This device has been used in the work presented in Chapters 3, 4, and 7, and in part of Chapter 6. A diagram of this setup can be found in Chapters 3 and 4. The second device (LRT2), which will be briefly described in the next section, was developed during this work, and used in the work presented in Chapter 5 and part of Chapter 6. LRT2 incorporates some additional features especially advantageous for measurements in ametropic eyes (Dorronsoro et al., 2003b, Llorente et al., 2004a). The most important advantage of LRT2 over LRT1 is the possibility of correcting large amounts of spherical defocus continuously by means of a Badal system (see Section 2.3.5.- of this chapter) and the presence of a plane conjugate to the pupil plane (CPP), where trial lenses can be placed. Other improvements include: 1) the use of infrared (IR) light in addition to visible green light; 2) increase of the speed to less than 2 seconds for an entire typical run; 3) continuous display of pupil images

during the measurement and simultaneous recording of the pupil and of retinal aerial images; 3) easy selection of the pupil sampling density and pattern by software; 4) fully automated control software; 5) it is more compact and lighter, what is especially advantageous to avoid misalignments of the optical components during transportation. The equivalence between both devices was verified, as will be shown in Section 2.3.8.- of this chapter, and was first reported in Llorente et al. (2004a). Measurements performed with both devices, unless differently indicated, followed the same protocols and were carried out under the same conditions (see section 2.4.-).

2.2.1.- EXPERIMENTAL SETUP

A schematic diagram of the LRT2 setup, as well as a photograph of the actual device are shown in Figure 2.2 A and B. The system consists of four channels; 1) Illumination channel, with two possible light sources (green 532 nm or IR 785nm laser diodes) focused on the XY scanner, and then collimated by the lens L3 in order to compose the desired sampling pattern on the pupil plane. 2) Retinal imaging channel, where the light reflected back from the retina is captured by the retinal CCD. 3) Pupil monitoring channel, where the pupil CCD captures the corresponding image of the eye's pupil, simultaneously with the retinal spots on the retinal CCD; 4) Fixation channel, where a target is displayed on a CRT monitor during the measurement. All channels share a Badal system, for compensation of defocus, formed by lenses L1 and L2 and mirrors M1, M2 and M3. P marks the position of a pupil conjugate planes, and R marks the position of retinal conjugate planes.

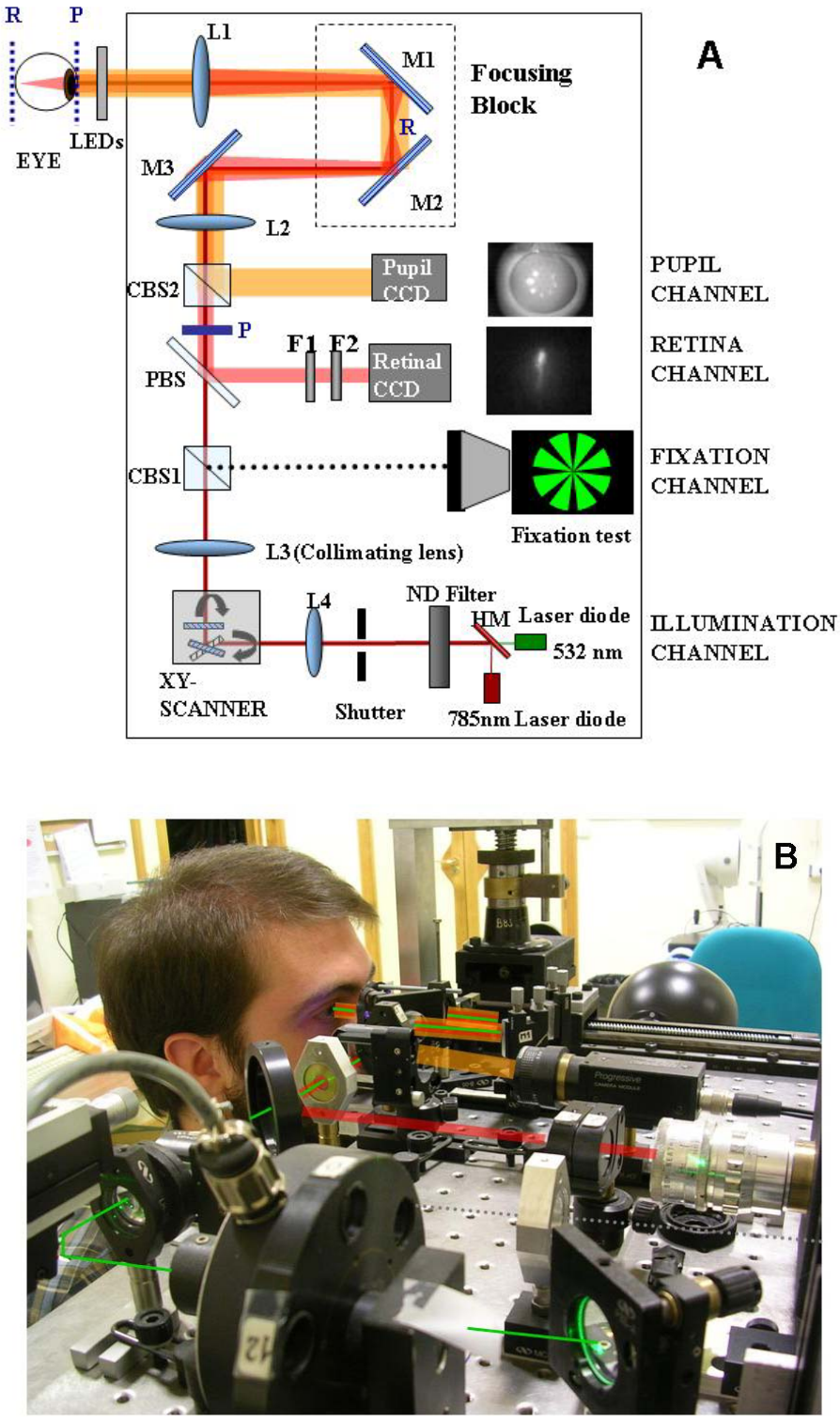

Figure 2.2. LRT2 setup described in the text.

A Schematic diagram of the device. L1 and L2 are 100-mm focal length achromatic doublets, and L3 and L4 are 50.8-mm focal length achromatic doublets, all with 25.4 mm diameters, M1, M2, and M3 are plane mirrors, HM is a hot mirror, CBS1 and CBS2 are cube beam splitters, PBS is a pellicle beam splitter, F1 and F2 are interferometric filters for 785 and 532 nm, respectively, and P and R are planes conjugate to the pupil and the retina, respectively. (B) Detail of the actual system during a measurement on a subject.

The light source can be selected between two diode lasers emitting in green (532 nm; Brimrose, Baltimore, USA) and IR wavelengths (785 nm; Schäfter + Kirchhoff, Hamburg, Germany). Prior to the systematic use of IR wavelength in the measurements, the equivalence of IR and green light in the measurement of ocular aberrations was confirmed (see Chapter 4). Both lasers were attenuated below safety limits using neutral density filters. The maximum permitted exposure (MPE) (ANSI, 2000, Delori et al., 2007) power thresholds for 532 nm and 785 nm (for 10 s exposure) were 576.2 μw and 54.μm respectively. At least three ND4 neutral density filters were used to attenuate the power down to 4.1 μw and 6.8 μw, and more filters where added when possible. Exposure times (about 1.5 seconds for a typical run with 37 samples) were controlled by an electronic shutter (Vincent Associates, Rochester NY, USA).

The XY scanner (mod.6210, Cambridge technologies, Lexington, USA), consists of two rotating mirrors that deflect the incoming unexpanded laser pencil in order to compose the sequential sampling pattern in combination with collimating lens L3 (f'=50.8 mm). Due to the distance between the two mirrors (~5 mm), some astigmatism is induced in the system (Navarro and Moreno-Barriuso, 1999), and therefore a trial lens attached to the collimating lens (+2.50 at 0^{o}) is used to correct this astigmatism (see Section 2.3.3.-). Lens L4 (f'= 50.8 mm) forms the image of the laser waist on the scanner in order to obtain the smallest sampling aperture on the pupil plane (~400 μm). The flexibility provided by the scanner to configure sampling patterns with different distributions and densities of the samples was essential for the study on sampling patterns reported in Chapter 5.

The light reflected off the retina is collected by a cooled highly sensitive CCD camera, conjugated to the eye retinal plane (retinal channel). The features of this camera are: 12 bits, 30 frames per second with 2x2 binning, 1024x1024 pixels, 14 μmx14 μm pixel size, 20% nominal

maximum quantum efficiency (700 nm); model 1M15 by Dalsa, Waterloo, Canada. In addition to record aerial images, this camera can display them in real time. This allows to find objectively the best focus position while assessing the aerial image for a centred ray. During the measurement, the retinal camera is synchronised with the scanner and the pupil camera.

In the pupil channel a CCD continually monitors the pupil and records pupil images during the measurement. The features of this camera are: 8 bits, 60Hz (video), 646 (horizontal) x 485 (vertical) pixels, 7.4μmx7.4μm pixel size; model XC-55 by Sony Corp., Tokyo, Japan. Pupil real time images combined with the marks superimposed to the pupil image in the control program (see Figure 2.3), help to verify that everything is ready for the measurement: pupil located on the corresponding plane (pupil edges focused), alignment of the centre of the pupil and the optical system (centration cross) and suitability of the sampling pattern to the pupil diameter (small circumferences for samples entry locations and circumferences of different diameters to estimate pupil size). Pupil monitoring during the measurement allows to verify that no anomalies, such as blinking, large eye movements, tear problems, etc, occurred as well as to ensure the eye's stability. Five IR LEDs (peak wavelength 880±80 nm) arranged in a circular frame in front of the eye illuminate the pupil during the alignment (frontal-illumination). In addition, back-illumination is also possible when only the measurement light is used, and has proved to be very useful to visualise some features, such as crystalline lens opacities or tear film break up. Recorded images can also be used for passive eye-tracking (see Section 2.2.2.3.-), i.e. post-measurement correction on the pupil sampling coordinates when the eye moved during the measurement.

Recordings of a typical run can be seen at http://www.journalofvision.org/4/4/5/article.aspx#Movie1 (find also file movieLRT.mov attached to the electronic copy of the manuscript). In

this file a video of the pupil (front-illuminated) as the entry beam scans discrete locations of the pupil is shown on the left. The ray entry position are marked with a circle. The corresponding retinal aerial images are shown on the right as the beam moves across the pupil. Figure 2.4 shows a frame of the movie.

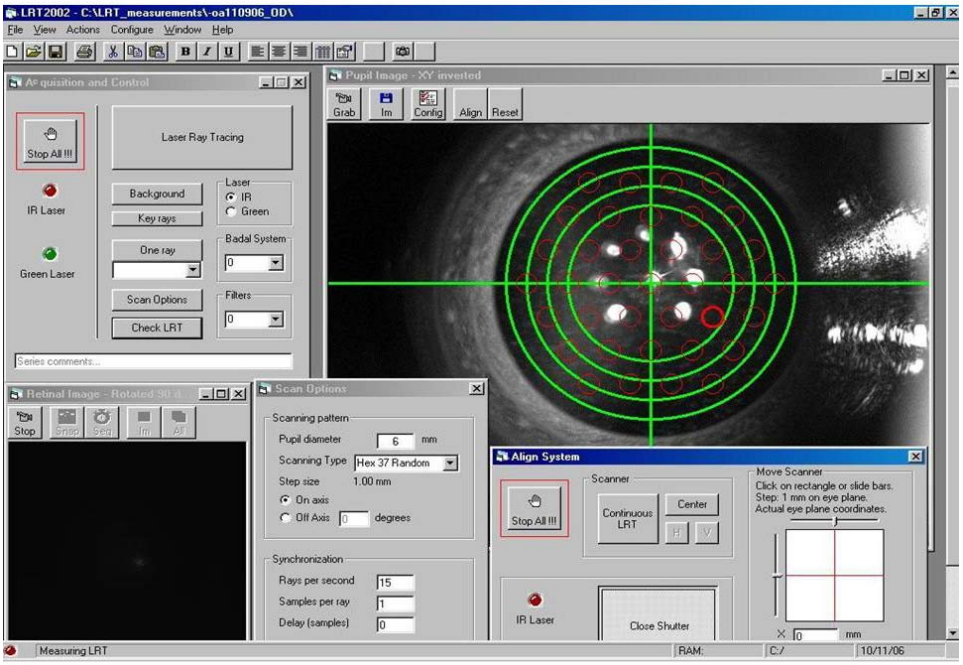

Figure 2.3 Snapshot of the control program developed by Carlos Dorronsoro for LRT2. Top right and bottom left are the pupil and retinal images, respectively

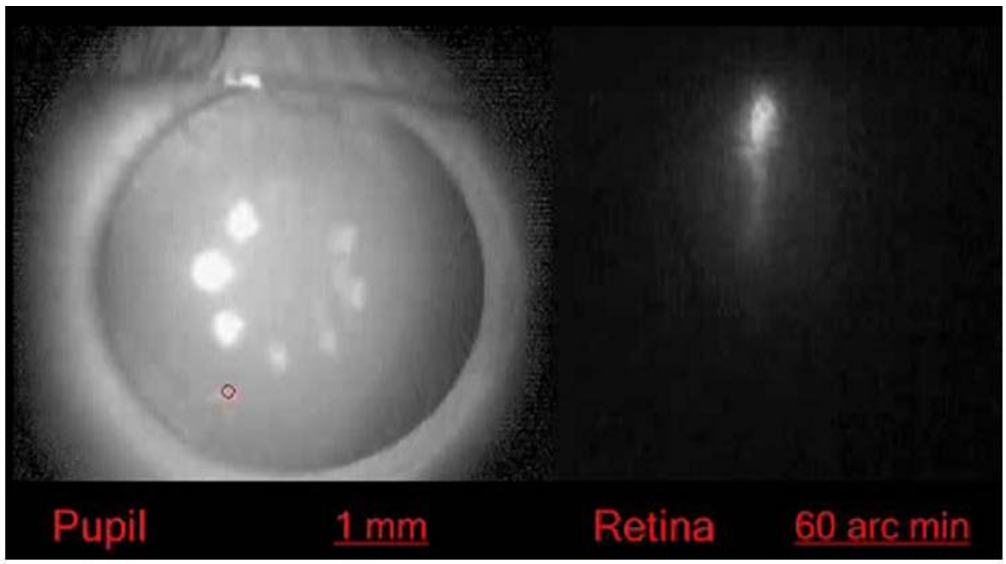

Figure 2.4. Frame of a movie showing a typical run with LRT2. The left image shows a frame of the (front-illuminated) pupil, with the entry point of the ray marked with a circle, and the right image shows the corresponding retinal aerial image. Both images belong to a frame of the movie that can be found at http://www.journalofvision.org/4/4/5/article.aspx#Movie1, showing recordings of a typical run with LRT2.

A 15 inches CRT monitor (Sony Corp., Tokyo, Japan) is used to project stimuli to help the subject to keep his/her eye fixed in optical axis direction of the system, and unaccommodated during the measurement. The fixation test, consisting of a green circle with black radial lines thickening towards the periphery (see fixation test in Figure 2.2 A), can be used to assess subjectively the refractive state of the subject's eye to be measured.

Finally, defocus correction in the system is carried out by a Badal system (Smith and Atchison, 1997), which allows to change the vergence of the rays (and hence defocus) without changing magnification, and therefore ensuring that the pupil magnification or the sampling density will not be affected by defocus correction. Our Badal system shares path with the different channels of the setup (see Figure 2.2 A), so that defocus is corrected in the illumination, imaging and fixation channels as well as the pupil monitoring channel. It is composed by two achromatic doublets (L1 & L2) of equal focal lengths (100 mm), that form an afocal system of magnification X1, and three flat mirrors: M3, which bends the optical path to obtain a more compact device, and M1 and M2, which can be moved as a block (Focusing Block) to change the optical path between the lenses, and consequently the dioptric correction (see Section 2.3.6.-). Moving the mirrors instead of the lenses has the advantage of not displacing the optical planes of the system. Spherical error corrections ranging from -5.50 D to +13 D can be induced with this system. Furthermore, easy access to pupil conjugate plane (P) allows to position trial lenses when a higher dioptric correction is needed.

2.2.2.- *SOFTWARE*

The software development was aimed at an intuitive and user-friendly, control program. The interface was written in visual basic (Microsoft Visual Basic; Microsoft Corp., USA), combined with Matlab (Matlab; Mathworks, Natik, MA) scripts. The data structure was organised

so that data interchange between programs, such as control and processing software, was efficient, and tracking error sources was straightforward. The next subsections describe the control software, and processing software for retinal and pupil images software.

2.2.2.1.- System Control Software

New control software was created for the LRT2 setup by Carlos Dorronsoro. The aim was to make the measurements faster (less than 2 seconds compared to 4 seconds for the former LRT1, for 37 samples), and more flexible. The program also allowed to change easily the sampling pattern (scanned pupil diameter, sampling arrangement and density), what was very useful for the study comparing sampling patterns presented in Chapter 5. Figure 2.3 shows a snapshot of the control program. Pupil and retinal images can be visualised in real time, so that measurements could be discarded on-line, and a new series immediately be run. The software also facilitates alignment and calibration operations (see sections 2.3.2.- and 2.3.3.-.)

Particularly, the routine "Test LRT" allows to verify the correct delivery of the programmed pattern on the pupil. When this routine is activated, a series of circumferences indicating the nominal position of the samples and a centration cross appear superimposed to the pupil image (see pupil image frame in Figure 2.3). Simultaneously the shutter opens and the scanner starts to scan the programmed sampling pattern. A thicker circumference indicates the nominal position for the corresponding sample, i.e., the position where the laser spot should lie. When the central position is selected for the beam, alignment of the laser and optical axis the overlapping between the spot and the centration cross can be verified.

2.2.2.2.- Processing Software for retinal images (ocular aberrations)

The software to estimate the ocular aberrations from the set of aerial images was profoundly improved from its original LRT1 (Moreno-Barriuso, 2000) version in order to make the computation of aberrations easier, quicker, more robust and efficient, with better quality and traceability of errors or problems detection, and adapted to the new setup parameters and possibilities. The contribution of the author of this thesis in this software includes: collaboration in the design of the new data structure; writing of the new Matlab code; testing and debugging of the software; collaboration in the Visual Basic interface. Some specific improvements in the software include:

1) Calculation of those parameters necessary for the processing that depend on specific characteristics of the optoelectronics setup and inclusion of their values in the corresponding calibration data file;

2) Adaptation of the software to the new data structure defined by the control software: input data were read from the files created during the measurements, and structured result files were created for the output data;

3) Organisation of the program as a modular structure to allow for a Visual Basic interface, more efficient for the processing and more user-friendly;

4) Regarding image processing: possibility of choosing different processing parameters (thresholds, Zernike order to fit), as well as using default values; manual selection of the region of interest or of the images to exclude from the processing when necessary; possibility of undoing the last change; on-line visualisation of parameters significant for the processing such as maximum intensity of the images or spot diagram (joint plot of the centroids of the images already processed).

5) A graphic as well as numeric presentation of the results that allows to easily detect series that do not follow the common trend or do not have the same measurement conditions as the rest of the series of the same session. The results file also includes a worksheet where corneal aberrations are saved when available (see chapters 6 and 7), in order to summarise all the related results in one file.

A snapshot of the processing software interface is shown in Figure 2.5. Basically, raw images are processed (background subtraction, filters and masks application, thresholds setting, etc) in order to isolate each aerial image and localise the corresponding centroid. Then, the relative distance of each centroid to the central ray centroid is calculated (transverse aberration), and the wave aberration is then estimated by fitting the transverse aberration corresponding to each sampled point to the derivatives of the Zernike polynomials, using a least squares method (Cubalchini, 1979). The interface, as shown in Figure 2.5, allows the user to visualise the raw images, select the next processing to apply to the image and check the image appearance after processing has been applied, with the corresponding centroid position superimposed on the image. As previously mentioned, a joint plot with all the centroids positions (spot diagram) is also available. The program extracts the input data necessary for the wave aberration estimation from the corresponding excel file stored during the measurement, and saves the results in a new excel file in the corresponding project folder.

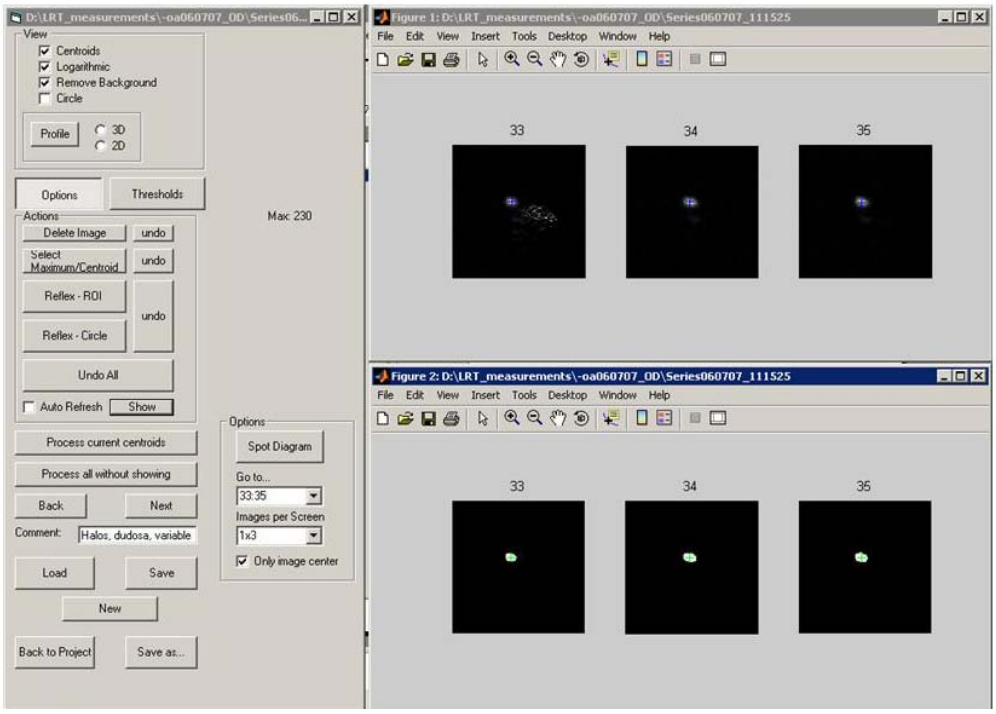

Figure 2.5. Snapshot of the processing software interface showing some images before (top right) and after (top left) processing.

2.2.2.3.- Processing software for pupil images (passive eye-tracking)

A passive eye-tracker, based on the pupil images obtained during the measurements, was developed using image processing techniques to detect the pupil edge. This program made it possible to account for the influence of eye movements in the uncertainty of the measurement (see Chapter 5, Section 5.5.1).

As in the previous processing software, the parameters from the measurement necessary for this program are automatically read from the corresponding excel files, and the pupil images in the series are automatically opened (Figure 2.6 A). The program detects the edges within each image, and labels them (Figure 2.6 B). The edge corresponding to the pupil is selected by choosing those labelled areas which extension is larger than a set minimum. Then a binary image containing only the

selected edge (Figure 2.6 C) is correlated with circumferences of different radius and thickness. The radius is chosen within a reasonable interval, considering the dimensions of the previously detected pupil edge, as well as realistic values for pupil radius, and the thickness is given by the desired tolerance. The greatest value across the maximum correlation values for each constructed circumference determines which circumference (radius) corresponds to the edge of the pupil, and its coordinates within the image indicate the position of the centre of the pupil (Figure 2.6 D). The circumference that yielded the best correlation is then used for the rest of the images of the series, as the changes in the dilated pupil radius are considered negligible within a series. Actual pupil coordinates (ray entry locations at the pupil, considering the pupil misalignment) are computed from the distance between the reference (optical axis of the system, where the pupil centre should be located during the measurement) and misaligned pupil centres (Figure 2.6 E). The output of the program includes the rays order, the nominal and actual ray pupil entry locations, and the radius and coordinates of the pupil centre (from the fitted circumference). Output figures include the outline (red dots) and centre (red cross) of the pupil circumference, as well as corresponding nominal (blue cross) and actual (red open circle) entry positions and the reference location (green cross) superimposed to each pupil image (Figure 2.6 E). Two summary images with joint plots are also produced: 1) nominal (blue crosses) and actual (red open circles) rays entry locations for all the images in the series (Figure 2.7 A), and 2) pupil centres computed for each images (blue Xs), with the reference (green cross) (Figure 2.7 B). The program takes about 255 seconds to process a series of 37 images. This speed was sufficient for our purposes, although further improvements of the program would result in a higher speed.

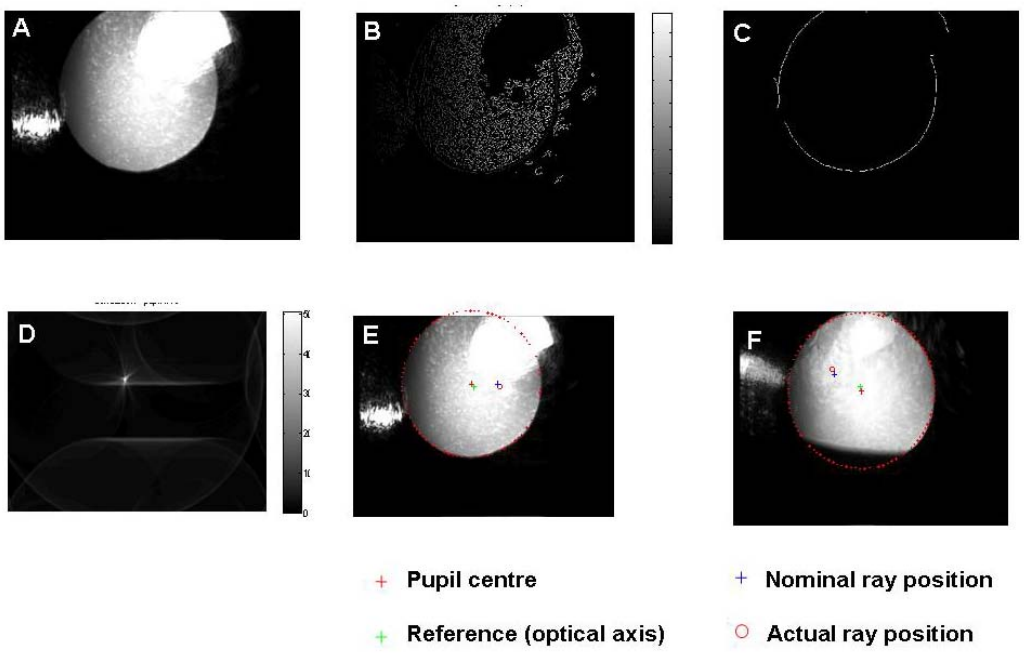

Figure 2.6. Illustration of the steps performed by the pupil processing software:. (A) input pupil image obtained from the control software; (B) same image labelled edges; (C) same image with only selected edges; (D) correlation values throughout the image for the selected construction circumference; (E) initial image with the resulting circumference outline (red dots) and centre (red cross) as well as corresponding nominal (blue cross) and actual ray (red open circle) entry locations.

This algorithm has proved to be robust for our back-illuminated images, even in the presence of strong reflections, or when the pupil was vignetted (see Figure 2.6 E) or partially occluded by the eyelid (see Figure 2.6 F). In the last case, it is important that the pupil is not occluded by the eyelid in the first image of the series. The algorithm was also tested for images of pseudophakic eyes, where the intraocular lens edge could be seen through the pupil. In this case, too many circles appeared in the image and the pupil could not be correctly identified. This algorithm may not work properly either for very elliptical (for example, in off-axis measurements) or asymmetric pupils. In the first case, using an ellipse instead of a circumference for the correlation would solve the problem. The second case is more complicated, as the pupil centre definition may not be very clear, to start from Since the algorithm was appropriate for

the images to process, no work further along this line was made although, as explained, there is room for improvement.

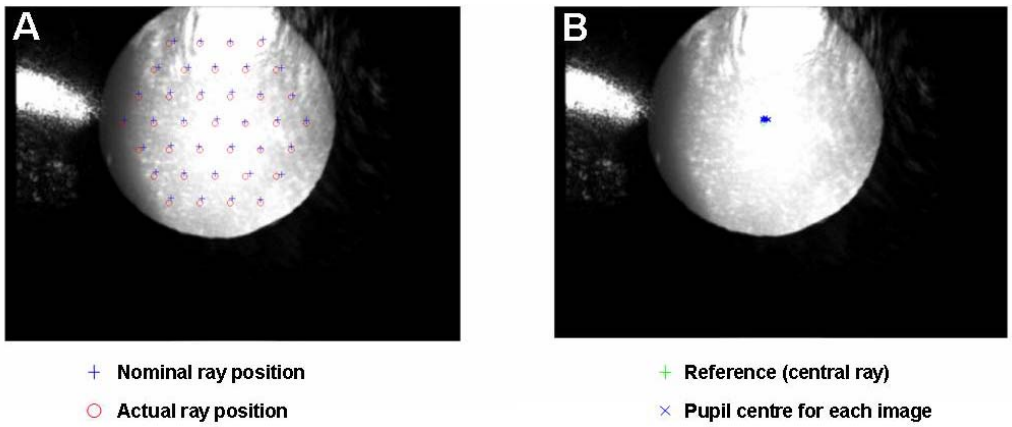

Figure 2.7. Example of output figures from the pupil processing showing: (A) joint plots of nominal (blue cross) and actual (red open circle) ray pupil entry locations, and (B) of the reference location and the pupil centre, across the pupil images corresponding to one series.

The analysis of the data provided by this programme allows to identify two different effects of the eye shift patterns: a shift similar to an offset that deviates the pupil from the reference position to another "balance" position (0 mm for x and 0.05mm for y, for the eye in Figure 2.7), and smaller shifts around this "balance" position during the measurement, where the pupil position changes slightly (0.05±0.06mm for x and 0.05±0.03mm for y for the eye in Figure 2.7). The first component will not only affect sequential techniques to measure eye aberrations, but any device that does not actively track the pupil and compensates for its shifts (active eye tracking). The actual pupil positions obtained from the programme can be used to compute the wave aberration and compare it with that obtained using the nominal positions. Figure 2.8 shows the wave aberration maps obtained for the eye in Figure 2.7, computed using the nominal coordinates (Figure 2.8 A), and the actual coordinates including only the second effect previously mentioned (Figure 2.8 B), and including both effects (Figure 2.8 C) as pupil sampling coordinates. Figure 2.8 D and F show the difference maps corresponding to the subtraction of A minus B and A minus C, respectively, both in the same scale. This algorithm was applied to the study reported in Chapter 5, where it was important to

rule out the influence of the eye movements in the comparison across patterns.

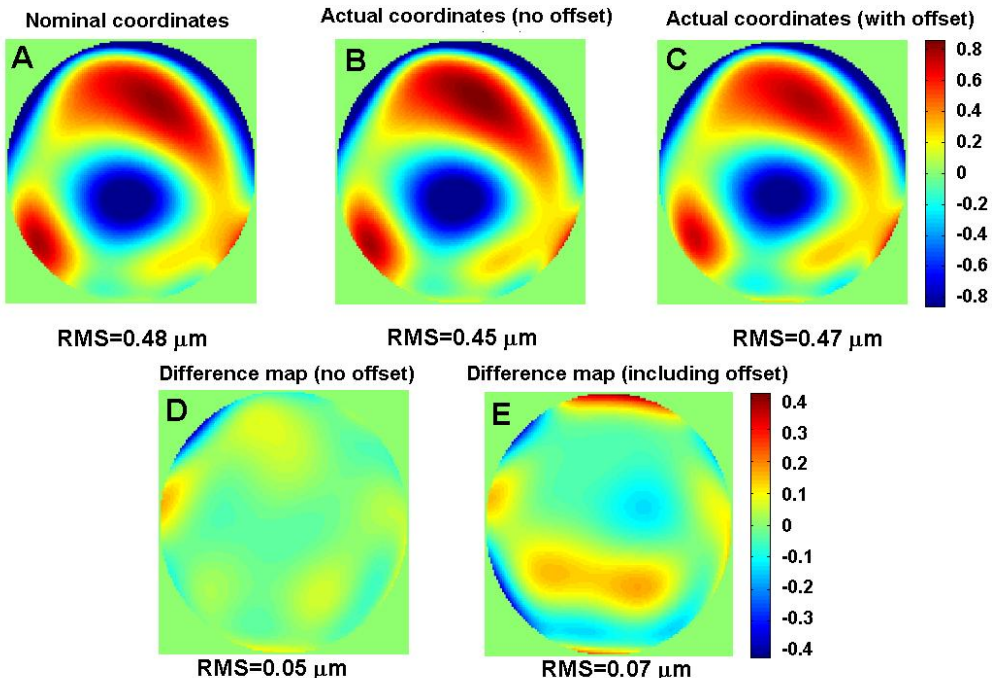

Figure 2.8. Wave aberration maps for the eye in figure 2.7 A computed using as pupil coordinates (A) the nominal entry pupil coordinates, (B) actual coordinates excluding offset effect , and (C) the actual coordinates including all eye movements effects. (D) and (F) show the difference maps (A) minus (B) and (A) minus (C), respectively, both represented in the same scale. The colour –bars unit is microns.

2.3.- SYSTEM CALIBRATION

2.3.1.- RETINAL CAMERA

Calibration of the equivalence between pixels and angles in the retinal camera images was achieved as follows. For this purpose, a metal calliper was placed at a plane conjugate to the sensor of the retinal camera, i.e., at the focus of the lens L2 (see Figure 2.2 A), and recorded the corresponding image with the CCD camera, illuminating the calliper with a lamp (see Figure 2.9A). In the recorded image (see Figure 2.9 B), the notches corresponding to a separation of 1 mm can be distinguished as lighter than the background. Matlab was used to process the image and determine the distance between notches in pixels. First the image was

rotated until the notches were parallel to the vertical arrays of pixels of the image. Then, the edges of the image were detected, obtaining a binary image, and discarded those edges smaller than a set threshold to eliminate noise. Next, a region of interest was detected within the image (see Figure 2.9 C), which included the six notches on the right side. The position of the edges of the notches in this image were found, and the distance between the left edges of the first and last (6^{th}) notches in the image computed. This distance was divided by 5 (number of separations between the notches) to find the distance separating the notches from each other. The result, averaged across the 89 rows of the image, was 27.0 pixels, and the standard deviation (std) was 0.8 pixels. This process was repeated for the right edges of the same notches, obtaining a value of 27.1 pixels with a std of 0.2 pixels. As a last verification, the distances between the centres of each notch were computed, obtaining an average of 27 pixels (std=1 pixel) across the 445 values (6 notches * 89 rows).

From Figure 2.9 A, α = arctan (1/100)=0.5729^o = 34.38 arc min=0.01 rad. Therefore 1mm (27 pixels) subtends 34.37 arc min , and 1 pixel subtends 1.27 arc min. Consequently, since 1mm=27 pixels subtends 0.01 rad, then 1 rad = 27/0.01=2700 pixels, and hence 1 pixel subtends 0.37 mrad[1]. This value is used in the processing program to compute transverse ray aberration from the deviations of the spots in the CCD.

[1] According to the manufacturer (Newport) the tolerance in the focal length of the lens L2, is ±2% at 589 nm. This implies an error of ±0.0002 rad (0.69 arc min) in α, and therefore an error of ±0.007 mrad in the angle subtended by 1 pixel, i.e., ±2% of the error in α. The effect of this error in the estimates of the RMS wavefront error is ± 2%.

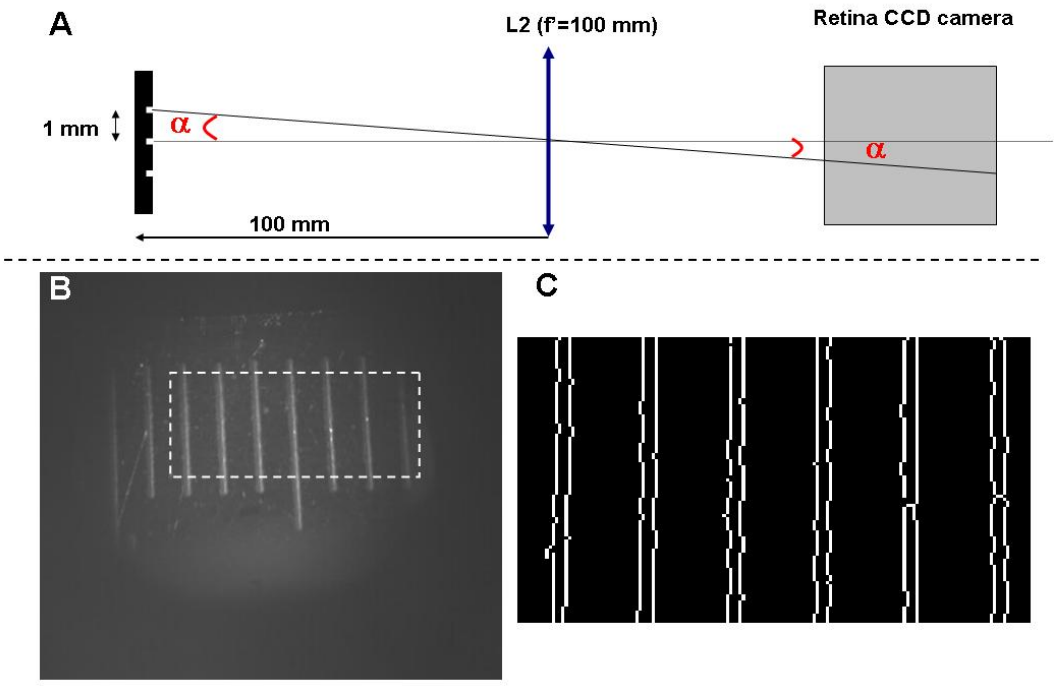

Figure 2.9. Retinal Camera Calibration: (A) Schematic diagram of the retinal camera calibration image acquisition. (B) Calibration image obtained; the lighter lines (corresponding to the notches of a calliper) are separated 1 mm. (C) Binary image showing the calliper notches edges of the region of interest delimited by the rectangle on image B, after rotation.

2.3.2.- PUPIL CAMERA

The pupil camera had several roles in the setup. It is used to ensure alignment of the eye pupil with the optical axis of the system, using the centration cross shown in Figure 2.3 as a reference. It can also be used to visualise the sampling pattern superimposed to the pupil, as well as to assess distances, such as the pupil diameter or pupil misalignment. Therefore, a) alignment between the centration cross (see section 2.2.2.1.-) and the optical axis must be ensured, by introducing the necessary offset, as the centre of the CCD might not coincide with the optical axis of the system and b) the scale of the camera must be calibrated so that distances and sizes can be accurately measured in the pupil images, or assessed in real time during the aberrations measurement session.

(a) Offset

Superimposition between the centration cross displayed on the pupil image shown by the control software (Figure 2.3) and the optical axis of the system was ensured by placing a paper screen at the pupil plane (plane where the subject's eye pupil is placed for the measurement), with the shutter open, and the scanner in the "centred" position, i.e., the measurement laser beam was co-aligned with the optical axis of the system. Under these conditions, the diffuse reflection of the laser (spot) was displayed on the pupil camera screen next (misaligned) or superimposed (aligned) to the centration cross. The cross was displaced by introducing new offset values for x and y directions in the calibration file, until overlapping the spot.

(b) Scale (equivalence between pixels and millimetres)

As mentioned above, the equivalence between pixels and millimetres on the pupil plane for the pupil camera was needed to measure distances in the pupil images. To determine this value, a graph paper screen was placed at the pupil plane so that the graph paper lines appeared as sharp as possible on the pupil camera, and captured the image under ambient light illumination. This image can be seen in Figure 2.10 A. The same procedure used for the retinal camera calibration to detect the edges of the squares could not be followed because the images were too noisy to detect the edges accurately. A different procedure was used instead. After rotating the image (-2.2^{o}) so that the lines coincided as much as possible with rows and columns of the image matrix, the intensity values of the image were added up across rows to obtain the profile shown in Figure 2.10 B, and then the local minima were found (with an accuracy of one pixel). The most abrupt minima (indicated by crosses) correspond to the black lines of the grid, the wider of which corresponds to the wider line. Two minima (indicated with open circles in the figure) were selected and the distance between both points was computed and divided by the

number of lines (millimetres) existing between them The value obtained was 43 pixels/mm. The procedure was repeated adding up the columns instead of rows and the same value was obtained, as expected, since the pixels of the camera are square.

2.3.3.- *ASTIGMATISM CORRECTION AND SCANNER CALIBRATION.*

In the absence of aberrations, a motionless spot was expected to appear at the focal point of L2 (see section 2.1.-) with the scanner on. However, a vertical line was scanned by the laser instead, indicating that some astigmatism was present in the system. As previously mentioned in section 2.2.1.-, some astigmatism was induced by the scanner due to the distance between its two rotating mirrors (Navarro and Moreno-Barriuso, 1999). The first mirror changed the horizontal (X) position of the beam, and this resulted on a line scanned on the second mirror, i.e., the object for the second mirror was a horizontal line. The theoretical astigmatism (Moreno-Barriuso, 2000) induced due to the distance between the mirrors of the scanner, d=4.9 mm, depended also on the focal length of the collimating lens used, f'=50.8 mm, and in this case was:

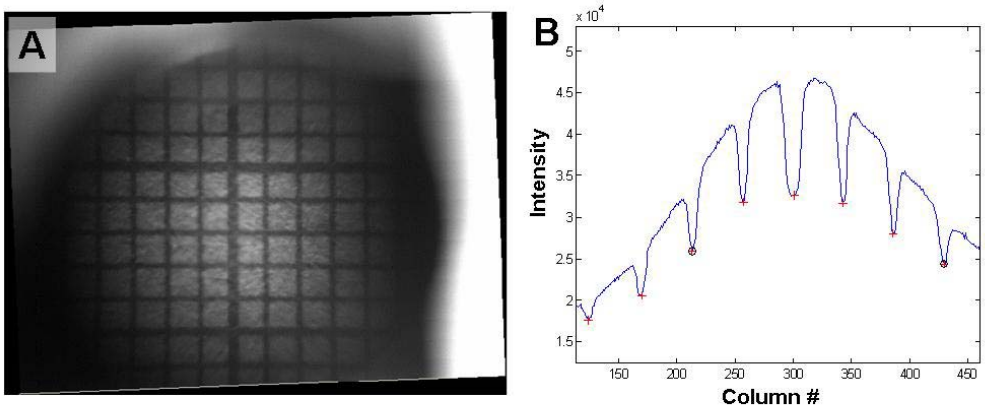

Figure 2.10. Illustration of the Pupil Camera Calibration process: (A) Image of a grid used for the calibration, after rotation. (B) Profile of the image intensity integrated across rows. Crosses indicate local minima, and circles indicate the points used to measure the distance.

$$Ast\ scanner = \frac{d}{(f'+d/2)(f'-d/2)} = 1.88D \qquad (2.2)$$

Some astigmatism could also be introduced by other elements of the setup, such as lenses not completely perpendicular to the optical axis.

(a) Astigmatism compensation

As the major contributor to the astigmatism in the system was the scanner (Navarro and Moreno-Barriuso, 1999) a cylindrical trial lens was placed right after the collimation lens of the scanner, with its axis perpendicular to the line joining the mirrors of the scanner (axis at 0^o). To estimate the power of the cylindrical lens experimentally a paper screen was placed on the focal plane of lens L2. This position was found experimentally by slightly changing the location of the screen until the image scanned by the measurement laser spot was a line, as previously mentioned. With this configuration, cylindrical trial lenses of different powers were tested until the lens (+2.50 D at 0^o) that minimised the astigmatism was found. With this lens, the spot appeared static on the retinal plane during the scanning, once defocus was corrected, indicating that the astigmatism was corrected and that the system did not include other significant aberrations.

(b) Scanner calibration

Scanner offset and slope were set up by Carlos Dorronsoro. The offset was chosen to obtain a laser beam aligned with the optical axis of the setup when coordinates (0,0) were selected. Regarding the slope, or ratio scanner voltage/laser displacement, it was selected to obtain the displacement of the laser spot necessary to obtain the desired pattern. For this purpose, a screen with a square grid pattern (1 mm squares) was placed at the pupil plane with the shutter open to see both the spot and the grid. The ratio scanner voltage/laser displacement was calculated as one tenth of the voltage needed to move 10 mm the laser spot impacting on the screen (as observed by the camera) and taking the grid as a

reference. After this calibration, most of the astigmatism introduced by the system was compensated. The residual astigmatism was then estimated by measuring the aberrations of an artificial eye consisting of an achromatic doublet of f'=200 mm and a screen acting as a "retina" placed on a sliding support that could be displaced to change the defocus of the eye. Therefore, this artificial eye may be considered nominally unaberrated. The value of the astigmatism was computed from the coefficients Z_2^{-2} and Z_2^2 (oblique and perpendicular astigmatism, respectively) using the equation:

$$Astigmatism(D) = \frac{4\sqrt{\left(Z_2^{-2}\sqrt{6}\right)^2 + \left(Z_2^2\sqrt{6}\right)^2}}{R_{pupil}} \qquad (2.3),$$

where R_{pupil} is the radius of the measured pupil. The value obtained was 0.18±0.03 D (mean ± std across 5 measurements). This value was subtracted from the astigmatism obtained in the measurements.

2.3.4.- *SAMPLING PATTERN VERIFICATION*

Once the astigmatism of the system was compensated and the scanner calibrated, verification of correct delivering of the sampling pattern selected on the pupil plane was made. To verify this objectively, a paper screen was placed at the pupil plane and captured the images of the spot reflected on the screen for each sample position during a typical run. These images were processed by fitting the spot to a 2-dimensional Gaussian function, with different widths for X and Y axis (because of the asymmetry of the IR laser spot due to astigmatism produced by the laser cavity). In this way the coordinates of the spot position are obtained as the coordinates of the peak, and the spot size in each direction as the corresponding half-width position of the fitted Gaussian function. Figure 2.11 A shows the peak position (red cross) and the position of the half-width on the X and Y axis (blue asterisk) of the fitted Gaussian function superimposed to the image of the corresponding spot. Figure 2.11 B shows

a comparison of the nominal sampling positions (black Xs) and those obtained experimentally (red asterisks); error bars indicate the size of the spot in X and Y directions. The largest difference between nominal and experimental coordinates was 0.18 mm, and the mean value (±std) across all 37 spot positions was 0.05 (±0.04) mm; 0.08 (±0.05) mm and 0.03 (±0.02) mm across X and Y coordinates, respectively. It should be noted that these differences are smaller than those found for some of our subjects due to their eye movements, and which were below the variability of the measurement (see Chapter 5, section 5.5.1). Same as described in section 2.2.2.3.-, the wave aberration maps obtained with the nominal and the actual (experimentally obtained) coordinates were compared using aberration data corresponding to one of the human eyes studied in Chapter 5 in order to confirm that these differences (some of which can be attributed to the image capture and processing algorithm) did not affect significantly the estimation of aberrations in real eyes. As can be seen in Figure 2.10 C, the differences between the wave aberration maps obtained from nominal (left) and actual experimental (right) coordinates for the same eye, are negligible. The RMSs for these wavefronts were 0.49 μm and 0.48 μm, respectively. The RMS of the corresponding difference map was

0.03μm, which is negligible compared to the values obtained for human eyes (see section 5.5.1 of Chapter 5).

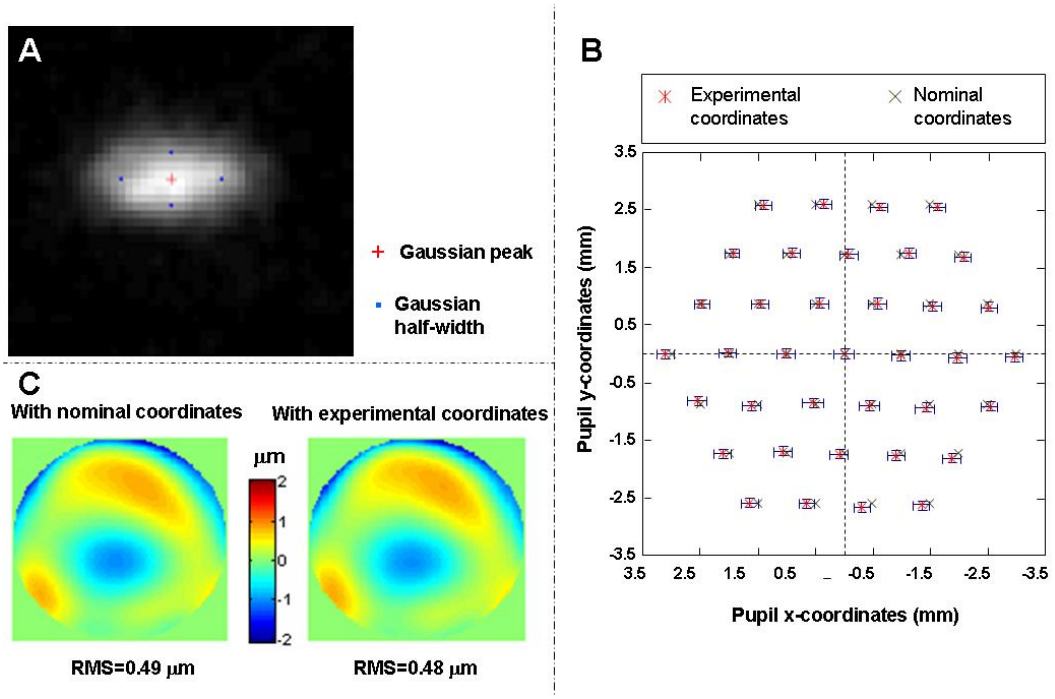

Figure 2.11. Verification of the pupil sampling pattern.

(A) Image of one of the laser spots at the pupil plane. The peak (+) and the half-with (·) positions for the main axes of the fitted Gaussian are superimposed. (B) Nominal (X) and actual (*) positions of the pupil samples. Error bars indicate the size (Gaussian half-width) of the spots in X and Y directions.

The correct delivery of the samples on the pupil plane was crucial to obtain a reliable measurement. Once the correct delivery of the samples on the pupil plane was confirmed, correct identification of the sampling rays with the corresponding retinal aerial images was ensured. For this purpose, the artificial eye described in Section 2.3.3.-(b) was used with the retina displaced closer to the doublet than the focal point in order to make the eye hyperopic. Thus, the spots of the retinal spot diagram will not overlap and no inversion will occur. Then, the correct labelling of the rays in the resulting spot diagram according to the programmed sampling pattern was verified. The spot diagram obtained is shown in Figure 2.12.

Finally, to verify that the processing programme was correct, transverse ray aberrations were computed from the wave aberration (obtained after processing the experimental data) and the corresponding spot diagram positions were verify to coincide with those of the spot diagram obtained experimentally.

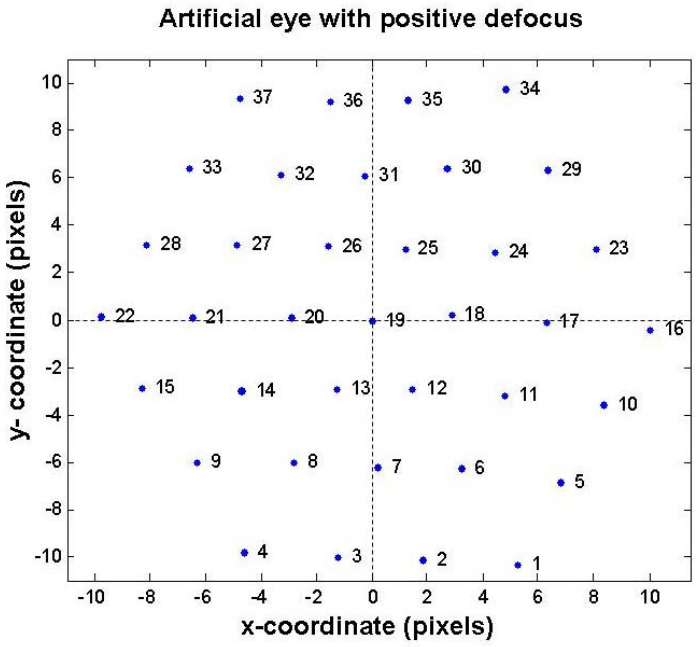

Figure 2.12. Spot diagram corresponding to an artificial eye with positive defocus. The typical sampling pattern used by LRT1 and LRT2 devices to measure aberrations as seen at the retinal plane when positive defocus is present.

2.3.5.- FOCUSING BLOCK SCALE CALCULATION

As explained in section 2.2.1.-, a Badal system was included in the set up to compensate for the subject's refractive error. Figure 2.13 shows the different configurations obtained for different distances between the lenses of the Badal system. For the sake of clarity, the mirrors used to change the distance between the Badal lenses have been removed from the diagram. When the distance between the lenses is equal to the sum of their focal lengths, an afocal configuration is obtained and therefore no correction is induced (see Figure 2.13 A). When the distance between the

lenses is longer than the addition of their focal lengths, rays converge towards the eye to compensate hyperopic refractive error (see Figure 2.13 B). When the distance between the lenses is shorter than the sum of their focal lengths, rays diverge towards the eye to compensate myopic refractive error (see Figure 2.13 C).

Since the Badal system in the setup fulfills $f'_1=f'_2=f'$, where f'_1 and f'_2 are the focal lengths of L_1 and L_2, respectively, the Abbe invariant was applied as follows. For L_1: $1/f'=1/s'_1-1/s_1 \Rightarrow s'_1=f'$, where s_1 and s'_1 are the object and image distances, respectively, for L_1. For L_2: $s_2=-(f'+d)$ and $1/f'=1/s'_2-1/s_2 \Rightarrow s'_2=f'(f'+d)/d$, where s_2 and s'_2 are the object and image distances, respectively, for L_2. The distance d_{eye} between the image yielded by L_2 and the position of the eye (at F'_2) is $d_{eye}=s'_2-f'=f'(f'+d)/d-f'=f'^2/d$, and therefore $D_{eye}=1000\,d/f'^2$, or:

$$d=\frac{D_{eye}\,f'^2}{1000}, \qquad (2.4)$$

where:

-d is the distance between the L_1 image focus (F'_1) and L_2 object focus (F_2),

- d_{eye} is the distance between the eye (pupil plane) and the position of its far point.

- D_{eye} is the refractive error of the eye.

If the block of two mirrors, or Focusing Block (FB), is moved instead of the lens L_2, to introduce a displacement d in the system the displacement of the mirrors should be $d/2$. Therefore, for a focal length of 100 mm for each Badal lens, the distance d should be 10 mm per dioptre. This means that, in order to induce +1D (i.e., to correct 1 D of hyperopia), the mirrors should be displaced +5 mm. Positive distances indicate the FB moves further away from the eye, and negative distances the opposite.

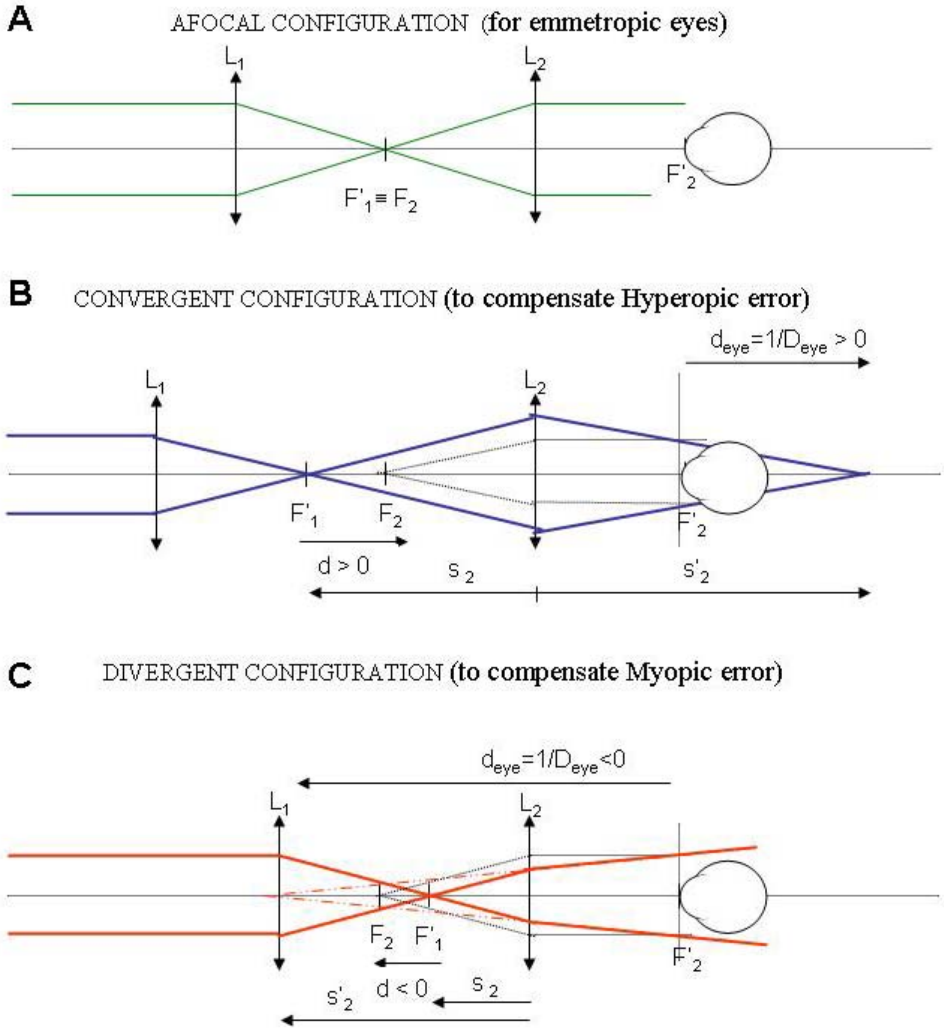

Figure 2.13. Different configurations of the Badal system for refractive error correction. (A) Afocal configuration: distance between the lenses is the sum of their focal lengths, and no correction is induced; (B) When the distance between the lenses is longer than the sum of their focal lengths, and rays converge towards the eye to compensate for hyperopic refractive error; (C) When the distance between the lenses is shorter than the sum of their focal lengths, and rays diverge towards the eye to compensate myopic refractive error.

The position in the setup where 0 D of the FB scale was determined by placing the same nominally non aberrated artificial eye described in Section 2.3.3.-(b) with the screen in its image focal plane (which was found by the autocollimation method) at the pupil plane of the setup. The mirrors were displaced until the scanning spot appeared motionless on the screen of the artificial eye and the retinal camera, and therefore the

defocus induced was 0, and that location was marked as 0 Dioptres. The precision in the focusing, computed as the magnitude of the Zernike term for defocus (Z_2^0) in Dioptres, obtained when measuring aberrations with defocus compensated (i.e., the measurement spot was motionless in the retina of the artificial eye while the scanning was on) was -0.05 ± 0.09D (average across 5 measurements ± std).

2.3.6.- COMPENSATION OF DEFOCUS BY THE FOCUSING BLOCK (FB)

In our experimental protocols defocus was systematically corrected using the FB in order to obtain more compact aerial images (and therefore reduce the variability in the processing) and to provide a sharper fixation for the subject. For this reason, a calibration of the defocus compensation by the FB was performed rather than a calibration of the defocus measured by the system. That is, instead of inducing defocus and measuring it, defocus was induced by using trial lenses just in front of an emmetropised (using autocollimation) unaberrated artificial eye (see section 2.3.3.-(b)), and this induced defocus was compensated with the FB. This procedure allowed us to confirm experimentally that the theoretical calculations made in the previous section worked for our system, and that defocus was perfectly compensated by our FB. For this purpose, the scanner was set for continuous scanning so that the green laser beam was constantly moving and turned on the retinal image real time display. Then, for each trial lens, the FB was displaced until the image of the spot in the camera was motionless, indicating that the refractive error induced on the artificial eye by the trial lens had been compensated by the FB. Finally, an aberration measurement was performed in these conditions to verify that the residual defocus after compensation was negligible. This procedure was repeated for different trial lenses (-4D, -3.25 D, -2 D, -1 D, +1 D, +2 D, +3 D, +4 D), obtaining for each lens a value of the FB position in dioptres that compensates for the trial lens power (the same magnitude, with opposite sign would be expected). Figure 2.14 A shows a plot of the

nominal compensation by the FB in diopters versus the nominal value of the trial lens (fit: y=-0.98x-0.53; r=0.9996; p<0.0001). As expected, the slope of the fit was practically -1. However, a slight off set was found (-0.53 D). This offset was due mainly to the FB, given that the distance between lenses L1 and L2 of the Badal system for the zero position was slightly shorter than the addition of their focal lengths, and therefore some negative defocus was being introduced in the system.

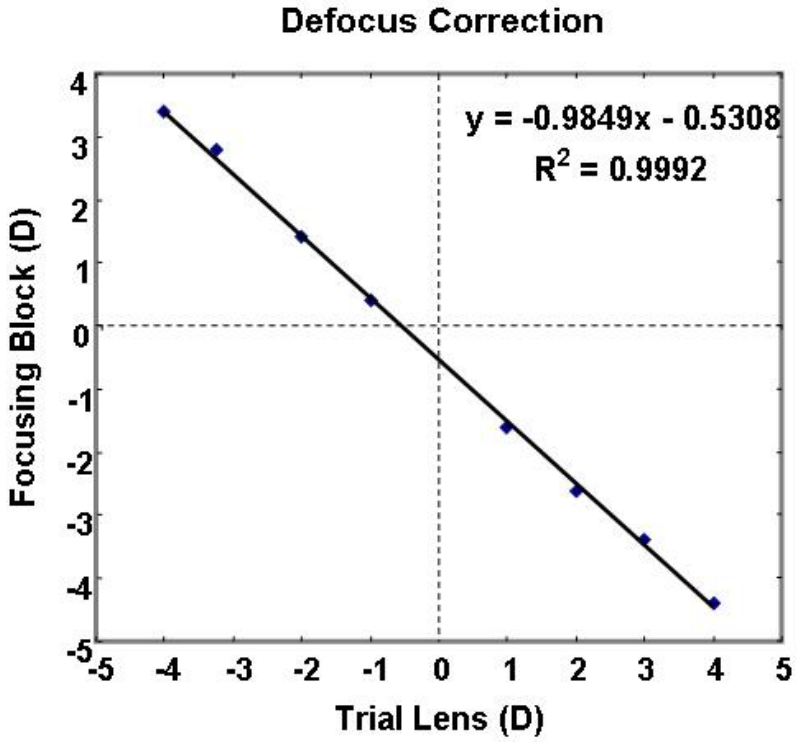

Figure 2.14. Spherical error correction by the Focusing Block versus the nominal value of the trial lens, with the corresponding regression line and equation. The correlation was statistically significant ($p<<0.0001$, $r^2=0.9996$).

For further confirmation, a commercial artificial eye with known defocus was measured, and a residual defocus value similar to the offset found was obtained. However, this small offset in the defocus would not have affected our studies, since refractive error was used in relative terms. In addition, our measurements were performed using IR wavelength and

spherical error varies with wavelength as will be described in more detail in Chapter 4. Refraction was also obtained from commercial autorrefractometer or subjective refraction, depending on the study.

Finally, regarding the residual uncorrected defocus accounted for by the aberrations measurement (Z_2^0), the average across the values obtained for the different trial lenses was -0.05±0.09 D. No correlation between the trial lens power and the corresponding residual defocus existed.

2.3.7.- *OPTICAL ABERRATIONS INTRODUCED BY THE SYSTEM*

Before measuring aberrations of human eyes, a verification that neither geometrical nor chromatic aberrations were being introduced by the system was carried out.

(a) Geometrical aberrations

In order to discard that geometrical aberrations were being introduced by the system, the aberrations of the nominally aberration-free artificial eye described in section 2.3.3.-(b) were measured. Table 2.1 shows the RMS values excluding: piston and tilts (2nd through 7th order); and piston, tilts and defocus and astigmatism (3rd through 7th order). Marèchal's criterion (Born and Wolf, 1993), states that an optical system can be considered well corrected in terms of optical aberrations if the RMS departure of the wavefront from the reference sphere is less than λ/14. In our case, this limit is 0.038 μm and 0.056 μm for λ=532 nm and λ=785 nm, respectively. From the table, the Marèchal's condition fulfils for 3rd and higher order aberrations up to the second decimal. Regarding 2nd order aberrations (defocus and astigmatism), the residual values (see sections 2.3.6.- and 2.3.3.-(b)) will be subtracted to the measured values. Therefore, the system can be considered sufficiently corrected for our purposes.

RMS/wavelength	λ=532 nm	λ=785 nm
2nd through 7th	0.19±0.02 μm	0.155±0.002 μm
3rd through 7th	0.0403±0004μm	0.047±0.001 μm
Marèchal's criterium (λ/14)	0.038μm	0.056μm

Table 2.1. RMS values for different orders for the two wavelengths of the setup.

(b) Chromatic aberrations

Absence of chromatic aberration in LRT1 was verified by measuring the aberrations of a phase plate (Navarro et al., 2000) in front of the artificial eye described in Section 2.3.3.-(b), but with a rotating diffuser acting as a retina. The measurements were performed using 543 nm and 786 nm as test wavelengths. The chromatic aberration introduced by the phase plate, which was 12 μm thick, can be considered negligible. The difference in defocus obtained with both wavelengths was 0.04 D.

Similarly, optical aberrations of the artificial eye described in Section 2.3.3.-(b) were measured using IR wavelength (785 nm), under the same conditions (defocus correction, artificial eye position) used for a wavelength of 532 nm. The difference between the values of defocus for both wavelengths was 0.12 D.

2.3.8.- HIGH ORDER ABERRATIONS IN HUMAN EYES

Since two different systems were used in work (particularly, in Chapter 6 both are used simultaneously), confirmation of the equivalence between both systems was required. Also LRT1 had been previously validated with systems from two other independent laboratories, SRR based in a psychophysical technique, in Boston (Moreno-Barriuso et al.,

2001a) and a HS sensor in London (Marcos et al., 2002b, Llorente et al., 2003), and therefore the technique, setup and routines to estimate aberrations were independent from ours. Hence, confirmation of the equivalence between both systems also implied a general verification of LRT2.

2.3.8.1.- LRT1 vs LRT2

(a) Phase Plate

As a first approach for the comparison of high order aberrations measurement by LRT1 and LRT2 a phase plate with an aberration pattern sculptured using a gray-level single-mask photo-sculpture in photoresist technique (Navarro et al., 2000) was used. This aberration pattern was obtained as the negative of a human eye pattern measured using LRT1. The phase plate was placed in front of the artificial eye described in Section 2.3.3.-(b). The coefficients corresponding to the measurement with LRT1 (dashed blue line) and LRT2 (continuous pink line) are shown on the top graph in Figure 2.15. The corresponding wave aberration maps (left and middle), and difference map (right) are shown on the bottom row. The tendency is very similar when comparing both sets of coefficients and corresponding aberration maps, although the coefficients of LRT2 set are in general larger in absolute value. According to the difference map, differences are concentrated rather in the periphery, near the edges, than in the centre. Although all maps shown in Figure 2.15 have the same diameter, the one corresponding to LRT1 had to be trimmed from 6.5 down to 6 mm. For these reason, some edge effects causing higher aberration values in the edges of the pupil in LRT2 could have been removed from the map corresponding to LRT1. A reliability test was applied to verify the equivalence between the measurements obtained with both systems. For the reliability analysis Cronbach's Alpha model was used, a model of internal consistency usually applied to test scales. The sets of coefficients obtained with the two devices are regarded as

scales measuring the same item, and the output of the test, Cronbach's α, indicates the correlation between both scales (1 indicates identity). A value for α as high as 0.94 was obtained, indicating a great correlation. In addition, a significant correlation was found between both measurements ($r=0.94$, $p<0.0001$), and no find significant differences were found between the means corresponding to the coefficients obtained with both devices when a Student T-test was applied ($p=0.70$).

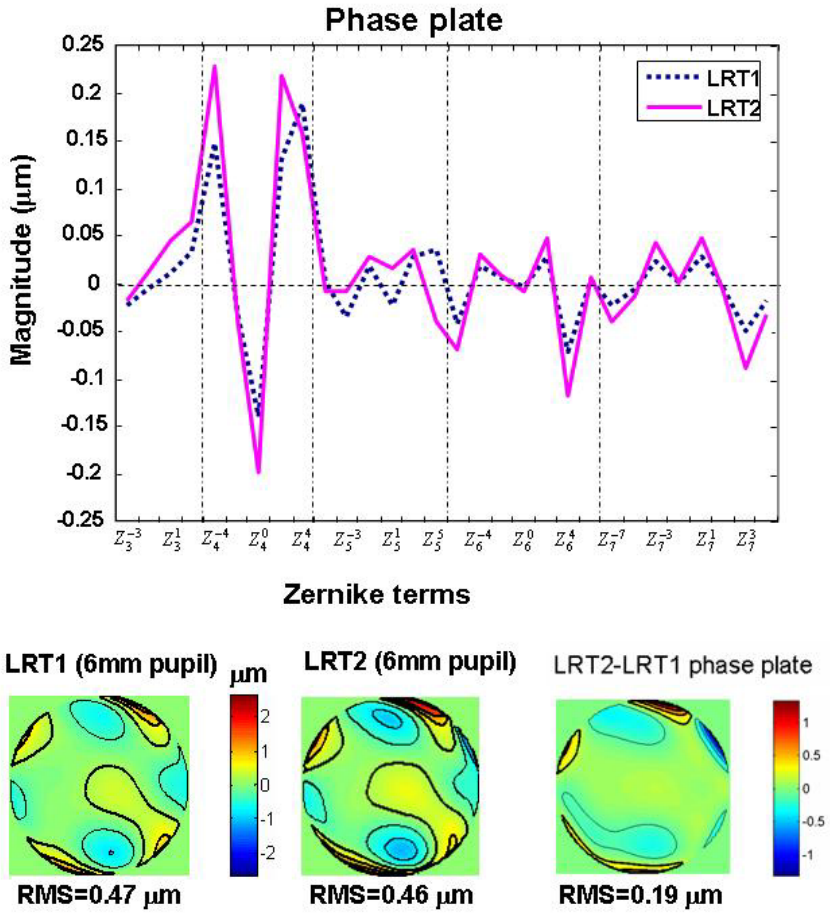

Figure 2.15. Aberrations of the phase plate measured with LRT1 and LRT2. The top graph shows the coefficients obtained with both devices. The wave aberration maps on the bottom row correspond to measurements with LRT1 (left), with LRT2 (middle) and to the difference between the previous two maps (right). Thicker contour lines indicate positive values of the wave aberration.

(b) Human Eyes

To confirm that the system measured higher order aberrations properly in human eyes the measurements obtained for two human eyes from different subjects using both, LRT1 and LRT2 devices were compared. It should be noted that due to the time difference between measurements (51 and 41 months respectively), and the fact that in human eyes the aberration pattern changes with time (Zhu et al., 2004, Mclellan et al., 2001), some differences are expected when comparing aberration patterns. Same as Figure 2.15, Figure 2.16 and Figure 2.17 show average Zernike coefficients (3rd to 7^{th} order) across 4 to 5 runs using LRT1 and LRT2, for eyes #1 and #2 respectively on the top row. Error bars indicate corresponding standard deviation. The similarities between measurements are evident visually when comparing the corresponding wave aberration maps for measurements with LRT1 (left) and LRT2 (middle), and the RMS values (below each map) for both eyes. Also, RMS values corresponding to the difference maps (right) are in the range of the variability of the measurement (0.11±0.04 μm, mean±std RMS of the difference maps from repeated measurements of the eyes studied in Chapter 5, section 5.4.2.2). The reliability test (Cronbach's α model) was applied to the means and standard deviations corresponding to the repeated measurements each device (LRT1 and LRT2), corresponding to each eye. Obtained α values were nearly 1 for the means (0.91 for eye #1 and 0.96 for eye #2), indicating that both devices are measuring practically the same, and slightly lower values for the standard deviations (0.81 for eye #1 and 0.69 for eye #2). When the reliability test was applied to the coefficients corresponding to the repeated measurements obtained with both devices, α was 0.98 for both eyes. A paired Student t-test was applied to verify the correlation between the means and standard deviations of the sets corresponding to each eye, and whether the differences were significant. The measurements with different devices were highly correlated with each other in means ($r=0.84$, $p<0.001$ and $r=$

0.92, p<0.001, for eyes #1 and #2, respectively) and in standard deviations (r=0.71, p<0.001 and r=0. 69, p<0.001 for eyes #1 and #2, respectively) of the sets. No significant differences were found between the mean set of coefficients corresponding to LRT1 and LRT2 (p=0.449 and p=0.775 for eyes #1 and #2, respectively) for both eyes, and the standard deviations corresponding to the sets of eye #1 (p=0.137), although the standard deviations corresponding to LRT1 and LRT2 were found to be different for eye #2 (p<0.001).

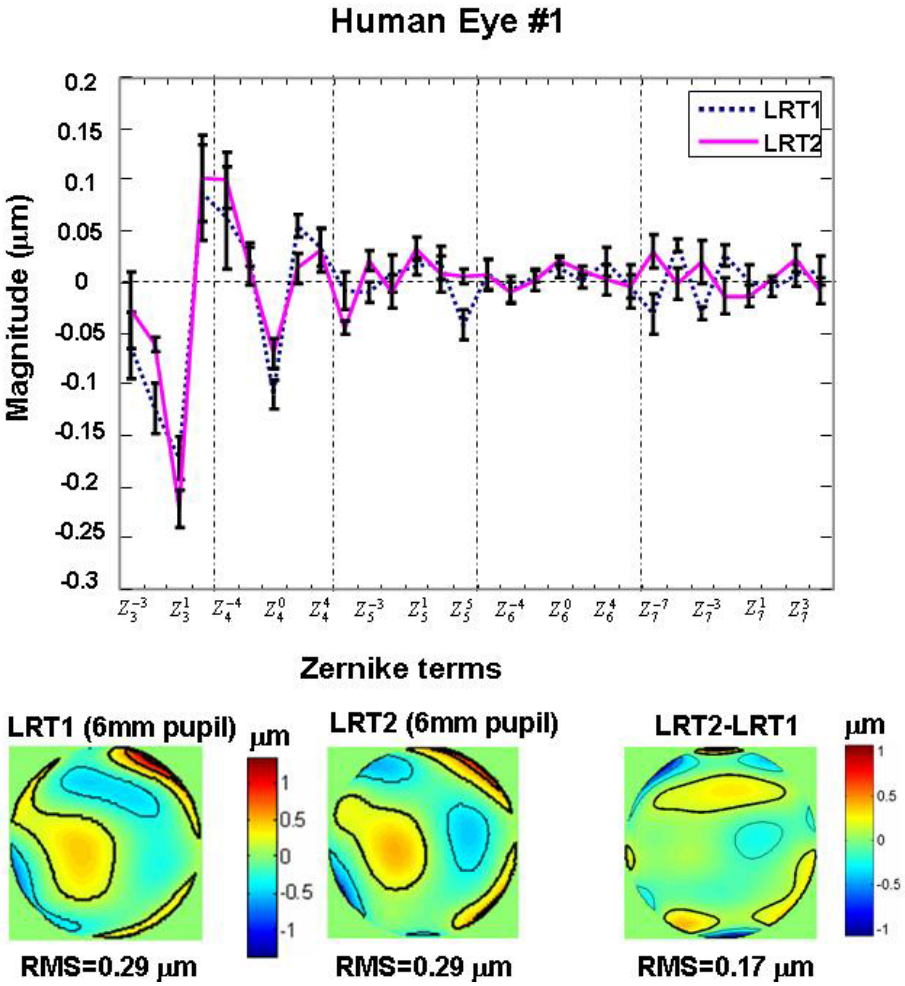

Figure 2.16. Aberrations of Eye #1 measured with LRT1 and LRT2. The top graph shows the average coefficients obtained from 4 to 5 runs with each device. Error bars stand for standard deviation. The wave aberration maps on the bottom row correspond to measurements with LRT1 (left) and LRT2 (middle), and to the difference between these two maps (right). Contour lines are plotted every 0.5 microns. Thicker contour lines indicate positive values of the wave aberration.

A further validation between LRT1 and LRT2 involving human eyes was carried out in the work presented in Chapter 6, where half the eyes were measured with each system. In this validation it was confirmed that the device used to measure ocular aberrations did not have any influence on the results.

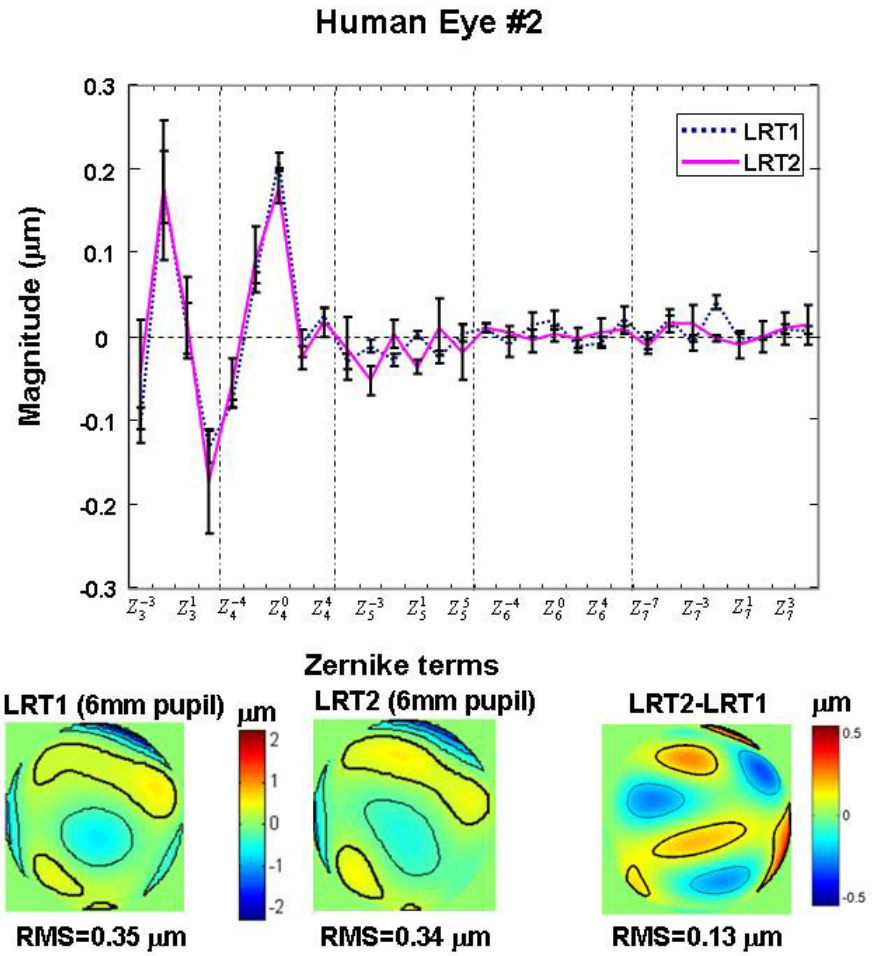

Figure 2.17. Aberrations of Eye #2 measured with LRT1 and LRT2. The top graph shows the average coefficients obtained from four to five runs with both devices. Error bars stand for standard deviation. The wave aberration maps on the bottom row correspond to measurements with LRT1 (left), with LRT2 (middle) and to the difference between the previous two maps (right). Contour lines are plotted every 0.5 microns. Thicker contour lines indicate positive values of the wave aberration.

2.4.- PROTOCOL FOR MEASUREMENTS IN SUBJECTS

Except when specified differently, the protocol used in the measurements with LRT is that described next. The procedures were reviewed and approved by institutional bioethics committees and met the tenets of the Declaration of Helsinki. All patients were fully informed and understood and signed an informed consent before enrolment in the study.

Pupils were dilated with one drop of tropicamide 1% prior to measurement, and the subjects were stabilised by means of a dental impression (LRT1 and LRT2), and a forehead rest. Spherical refractive errors were corrected with spherical lenses (LRT1) or with the Badal system (LRT2) when necessary. As previously mentioned, best focus was assessed by the subject while viewing the fixation stimulus, which was aligned with respect to the optical axis of the system and focused at infinity to keep the subject's accommodation stable during the measurement.

All measurements were done foveally, with a fixation stimulus consisting either on a laser spot corresponding to a 633 nm wavelength He-Ne laser (LRT1) (see Figure 3.1 and Figure 4.1 in chapters 3 and 4, respectively for a diagram of the setup) or a green circle with black radial lines thickening towards the periphery (see fixation test in Figure 2.2 A) (LRT2) and using the centre of the pupil as the reference axis. For proper alignment and continuous monitoring, the pupil was illuminated with IR light and viewed on a CCD centred on the optical axis of the instrument. For LRT2, the pupil was monitored (and recorded) during each run using back-illumination (see section 2.2.1.-), which allowed us to detect issues that would affect the measurements such as tear film break up, blinking or large eye movements. When any of these was detected during a run, the subject was asked to blink a few times until feeling comfortable again, rest

or fixate more accurately, respectively, and the measurement was repeated. This was particularly important when sampling patterns with a large number of samples were used (Chapter 5), extending the measurement time.

Each measurement consisted on five runs for each condition to be tested. The pupil sampling pattern used, unless differently specified (Chapter 5), was a hexagonal arrangement of 37 samples which scanned a 6 (LRT2) or 6.5-mm pupil (LRT1). Left and right eyes were analyzed independently for each subject.

Chapter 3

INFLUENCE OF POLARISATION ON OCULAR ABERRATIONS

This chapter is based on the article by Marcos, S. et al.," Ocular aberrations with ray tracing and Shack–Hartmann wave-front sensors: Does polarisation play a role?", Journal of the Optical Society of America 19, 1063-1072 (2002b). The coauthors of the study are: Luis Diaz-Santana, Lourdes Llorente and Chris Dainty. The contribution of the author of this thesis to the study was the participation in the data collection and processing at Instituto de Óptica (LRT), as well as data and statistical analysis (HS and LRT).

3.1.- ABSTRACT

PURPOSE: To investigate whether polarisation may have an effect on reflectometric measurements of wave aberrations.

METHODS: Ocular aberrations were measured in 71 eyes by using two reflectometric aberrometers: LRT (60 eyes) and HS (11 eyes). The effect of different polarisation configurations in the aberration measurements, including linearly polarised light and circularly polarised light in the illuminating channel and sampling light in the crossed or

parallel orientations was studied. In addition, completely depolarised light in the imaging channel from retinal lipofuscin autofluorescence was studied for the HS measurements.

RESULTS: The intensity distribution of the retinal spots as a function of entry (for LRT) or exit pupil (for HS) depends on the polarisation configuration. These intensity patterns show bright corners and a dark area at the pupil centre for crossed polarisation, an approximately Gaussian distribution for parallel polarisation and a homogeneous distribution for the autofluorescence case. However, the measured aberrations are independent of the polarisation states.

CONCLUSIONS: These results indicate that the differences in retardation across the pupil imposed by corneal birefringence do not produce significant phase delays compared with those produced by aberrations, at least within the accuracy of these techniques. In addition, differences in the recorded aerial images due to changes in polarisation do not affect the aberration measurements in these reflectometric aberrometers.

3.2.- INTRODUCTION

Since polarised light interacts with the ocular optical components and the retina, the polarisation of the incident (and returning light in the imaging systems) might affect aberration measurements. Birefringence of the optical components of the eye, cornea (Van Blokland and Verhelst, 1987) and crystalline lens (Bueno and Campbell, 2001), produce a retardation of linearly polarised light (Van Blokland, 1986) (see Chapter 1, section 1.2.5.1). However, a published study (Prieto et al., 2001) using a psychophysical technique (SRR) showed no difference in the wave aberration measured with different states of polarisation of the illuminating channel suggesting that this retardation was negligible in terms of wavefront error. On the other hand, the use of polarisers in the

illumination and detection channels affects the intensity of the raw data (aerial retinal images captured on a CCD camera). Bueno and Artal (Bueno and Artal, 1999) used an ellipsometry approach to study the influence of polarization in double-pass estimates of the image quality of the eye. They found that the double-pass aerial image, autocorrelation of the ocular PSF (Artal et al., 1995), was influenced by the relative orientation of the polarizer and the analyzer (placed in the illumination channel and the imaging channel, respectively). These differences caused significant variations in the resulting modulation transfer function and therefore in the estimated image quality. Relative differences in intensity in the core and tails of the retinal image, or differences in shape could result in changes in the estimation of the centroid and have an impact on the wave aberration estimate.

In the work reported in this chapter the effect of polarisation on the intensity of the aerial images and on the wave aberration estimated from reflectometric measurements was studied. Data from a HS system (Chapter 1, section 1.2.3) implemented at the Imperial College, London, UK were analysed in combination to data obtained from the LRT described in the methods section (Chapter 2, section 2.1). The aim of this work was not to fully characterise the wave aberration with respect to state of polarisation, but rather to test whether some typical combinations of polarisation in the incident and detection channels may influence wave aberration measurements. These different combinations together with retardation across the pupil produce differences in the relative intensity of the aerial images captured. Additionally, a non-polarised condition was studied with the HS wavefront sensor. Our experiments show that these polarisation states do not influence reflectometric aberration measurements in the eye, at least within the error of the measurements.

3.3.- METHODS

3.3.1.- LASER RAY TRACING

3.3.1.1.- Setup and procedures

The device used in this study was LRT1 (see Chapter 2, section 2.2). A schematic diagram of the configuration of the device used in this work is shown in Figure 3.1. In order to induce the different polarisation conditions to study, a linear polarizer (LP) and a polarising cubic beam splitter (PCBS) were introduced in the setup, as well as a quarter wave plate (QWP) when required (see section 1.3.1.2).

3.3.1.2.- Experiments

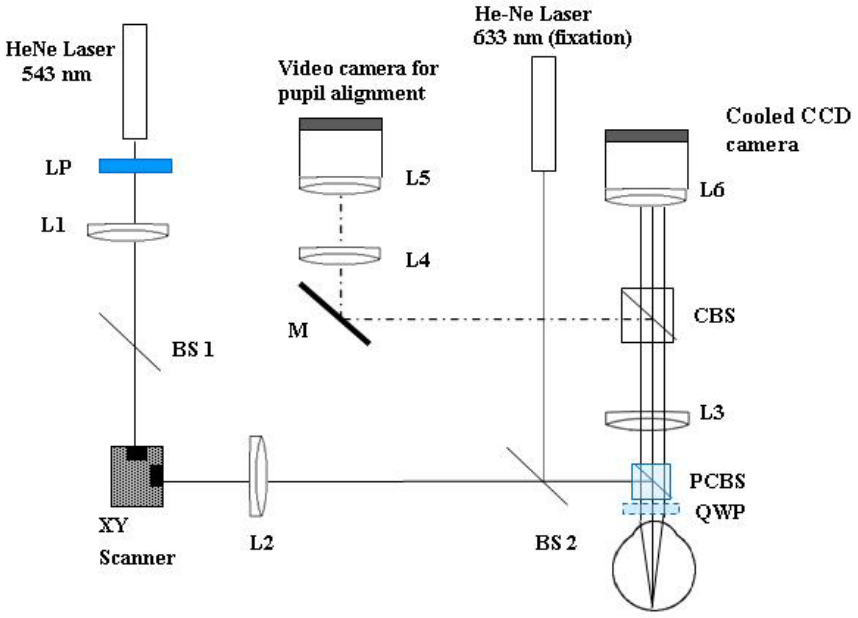

Figure 3.1. Schematic diagram of the configuration of LRT1 used in this study: LP is a linear polariser; L indicates lens; BS1 and BS2 are pellicle beam splitters; CBS is a cube beam splitter and M is a mirror. The polarising beam splitter (PCBS) and the quarter wave plate (QWP) contribute to obtain the different polarisation conditions.

Two different experiments were performed: 1) In the first one, the eye was illuminated with linearly polarised light and light was collected linearly polarised in the crossed direction. This was achieved by using a polarising beam splitter, which reflects linearly polarised light, and transmits linearly polarised light rotated 90º (see Figure 3.2 A). 2) In the second one, a quarter-wave plate was introduced between the polarising beam splitter and the eye. Light in the illumination channel was then circularly polarised, and light with the same state of polarisation was fully transmitted into the imaging channel (see Figure 3.2 B).

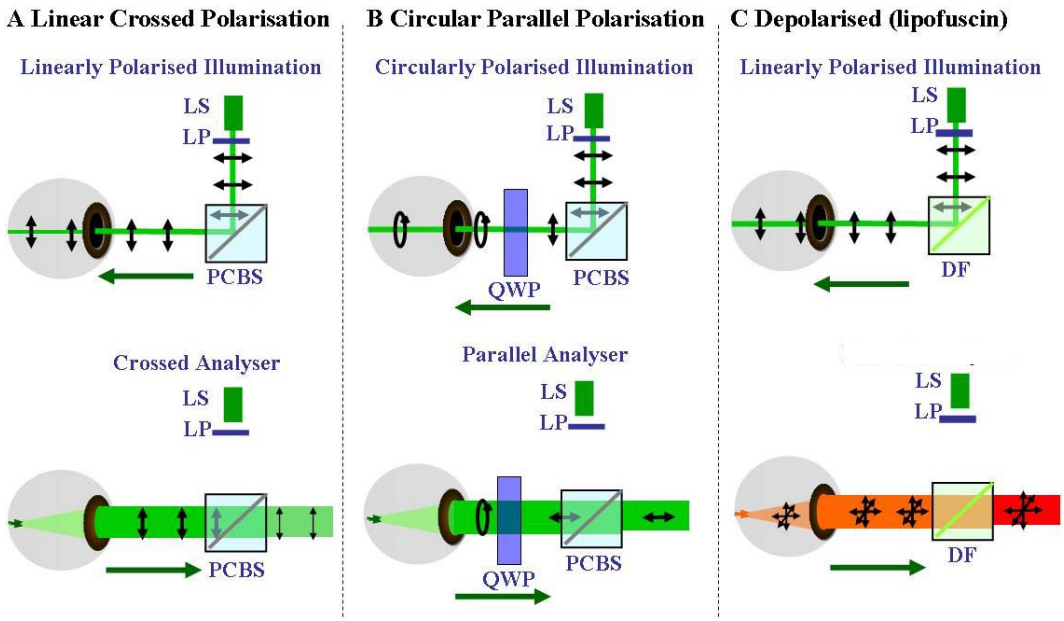

Figure 3.2. Configurations of the set-ups to obtain the different polarising conditions. (A) Linear crossed polarisation: linearly polarised light enters the eye, and light from the eye polarised in the perpendicular orientation is transmitted by the polarising beam splitter (PCBS) (crossed analyser), so that little light preserving the original polarisation orientation reaches the detector (see thinner arrows). (B) Circular parallel polarisation: light circularly polarised by a quarter wave plate (QWP) enters the eye, and light from the eye is linearly polarised in the orientation transmitted by PBS (parallel analyser). (C) Depolarised condition: partially polarised light enters the eye and stimulates lipofuscin molecules, which emit depolarised light that is transmitted by the dichroic filted (DF).

3.3.1.3.- Subjects

Twenty-eight subjects participated in the experiment. Ages ranged from 18 to 46 years and refractive errors ranged from –10.47 to 0.68 D. A total of 60 measurements (E#1-E#60). Both normal and atypically highly aberrated eyes were included, since the group under test includes 22 eyes after (at least one month) LASIK surgery, which typically increases the amount of higher order aberrations (Moreno-Barriuso et al., 2001b). Eleven eyes were tested both before and after LASIK, and were considered as independent measurements. The experimental protocol used was that described in section 2.4 of Chapter 2, for each polarisation condition.

3.3.2.- HARTMANN-SHACK

3.3.2.1.- Setup and procederes

The implementation of the HS wavefront sensor at Imperial College, London (Diaz-Santana and Dainty 1999, Diaz-Santana Haro, 2000), as well as the technique itself (Chapter 1, section 1.2.3) have been described in detail elsewhere. A schematic diagram of the HS sensor configuration used in this work is shown in Figure 3.3. The emerging beam was sampled by a rectangular lenslet array placed in a plane conjugate to the pupil. Each lenslet was 0.8 mm x 0.8 mm over the eye pupil and 35-mm focal length. The number of sampling lenslets (32 to 48 lenslets) was defined by the subject's pupil size (ranging from 5 mm to 6.5 mm). A CCD camera, placed on the focal plane of the lenslet array and conjugated with the retina recorded the HS spot pattern. Deviations from the ideal spot pattern are proportional to the local slopes of the wave aberration. The slopes were fitted to a 6^{th} order Zernike polynomial (27 terms) and the wave aberration was computed using a least-squares procedure. Same as for LRT, a LP and a PCBS were introduced in the setup, as well as a QWP or when required (see next section of this chapter), in order to induce the different polarisation conditions to study.

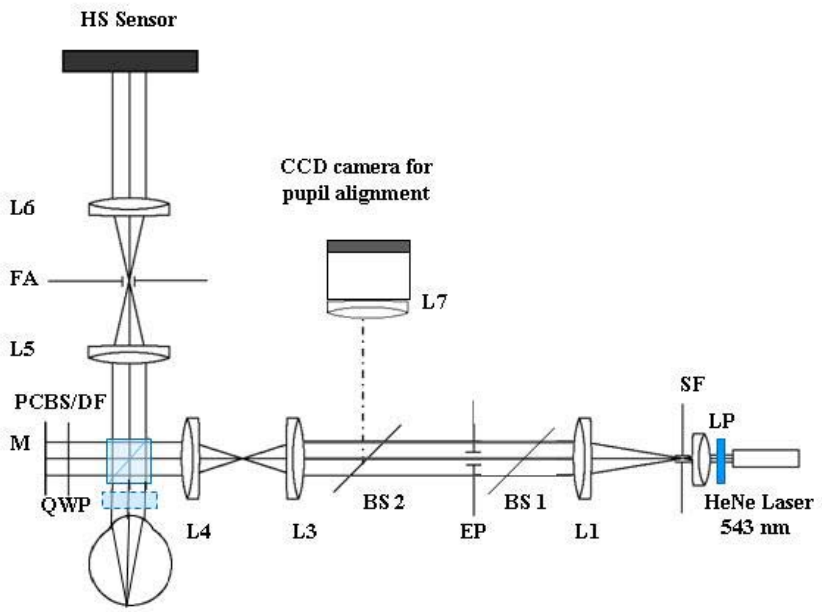

Figure 3.3. Schematic diagram showing the configuration of the HS sensor used in this study: LP is a linear polariser; SF is a spatial filter; L indicates lens; BS1 and BS2 are pellicle beam splitters; M is a mirror; EP is an entry pupil aperture (diameter=1.5 mm), and FA is a field aperture; PBS is a polarizing cube beam splitter, DF a dichroic filter, and QWP is a quarter wave plate which are combined in the setup to obtained the different polarising conditions.

3.3.2.2.- Experiments

The author did not participate in the experimental sessions, which took place at Imperial College (London), or in the data processing, but performed the analysis of the data from the different conditions. Three different experiments were performed, using different configurations for the state of polarisation in the illuminating channel, and state of polarisation of the light sampled in the imaging channel: 1) In the first experiment, the eye was illuminated with linearly polarised light (635 nm) and collected the light linearly polarised in the crossed direction. This was achieved by using a PCBS, which reflects linearly polarised light, and transmits linearly polarised light rotated 90^{o} (see Figure 3.2 A). 2) In the second experiment, the illumination channel was circularly polarised, and light with the same state of polarisation was maximally sampled in the imaging channel. This was achieved by placing a QWP between the PCBS and the eye (see Figure 3.2 B). 3) In the third experiment the eye was

illuminated using partially polarised light (from a He-Ne laser at 543nm), and completely depolarised light was sampled by the imaging channel. To achieve a depolarised state, a fluorescence technique was used (Delori et al., 1995, Diaz-Santana and Dainty 1999). Fluorescent light was collected by replacing the PCBS by a DF, reflecting the sampling light (543 nm) and transmitting wavelengths other than the excitation wavelength (see Figure 3.2 C). Fluorescence is known to originate in the lipofuscin molecules at the retinal pigment epithelium (see section 1.1.6 of Chapter 1). A fluorescent source is equivalent to a perfectly incoherent source. Light is completely unpolarised and speckle is not present. The peak of the fluorescent spectrum is close to 635 nm. All experiments were done foveally, and using the pupil centre as a reference. Subjects were stabilised with the help of a dental impression. Alignment was achieved by measuring the displacement required for the subject to stop seeing the beam coming into his/her eye on the left, right, top and bottom, and finally computing the pupillary centre. For each condition, at least ten measurements were obtained consecutively. The alignment procedure was repeated every ten measurements.

3.3.2.3.- Subjects

Eleven normal subjects participated in these experiments. Only left eyes were used (E#61-E#71). Ages ranged between 26 and 52 years. Spherical refractive errors ranged between -3.25 D and 2.25D. Seven subjects participated in comparative measurements of experiments 1 and 3; two subjects in comparative measurements of experiments 2 and 3; and two subjects in experiments 1 and 2. All eyes were dilated and cyclopleged with one drop of tropicamide 1% and one drop of phenylephrin 2.5% .

3.3.3.- COMPARISON OF HS AND LRT SET UPS

Previous studies have shown that measurements on the same normal subjects using HS and LRT techniques provide identical results, within the

accuracy of the methods (Moreno-Barriuso and Navarro, 2000, Moreno-Barriuso et al., 2001a). To test the equivalence of the two systems used in this study measurements were conducted on two control subjects who travelled between London and Madrid. These subjects did not participate in the full measurements reported in this study, and were tested with the standard conditions in each lab (543 nm illumination and linear polarisation with an arbitrary orientation for LRT, and 543 nm illumination and crossed polarisation for HS). Figure 3.4 shows wave aberration contour plots for the right eyes of both control subjects, for 3rd order and higher aberrations, for LRT (left panels) and HS (right panels). Pupil size was 6.5 mm in the LRT experiment and 6 mm in the HS experiment. Both systems captured similar wave aberration maps. The larger differences found for control eye #2 are likely due to slight differences in the alignment. RMS wavefront error for 3rd order aberrations and higher (computed for 6 mm pupils in both systems) was 0.46 μm and 0.43 μm for LRT and HS respectively, for control eye #1, and 0.48 μm and 0.57 μm, respectively for control eye #2. For both eyes, the SA 4^{th} order term was the major contributor to wavefront error: 0.30 μm and 0.33 μm for LRT and HS (control eye #1), and 0.28 μm and 0.35 μm for

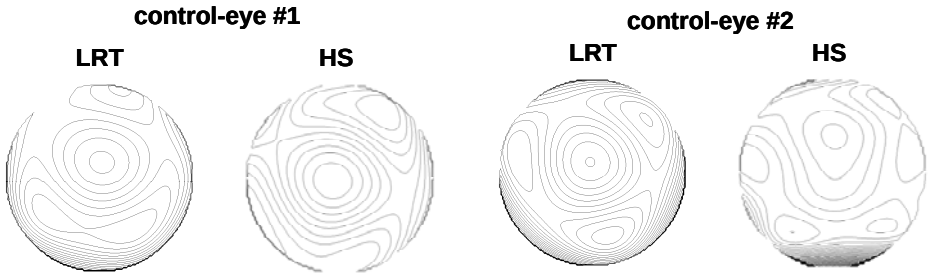

Figure 3.4. Wave aberration contour for control eyes measured in both the LRT setup in Madrid and the HS system in London. First- and second-order aberrations have been canceled. Pupil diameter was 6.5 mm for LRT and 6 mm for the HS. Contour spacing was 0.3 mm.

LRT and HS (control eye #2).

3.3.4.- STATISTICAL ANALYSIS

Despite discrete and limited sampling of the wave aberration (Wang and Silva, 1980), the Zernike polynomials can be considered practically orthogonal. A univariate statistical analysis (Student t-test) was therefore performed on each Zernike coefficient to assess possible differences across conditions, rather than performing a multivariate analysis (Hotelling t-squared test) on Zernike sets (Sokal and Rohlf, 1995). This allows us to assess whether some particular coefficients are more likely to show differences.

3.4.- **RESULTS**

3.4.1.- RAW DATA

LRT captures a set of retinal aerial images of a distant point source as a function of entry pupil position. An example of such a series of retinal images for a single run on Eye #23 for circularly parallel (A) and linearly crossed (B) polarisation conditions is shown in Figure 3.5 A and B, respectively. The images have been placed at their corresponding entry pupil position. The shape of aerial images (slightly defocused for this subject) remains approximately constant across the pupil for each condition. The relative intensity of the aerial images across the pupil is different in each condition: brighter in the centre in A, and brighter in the corners in B. Figure 3.5 C shows the corresponding retinal spot diagram of the sets of images in A (circles) and B (crosses), for this subject. Data across five consecutive runs have been averaged. The error bars indicate the standard deviation of the angular locations. For most positions, the difference between the two polarisation conditions is within the error. Figure 3.5 D and E shows HS images for circularly parallel (A) and

linearly crossed (B) polarisation conditions, for Eye #63. Figure 3.5 F shows the HS centroids corresponding to D (circles) and E (crosses). Despite the difference in brightness between both HS images, the centroid locations are very similar.

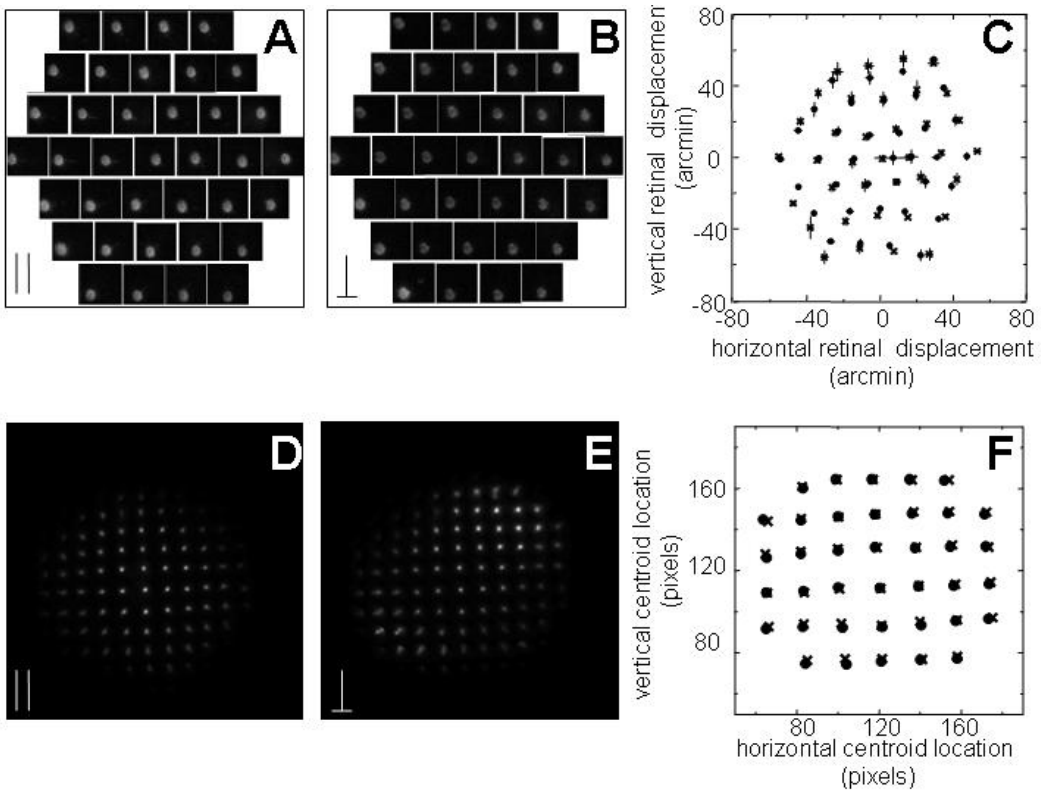

Figure 3.5. Raw data as captured by LRT (panels A–C) and HS (panels D-F) for different polarisation configurations. In LRT a series of retinal images is captured sequentially as a function of entry pupil position. Examples are shown for eye #23 for circular parallel polarization (A) and linear crossed polarization (B). Each image is placed at the corresponding entry location (as looking at the subject's pupil). Panel C shows the corresponding spot diagram of the images shown in A and B. Circles stand for circular parallel polarization and crosses for linear crossed polarization. Panels D and E show HS images for eye #63 for circular parallel polarization (D) and linear crossed polarization (E). Panel F plots the corresponding centroids of the HS images; symbol notation is the same as for the spot diagrams in C.

3.4.2.- INTENSITY PATTERNS

Figure 3.7 shows pupillary intensity patterns (intensity modulation of the raw images as a function of pupil position) corresponding to experiments 1 and 2 using a LRT, for 5 individual eyes (#24, #48, #23, #10). Each square represents the total intensity (average of 5 runs) of the aerial image of the corresponding pupil position. Pupil positions range from -3 to +3 mm both horizontally and vertically. Positive horizontal positions indicate nasal positions in right eyes and temporal positions in left eyes, and positive vertical positions indicate superior pupil. For each subject, data corresponding to the two polarisation combinations, crossed linearly polarised (experiment 1) and parallel circularly polarised (experiment 2), collected consecutively while keeping the rest of experimental conditions identical are shown. Each image is normalized to the maximum intensity value of the series. The intensity distribution changes completely depending on the polarisation combination. The parallel circularly polarised patterns (Figure 3.7, upper row) show a bright area in the central part of the pupil, with the location of the maximum depending on the subject, and the relative intensity decreasing towards the margins of the pupil. The crossed polarisation patterns (Figure 3.7, lower row) show a dark area in the central pupil, and bright areas at the corners of the pupil. It resembles the corneal cross, vignetted by the edges of the pupil, or the hyperbolic shape associated with corneal birrefringence, and observed when the cornea is imaged through two crossed polarisers (Van Blokland and Verhelst, 1987, Stanworth and Naylor, 1950, Cope et al., 1978) (Figure 1.12 B in Chapter 1). As found in previous studies (Van Blokland and Verhelst, 1987) these intensity patterns show bilateral mirror symmetry (Figure 3.6, for right and left eye of the same subject).

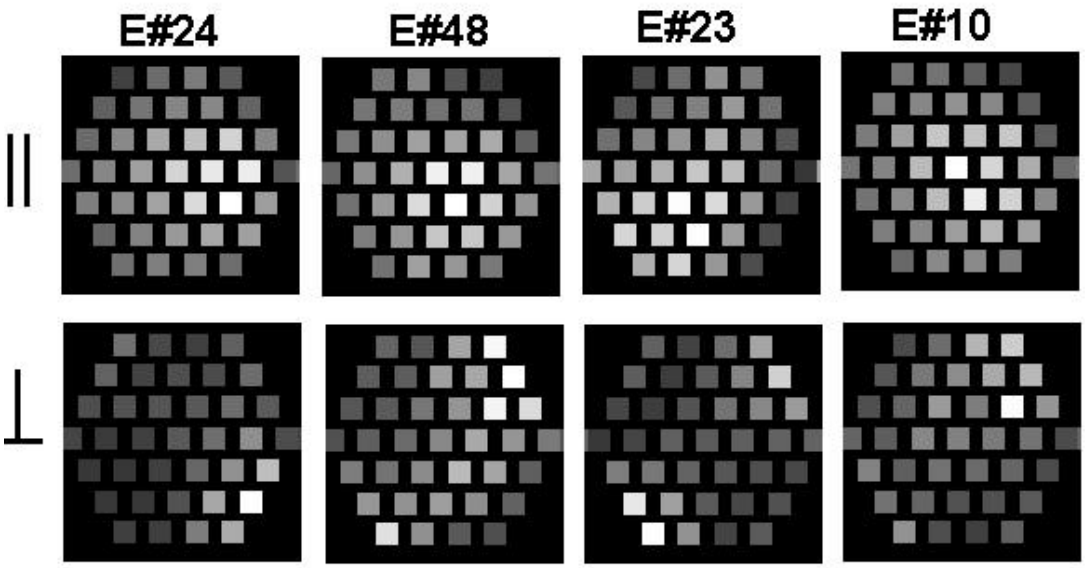

Figure 3.7. Pupillary intensity maps computed from the intensity of the LRT aerial images for eyes #24 (OS); #48 (OD); #23 (OS) and #10 (OD). Each square represents the total intensity (average of five runs) of the aerial image of the corresponding pupil position. Upper row, circular polarization in the illumination channel, analyzer in the same orientation. Lower row, linear polarization in the illumination channel, analyzer in the crossed orientation. Pupil positions range from 23 to 13 mm. Right horizontal positions indicate nasal positions in right eyes and temporal positions in left eyes, and superior vertical positions indicate superior pupil.

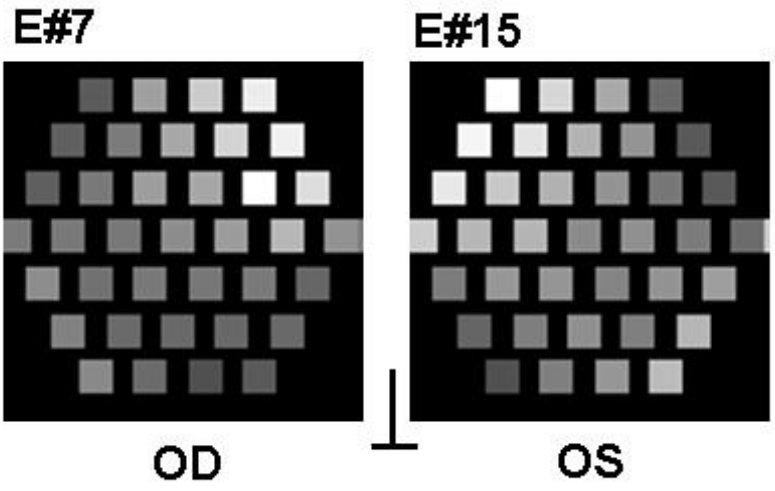

Figure 3.6. Pupillary intensity maps (computed from LRT aerial images, as in Figure 3.5) for right (E#7) and left (E#15) eyes of the same subject, using linear crossedpolarisation. The maps show a dark central area and bright nasal-superior corners, and they are bilaterally symmetric.

Figure 3.8 shows the HS spot patterns, for 3 different eyes (all left eyes). Upper and lower rows represent data corresponding to different conditions of state of polarisation. Left panels show cross-polarised (top) and autofluorescence (bottom) patterns for eye #67; middle panels show parallel circular polarisation (top) and autofluorescence (bottom) for eye #71; and right panels show parallel circular (top) and crossed (bottom) polarisations for eye #63. Intensity patterns in the crossed polarised and parallel circular contributions are similar to those described for Figure 3.7. The autofluorescence spot patterns show the most homogenous intensity distribution.

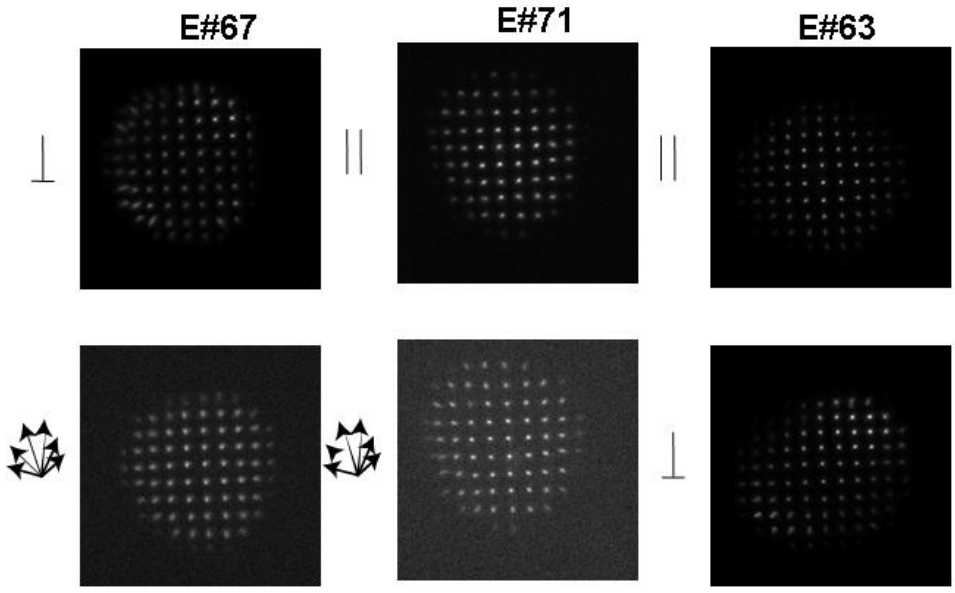

Figure 3.8. Hartmann-Shack spot image for eyes #67 (OS), #71 (OS), #63 (OS).

The left panels compare linear polarization in the illumination channel and analyzer in the crossed orientation (top) with autofluorescence (totally depolarized) sampled light (bottom). The middle panels compare circular polarization in the illumination channel and analyzer in the parallel orientation (top) with autofluorescence (bottom). The right panels compare circular parallel (top) with linear crossed polarizations (bottom). Right horizontal positions indicate temporal pupil positions, and superior vertical positions indicate superior pupil. See (Marcos et al., 2002)

3.4.3.- WAVE ABERRATION PATTERNS

Figure 3.9 A shows contour plots of the wave aberration corresponding to the four typical eyes and the two experimental conditions shown in Figure 3.5, measured using LRT. Each map is the

average of at least three experimental runs. Tilt and defocus were set to zero. Eyes #24 (OS) and #48 (OD) are eyes following LASIK refractive surgery; Eyes #23 (OS) and #10 (OD) are normal eyes. Figure 3.9 B shows contour plots of the wavefront aberration corresponding to 3 eyes measured with HS (#67, #71 and #70) and combinations of experimental conditions shown in Figure 3.8. Wave aberration patterns of the same eyes are quite similar for the different conditions.

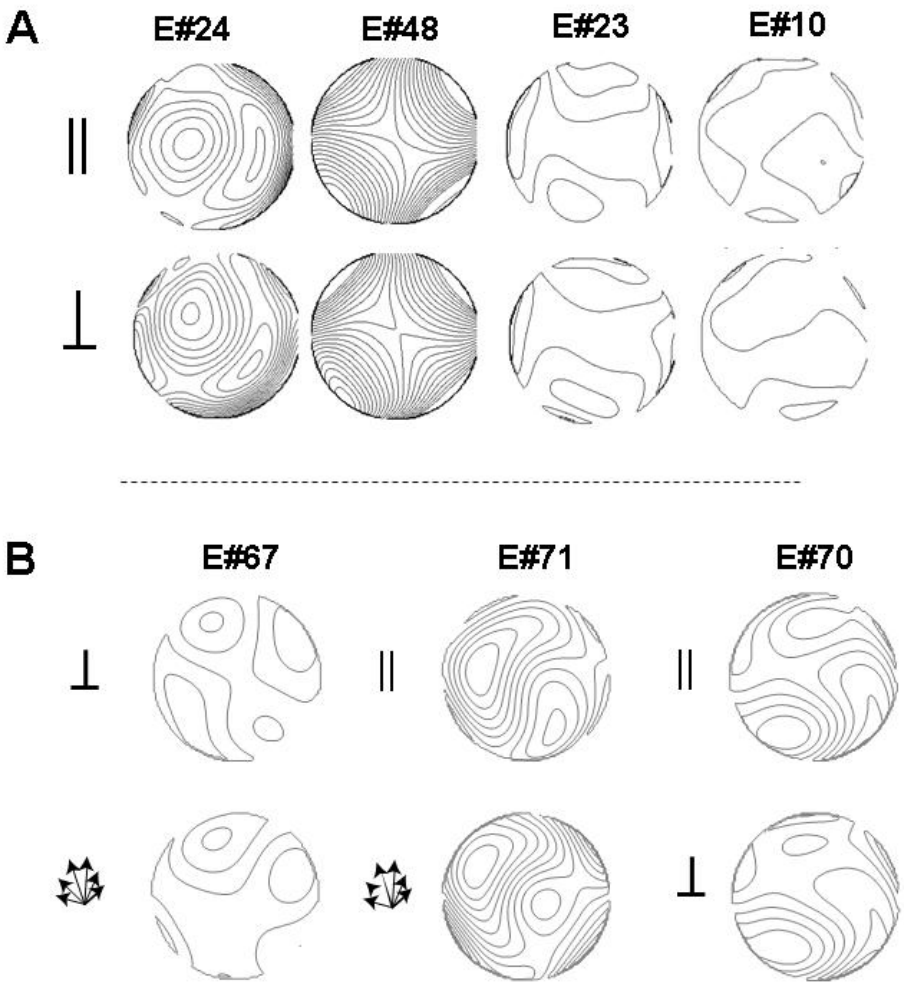

Figure 3.9. Wave aberration contour maps for some of the eyes measured with LRT (A) and HS (B).

(A) For eyes #24, #48, #23, and #10, measured with LRT, lines are plotted every 1 μm. Upper and lower panels as in Figure 3.7. Defocus has been removed. Pupil diameter was 6.5 mm for all eyes. (B) For eyes #67, #71, and #70, measured with the HS lines are plotted every 0.2 μm. Polarization combinations as explained in Figure 3.8. Tilt and defocus have been removed. Pupil diameter was 6.5 mm for #67 and #71 and 6 mm for #70.

3.4.4.- ZERNIKE COEFFICIENTS

Figure 3.10 shows examples of comparisons of Zernike coefficients measured with different pairs of polarisation states, for one of the eyes shown in Figure 3.9 A and the three eyes of Figure 3.9 B: (A) E#23, OD, measured with linear crossed polarisation (crosses) and circular parallel polarisation (circles), using LRT; (B) E#71, OS, measured with circular polarisation (circles) and fluorescence mode (triangles), using HS; (C) E#67, OS, measured with crossed linear polarisation (crosses) and fluorescence mode (triangles), using HS; and (D) E#70, OS, measured with crossed linear polarisation (crosses) and circular polarisation (circles), using HS. Error bars indicate the mean standard deviation. The Zernike coefficient patterns vary substantially across individuals, but measurements on the same subject differing only by the polarisation states are very similar. The discrepancy in defocus term at Figure 3.10B is due to autofluorescence light coming from a deeper retinal layer.

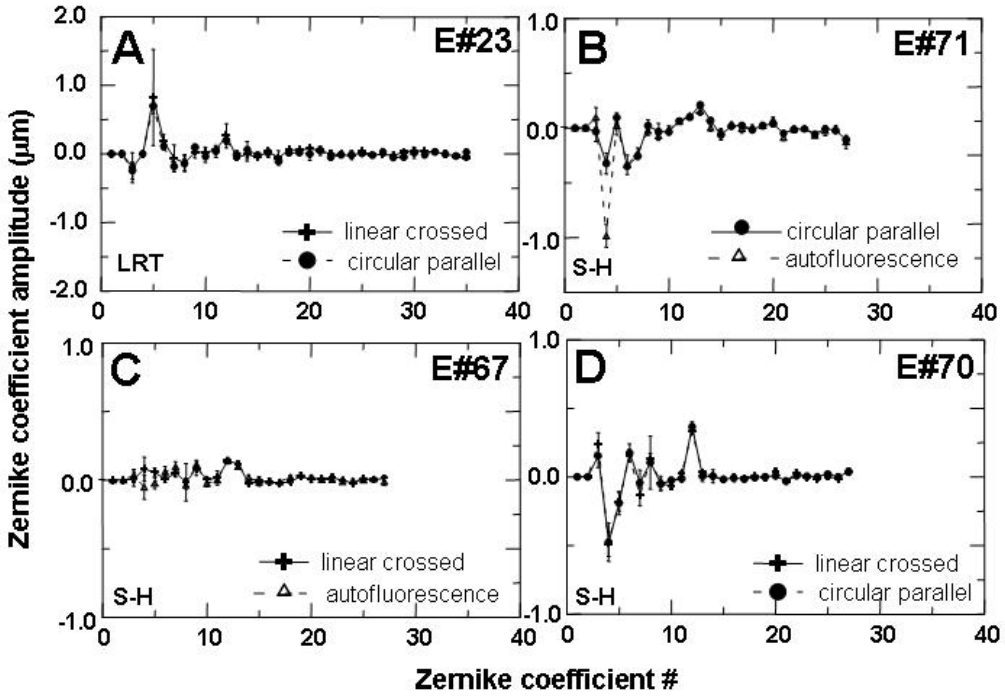

Figure 3.10. Zernike coefficients for eye #23 from Figure 3.9 A (A) and the three eyes (#71, #67, #70) from Figure 3.9 B (B)– (D), comparing different combinations of polarization conditions. Each symbol is the average of several measurements in the same conditions. Error bars stand for the mean std.

Figure 3.11 shows examples of individual coefficients Z_2^0 (A), Z_2^{-2} (B), Z_3^1 (C), and Z_4^0 (D), for the 60 eyes and the two experimental conditions of the LRT measurements (left panels) and the 11 eyes and three experimental conditions of the HS measurements (right panels). Eyes are ranked by decreasing defocus coefficient (from higher to lower myopes).

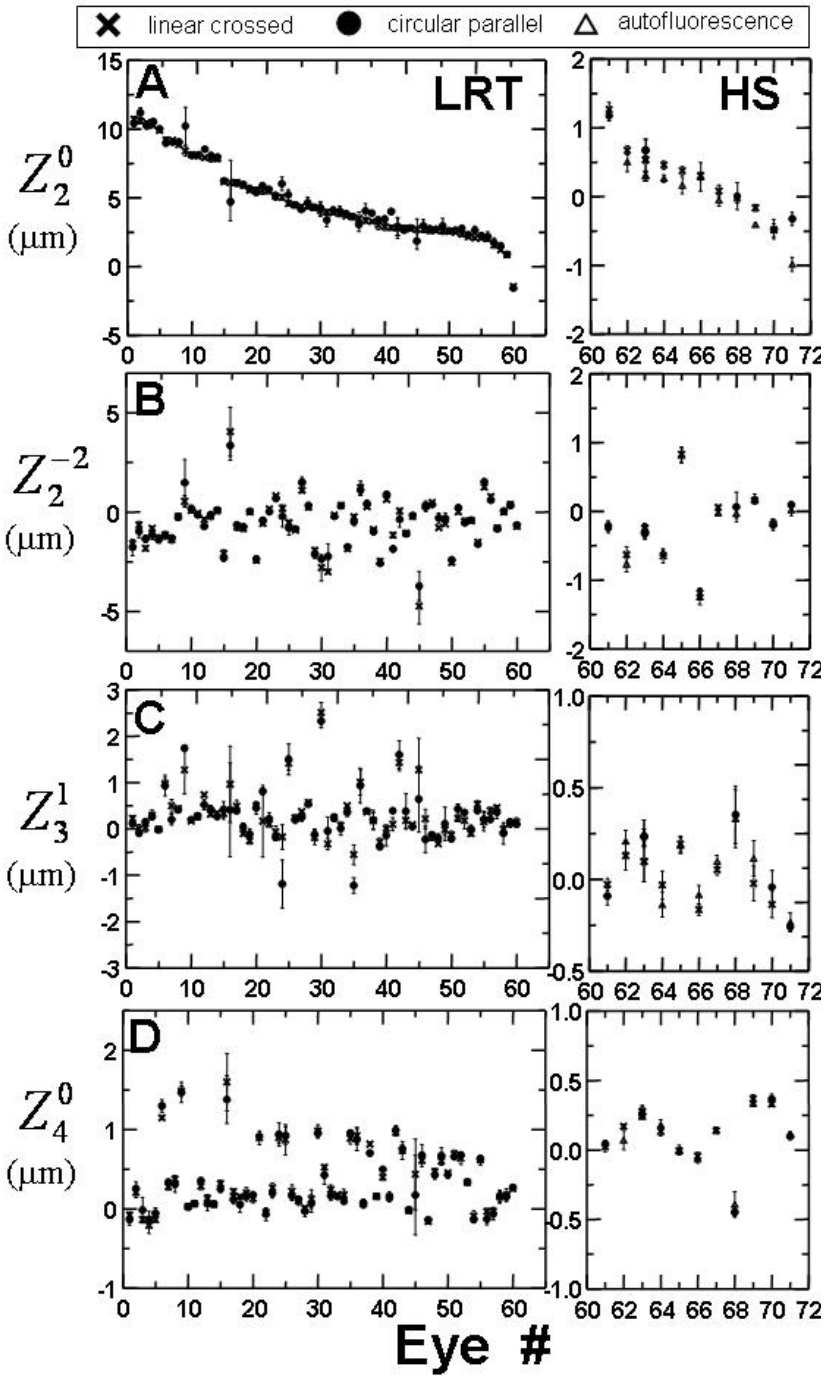

Figure 3.11. Zernike coefficients Z_2^0 (A), Z_2^{-2} (B), Z_3^1 (C), and Z_4^0 (D), for all eyes of this study (E#1–60 measured with LRT and E#61–71 with the HS), comparing at least two different polarization states (represented by different symbols). Error bars stand for the mean std.

For the 60 eyes measured with the LRT, only 44 coefficients out of 1980 (60 x 33 terms), i.e. 2.2%, showed statistically significant differences (t-test $p<0.001$) between the linear crossed and circular parallel polarisation. The defocus term (Z_2^0) was significantly different in 7 eyes. This term along with Z_3^{-3} was the one showing differences in more eyes (8.5%). A least square difference multiple comparison test showed only significant differences ($p=0.0002$) on the defocus term. The mean standard deviation of the Zernike coefficients (averaged across subjects and Zernike terms) was 0.065 μm, averaging the standard deviations obtained for each polarisation state. When pooling together data from all polarisation states, the mean standard deviation of the Zernike coefficients was 0.077 μm, only slightly higher than within the same polarisation state. For the 11 eyes measured with HS, 37% of the coefficients showed statistically significant differences (t-test, $p<0.001$) between linear crossed and autofluorescence, 37% between circular parallel and linear crossed polarisation and 46% between circular parallel and autofluorescence. Comparing sets of measurements under similar polarisation conditions, but repositioning the subject between sets of 10 consecutive runs provided similar percentages of significantly different (t-test, $p<0.001$) coefficients: 40% comparing linear crossed polarisation sets of measurements, 52% for circular parallel, and 60% for autofluorescence. The mean std of the Zernike coefficients (across all polarisation conditions) was 0.126 μm, within a single polarisation state was 0.102 μm on average, and across identical consecutive runs was 0.039 μm.

3.5.- **DISCUSSION**

It has been shown that when using different states of polarisation in the illumination and detection channels, the intensity of the retinal images captured by imaging aberrometers depended on the position over the pupil of the entry (or exit) ray. This modulation depended on both the

pupil relative luminous efficiency, in case of light interacting with cone photoreceptors (Burns et al., 1995) and the interaction of the state of polarisation with birefringence properties, particularly those of the cornea (Van Blokland and Verhelst, 1987, Stanworth and Naylor, 1950, Cope et al., 1978). Retinal polarisation effects were probably irrelevant, since the foveal area sampled (a few minutes of arc) was much smaller than the retina brushlike patterns (4-5^{o}) observed in retinal photographs between polarisers, which are attributed mainly to the retinal fibre layer. In addition, retardation by photoreceptors as suggested by Hocheimer & Kues (Hocheimer and Kues, 1982) has been proved small (Van Blokland, 1986). Whereas the crossed polarisation patterns (polarisation cross) seems related to corneal birefringence, the Gaussian distribution observed in parallel circularly polarised patterns is very likely associated with directionality properties of the cone photoreceptors (Burns et al., 1995, Marcos and Burns, 1999, Marcos et al., 2000).The autofluorescence spot patterns show the most homogenous intensity distribution, consistent with the fact that cones do not recapture light scattered by lipofuscin (Burns et al., 1997).

However, in spite of the effect of polarisation on the intensity distribution of the images, this had little effect on the aberrations measured, within the accuracy and sampling density of the technology used. The larger statistical differences found across Zernike coefficients obtained with different polarisation states for HS measurements are very likely due to differences in alignment between measurements, and not differences intrinsic to the polarisation state. The larger variability of the autofluorescence data is likely due to the lower signal to noise associated to this type of measurements (Diaz-Santana and Dainty 1999).

The fact that ocular aberrations measured using imaging methods, such as the LRT or HS, are insensitive to polarisation has important practical implications. For example, when building such an instrument,

one can choose the polarisation states for illumination and detection that result in the best light efficient configuration, or that which avoids reflections or artefacts. This differs from conventional double-pass measurements, where differences in polarisation produced variations in the PSF and MTF (Bueno and Artal, 1999, Gorrand et al., 1984, Gorrand, 1979).

Published data obtained using the SRR also show that ocular aberrations do not depend on the state of polarisation (Prieto et al., 2001). This is a psychophysical technique, and the subjects did not perceive differences as a linear polariser in the test channel was moved, for any of the pupil locations under test. These results, along with those shown in the present study, suggest that the differences in retardation across the pupil imposed by corneal birefringence, produce non-significant phase delays compared to those produced by aberrations, at least within the accuracy of the measurements. Interestingly, these results also hold for patients following LASIK surgery. Along with a change in corneal shape, producing a significant increase of aberrations (see Chapter 7), these patients may have suffered a change in corneal birrefringence due to re-organization of stromal collagen fibrils induced by surgery (Farrell et al., 1999, Meek and Newton, 1999, Brinkmann et al., 2000). Even if only a fraction of stromal fibres undergo reorganization, the stromal bed is substantially reduced in the higher myopic patients. However, the intensity distribution patterns obtained by LRT did not change with surgery (neither for crossed linear or parallel circular polarisations). This is in agreement with Bueno et al. (2006), who measured four normal and four post-LASIK young eyes using an aberropolariscope. However, although they found no differences in aberration measurements for different polarisation states in both groups, they did find changes in the polarisation characteristics. Post-LASIK eyes showed larger levels of depolarisation and more irregular patterns of retardation and corneal slow axis.

Chapter 4

ABERRATIONS OF THE HUMAN EYE IN VISIBLE AND NEAR INFRARED ILLUMINATION.

This chapter is based on the article by Llorente, L. et al.,"Aberrations of the human eye in visible and near infrared illumination", Optometry and Vision Science 80, 26-35 (2003). The coauthors of the study are: Luis Díaz-Santana, David Lara Saucedo and Susana Marcos. The contribution of the author of this thesis to the study was the participation in the data collection and processing at Instituto de Óptica (LRT), as well as data and statistical analysis (HS and LRT).

4.1.- ABSTRACT

PURPOSE: To compare optical aberration measurements using IR (787 nm) and visible light (543 nm) in a heterogeneous group of subjects in order to assess whether aberrations are similar in both wavelengths and to estimate experimentally the ocular chromatic focus shift.

METHODS: Ocular aberrations were measured in near IR and visible light using LRT and HS wavefront sensor. Measurements were conducted on 36 eyes in total (25 and 11 eyes respectively), within a wide range of ages (20 to 71), refractive errors (-6.00 to +16.50 D) and optical quality

(RMS, excluding defocus, from 0.40 to 9.89 μm). The Zernike coefficients and the RMS corresponding to different terms between IR and green illumination were compared.

RESULTS: A Student t-test performed on the Zernike coefficients indicates that defocus was significantly different in all of the subjects but one. Average focus shift found between 787 nm and 543 nm was 0.72 D. A very small percentage of the remaining coefficients was found to be significantly different: 4.7% of the 825 coefficients (25 eyes × 33 terms) for LRT and 18.2% of the 275 coefficients (11 eyes × 25 terms) for HS. Astigmatism was statistically different in 8.3% of the eyes, RMS for 3rd order aberrations in 16.6%, and SA (Z_4^0) in 11.1%.

CONCLUSIONS: Aerial images captured using IR and green light showed noticeable differences. Apart from defocus, this did not affect centroid computations since, within the variability of the techniques, estimates of aberrations with IR were equivalent to those measured in green. In normal eyes, the LCA of the Indiana Chromatic Eye Model can predict the defocus term changes measured experimentally, although the intersubject variability could not be neglected. The largest deviations from the prediction were found on an aphakic eye and on the oldest subject.

4.2.- INTRODUCTION

Most of the currently available wavefront sensing techniques use IR illumination, due to the advantages that it presents over visible light (Chapter 1, section 1.2.5.2). However, for direct comparison between optical measurements (estimated from the wave aberration) and visual performance the equivalence between results obtained using IR and visible light has to be assured. Particularly, knowledge of the defocus shift between IR and visible wavelengths is essential if the results are to be used

to predict refraction. It is therefore essential to confirm that aberrations measured with IR and green light are equivalent, and to verify whether the focus difference between IR and green predictable by the LCA, and therefore reasonably predictable across subjects.

Previous measurements of aberrations at different visible wavelengths (450 through 650 nm) using a psychophysical technique (SRR) showed slight differences in some aberration terms as a function of wavelength (Marcos et al., 1999). The chromatic difference of focus they found agreed with previous psychophysical results from the literature. Previous studies (Lopez-Gil and Artal., 1997, Lopez-Gil and Howland, 1999) using reflectometric techniques to compare measured optical quality in visible (545 and 633 nm, respectively) and near IR (780 nm) did not find differences in HOA. Double-pass measurements (Santamaría et al., 1987) of MTFs in IR and green light appear to be similar, although subtraction of background halos (noticeably different between IR and green) was critical (Lopez-Gil and Artal., 1997). Another study using an objective crossed-cylinder aberroscope to measure aberrations reported that aberrations are virtually identical in near IR and green light (Lopez-Gil and Howland, 1999). However, the data analysis was mainly qualitative and limited to three eyes. Recent studies have expanded the wavelength range experimentally studied either towards the ultraviolet (Manzanera et al., 2008) or the IR boundaries (Fernandez and Artal, 2008, Fernandez et al., 2005). They confirm that monochromatic aberrations hardly change with wavelength, except for defocus, as found in the study reported in this chapter. They also studied how accurately their data fit the predictions of the LCA from theoretical equations, although only a few subjects were measured.

In this chapter ocular aberrations between near IR (786 nm for LRT and 788 nm for HS) and visible illumination (543 nm) are compared. Aberrations were measured with two objective experimental setups, LRT

and HS (see sections 2.2 in Chapter 2 and 3.3.2.1 in Chapter 3, respectively), although the conclusions drawn here can be extrapolated to unrelated commercially available instruments, based on similar principles. Measurements were performed on 36 subjects, with a wide range of ages, refractions, and ocular conditions (including old and surgical eyes), thus covering a wide range of aberrations, and potentially ocular and retinal structural differences. In addition, the intensity distribution of the aerial images obtained with both wavelengths were compared.

4.3.- METHODS

4.3.1.- LASER RAY TRACING

4.3.1.1.- Setup and procedures.

For this study, the device LRT1 (Moreno-Barriuso et al., 2001) (see Chapter 2, section 2.1) was used to measure ocular aberrations. Figure 4.1 shows the particular implementation for this study, which included a 543 nm He-Ne laser beam (Melles Griot, Alburquerque, USA; 5mW), and 785 nm diode IR laser beam co-aligned (Schäfter + Kirchhoff, Hamburg, Germany; 15mW).

4.3.1.2.- Setting and control experiment

Measurements were conducted following the protocol described in section 1.4, Chapter 1. Previous to the measurements, the system was calibrated to verify that it did not introduce chromatic aberration (see section 2.3.7 (b), Chapter 2).

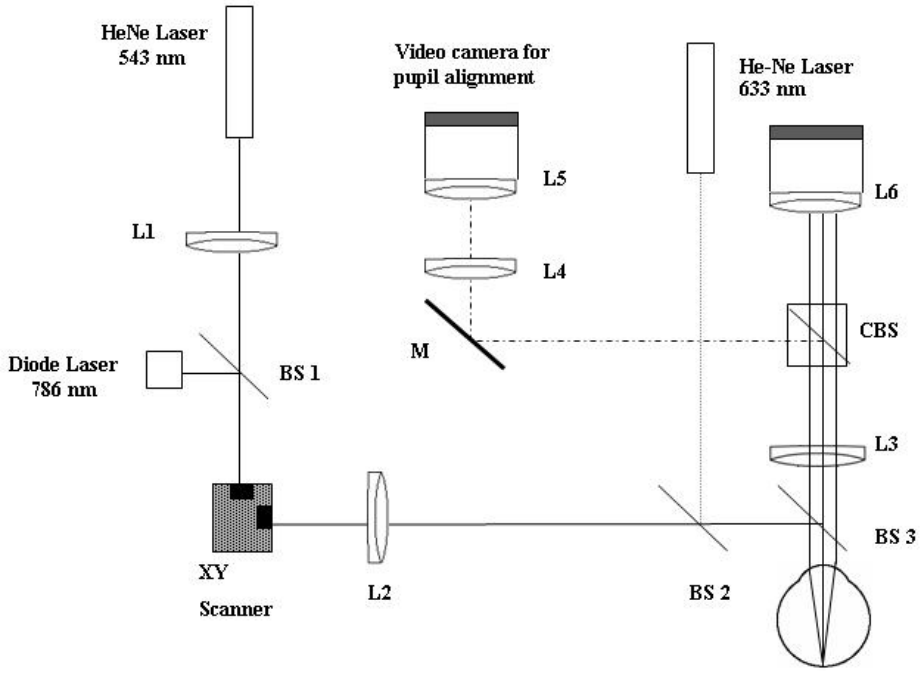

Figure 4.1. Schematic diagram of LRT1, used in this study .

A He-Ne (543 nm) laser or a diode laser (786 nm) samples the pupil plane and, simultaneously, light reflected off the retina is captured by a CCD camera. A red He-Ne laser (633 nm) acts as a fixation point. A video camera monitors pupil centration. BS1 and BS2 are pellicle beam splitters, BS3 is a glass beam splitter, CBS is a cube beam splitter, M is a mirror and L indicates lens.

4.3.1.3.- Subjects.

Twenty-five eyes (#1-#25) from 16 subjects were measured. Nineteen eyes were normal, one eye was aphakic (#8), and 5 eyes had undergone LASIK refractive surgery (#5, #6, #10, #12, #13). Ages ranged from 20 to 71 years (mean±std, 33±11 years), spherical error ranged from -6.00 to +16.50 D (-1.62±4.42 D), and astigmatism ranged from 3.78 to 0.07 D (1.07±0.98D).

4.3.1.4.- Measurements

Measurements were performed under the same protocol specified in Chapter 2, section 2.4 for the two different conditions tested: green (543 nm) and near IR illumination (786 nm).

4.3.2.- HARTMANN-SHACK

4.3.2.1.- Setup and procedures.

A detailed description of a similar system can be found in Chapter 3 without the minor modifications introduced for this study. Figure 4.2 shows a schematic diagram of the HS wavefront sensor used in this study, including this modifications. For this study, light from an IR (788 nm) super-luminiscent diode (Anritsu, 10 μw) was introduced by means of a pellicle beam splitter and co-aligned to the green (543 nm) He Ne laser beam (Melles Griot, 1 mw) used in previous measurements. The He-Ne laser was spatially filtered and expanded prior to collimation, bringing the maximum power reaching the eye to less than 5 μw over an 8 mm diameter pupil. Further power reduction was achieved by reducing the beam diameter to 1.5 to 2 mm and by the use of neutral density filters before spatial filtering. The SLD power was largely reduced after fibre coupling (to about 10% of its maximum nominal power), further power reduction was electronically controlled with its driver. In all cases the maximum power reaching the eye was at least one order of magnitude below the safety limits (ANSI, 2000). The principle of the HS system as well as the particular characteristics of the HS sensor have been described in Chapter 1, Section 1.2.3 and Chapter 3, section 3.3.2.1, respectively, of this thesis. The pupil size was 6 mm.

4.3.2.2.- Setting and control experiment

Measurements were conducted at Imperial College of Science Technology and Medicine, London, United Kingdom. The system was calibrated to ensure that it did not introduce chromatic aberration. Two reference HS images using green and IR light were compared. The green reference was used to calculate the aberrations of the IR reference. The order of magnitude of every Zernike coefficient was always smaller than or equal to the stds of any series of ten measurements of ocular aberrations using only one wavelength. This procedure proves that no significant amount of chromatic aberration was introduced by the optics of the system.

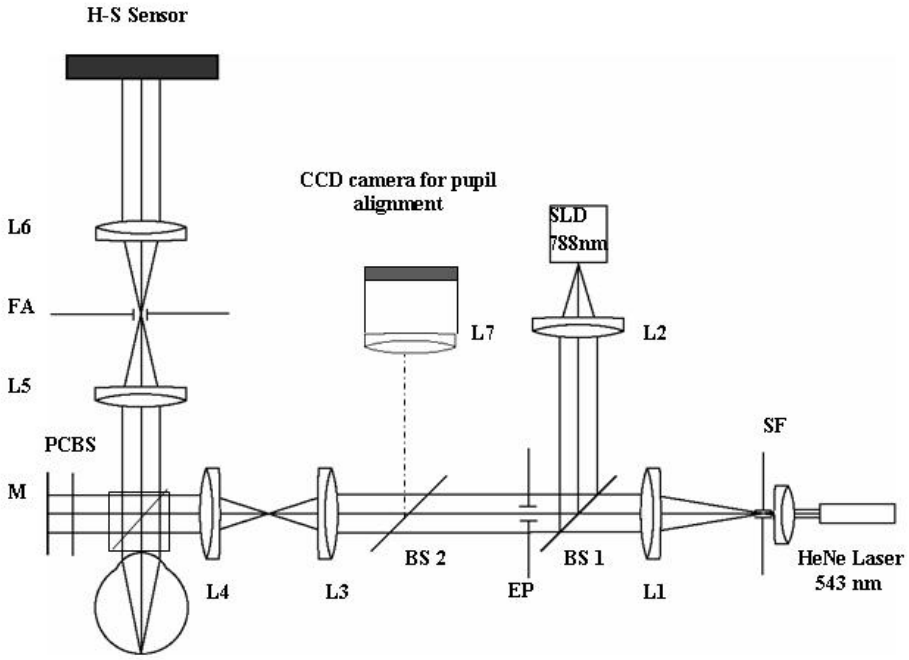

Figure 4.2. Schematic diagram of the HS wavefront sensor. Light coming from an expanded He-Ne (543 nm) laser or from a super luminescent diode (SLD) forms a point on the retina. SF is a spatial filter, and L1 and L2 are collimating lenses. L3, L4 and L5, L6 are relay systems in the illumination and imaging channels, respectively. EP is an entry pupil aperture (pupil diameter = 1.5 mm), and FA is a field aperture. Light reflected off the retina is imaged by a HS sensor (HS Sensor) on a cooled CCD camera. Images of the pupil are projected onto a CCD camera by objective lens L7 and monitors pupil centration. BS1 and BS2 are pellicle beam splitters, and PCBS is a polarizing cube beam splitter. M is a mirror that serves in reference image capture.

4.3.2.3.- Subjects.

Eleven 11 normal eyes (#26-#36) from 6 subjects were measured. Ages ranged from 22 to 26 years (23±1.47 years), spherical error ranged from –6.00 to +0.75 D (2.51±3.24 D) and astigmatism ranged from 0.07 to

4.00 D (1.30±1.57 D). The institutional research and ethical committee approved the use of the wavefront sensor and the experimental design. Written consent was obtained from all subjects participating in the study, according to the tenets of the Declaration of Helsinki. Pupils were dilated using Tropicamide 1% and Phenylephrine 2.5% 30 minutes prior to the beginning of the measurements.

4.3.2.4.- Measurements

Subjects were stabilized with the help of a dental impression and the pupil of the eye was aligned to the optical axis of the instrument, while it was continuously monitored with a CCD camera. The illumination source was used as the fixation point. Sphero-cylindrical refractive errors were compensated when necessary. At least six series of 10 HS images were collected, three using green illumination (543 nm) and the rest using IR illumination (788 nm). Images with the same wavelength were collected consecutively.

4.4.- RESULTS

4.4.1.- RAW DATA

Figure 4.3 A and Figure 4.3 B show a set of aerial images obtained with LRT for eye #5, for green and IR light respectively. Each image has been placed at the corresponding entry pupil position. The intensity patterns differ significantly across wavelengths. Figure 4.3 C shows the spot diagram corresponding to the average data of 3 consecutive runs with green light (crosses) and 4 consecutive runs with IR light (circles) for eye #5. The error bars indicate the std of the positions of the centroid between runs. Chromatic defocus was responsible for the consistent shift in the centroid locations between wavelengths, which increases with entry pupil eccentricity. Figure 4.3 D and Figure 4.3 E show HS images for green and IR light respectively, for eye #29. The presence of a halo surrounding

the centroid was more evident for the image with IR illumination than for that with green illumination. The spots at the upper right and the lower left corners of the image appear dimmer (particularly for green illumination) due to the use of crossed polarisation between illumination and recording (See Chapter 3, Section 3.4.2). Figure 4.3 F shows the HS centroids corresponding to D (crosses) and E (circles). As in LRT, the shift between the green and IR spots increases towards the periphery of the image.

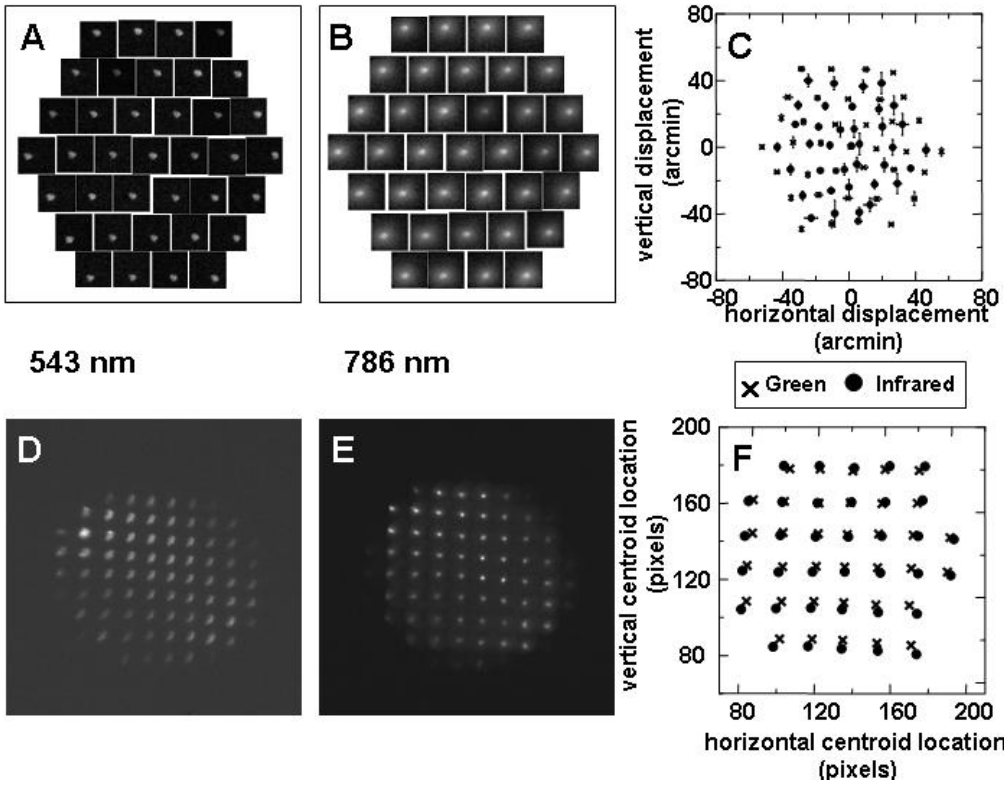

Figure 4.3. Raw data as obtained from LRT (panels A, B, and C) and HS wavefront sensor (panels D, E, and F).

In LRT, a series of retinal images is captured sequentially as a function of the entry pupil position. Aerial images obtained for eye #5 using green and IR light are shown in panels A and B, respectively. Panel C shows the corresponding spot diagram. Crosses represent green illumination, and circles represent IR illumination. Panels D and E show HS images for eye #29 for green and IR light, respectively. Panel F plots the corresponding centroids of the HS images. Symbol notation is the same as for panel C.

4.4.2.- *WAVE ABERRATION MAPS*

Figure 4.4 A shows wave aberration maps from LRT measurements for both wavelengths, for HOA. Eyes #9 and #22 were normal eyes, while #13 had undergone LASIK surgery. Each map is the average of at least three experimental runs. Contour lines are plotted every 0.2 μm. Figure 4.4 B shows wave aberration maps for three normal eyes (#29, #30 and #31) measured with HS for both wavelengths, excluding tilt and defocus. Contour lines are plotted every 0.5 μm. For both systems, the wave aberration patterns corresponding to green and IR wavelengths for the same subject are very similar.

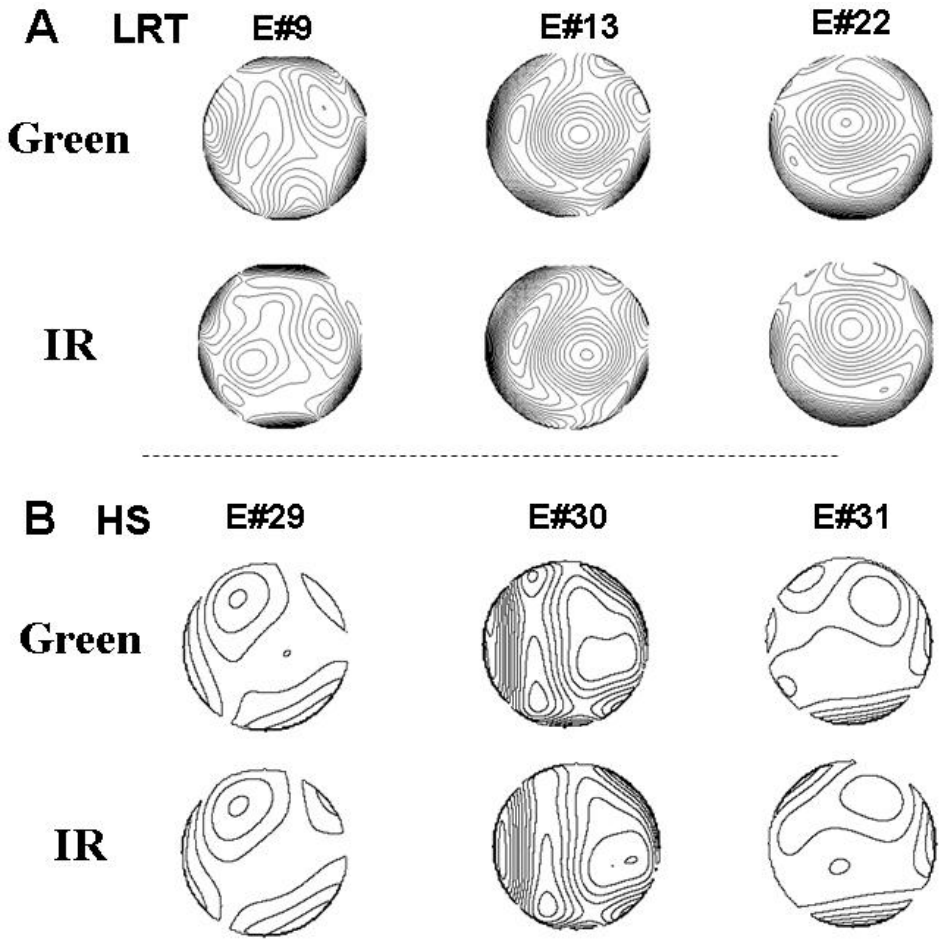

Figure 4.4. Wave aberration maps from LRT (A) and HS (B) for green and IR light.

A First- and second-order terms have been excluded. Eyes #9 and #22 were normal eyes, and #13 had undergone LASIK. Contour lines are plotted every 0.2 μm, and pupil size was 6.5 mm. B Tilts and defocus have been excluded. All three eyes were normal. Contour lines are plotted every 0.5 μm, and pupil size was 6 mm.

4.4.3.- ZERNIKE COEFFICIENTS AND RMS

Figure 4.5 shows plots of sets of Zernike coefficients for green (crosses) and IR (circles) light for the same eyes as in Figure 4.4. First and second order terms have been excluded to allow a higher resolution view of higher order terms. Error bars represent the std of the measurement. Mean variability (std), averaged across Zernike coefficients and subjects, was 0.10±0.06 (mean±std) for green light and 0.07±0.04 for IR light, for the measurements performed with LRT, and 0.019±0.009 (mean±std) for green light and 0.015±0.009 for IR light, for the measurements performed with HS. The differences between the Zernike coefficients measured with green and IR light, shown in Figure 4.5, are within the inherent variability of the techniques.

A univariate statistical analysis (Student t-test) on each Zernike coefficient for each eye was performed to detect which subjects and particular terms showed significant differences ($p<0.01$) when measured in green and IR light. For the 25 eyes measured with LRT 39 terms (excluding defocus) out of 825 (25 eyes x 33 terms), i.e. 4.7 %, were statistically different. The defocus term (Z_2^0) was statistically different in 24 of the 25 eyes (96% of the subjects). All the other statistically different terms were randomly distributed. For the 11 eyes measured with HS 61 terms out of 275 (11 eyes x 25 terms), i.e., 22% of the coefficients were statistically different. The defocus term was statistically different in all of the eyes. Among terms other than defocus, 50 out of 275 (18%) were found to be significantly different.

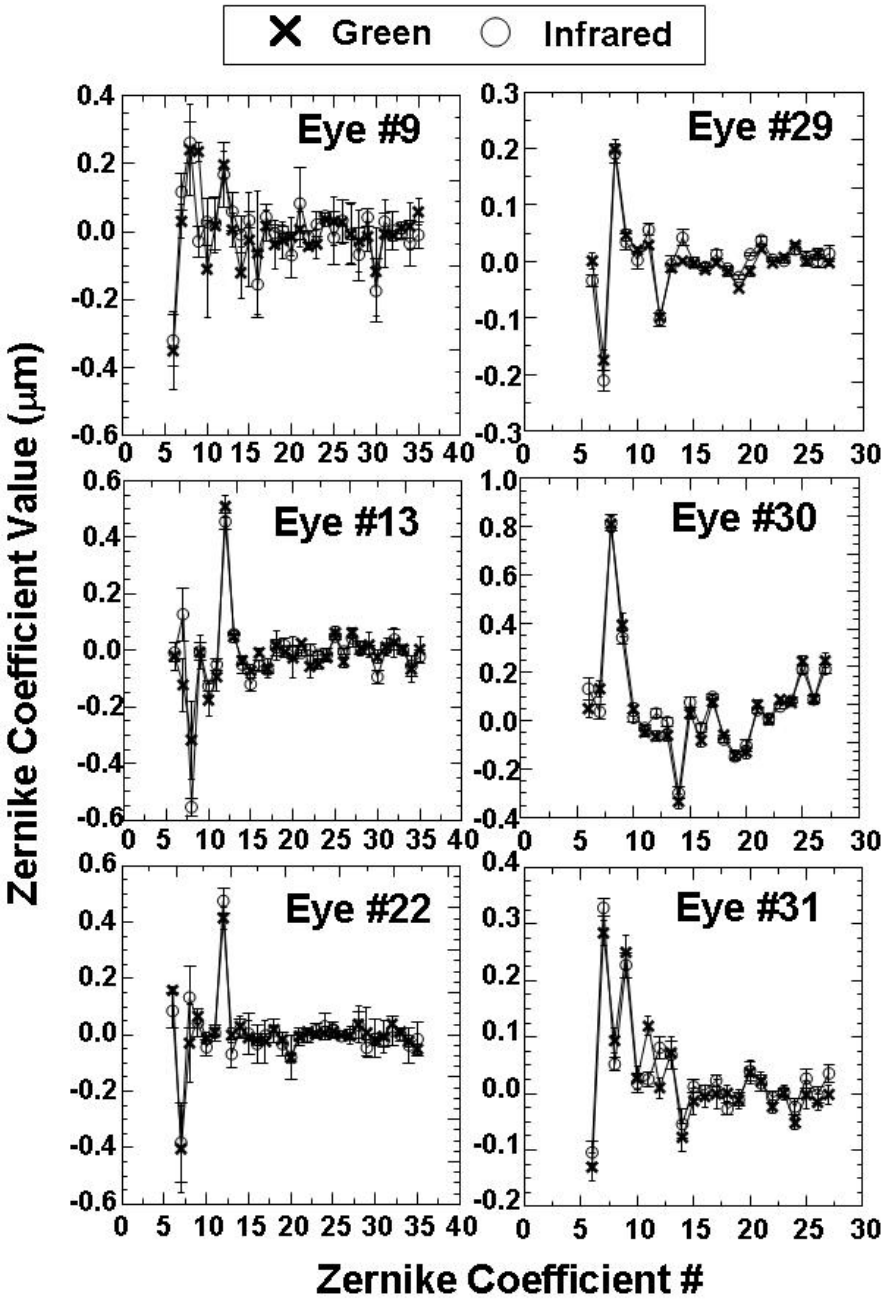

Figure 4.5. Plots of sets of the Zernike coefficients for green (crosses) and IR (circles) light for the same eyes as in Figure 4.4. First- and second-order terms have been cancelled. Error bars represent the std of the measurement.

Defocus for IR wavelength versus defocus for green wavelength in dioptres for all subjects is shown in Figure 4.6. There is a good linear correlation (R^2=0.98), and the slope of the linear fit is close to one (0.96). The focus shift between IR and green, given by the fitting equation is 0.72 D. The experimental focus shift was 0.78±0.29 D.

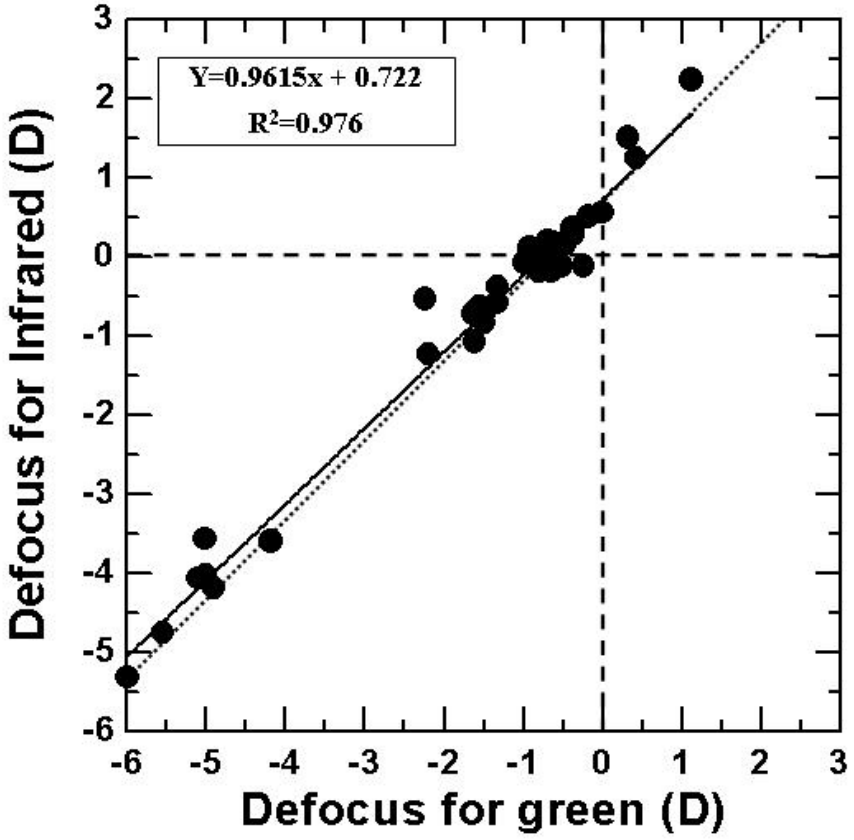

Figure 4.6. Defocus for IR vs. green wavelength in dioptres for all subjects.

The solid line represents the best linear fit to the data (R^2 = 0.976). The focus shift between infrared and green given by the fitting equation is 0.72 D. The slope of the linear fit is close to one (0.9615). The dashed line corresponds to a fitting line with slope equal to one and falls within the data variability

Bar diagrams in Figure 4.7 compare individual terms (astigmatism and SA) and the RMS including different terms, obtained with green (black bars) and IR (grey bars) for all subjects. Eyes #1 to #25 were measured with LRT, and #26 to #36 with HS. Asterisks indicate those eyes showing statistically significant differences ($p<0.01$). Astigmatism (Figure 4.7A) was statistically different in 3 of the 36 subjects (8.3 %). RMS for 3rd order aberrations (Figure 4.7 B) was statistically different in 6 of the 36 subjects (16.6 %). RMS for HOA (Figure 4.7 C) was statistically different in 5 of the 36 subjects (13.5 %). Spherical aberration (Z_4^0) (Figure 4.7 D) was statistically different in 4 of the 36 subjects (11.1%). Only one normal eye (#35) came out significantly different for all the terms or orders reported above (RMS for HOA, 3rd order aberrations, SA and astigmatism).

4.5.- DISCUSSION

This study shows that while the intensity distribution of LRT aerial images or HS images is notably different between green and IR illumination, both wavelengths provide aberration estimates within the experimental error (except for defocus). Our sample includes eyes with large differences in optical quality (from normal eyes to surgical eyes) and ages (20 through 71), suggesting that this conclusion holds for most of the population.

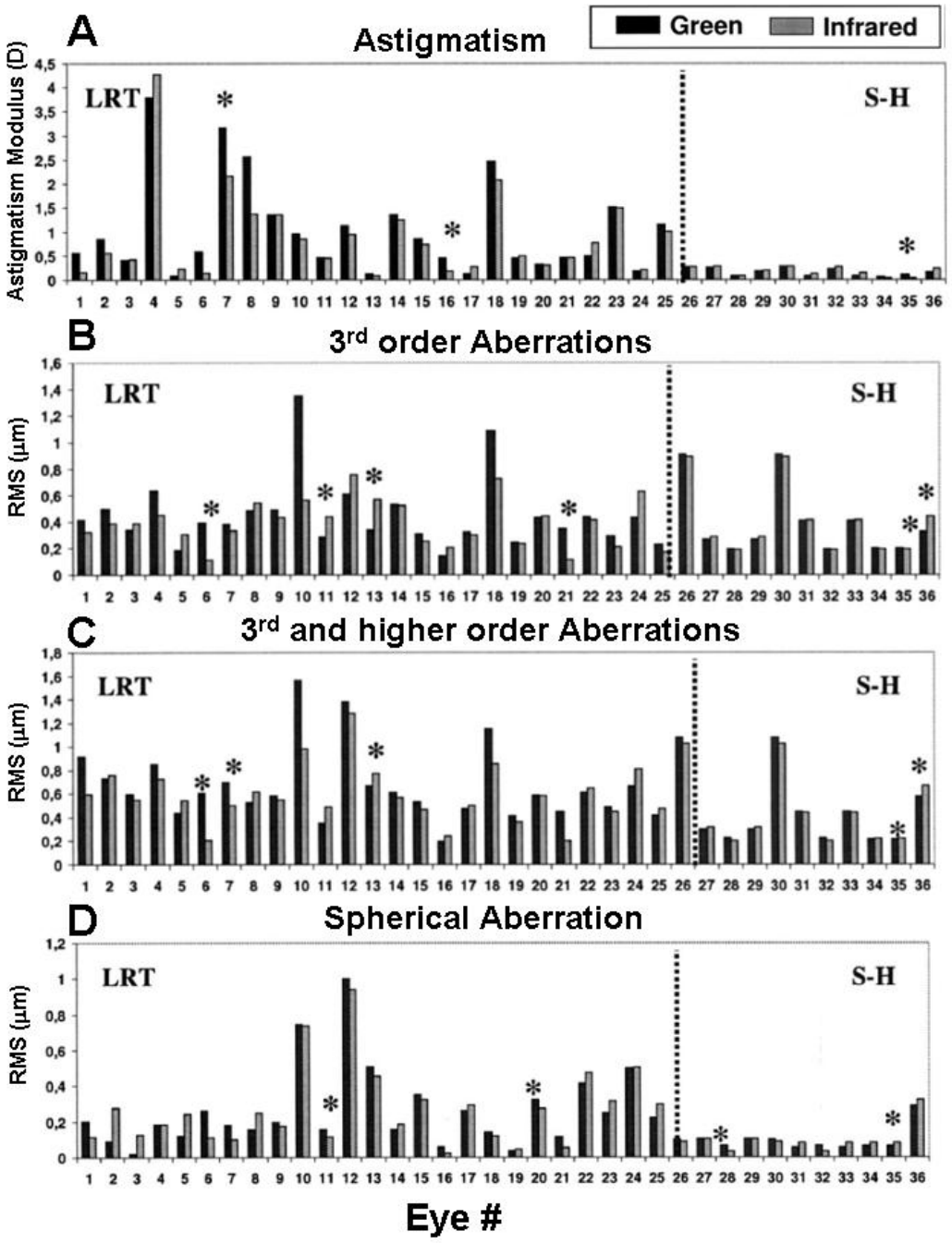

Figure 4.7. Bar diagrams comparing individual terms (astigmatism, A, and SA, D) and the root mean square wavefront error (RMS) for different orders (third order aberrations, B, and HOA, D), obtained with green (black bars) and IR (grey bars) for all subjects. Asterisks indicate the statistically different coefficients. Astigmatism was compensated during the measurement only for those eyes measured with HS.

4.5.1.- DIFFERENCES IN IMAGE INTENSITY PROFILES

Figure 4.3 shows relevant intensity differences between the aerial images obtained with IR and those obtained with green illumination. IR images are typically more spread and are surrounded by a broad halo. It has been suggested that most of the light contributing to the core of double-pass aerial images is probably due to the light captured and guided back from the photoreceptors (Lopez-Gil and Artal., 1997, Williams et al., 1994). The halo is probably produced by effects other than aberrations, such as retinal stray light scattered at the choroid (Westheimer and Campbell, 1962, Westheimer and Liang, 1995). Retinal scattering increases for longer wavelengths due to their deeper penetration within the retina and the choroid (Elsner et al., 1992, Gorrand et al., 1984).

Some previous comparisons of optical quality in IR and green light were based on estimates from double-pass aerial images. A computer simulation was performed to evaluate the contribution to the aerial image spread caused by degradation other than the ocular aberrations, and the influence of wavelength on this additional contribution. LRT double-pass aerial images were simulated from the estimated wave aberration function. LRT aerial images are the cross-correlation of the entry (1st pass) and exit (2nd pass) PSF. The entry pupil is a narrow incoming Gaussian beam (variance=0.10 mm and = 0.13 mm respectively, for green and IR illumination) and the exit pupil is a 3-mm circular pupil. The entry and exit pupil sizes correspond to the experimental values in the LRT setup. Insets in Figure 4.8 show real images and simulated images, corresponding to an entry pupil centered at coordinates (+1.5, -2.6 mm). Figure 4.8 A and Figure 4.8 B show experimental and simulated results for green and IR light respectively, for eye #22. The plots represent the normalized radial intensity profile of the corresponding real (solid) and simulated (dashed) aerial images. The distance from the peak position to

the zero position represents the centroid deviation from the chief ray (which is practically the same for the simulated and real images). The width of the simulated images accounts for the spread caused exclusively by the measured aberrations, while the real images are further enlarged by scattering and non-measured higher-order aberrations.

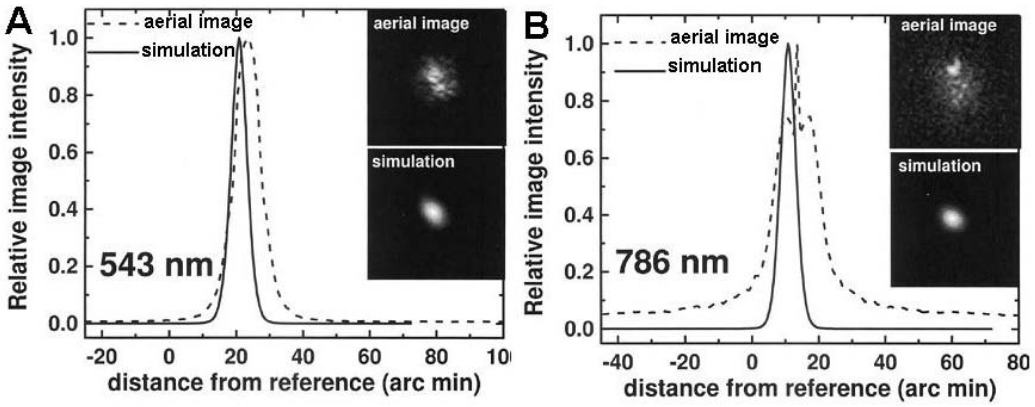

Figure 4.8. Experimental and simulated aerial images for green (A) and infrared (B) light, respectively, for eye #22 and entry pupil at coordinates (+1.5, -2.6 mm). The image on the upper left corner of the plot is the aerial image obtained experimentally, and the image below is the aerial image simulated from measured aberrations as the autocorrelation of first- and second- pass PSFs. The plots represent the normalized radial intensity profile of the corresponding real (dashed) and simulated (solid) aerial images. The distance to zero position represents the centroid deviation from the chief ray. The width of the simulated images accounts for the spread caused exclusively by the measured aberrations, whereas that of the real images also includes other effects, such as scattering and non measured higher-order aberrations, together with the measured aberrations.

The HS images in Figure 4.3 C also suggest a larger contribution of scattered light in IR. A crossed polarization configuration was used, which explains the "polarization cross" pattern observed in green light illumination (see Chapter 3, section 3.4.2) (Marcos et al., 2002b). Green illumination maximizes the light reflected by the photoreceptor outer segments (Elsner et al., 1992) which are thought to partly retain polarization (Gorrand et al., 1984) Light multiply scattered by deeper layers (probably a significant component of the IR images (Elsner et al., 1996)) does not retain polarization, and therefore the HS spots will show

little polarization-related intensity differences across the image (See Chapter 3).

The effects mentioned above affect the shape and intensity distribution of the aerial image and are critical in double-pass measurements of the optical quality of the eye. In this technique, MTF estimates are directly obtained from double-pass aerial images. An appropriate halo subtraction is critical to obtain MTFs in IR consistent to those measured in green light (Lopez-Gil and Artal., 1997). However, reflectometric techniques for wave aberration measurements only rely on centroid deviation computations, which as shown, are not significantly affected by wavelength.

4.5.2.- CHROMATIC DIFFERENCE OF FOCUS

The defocus term was significantly different across wavelengths in all but one subject. The mean focus difference between green and IR across subjects was 0.78±0.29 D, close to the shift estimated by the linear fitting shown in Figure 4.6 (0.72 D). This value agrees well, within the inherent variability, with the chromatic focus shift predicted by the Indiana chromatic reduced eye model (Thibos et al., 1992) (see equation (4.1)).

$$R_E = 633.46 \cdot \left[\frac{1}{(\lambda_G - 214.102)} - \frac{1}{\lambda_{IR} - 214.102} \right] = 0.82\,D \qquad (4.1)$$

where λ_G=543 nm and λ_{IR}=787 nm (mean between IR wavelength used for LRT, 786 nm, and HS, 788 nm).

Thibos et al. (Thibos et al., 1992) obtained the parameters of their eye model by fitting experimental data for a range of wavelengths between 400 nm and 700 nm, and using Cornu's expression for the dependence of the index of refraction with wavelength. Equation (4.1) agrees well with experimental data in the literature for wavelengths up to 760 nm (close to

the wavelength used in this study), with variations close to the intersubject variability in our sample (Thibos et al., 1992). Fernandez et al. (Fernandez et al., 2005) measured the ocular aberrations with wavelengths ranging from 700 to 900 nm for four eyes, and found a good agreement with the values predicted by equation (4.1), even though the wavelength values they used extended even further in the IR. They reported a value for the chromatic difference in defocus between their wavelengths of 0.4 D. A recent study (Fernandez and Artal, 2008) extended the range of wavelengths for measured aberrations even further in the IR (632.8-1070), finding a defocus difference of 1 D. They compared their defocus values for each of the five wavelengths measured with those given by the Cauchy equation, proposed by Atchison and Smith (Atchison and Smith, 2005), for the same wavelengths and found that values corresponding to 1030, 1050 and 1070 nm were located away from the theoretical curve. They thought this difference, supposing that Cauchy equation is still valid in IR, might be due to the deeper penetration and consequent backscattering at this longer wavelengths.

It has been frequently argued that differences in the retinal layer where light is reflected may cause differences between manifest refraction and retinoscopy (Millodot and Sivak, 1979, Millodot, 1980). Charman and Jennings (1976) and Williams et al. (1994) for red light, and later López-Gil and Artal (1997) for near IR light showed that the differences between subjective and reflectometric focus were negligible, and concluded that reflection contributing to the central core of the PSF occurred within the photoreceptor layer. Our results, based on the Zernike defocus term of wave aberration reflectometric estimates, also support this conclusion. The focus shift found is slightly lower than the chromatic shift prediction (by 0.10 D), consistent with a reflection plane behind the photoreceptor layer. However, this shift is of the order of the measurement error (0.12 D for green light and 0.08 D for IR light on average), and lower than the intersubject variability (0.29 D). No particular trend was found for the

focus shift in normal, young subjects as a function of refractive error (coefficient of correlation, r=0.17, p=0.44). In addition, no particular difference was found for the focus shift in eyes with abnormal corneas by LASIK surgery. However, the focus shift found was much higher than the average for the oldest and the aphakic eyes (1.5 D and 1.7 D; eyes #4 and 8, respectively). Although our population did not sample different age groups homogeneously, a slight increase of focus shift with age (r=0.45, p=0.02) was found when including all our subjects. However, the majority of subjects were young or middle-aged (20-43 years old) and no aged-related trend (r=0.26, p=0.20) was found within this age range.

4.5.3.- CONCLUSION

The equivalence of high order aberrations measured in visible or near IR illumination with LRT and HS within the accuracy of the techniques has been shown. The shift found in the defocus term was consistent with the shift predicted by chromatic aberration

These results are relevant because typical commercial wavefront sensing devices and ocular examination devices use IR illumination. It has been shown that despite the longer tails of the aerial images at this wavelength, IR can be successfully used in all the tested conditions, including old and surgical eyes. An experimental value for the focus shift between near IR (786-788 nm) and green (543 nm) illumination in two reflectometric aberrometers (LRT and HS) has also been provided. One of the most promising applications of wavefront sensing devices is their use as sophisticated autorefractometers. They are now being applied for use in refractive surgery to guide ablation with the aim of compensating both low (2^{nd} order aberrations) and HOA aberrations. An accurate transformation of the IR estimates of spherical error into visible wavelengths is crucial to determine the actual correction that should be applied. It has been shown that Thibos's chromatic reduced eye model equation is a valid expression to predict focus shift for our wavelength.

However, for longer wavelengths there is no evidence of the validity of this equation, and new expressions for the refractive index and chromatic difference of refraction may need to be developed. In addition, it has been found that discrepancies can occur in aphakic eyes, and that there might be age-dependent corrections to equation (4.1).

Several reports in the literature found differences in the LCAs of aphakic eyes (Millodot, 1976) and pseudoaphakic eyes (Negishi et al., 2001) with respect to normal eyes. Possible age-related changes of LCA have been a matter of controversy (Howarth et al., 1988, Mordi and Adrian, 1985, Morrell et al., 1991, Calver et al., 1999). Although much of these refractive discrepancies are small, their magnitude can be comparable to that of HOA, and therefore accurate predictions of spherical errors for visible light from IR measurements are important.

Chapter 5

EFFECT OF SAMPLING ON REAL OCULAR ABERRATION MEASUREMENTS.

This chapter is based on the article by Llorente, L. et al.,"The effect of sampling on real ocular aberration measurements", Journal of the Optical Society of America A 24, 2783- 2796 (2007). The co-authors of the study are: Susana Marcos, Carlos Dorronsoro and Steve Burns. A preliminary version of this work was presented as an oral paper (Llorente et al., 2004b) at the II EOS Topical Meeting on Physiological Optics in Granada. The contribution of the author to the study was the performance of the experimental measurements, and data processing and analysis, as well as statistical analysis of the experimental data and of the data from simulations performed by Steve Burns.

5.1.- ABSTRACT

PURPOSE: To assess the performance of different sampling patterns in the measurement of ocular aberrations and to find out whether there was an optimum pattern to measure human ocular aberrations.

METHODS: Repeated measurements of ocular aberrations were performed in 12 healthy non surgical human eyes, and 3 artificial eyes,

with a LRT using different sampling patterns (Hexagonal, Circular and Rectangular with 19 to 177 samples, and three radial patterns with 49 samples coordinates corresponding to zeroes of the Albrecht, Jacobi, and Legendre functions). Two different metrics based on the RMS of difference maps (RMS_Diff) and the proportional change in the wave aberration (W%) were used to compare wave aberration estimates as well as to summarize results across eyes. Some statistical tests were also applied: hierarchical cluster analysis (HCA) and Student's t-test. Computer simulations were also used to extend the results to "abnormal eyes" (Keratoconic, post-LASIK and post-RK eyes).

RESULTS: In general, for both artificial and human eyes, the "worst" patterns were those undersampled. Slight differences were found for the artificial eye with different aberrations pattern, compared to the other artificial eyes. Usually those patterns with greater number of samples gave better results, although the spatial distribution of the samples also seemed to play a role, for our measured, as well as our simulated "abnormal" eyes. There was agreement between the results obtained from our metrics and from the statistical tests.

CONCLUSIONS: Our metrics proved to be adequate to compare aberration estimates across sampling patterns. There may be an interaction between the aberration pattern of an eye and the ability of a sampling pattern to reliably measure the aberrations. This implied that just increasing the number of samples was not as effective as choosing a better sampling pattern. In this fashion, moderate density sampling patterns based on the zeroes of Albrecht cubature or hexagonal sampling performed relatively well, being a good compromise between accuracy and density. These conclusions were also applicable in human eyes, in spite of the variability in the measurements masking the sampling effects except for undersampling patterns. Finally, the numerical simulations

proved to be useful to assess *a priori* the performance of different sampling patterns when measuring specific aberration patterns.

5.2.- INTRODUCTION

As previously described in Chapter 1, aberrometry techniques currently used for human eyes consist on measuring ray aberrations at a discrete number of sampling points, and then estimate the wave aberration using modal, zonal or combined reconstruction methods (Chapter 1, section 1.2.2). It is, therefore, crucial for these techniques to find out which is the minimum number of samples necessary to fully characterize the aberration pattern of the eye. This is a question under debate in the clinical as well as the scientific community. The optimal number of sampling points represents a trade-off between choosing a number of samples large enough to accurately estimate the wave aberration (see Chapter 1, section 1.2.5.3), and reducing the measuring and processing time. In addition, the distribution of the samples throughout the pupil of the eye may also play a role. In this chapter, the influence of the number and distribution of samples used in the aberrations measurement on the resulting estimated wave aberration will be studied.

To our knowledge, there has not been a systematic experimental study investigating whether increasing the sampling density over a certain number of samples provides significantly better accuracy in ocular aberration measurements, or whether alternative sampling configurations would be more efficient. There have been theoretical investigations of sampling configuration from both analytical and numerical approaches which are described below. However, the applicability to human eyes should be ultimately tested experimentally.

Cubalchini (Cubalchini, 1979) was the first to study the modal estimation of the wave aberration from derivative measurements using a least squares method, concluding that the geometry and number of

samples affected the wavefront estimations and that the variance of higher order Zernike terms could be minimised by sampling as far from the centre of the aperture as possible and minimising the number of samples used to estimate a fixed number of terms and to take the measurements.

In 1997, Rios et al. (1997) found analytically for Hartmann sensing that the spatial distribution of the nodes of the Albrecht cubatures (Bará et al., 1996) made them excellent candidates for modal wavefront reconstruction in optical systems with a centrally obscured pupil. This sampling scheme could also be a good candidate for ocular aberrations, due to the circular geometry of the cubature scheme. In addition, as the Zernike order increases (i.e., higher order aberrations), the area of the pupil more affected by aberrations tends to be more peripheral (McLellan et al., 2006, Applegate et al., 2002, Cubalchini, 1979), and therefore ocular wavefront estimates would potentially benefit by a denser sampling of the peripheral pupil.

He et al. (1998) used numerical simulations to test the robustness of the fitting technique they used for their SRR (least-square fit to Zernike coefficients) to the cross-coupling or modal aliasing (interaction between orders) as well as the error due to the finite sampling aperture. They found that the error could be minimized by extracting the coefficients corresponding to the maximum complete order possible (considering the number of samples), in agreement with Cubalchini (Cubalchini, 1979), and by using a relatively large sampling aperture, which practically covered the measured extent of the pupil. Although this large sampling aperture introduced some error due to the use of the value of the derivatives at the centre of the sampling apertures to perform the fitting, and the rectangular pattern they used did not provide an adequate sampling for radial basis functions, simulations confirmed that the overall effect was relatively small.

In 2003, Burns et al. (2003) computationally studied the effect of different sampling patterns on measurements of wavefront aberrations of the eye, by implementing a complete model of the wavefront processing used with a "typical" HS sensor and modal reconstruction. They also analyzed the effect of using a point estimator for the derivative at the centre of the aperture, versus using the average slope across the subaperture, and found that the second decreased modal aliasing somewhat, but made little practical difference for the eye models. Given that the higher order aberrations tended to be small, the modal aliasing they found was subsequently small. Finally, they found that non-regular sampling schemes, such as cubatures, were more efficient than grid sampling, when sampling noise was high.

Díaz-Santana et al (Diaz-Santana et al., 2005), and Soloviev and Vdovin (2005) developed analytical models to test different sampling patterns applied to ocular aberrometry and HS sensing in astronomy, respectively. Díaz-Santana et al. (2005) developed an evaluation model based on matrices that included as input parameters the number of samples and their distribution (square, hexagonal, polar lattice), shape of the subpupil, size and irradiance across the pupil (uniform irradiance vs. Gaussian apodisation), regarding the sampling. The other input parameters were the statistics of the aberrations in the population, the sensor noise, and the estimator used to retrieve the aberrations from the aberrometer raw data. According to their findings, no universal optimal pattern exists, but the optimal pattern will depend, among others on the specific aberrations pattern to be measured. Soloviev et al.'s model (Soloviev and Vdovin, 2005) used a linear operator to describe the HS sensing, including the effects of the lenslets array geometry and the demodulation algorithm (modal wavefront reconstruction). When applying this to different sampling configurations, using the Kolmogorov statistics as a model of the incoming wavefront, they found that their pattern with 61 randomly spatially distributed samples gave better results

than the regular hexagonal pattern with 91 samples of the same sub-aperture size (radius=1/11 times the exit pupil diameter), which covered completely the extent of the pupil in the case of the 91-sample pattern. In these theoretical models, an appropriate statistical input was crucial so that their predictions can be generalized in the population. McLellan et al. found (McLellan et al., 2006) that high order aberration terms show particular relationships (i.e. positive interactions that increase the MTF over other potential combinations), suggesting that general statistical models should include these relationships in order to describe real aberrations.

In this study, LRT2 was used to measure wave aberrations in human eyes, with different sampling patterns and densities. Hexagonal and Rectangular configurations were chosen because they are the most commonly used. Different radially symmetric geometries were also used to test whether these patterns were better suited to measuring ocular aberrations. These geometries included uniform polar sampling, arranged in a circular pattern, and three patterns corresponding to the zeroes of the cubatures of Albrecht, Jacobi and Legendre equations. Additionally, different densities were tested for each pattern in order to evaluate the trade-off between accuracy and sampling density. To separate variability due to biological factors from instrumental issues arising from the measurement and processing, measurements on artificial eyes were also performed. Noise estimates in human eyes as well as realistic wave aberrations were used in computer simulations to extend the conclusions to eyes other than normal eyes (meaning healthy eyes with no pathological condition and that have not undergone any ocular surgery). For all these three cases (human, artificial and simulated eyes), two metrics (defined below, in section 5.3.4.2.-) to assess the differences across the aberration maps obtained with the different sampling patterns were tested, and the estimated Zernike terms which changed depending on the sampling pattern used were identified.

5.3.- METHODS

5.3.1.- LASER RAY TRACING

Optical aberrations of the eyes were measured using the device LRT2 which allowed the selection of distribution and density of the sampling pattern by software (see Chapter 2, section 2.2.2.1). For this study the following sampling patterns were used: Hexagonal (H), evenly-distributed Circular (C), Rectangular (R) and three radial patterns with 49 samples coordinates corresponding to zeroes of Albrecht (A49), Jacobi (J49) and Legendre (L49) functions (see Figure 5.1). Different densities for the Hexagonal, and Circular patterns were also used to sample the pupil: 19, 37 and 91 samples over a 6 mm pupil. In addition, for the artificial eyes, Rectangular patterns with 21, 37, 98 and 177 samples were also used. The coordinates of the samples of Jacobi, Legendre and Albrecht patterns can be found in the appendix of this thesis. In order to simplify the reading, an abbreviated notation throughout the text was used: the letter indicates the pattern configuration and the number indicates the number

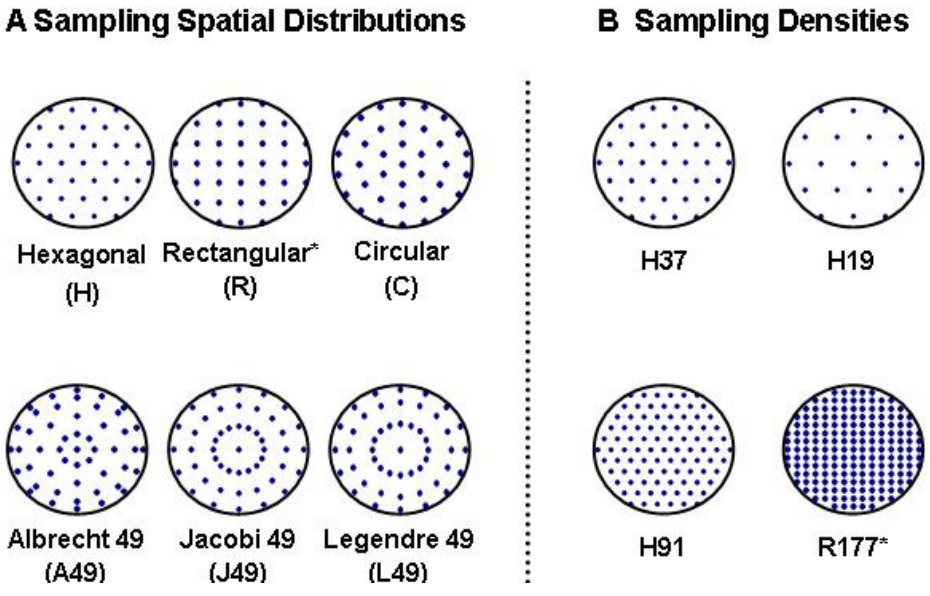

Figure 5.1. Pupil sampling patterns used in this work. A Spatial distributions include equally spaced hexagonal (H), rectangular (R) and polar distributions (C), and radial distributions with 49 coordinates corresponding to zeroes of Albretch, Jacobi and Legendre functions (A49, J49, and L49, respectively). B Sampling densities include patterns with 19, 37, 91, and 177 samples over a 6 mm pupil. Asterisks indicate those patterns only used for artificial eyes.

of sampling apertures, i.e., for example H91 stands for a hexagonal pattern with 91 samples.

5.3.2.- EYES

The three polymetylmethacrylate artificial eyes used in this work, A1, A2 and A3, were designed and extensively described by Campbell (Campbell, 2005). Nominally, A2 shows only defocus and SA. A1 and A3 show nominally, in addition to defocus and SA, different amounts of 5th (term Z_5^{-1}, secondary vertical coma) and 6th (term Z_6^2, tertiary astigmatism) Zernike order aberrations.

Twelve healthy non surgical eyes (eyes R1 to R12, where even numbers indicate left eyes, odd numbers right eyes) of six young subjects (age = 28±2 years) were also measured. Spherical error ranged from –2.25 to +0.25 D (1.08 ± 1.17 D), and 3rd and higher order RMS from 0.17 to 0.62 μm (0.37±0.15 μm).

5.3.3.- EXPERIMENTAL PROCEDURE

5.3.3.1.- Artificial Eyes

A specially designed holder with a mirror was attached to the LRT apparatus for the measurements on the artificial eyes. This holder allowed the eye to be placed with its optical axis in the vertical perpendicular to the LRT optical axis. In this way, the variability due to mechanical instability or the effect of gravity was minimised. The pupil of the artificial eye was aligned to the optical axis, and optically conjugated to the pupil of the setup. Defocus correction was achieved in real time by minimizing the size of the aerial image for the central ray.

The pattern sequence was almost identical in the three artificial eyes: H37, H19, H91, C19, C37, H37_2, C91, R21, R37, R98, H37_3, R177, A49, J49, L49, H37_4. However, for L2 the pattern A49 was the last pattern measured in the sequence. As a control, identical H37 patterns were

repeated throughout the session (indicated by H37, H37_2, H37_3 and H37_4). A measurement session lasted around 40 minutes in these artificial eyes.

5.3.3.2.- Human Eyes

The protocols used during the measurements in human eyes were those described in Chapter 2, section 2.4 of this thesis, considering each different sampling pattern as a condition to test. Custom passive eye-tracking routines (see Chapter 2, section 2.2.2.3) were used to analyse the pupil images, captured simultaneously to retinal images, and to determine the effective entry pupil locations as well as to estimate the effects of pupil shift variability in the measurements. Scan times for these eyes ranged from 1 to 6 seconds, depending on the number of samples of the pattern. In the measurements of these eyes fewer patterns (H37, H19, H91, C19, C37, C91, A49, J49, L49, H37) were used to keep measurement sessions within a reasonable length of time. To assess variability, each pattern was repeated 5 times within a session. In addition, the H37 pattern was repeated at the end of the session (H37_2) to evaluate whether there was long term drift due to fatigue or movement. An entire measurement session lasted around 120 minutes for both eyes.

5.3.4.- DATA PROCESSING

5.3.4.1.- Wave aberration estimates

LRT measurements were processed as described in Chapter 2. Local derivatives of the wave aberrations were fitted to a 7th order Zernike polynomial, when the number of samples of the sampling pattern allowed (36 or more samples), or to the highest order possible. From each set of Zernike coefficients the corresponding third and higher order (i.e., excluding tilts, defocus and astigmatism) wave aberration map and the corresponding RMS were computed. All processing routines were written in Matlab (Mathworks, Nathick, MA). Processing parameters were chosen

(as were filters during the measurement, to obtain equivalent intensities at the CCD camera) so that in both, human and artificial eyes, the computation of the centroid was similar and not influenced by differences in reflectance of the eye "fundus".

The wave aberration estimated using the H91 sampling pattern was used as a reference when computing the metrics, as there was no "gold standard" measurement for the eyes. This fact can limit the conclusions based on the metrics, which use a reference for comparison. The influence of this choice in the results was tested by checking the effect of using the other pattern with the highest number of samples (C91) as a reference. Similar results were obtained.

5.3.4.2.- Wave aberration variability metrics

Two metrics were defined to evaluate differences between sampling patterns:

RMS_Diff: A difference pupil map (Diff. Map) was obtained by subtracting the wave aberration for the reference pattern from the wave aberration corresponding to the pattern to be evaluated. RMS_Diff was computed as the RMS of the difference pupil map computed. Larger RMS_Diff values corresponded to less accurate sampling pattern. For each eye, a threshold criterion was established to estimate the differences due to factors other than the sampling patterns. This threshold was obtained by computing the value of the metric for maps obtained using the same pattern (H37) at different times within a session. Differences lower than the threshold were considered within the measurement variability. For artificial eyes, the map obtained from one of the measurements was subtracted from the map obtained for each of the other three measurements and the threshold was computed as the average RMS_Diff value corresponding to each map. For human eyes, the threshold was determined based on two sets of five consecutive measurements each, obtained at the beginning and at the end of the session using the H37

pattern (H37 and H37_2, respectively). Each of the five wave aberration maps of the H37_2 set was subtracted from each of the corresponding wave aberration map of the H37 set to obtain the corresponding five difference maps. The threshold was computed as the RMS corresponding to the average map of the five difference maps.

W%: This is the percentage of the area of the pupil in which the wave aberration for the test pattern differs from the wave aberration measured using the reference pattern. Wave aberrations were calculated on a 128x128 grid, for each of the five repeated measurements for each sampling pattern and for the reference. Then, at each of the 128x128 points, the probability that the differences found between both groups of measurements (for the sampling and for the reference) arose by chance was computed. Binary maps were generated by setting to one the areas with probability values below 0.05, and setting to zero those areas with probability values above 0.05. W% was then computed as the number of pixels with value one divided by the total number of pixels in the pupil, all multiplied by 100. The larger W% the less accurate the corresponding sampling pattern was. This metric was applied only for human eyes, where, as opposed to artificial eyes, variability was not negligible, and repeated measurements were performed.

Ranking: To summarize the results obtained for all measured eyes, a procedure that was named Ranking was performed. It consisted of 1) sorting the patterns, according to their corresponding metric values, for each eye; 2) scoring them in ascending order, from the most to the least similar to the reference, i.e., from the smallest to the greatest value obtained for the metric (from 0, for the reference, to the maximum number of different patterns: 9 for the human eyes and 15 for the artificial eyes); 3) add up the scores for each pattern across eyes. Since this procedure was based on the metrics, and therefore used the reference, the conclusions obtained were relative to the reference.

5.3.4.3.- Statistical analysis

A statistical analysis was also performed. It involved the application of 1) a HCA represented by a dendrogram plot (tree diagram shown to illustrate the clustering) using average linkage (between groups), and 2) an ANOVA (General Linear Model for repeated measurements, with the sampling patterns as the only factor) to the Zernike coefficients obtained for each pattern, followed by a pair-wise comparison (Student t-test) to determine, in those cases where ANOVA indicated significant differences ($p<0.05$), which patterns were different. The statistical tests were performed using SPSS (SPSS, Inc., Chicago, Illinois).

The aim of the HCA was to group those patterns producing similar Zernike sets, in order to confirm tendencies found in the metrics (i.e., patterns with large metrics values can be considered as "bad", whereas those with small metrics values can be considered as "good"). Each significant cluster indicated by the dendrogram was framed in order to group patterns yielding the same results. The colour and contour of the frame indicates whether the group was considered as "good" (green solid line), "medium" (amber dashed line) or "bad" (red dotted line) according to the metrics. The algorithm for this test starts considering each case as a separate cluster and then combined these clusters until there was only one left. In each step the two clusters with minimum Euclidean distance between their variables (Zernike coefficients values) were merged. The analysis was performed eye by eye, and also by pooling the data from all eyes (global) to summarize the results.

The ANOVA was computed coefficient by coefficient, with Bonferroni correction (the observed significance level is adjusted to account for the multiple comparisons made), by pooling the data from all the eyes. When probability values were below a threshold of 0.05, i.e., significant differences existed, the pair-wise comparison allowed us to identify those particular sets significantly different, and therefore which

sampling patterns produced significantly different results. Given that the number of artificial eyes measured was smaller than the number of sampling patterns, using an ANOVA on these eyes was not possible. Instead, a Student t-test for paired samples was performed on the three eyes, Zernike coefficient by Zernike coefficient, with Bonferroni correction. In the human eyes, the number of Zernike coefficients significantly different according to the Student t-test relative to total number of possible Zernike coefficients (33 coefficients x 9 alternative patterns) was computed. In addition, those coefficients which were repetitively statistically different across pairs of patterns (statistically different across the greatest number of patterns) were identified. In the case of statistical analysis no references were used, and therefore the results are not relative to any particular sampling pattern.

5.3.4.4.- Numerical Simulations

Some numerical simulations were performed to extend further the conclusions obtained from experimental data. Simulations were performed as follows. First, a "true" aberration pattern for a simulated eye, which was basically represented by a set of Zernike coefficients (either 37 or 45 terms) was assumed. From these coefficients, a wave aberration function was computed ("true" wave aberration). The simulation then involved sampling the wave aberration. The sampling was performed by computing a sampling pattern (sample location and aperture size) and computing the wave aberration slopes across the sampling aperture. Noise was then introduced into the slope estimates. For this simulation, the noise values estimated from the actual wave aberration measurements described above were used. While the simulation software can include light intensity and centroiding accuracy, for the current simulations it was deemed most important to set the variability of the centroid determinations to experimentally determined values. Once a new set of centroids was computed, for each sample, a

wave aberration was estimated using the standard least-squares estimation procedure used for the actual data, fitting up to either 17 (for the Hex19 and Circ19) or 37 terms. Twenty-five simulated wave aberrations for each simulated condition were calculated, although only the five first sets of Zernike coefficients were used to compute the metrics, in order to reproduce the same conditions as in the measurements.

First, it was verified that the results obtained from the simulations were realistic by using the Zernike coefficients of the real eyes (obtained with the H91 pattern). The aberrations obtained with the sampling patterns used in the measurements of our human eyes as well as with R177 (previously used in the artificial eyes) were sampled, and the corresponding coefficients computed. Finally, the different metrics and ranking were applied to these simulated coefficients, sorting the patterns for each metric across all eyes. The HCA was also applied to these simulated data eye by eye.

Once the simulations were validated in normal (healthy, non surgical) human eyes, they were applied to three different sets of Zernike coefficients corresponding to: 1) A keratoconus eye measured using LRT with H37 as sampling pattern (Barbero et al., 2002b). The main optical feature of these eyes is a larger magnitude of 3rd order terms (mainly coma) than in normal eyes. RMS for HOA was 2.362 μm for the original coefficients used to perform the simulation; 2) A post LASIK eye measured using LRT with H37 as sampling pattern (Marcos et al., 2001). These eyes show an increase of SA towards positive values, and a larger amount of coma, after the surgery. RMS for HOA was 2.671 μm for the original coefficients used to perform the simulation; 3) an eye with aberrations higher than 7th order. In this case the coefficients up to 7th order corresponding to the previous post LASIK eye were used, with additional 0.1 microns on the coefficient Z_8^8, simulating a post-Radial

Keratotomy (RK) eye. RMS for HOA was 2.67 μm for the original coefficients used to perform the simulation.

5.4.- RESULTS

5.4.1.- ARTIFICIAL EYES

5.4.1.1.- Wave Aberrations

Figure 5.2 shows the wave aberration (W.A. map), and the difference (Diff. map) maps (subtraction of the reference map from the corresponding aberration map) for third and higher order corresponding to the sixteen patterns used to measure the artificial eye A3. The wave aberration map at the top right corner is that obtained using the pattern H91, used as the reference. On the left of this map, the corresponding RMS is indicated. The contour lines are plotted every 0.5 μm for the wave aberration maps, and 0.1 μm for the difference maps. Positive and negative values in the map indicate that the wavefront is advanced or delayed, respectively, with respect to the reference. The value below each map is the corresponding RMS.

Qualitatively, the wave aberration maps are similar among patterns, except for those corresponding to the patterns with the fewest samples (H19, C19 and R21). Spherical aberration was predominant in these undersampled patterns, which fail to capture higher order defects. These differences among patterns are more noticeable in the difference maps, which reveal the highest values for the patterns with the fewest samples, followed by L49, J49 and C37. The RMS_Diff values for these six patterns were larger than for the other patterns.

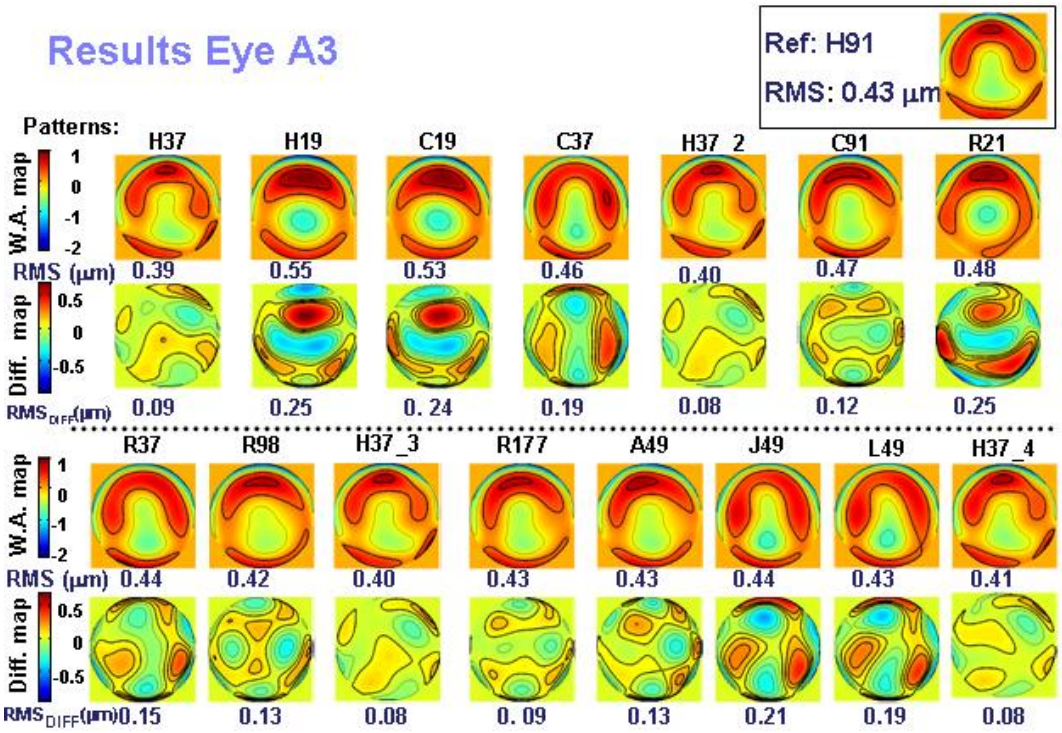

Figure 5.2. Wave aberration maps for 3rd and higher Zernike order, and corresponding difference maps (after subtracting the reference) obtained using the different sampling patterns for the artificial eye A3. Contour lines are plotted every 0.5 microns and 0.1 microns, respectively. Maps are sorted in the order used during the measurement. Thicker contour lines indicate positive values. Corresponding RMSs are indicated below each map. The number after H37_ indicates four different repetitions throughout the measurement. The wave aberration map corresponding to the reference (H91) is plot on the top right corner, with its corresponding RMS on the left of the map.

5.4.1.2.- Difference Metrics

RMS_Diff ranged from 0.06 to 0.46 µm (0.15±0.05 µm) across eyes and patterns. The values obtained for the threshold, averaged across measurements were 0.07±0.01µm, 0.09±0.08 µm, and 0.05±0.01µm for eyes A1, A2 and A3, respectively (0.07±0.03 µm averaged across the three eyes).

Figure 5.3 A, B and C show the values for the metric RMS_Diff obtained for each pattern, for artificial eyes A1, A2 and A3, respectively. Within each eye, patterns are sorted by RMS_Diff value in ascending order (from most to least similarity to the reference). The thick horizontal line in each graph represents the threshold for the corresponding eye, indicating that differences below this threshold can be attributed to variability in the measurement. The results of eyes A1 and A3 for RMS_Diff are similar: the

values for all the patterns are above the corresponding threshold, and the worst patterns (largest value of the metric) are those with the smallest number of samples (H19, C19 and R21), as expected. H37 patterns, R177, A49 and C91 were the best patterns for these eyes. In the case of A2, the values of some of the patterns (H37, H37_2, C37, and H19) were below the threshold, indicating that the differences were negligible. The ordering of the patterns for this eye was also different, with H19 and C19 obtaining better results (4^{th} and 6^{th} positions out of 15, respectively) than for the other eyes.

When comparing the outcomes for all three eyes, the following consistent trends were found: C91 gave better results than R98, and A49 was better than L49, and J49. For patterns with 37 samples, H patterns were found to give better results than the R patterns.

5.4.1.3.- Statistical Tests

A HCA was performed for A1, A2 and A3, and plotted the resulting dendrogram in Figure 5.3 D, E and F, respectively, below the RMS_Diff plot corresponding to each eye. The groups of patterns obtained in the dendrogram for each eye was consistent with the RMS_Diff plot. C37, R37 and R21 differ for A1 and A3. For A2 (with only defocus and SA), H19 and C19 provide similar results to a denser pattern, as found with RMS_Diff. For the t-test, significant differences were found only for coefficient Z_5^5, between the patterns R177 and H37.

Summarizing, for these eyes, the worst patterns, according to RMS_Diff metric, were H19, C19 and R21 (least samples), and H37, R177, A49 and C91 were the best. For A2, with only defocus and SA, R21, J49 and L49 were the worst patterns, although the differences with the other patterns were small. The grouping obtained from the metrics was in agreement with the groups formed by the HCA, which does not depend on the reference. Results from a metric that compares individual Zernike

terms (Student t-test with Bonferroni correction) showed very few significant differences.

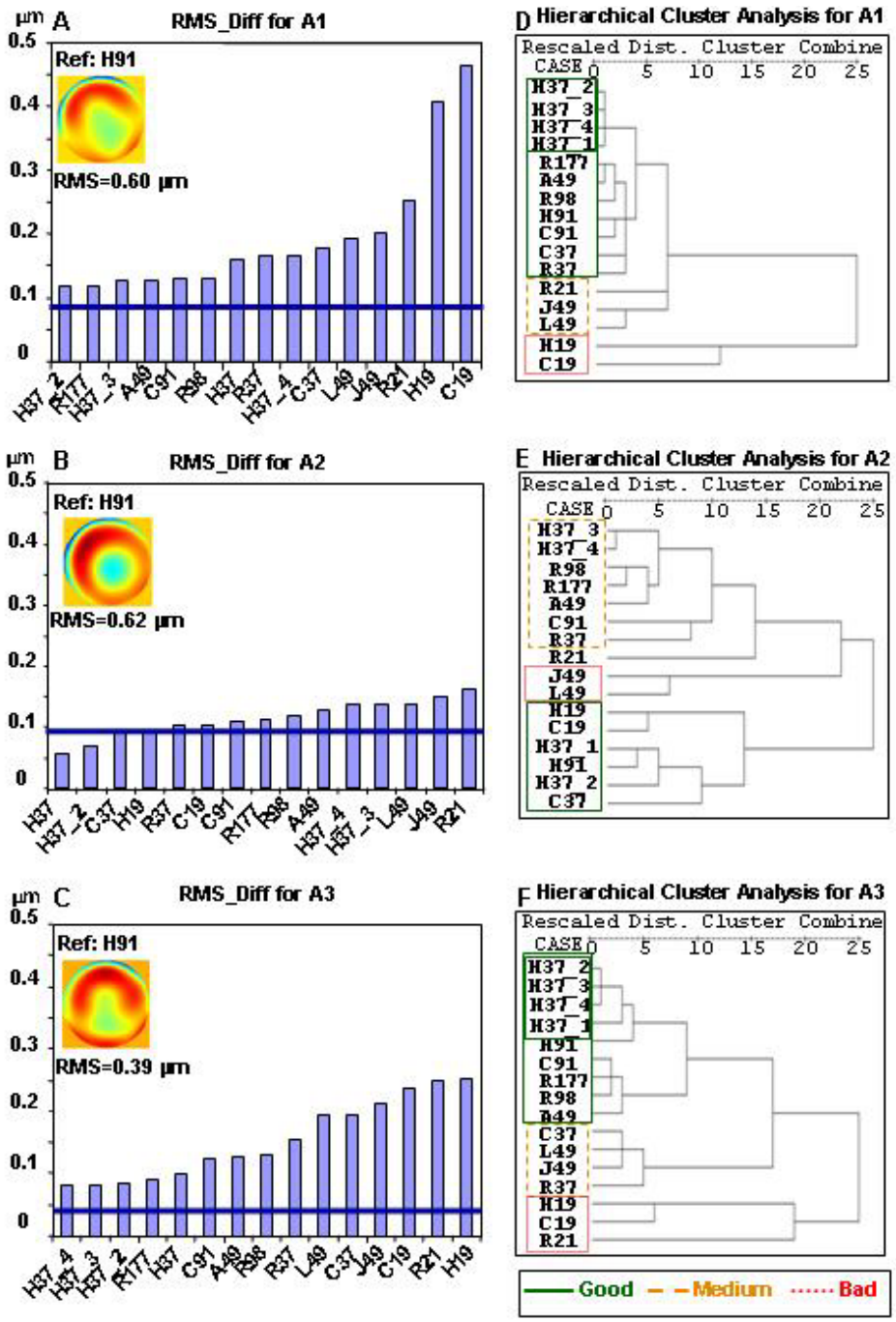

Figure 5.3. RMS_Diff values corresponding to each pattern for the artificial eyes A1 (A), A2 (B) and A3 (C). Greater values indicate more differences with the reference. The horizontal line represents the threshold for to each eye. Values below this threshold indicate that the differences are due to variability in the measurement and not differences between patterns.Wave aberration maps corresponding to each eye,obtained with pattern H91, are shown in the upper left corner with the corresponding RMS value. D, E and F are dendrograms from the HCA for the same eyes. The less distance (Dist) between patterns, the more similar they are.

5.4.2.- *HUMAN EYES*

5.4.2.1.- Wave Aberrations

Figure 5.4 shows in the first row HOA maps (W.A.map), and corresponding RMS, for each sampling pattern, for human eye R12. The contour lines are plotted every 0.3 μm. The map on the top right corner is that corresponding to the reference pattern, H91. Each map is obtained from an average of four (H19) to five measurements. Qualitatively, the aberration maps are quite similar across patterns, although those with fewer samples (H19 and C19) appear less detailed than the others, as expected.

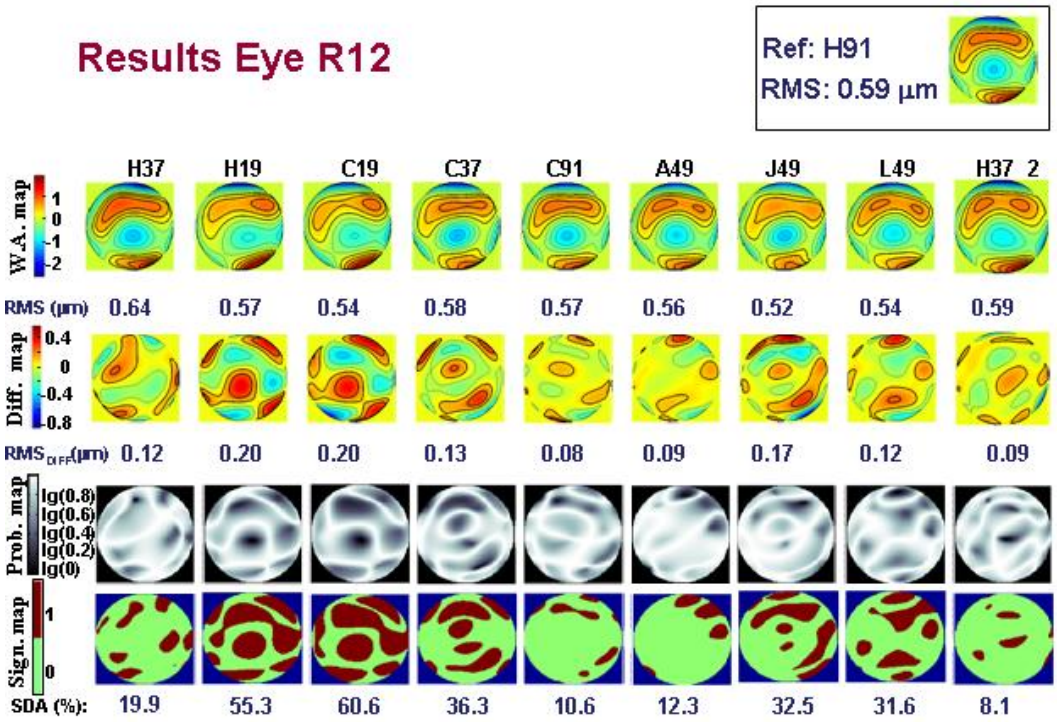

Figure 5.4. Results obtained for the human eye R12, using the different sampling patterns. First row: wave aberration maps for HOA. Second row: corresponding difference maps (after subtracting the reference). Contour lines are plotted every 0.3 microns, and 0.15 microns for the wave aberration maps and the difference maps, respectively. Maps are sorted in the order used during the measurement. Thicker contour lines indicate positive values. RMSs for wave aberration and difference maps are indicated below each map. Third row: Probability maps, representing the probability values obtained, point by point, when comparing the wave aberration height values obtained using the reference pattern, and those corresponding to the assessed pattern. Fourth row: Regions of the pupil where the significance values were above 0.05 (significantly different areas). The number below each map indicates the corresponding value of the metric W%, i.e., the percentage of the pupil significantly different between the pattern and the reference. The reference wave aberration map and its corresponding RMS are located on the top right corner.

5.4.2.2.- Difference Metrics

Difference maps (Diff.map), obtained by subtracting the reference map from the map corresponding to each pattern, are plotted in the second row of Figure 5.4 , with the corresponding RMS (RMS_Diff) indicated below each map. RMS_Diff ranged from 0.04 to 0.38 μm (0.13±0.06μm) across eyes and patterns. The value of the threshold for the eye in Figure 5.4 (R12) was 0.15 μm. Therefore, in principle, only J49, H19, and C19, with values over the threshold, are considered different from the reference. The most similar patterns were H91, A49 and H37_2. The mean threshold value obtained for all our human eyes (mean RMS_Diff for measurements obtained with H37) was 0.11±0.04 μm, an order of magnitude larger than the std of the RMS for the two sets of five repeated measurements using H37, which was 0.05±0.03 μm. This indicates that std (RMS) is less sensitive to differences between wave aberrations than RMS_Diff.

The third row shows maps (Prob.map) representing the value of significance obtained point by point when computing W% metric. The darker areas indicate a higher probability of a difference. The maps on the fourth row (Sign.map) indicate those points for which the significance value is below the threshold (<0.05), i.e., those points that are significantly different from the reference. The number below each map indicates the corresponding value of the W% metric. W% ranged from 0.7 to 80% (29±13%) across eyes and patterns. A threshold was also computed for this metric, using the two sets of measurements with H37 obtained in each session. For the eye of the example (R12), a value for the threshold of 20.6% was obtained. This implies that differences in patterns other than L49, J49, C37, H19, and C19 (with values for W% above the threshold) can be attributed to the variability of the experiment. The patterns that differ most from the reference, according to this metric are C19, H19, C37 and

J49. Although H37_2, C91 and A49 are the most similar patterns to the reference, the differences are not significant, according to the threshold.

Figure 5.5 A and B show the results obtained for the metrics RMS_Diff and W%, respectively, after Ranking across all the human eyes. The scale for the y axis indicates the value that each pattern was assigned in the Ranking. This means that the "best" possible score for the ordinate (y) would be 12 (for a pattern that was the most similar to the reference for each of the twelve eyes). Similarly, for a pattern being the least similar to the reference for each of the twelve eyes, the ordinate value would be 120 (12 eyes*10 patterns). In both graphs, patterns are sorted from smallest to greatest value of the metric, i.e., from most to least similarity with the reference. The resulting order of the patterns is very similar for both metrics, showing that the worst results are obtained for the 19-sample patterns. The best results are obtained for H91, A49, L49 and H37. The H patterns were found to provide in general better results than C patterns (for thirty seven and nineteen samples), in the Ranking for both metrics. Among the forty nine samples patterns, J49 produced the worst results.

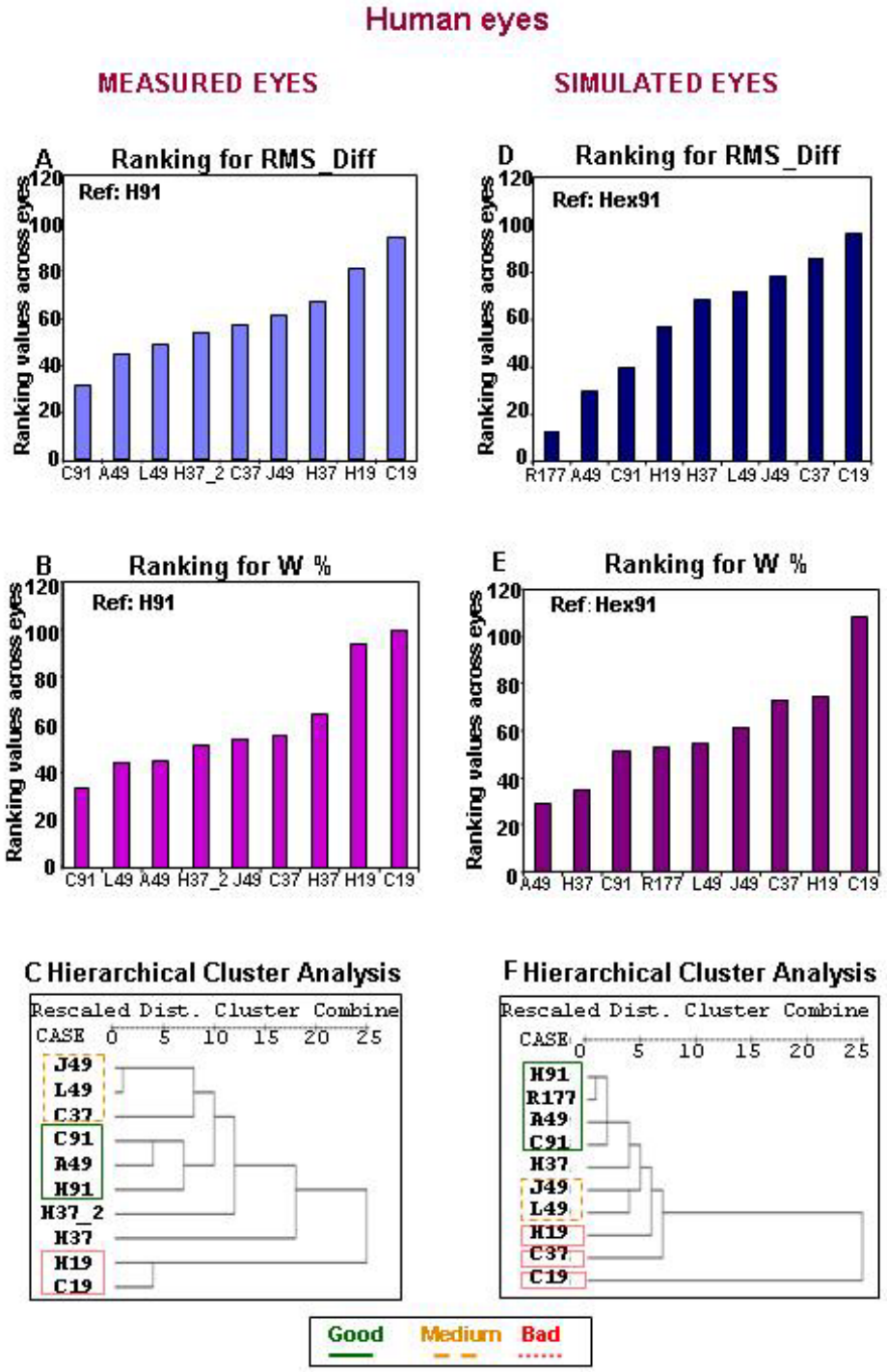

Figure 5.5. Ranking values for RMS_Diff (A and D) and W% (B and E) corresponding to each sampling pattern across the measured and simulated human eyes, respectively, and. dendrograms from the HCA for the measured (C) and simulated (F) human eyes. Solid green, dashed amber and red dotted lines indicate "good", "medium" and "bad " clusters, according to the classification obtained from the metrics. "Dist." stands for "Distance".

5.4.2.3.- *Statistical Tests*

The HCA was applied to the human eye data. While the test was performed eye by eye (i.e., one dendrogram per eye was obtained), a summary dendrogram obtained by pooling the data of all the eyes in the analysis (global) is shown in Figure 5.5 C is. This plot is representative of the plots corresponding to the individual eyes. The sampling patterns are distributed in three clusters: C91-A49-H91, J49-L49-C37 and H19-C19, which can be considered as "good", "medium" and "bad", respectively. Although this is the trend across eyes, some individual eyes yielded different results, as shown in Figure 5.6. H37 and H37_2 did not form a specific cluster in the global dendrogram, and did not follow a specific trend across the eyes, so they were not included in the table. The most different eyes were #6, 7 and 8 (#7 and 8 belong to the same subject), for which the cluster H19-C19 gets separated out. The least reproducible cluster across eyes was C91-A49-H91.

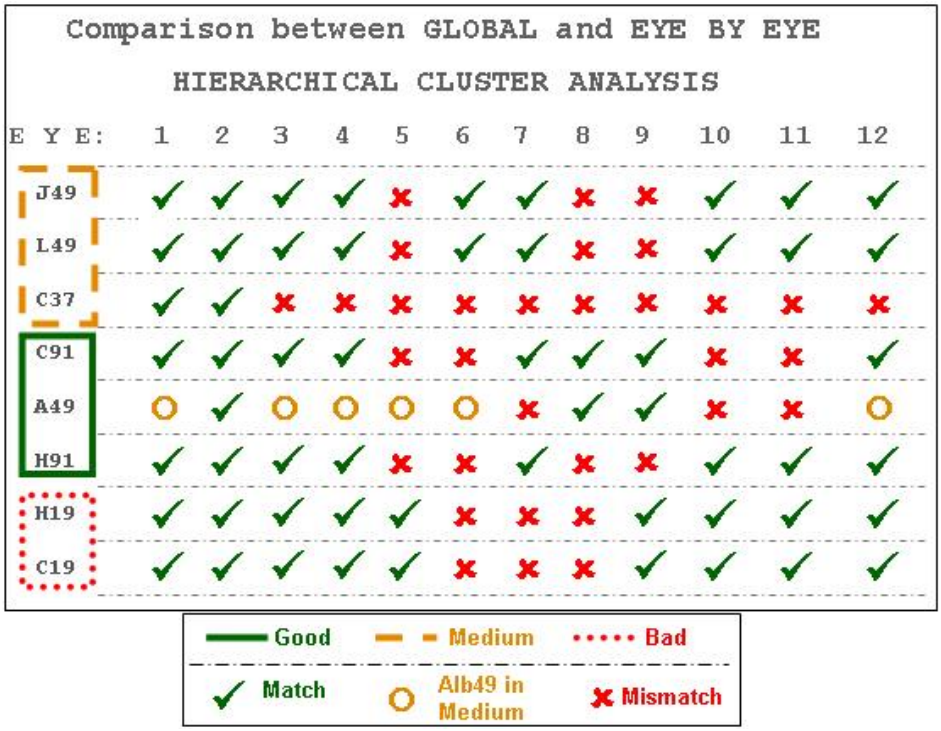

Figure 5.6. Comparison of the classification yielded by the global HCA on the 12 human eyes with the classifications yielded by eye by eye HCA for these eyes. The tick mark indicates that. the pattern obtained for the corresponding eye belongs to the same cluster indicated by the global analysis), whereas the cross mark means there is no matching between the results of both HCA for that eye. The circle indicates that A49 was grouped with J49 and L49.

The patterns showing more differences according to the t-test were C19 (4.7%) and H19 (6.4%), and those showing less differences were H37, H91, C37 and C91 (1.01% each). Differences were found only for the following coefficients: Z^{-3}_7 (2.20%), Z^{-1}_7 (3.30%), Z^{-1}_5 (4.40%), Z^0_4 (5.50%), Z^0_2 (12.09%), and Z^0_6 (13.19%).

To summarize, similar results were obtained using both metrics comparing the shape of the wave aberrations (which depends on our reference) in consistency with the cluster analysis (which does not depend on the reference): C91, A49 and H37 were the best patterns and C19, L49 and H37_2 the worst. However, the differences were of the order of the variability in most cases. When computing the percentage of differing patterns, those showing most differences were C19 and H19, whereas H37, H91, C37 and C91 showed the least differences. Regarding Zernike coefficients, only a few coefficients were significantly different: Z_7^{-3}, Z_7^{-1}, Z_5^{-1}, Z_4^0, Z_2^0, and Z_6^0.

5.4.3.- NUMERICAL SIMULATIONS

Figure 5.5 D and E show the Ranking plot for RMS_Diff and for W%, respectively, and Figure 5.5 F shows the dendrogram corresponding to the global HCA (i.e. including all the eyes) for the simulated human eyes. The results of the global HCA are presented, similar to the experimental data, as a summary of the results for each of the twelve simulated eyes. Similar trends to the measured human eyes are seen, with the main clusters repeating, although individual pairings changed. As with the measured human eyes, shown in Figure 5.5 C, H91, C91 and A49 are in the "good" group, J49 and L49 belong to the "medium" group, and H37, H19 and C19, although not clearly within any group, appear in borderline positions. The pattern R177 was included in the "good" group.

Figure 5.7 shows the results obtained for the three simulated pathological/surgical eyes, for RMS_Diff (A, B and C), for W% (D, E and

F), and for the HCA (G, H, and I). The results were repetitive across the three eyes, with R177, H37 and A49 resulting as the best patterns, and C19 as the worst, for both RMS_Diff and W%. The values for RMS_Diff for the keratoconic eye were smaller (the three first patterns were not above the threshold for RMS_Diff) compared to the other two eyes, i.e., differences with the reference pattern were smaller. The fact that most of the metric values are above the threshold indicates that in these eyes differences are not attributable to variability. The HCA results are similar across the three eyes, with the exception of H19, which for the surgical eyes is close to the "good" patterns group.

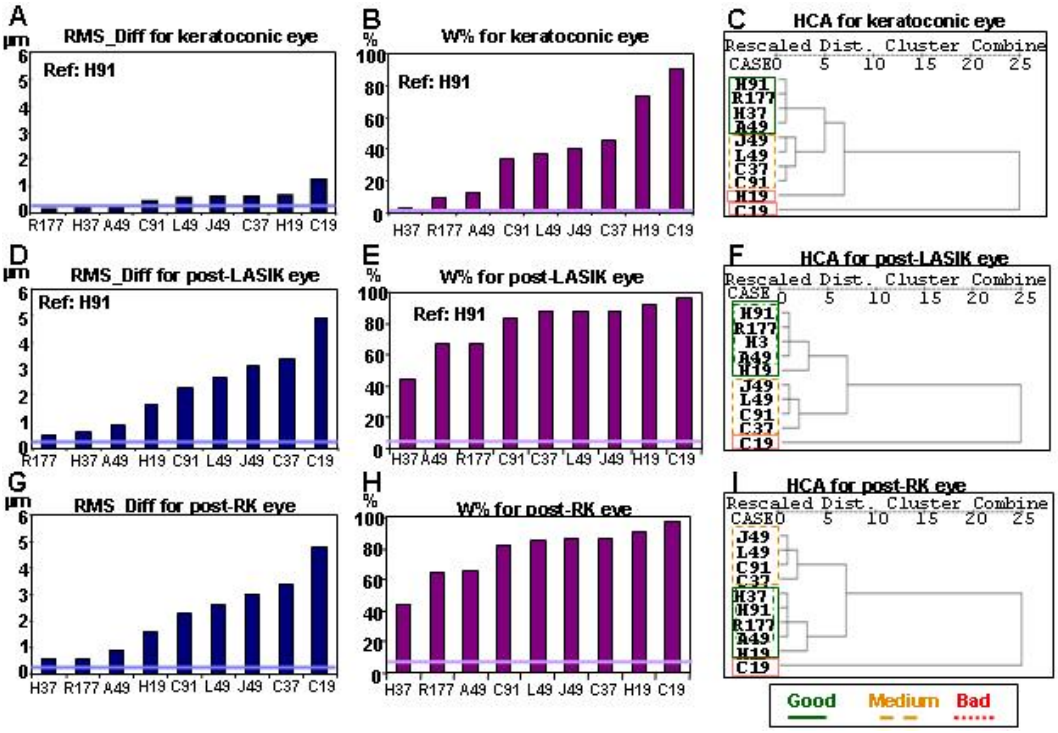

Figure 5.7. Results obtained for the keratoconic (first row: A, B, C), post-LASIK (second row: D, E, F), and post RK (third row: G, H, I) eyes.

The first (A, D, G) and second columns (B, E, H) show the results for the metrics RMS_Diff and W%, respectively, corresponding to each pattern. The thicker horizontal line represents the threshold corresponding to each eye for the corresponding metric. Values of the metric below this threshold indicate that the differences are due to variability in the measurement and not differences between patterns. The third column (C, F, I) shows the dendrograms corresponding to the hierarchical cluster analysis (HCA) for the keratoconic, post-LASIK and post-RK eyes. "Dist." stands for "Distance". The less distance between patterns, the more similarity exists. Solid, dashed and dotted lines indicate "good", "medium" and "bad " clusters, according to the classification obtained from the metrics.

5.5.- DISCUSSION

5.5.1.- ARTIFICIAL AND HUMAN EYES

Artificial eyes are a good starting point to study experimentally differences in the sampling patterns for wavefront sensing because they have fewer sources of variability (only those attributable to the measurement system, such as thermal noise in the CCD, photon noise, etc.) than real human eyes (including also variability due to the subject such as eye movements or microfluctuations of accommodation). The centroiding noise was estimated by computing the std of the coordinates of the centroids for each sample across different repetitions for pattern H37. The mean error averaged between x and y coordinates was 0.09 mrad for artificial eyes (37 samples and three eyes) and 0.34 mrad for human eyes (37 samples and twelve eyes). RMS_Diff seems to be a good metric for artificial eyes, since it provides quantitative differences between the patterns. However, it would be desirable to rely on an objective independent reference for the computation of this metric, such as an interferogram. The differences in the ordering observed with eye A2 (with no higher terms than SA), where patterns with less samples gave slightly better results than for the other eyes, supports the idea that the wave aberrations present in each particular eye affect the optimum pattern, as would be expected from sampling theory. This finding was fundamental in previous theoretical work (Diaz-Santana et al., 2005, Soloviev and Vdovin, 2005), where the statistics of the aberrations to be measured is an input of the analytical models. The different sorting orders for repeated measures of the same pattern (H37, H37_2, H37_3, and H37_4) indicate that the differences of this magnitude are not significant. However, the sorting of the different patterns is consistent across metrics and statistics for each eye. To evaluate if sample density affects variability, the std of

RMS_Diff across eyes was computed for each pattern, and then the patterns were sorted in descending order, according to their corresponding variability. The worst patterns (C37, H19, C19, R21) also showed a larger variability, indicating that they were less accurate when sampling the aberrations pattern, in agreement with Diaz-Santana et al. (2005).

Conclusions based on the artificial eyes have the advantage of avoiding biological variability, but are restricted because they have very different aberration structures than human eyes. In our human eyes, the RMS_Diff metric allowed us to sort the patterns systematically, and the values of the metric obtained for human and artificial eyes were of the same order. The W% metric was consistent with RMS_Diff, and more sensitive. The Ranking procedure was successful at summarizing information obtained from the metrics, since the metric values are not as important as sorting the patterns within each eye. However, the main drawbacks of this procedure are that it does not provide information on statistical significance (although the results for the same pattern, H37, obtained for different measurements help to establish significant differences), and that the conclusions are relative to our reference, obtained in the same conditions as the assessed patterns, and therefore these rankings might be dependant on the chosen reference. These drawbacks are overcome by the HCA which classifies the patterns into different groups according to the values of the corresponding vectors of Zernike coefficients and therefore distinguishes between patterns yielding different results. It also helps to place the results obtained from the metrics in a more general context. Same as with the artificial eyes, the grouping of the sampling patterns is consistent across metrics. The spatial distribution of the samples is important, given that some patterns with the same number of samples (49) fall into the same group or can even be worse than patterns with a lower number of samples. Similarly, a "good" sampling pattern (A49) is grouped with patterns with a larger number of samples.

However, for the real eyes, the conclusions are weaker than for artificial eyes (only differences in patterns with 19 samples are significant), presumably because biological variability plays a major role, and because they have a discrete number of modes compared to human eyes, where the magnitude of the modes keeps decreasing as the orders increase (see Chapter 1, section 1.2.4.1). Overall, the undersampling patterns C19 and H19 were consistently amongst the most variable patterns, and this was confirmed by the ANOVA for Zernike coefficients. Long term drift was not problematic in these eyes, since final H37 measurements were not more variable than the standard measurements.

Measurement errors in human eyes prevented from finding statistically significant differences between most sampling patterns. However, stds of repeated measurements of this study were less or equal to other studies. The mean variability across patterns and eyes for our human eyes was 0.02 μm (average std across runs of the Zernike coefficient, excluding tilts and piston) for Zernike coefficients. This value is smaller than those obtained by Moreno-Barriuso et al. (2001a) on one subject measured with a previous version of the LRT system (0.06 μm), with a HS sensor (0.07 μm) and a Spatially Resolved Refractometer (0.08 μm), and than those obtained by Marcos et al. (2002b), using the same LRT device (0.07 μm for 60 eyes), and a different HS sensor (0.04 μm for 11 eyes). A similar value (0.02 μm) is obtained when computing the average of the std of the Zernike coefficients (excluding piston and tilts) corresponding to the eye reported by Davies et al. (2003) using HS. The negligible contribution of random pupil shifts during the measurements on the wave aberration measurement and sampling pattern analysis was further studied by examining the effective entry pupils obtained from passive eye-tracking analysis. The most variable set of series (according to std of RMS, and std of Zernike coefficients across series), which corresponded to Eyes #1 (H19) and 2 (H37_2), respectively, was selected. Absolute random pupil shifts across the measurements were less than 0.17

mm for coordinate x and 0.11 mm for coordinate y. The mean shift of the pupil from the optical axis (i.e. centration errors, to which both sequential and non-sequential aberrometers can be equally subject) was in general larger than random variations. The estimates of the wave aberrations obtained using the nominal entry pupils were compated to those obtained using the actual pupil coordinates (obtained from passive eye tracking routines). When pupil shifts were accounted for by using actual coordinates, measurement variability remained practically constant both in terms of RMS std (changing from 0.09 when nominal coordinates were used to 0.07 μm when actual coordinates were used and from 0.14 to 0.13 μm for eyes #1 and 2 respectively), and in terms of average Zernike coefficients std (changing from 0.06 when nominal coordinates were used to 0.05 μm when actual coordinates were used and from 0.03 to 0.03 μm, for eyes #1 and 2, respectively). On the other hand, the differences between average RMS using nominal or actual entry locations (0.51 μm vs 0.49 μm for eye #1 and 0.61 μm vs 0.59 μm for eye #2) are negligible. Also, RMS_Diff values (using the wave aberrations with nominal entry locations as a reference, and wave aberrations with the actual entry locations as a test), 0.02±0.01 μm for eye #1 (mean±std across repeated measurements for the same pattern), and 0.04±0.02 μm for eye #2, are below the threshold for these eyes.

5.5.2.- NUMERICAL SIMULATIONS

It has been shown with artificial eyes that sampling patterns with a small number of samples (19) are good at sampling aberration patterns with no higher order terms (eye A2), as expected from sampling theory. When analyzing our ranking results on normal human eyes, remarkable differences were found only in the patterns with a small number of samples. This is due to the presence of higher order aberrations and larger measurement variability in these eyes.

Due to the lack of a "gold standard" measurement, there are some issues that have not been addressed in the experimental part of this work, such as: 1) Does the magnitude of some particular aberrations determine a specific pattern as more suitable than others to sample that particular eye?; 2) Will eyes with aberration terms above the number of samples be properly characterised using the different patterns?; 3) Will measurements in eyes with aberration terms of larger magnitude than normal eyes yield different results?. From the results shown in section 5.3.4.4.- it can be concluded that the simulations provide a good estimate of the performance of the repeated measurements using different sampling schemes in real normal human eyes. Therefore, computer simulations were used as a tool to address these issues.

From the results corresponding to the pathological/surgical eyes, it should be noted that: 1) The pattern H37 is consistently classified as the best pattern apparently because this is the pattern used to perform the original measurement of aberrations from which the wave aberration was computed for the simulations; 2) The variability values used in the simulations were obtained from normal eyes, and they may be smaller than those corresponding to pathological/surgical eyes; 3) The pattern H19 was close to the "good" patterns group for the surgical eyes only, what may be due to the predominance of SA, characteristic of these eyes..

Although the values of the metrics are larger for these pathological/surgical eyes, the conclusions obtained from our real eyes seem applicable to eyes with greater amounts of aberrations: even though patterns with more samples tend to give better results, the spatial distribution of the samples is important. While a large number of samples helps (R177), the correct pattern at lower sampling was more efficient (A49, H91) for eyes dominated by some specific aberrations.

It should be pointed out that the conclusions related to pathological eyes displayed in this section are obtained from simulations, and should

be regarded as a preliminary approximation to the study of sampling pattern in pathological eyes, which should include experimental data.

5.5.3.- *COMPARISON TO PREVIOUS LITERATURE*

Díaz-Santana et al.'s analytical model (Diaz-Santana et al., 2005), previously described in the introduction of this chapter, allowed them to test theoretically different sampling patterns using as a metric the RMS introduced in wave aberration measurements by the different geometries. This model uses as an input the second order statistics of the population and hence it is bound to include the interactions reported by McLellan et al. (2006), as long as the population sample and number of Zernike terms are large enough to reflect all possible interactions. This fact also implies that the conclusions of their model are strongly dependent on the characteristics of the population. As an example, they applied their model to a population of 93 healthy non-surgical eyes, with aberration terms up to the 4th order, to compare square, hexagonal and polar geometries. They found that, for their population, the sampling density did not influence much RMS error for hexagonal and square grids, whereas lower sampling densities produced a smaller error for polar grids. When comparing grids with different geometries and similar densities they found, in agreement with our results, that the polar geometry was best (in terms of smaller error), followed by the hexagonal grid. Differences in performance between patterns decreased as density increased.

Soloviev et al.'s analytic model (Soloviev and Vdovin, 2005) of Kolmogorov's statistics, indicates that random sampling produces better results than regularly spaced ones. They also reported that aliasing error increases dramatically for regular samplings for fits reconstructing more modes, whereas the associated error of the HS sensor was smaller for irregular masks (with 61 subapertures of 1/11 of the pupil diameter of size), probably because an irregular geometry helps to avoid cross-coupling. Our experimental study supports their conclusion that simply

increasing the number of samples does not necessarily decrease the error of measurement, and that sampling geometry is important.

In the current study, the Zernike modal fitting was used to represent the wave aberration because it is the standard for describing ocular aberrations. Smolek and Klyce (Smolek and Klyce, 2003) questioned the suitability of Zernike modal fitting to represent aberrations in eyes with a high amount of aberrations (keratoconus and post-keratoplasty eyes), reporting that the fit error had influence in the subject's best corrected spectacle visual acuity. Marsack et al. (2006) revisited this question recently concluding that only in cases of severe keratoconus (with a maximum corneal curvature over 60 D), Zernike modal fitting failed to represent visually important aberrations. In the current study this question was not addressed, but our conditions were rather restricted to those more commonly encountered, and for which Zernike modal fitting is expected to be adequate.

5.5.4.- CONCLUSIONS

From this study we can conclude:

1) Comparison of optical aberrations of healthy non surgical human and artificial eyes measured using different sampling patterns allowed us to examine the adequacy of two spatial metrics, the RMS of difference maps and the wave aberration difference (W%) to compare estimates of aberrations across sampling schemes.

2) For artificial eyes, there is an interaction of the aberrations present and the ability of a given spatial sampling pattern to reliably measure the aberrations. Simply increasing the number of samples was not always as effective as choosing a better sampling pattern.

3) Moderate density sampling patterns based on the zeroes of Albrecht's cubature (A49) or hexagonal sampling performed relatively well.

4) For normal human eyes individual variability in local slope measurements was larger than the sampling effects, except, as expected, for undersampling patterns (H19 and C19). However, in these eyes it has also been found that the spatial distribution of the sampling can be more important than the number of samples: A49 and H37 were a good compromise between accuracy and density.

5) The numerical simulations are a useful tool to *a priori* assess the performance of different sampling patterns when measuring specific aberration patterns, since in general, the results are similar to those found for our measured normal human eyes.

This study should be taken as a first experimental approach to the problem of finding optimal patterns. Future studies on a larger number of eyes and with very different aberration patterns should be carried out in order to find the different patterns more suitable for different groups of population (young eyes or myopic eyes for example) or specific conditions (keratoconic or postsurgical eyes). However, finding a generic pattern that performs relatively well for general population is also necessary for screening and quick characterisation of the aberration pattern. Also, a reference independent of any particular sampling pattern is desirable in order to have a gold standard to compare to, rather than assume the "goodness" of some patterns.

Finally, the implementation of some of the patterns presented in this study in a HS, for example, would not be straight forward. Even if the manufacturers could produce lenslets distributed according to Jacobi, Legendre or Albrecht patterns, there are some issues such as the loss of resolution in those locations where the lenslets are too close (leakage of light from a lenslet into the pixels corresponding to the neighbour lenslet) that should be solved.

Chapter 6

OPTICAL ABERRATIONS IN MYOPIC AND HYPEROPIC EYES.

This chapter is based on the article by Llorente, L. et al., "Myopic versus hyperopic eyes: axial length, corneal shape and optical aberrations", Journal of Vision, 4(4):5, 288-298 (2004), http://journalofvision.org/4/4/5/. The coauthors of the study are: Barbero, S., Cano, D., Dorronsoro, C., & Marcos, S.

The contribution of the author of this thesis to the study includes the experimental measurements, data processing and analysis, and statistical analysis (the statistician Laura Barrios performed the ANOVAs).

6.1.- ABSTRACT

PURPOSE: To investigate differences in geometrical properties and optical aberrations between hyperopic and myopic eyes.

METHODS: Measurements were performed in a group of myopic and a group of hyperopic eyes (age-matched 30.3±5.2 and 30.5±3.8 years old, respectively, and with similar absolute refractive error 3.0±2.0 and –3.3±2.0, respectively). Axial length (AL) was measured by means of optical

biometry, and corneal apical radius of curvature (CR) and asphericity (Q) were measured by fitting corneal topography data to biconic surfaces. Corneal aberrations were estimated from corneal topography by means of virtual ray tracing, and ocular (total) aberrations were measured using Laser Ray Tracing (LRT). Internal aberrations were estimated by subtracting corneal from ocular aberrations.

RESULTS: AL was significantly higher in myopes than in hyperopes and AL/CR was highly correlated with refractive error spherical equivalent (SE). Hyperopic eyes tended to have higher (less negative) Q and higher ocular and corneal spherical aberration (SA) than myopic eyes. RMS for third-order aberrations was also significantly higher for the hyperopic eyes. Internal aberrations were not significantly different between the myopic and hyperopic groups, although internal SA showed a significant age-related shift towards less negative values in the hyperopic group.

CONCLUSIONS: For these age and refraction ranges, our cross-sectional results do not support evidence of cause-effect relationship between ocular aberrations and ametropia onset (regarded as a fail in the emmetropisation process). Our results may be indicative of presbyopic changes occurring earlier in hyperopes than in myopes.

6.2.- INTRODUCTION

There is a clear motivation for studying myopia due to its high prevalence in developed countries and the public health issue it represents because of its associated ocular pathologies. Research on myopia is mainly aimed at finding optimal alternatives for optical correction of this condition, as well as understanding the mechanisms of emmetropisation and the factors leading the eye to become myopic in order to prevent it. Hyperopia, however, has been less studied due to its lower prevalence in

developed countries, relative stability over time, and difficulties in measuring its magnitude accurately in young subjects (Strang et al., 1998).

Most of the existing studies on ametropia have used a biometric approach. However their results are contradictory, probably due to different age groups, refractive error ranges, populations and ethnicities, differences in the statistical power of the studies, and differences across methods of measurement of the different parameters (Gilmartin, 2004). Ametropia can be considered a lack of coordination between the AL and the refractive power of the eye, so that the focused image yielded by the optical system of the eye does not lie on the retina. Therefore, studies on geometrical properties of the eye have mainly focused on AL and corneal parameters.

Myopic eyes are larger than hyperopic eyes, not only in the anteroposterior axis (Strang et al., 1998, Carney et al., 1997, Mainstone et al., 1998, Grosvenor and Scott, 1994), but in all three dimensions (i.e., equatorial, anteroposterior, and vertical axes) (Cheng et al., 1992), with a prolate shape (Atchison et al., 2004). In terms of CR and Q, myopic eyes have steeper corneas (Grosvenor and Goss., 1998, Carney et al., 1997) than hyperopic eyes (Sheridan and Douthwaite, 1989).

Whereas some studies have reported significant differences between refractive groups (Sheridan and Douthwaite, 1989), or significant correlation between CR and refractive error in myopes (Carney et al., 1997) and hyperopes (Strang et al., 1998), other authors did not find significant correlation (Mainstone et al., 1998, Grosvenor and Goss, 1999). The axial length/corneal radius of curvature ratio (AL/CR) seems to be negatively correlated with refractive error more strongly than CR itself in both refractive groups (Strang et al., 1998, Grosvenor and Scott, 1994). Regarding Q, cross-sectional (Carney et al., 1997) and longitudinal (Horner et al., 2000) studies report higher Q (less negative or even positive) with increasing myopia, although this tendency is reduced when

only low and moderate myopes are considered (Marcos et al., 2002a). For hyperopes, no correlation has been found between Q and refractive error (Mainstone et al., 1998, Sheridan and Douthwaite, 1989, Budak et al., 1999, Carkeet et al., 2002), although Budak et al. (1999) reported more positive Q values for their moderately myopic eyes than for their hyperopic eyes and for the high myopic eyes included in their study.

In terms of ocular (total) aberrations, whereas some authors did not find a correlation between aberrations and refractive error (Porter et al., 2001, Cheng et al., 2003) or differences in the amount of aberrations across refractive groups (Cheng et al., 2003), other authors reported higher amounts of aberrations in myopes when compared to emmetropes (Collins et al., 1995, He et al., 2002, Paquin et al., 2002, Marcos et al., 2002). For SA specifically, some authors found significant correlation between SA and myopia (Collins et al., 1995), consistent with higher corneal Q with increasing myopia. Some authors found significant differences in SA across high myopes with respect to low myopes, emetropes, or hyperopes (Carkeet et al., 2002), whereas others did not find a significant correlation between SA and a wide range of myopia (Marcos et al., 2002). Ocular aberrations have been reported to increase with age (Mclellan et al., 2001, Artal et al., 2002, Smith and al, 2001, Calver et al., 1999), probably due to a disruption (Artal et al., 2002) of the balance between corneal and internal optics found in young eyes (Artal and Guirao, 1998). In particular, the increase of SA with age has been attributed to a shift of the SA of the crystalline lens towards more positive values (Glasser and Campbell, 1998). Although age-related effects would not be expected within the small range of ages of our subjects (≤40 years) (Mclellan et al., 2001, Artal et al., 2002, Smith et al., 2001, Calver et al., 1999), some studies found differences related to presbyopia (reading glasses demand, reduced amplitude of accommodation) between hyperopes and myopes within our ages range (Spierer and Shalev, 2003, Abraham, 2005).

In this study, a comparison of geometrical properties (AL, CR, and corneal Q) and optical aberrations (ocular, corneal, and internal) between two age- and absolute refraction-matched groups of myopic and hyperopic eyes is presented. The aim of this work is to understand the optical and geometrical properties of the ocular components associated with myopia and hyperopia, and to find out whether differences in these properties between myopic and hyperopic eyes may cause differences in the aberration pattern. Furthermore, this comparison will shed some light on the hypothetical cause-effect relation between myopia and aberrations: retinal image degradation has been reported to induce excessive eye elongation (Schaeffel and Diether, 1999, Rasooly and BenEzra, 1988, Gee and Tabbara, 1988), and since aberrations degrade retinal image, an increased amount of aberrations might be involved with myopia development. Finally, potential differences in the corneal/internal compensation of the SA between myopes and hyperopes were studied, and particularly whether age-related differences exist in the degree of compensation between both groups. Studies of these effects in different refractive groups, particularly if the time scale of those changes is different between these groups, may provide insights to the understanding of the mechanisms of presbyopia.

6.3.- METHODS

6.3.1.- SUBJECTS

Twenty-four myopic and 22 hyperopic eyes with SE ranging from –0.8 to –7.6 D (-3.3 ± 2.0 D) and from +0.5 to +7.4 D (3.0 ± 2.0D), respectively, were measured. Both groups were age-matched: mean ± std was 30.5 ± 3.8 years (range, 26-39 years) for the myopic and 30.3 ±5.2 years (range, 23-40 years) for the hyperopic group.

6.3.2.- *AXIAL LENGTH AND CORNEAL SHAPE*

Axial length was obtained using an optical biometer based on optical coherence interferometry (IOL Master; Carl Zeiss, Germany). Each measurement consisted on the average of 3-5 scans.

Corneal shape (CR and Q) were obtained by fitting the anterior cornea height data from the placido disk videokeratographer (Atlas Mastervue; Humphrey Instruments-Zeiss, San Leandro, CA) to a biconic surface (Schwiegerling and Snyder, 2000) using custom software written in Matlab (Matlab; Mathworks, Natik, MA)(Marcos et al., 2003). The average corneal apical radius of curvature and asphericities are reported for a 6.5-mm diameter.

6.3.3.- *OCULAR ABERRATIONS*

Two different devices were used for the measurement of ocular aberrations in this study: 11 hyperopes and 12 myopes were measured using LRT1, and 11 hyperopes and 12 myopes were measured with LRT2. Both instruments were calibrated before this study and provided similar Zernike coefficients (within 6 mm diameter) on an artificial eye with a phase plate with known aberrations and two real eyes (see Chapter 2, section 2.3.8.1). In addition, the influence of the LRT device in the results was discarded (section 6.4.2.-).

6.3.4.- *CORNEAL TOPOGRAPHY: ESTIMATION OF CORNEAL AND INTERNAL ABERRATIONS.*

The procedure used to estimate the optical aberrations produced by the anterior surface of the cornea has been described in depth by Barbero et al. (2002b, 2002a, 2004): height data of the anterior surface of the cornea obtained from a placido disk videokeratographer (Atlas Mastervue; Humphrey Instruments-Zeiss, San Leandro, CA) were processed using custom routines in Matlab (Matlab; Mathworks, Natik, MA) and exported

to an optical design software (Zemax V.9; Focus software, Tucson, AZ), which computes the optical aberrations of the anterior surface of the cornea by virtual ray tracing. Corneal wave aberration was described in the same terms as ocular wavefront aberration (by a 7th Zernike polynomial expansion, using the same pupil diameter). The refractive indices used for the computations were those of the air and aqueous humour (1.3391) corresponding to the same wavelength used to measure ocular aberrations (785 nm). Custom routines in Matlab were used to change the reference of the corneal aberrations from the corneal reflex (keratometric axis) to the pupil centre (line of sight) to ensure alignment of ocular and corneal wave aberration patterns (Barbero et al., 2001, Marcos et al., 2001). For simplicity, the term "corneal aberrations" will be used reference to the aberrations of the anterior surface of the cornea.

Internal aberrations were computed by subtracting, term by term, corneal aberrations from ocular aberrations (after realignment), both expressed in terms of Zernike polynomials. Internal aberrations included, apart from crystalline lens aberrations, the aberrations corresponding to the posterior corneal surface. However, due to the small difference between refractive indices of the aqueous humour and the cornea, these aberrations are negligible in normal eyes (Barbero et al., 2002a).

A compensation factor was defined to quantify the compensation between corneal and internal SA. This factor was 1 when there was compensation and 0 when there was not compensation. The compensation was considered to occur when the sign of the corresponding internal and corneal SA was different and their ratio (internal/corneal) was equal to or greater than 0.5 (compensation of at least 50%).

6.3.5.- REFRACTION

Refraction measurements with the Autorefractometer HARK-597 (Carl Zeiss) were performed in 40 of the 46 subjects included in this study.

In the hyperopic eyes, measurements were performed both prior and after instillation of the tropicamide.

Defocus and astigmatism were also estimated from the corresponding Zernike terms (Z_2^0, Z_2^{-2} and Z_2^2) of the ocular aberration measurement, expressed in dioptres (D). Because the aberration values were estimated from IR measurements, the defocus difference (-0.78 D) between visible (543 nm) and infrared light (786 nm) was added. This value was obtained experimentally (see Chapter 4) and is close to the reported value of longitudinal chromatic aberration between these wavelengths (-0.82 D) (Thibos et al., 1992). When correction for spherical error was necessary during the measurement, the corresponding values in dioptres of the focusing block and trial lenses were considered in the estimation of the final defocus.

The SE obtained from the autorefractor measurements was compared to that estimated from the aberrometry in the 40 eyes. A good agreement between both types of measurements (coefficient of linear correlation r=0.97, and a slope of 0.9997) was found. Autorefraction was shifted by -0.28 D on average with respect to the aberrometry refraction corrected for visible (see Chapter 4). This offset could be due to the refractometer not being perfectly calibrated or a deeper penetration in the retina of the longer wavelengths used in the autorefractometer.

6.3.6.- STATISTICAL ANALYSIS

Student's t-test was used to verify the significability of the differences between groups, and Pearson's correlation test was used to analyse the correlations between two variables. A two-way ANOVA was applied to analyse , using the age as the dependent variable and the refractive group (myope or hyperope) and compensation factor as fixed factors. A three-way ANOVA of the internal SA with the age as the covariate (in order to control its influence), and compensation factor,

refractive group and the LRT device used to measure ocular aberrations as fixed factors was performed.

6.4.- RESULTS

6.4.1.- AXIAL LENGTH AND CORNEAL SHAPE

The AL of the hyperopic eyes (22.62 ± 0.76 mm) was significantly lower ($p<0.001$) than the AL of the myopic eyes (25.16 ± 1.23 mm) (Figure 6.1 A). Myopic eyes showed a statistically significant linear correlation of AL with absolute SE ($p=0.001$, $r= 0.57$, slope =0.38 mm/D, intercept at 0 D=24.2 mm). Hyperopic eyes tended to be shorter as AL increased but the correlation was not statistically significant within the sampled SE ($p=0.25$, $r=–0.26$, slope=–0.10 mm/D, intercept at 0 D=22.9 mm).

The CR (Figure 6.1 B) was, on average, steeper in the myopic eyes (7.86 ± 0.37 mm) than in the hyperopic eyes (7.97 ± 0.30 mm). However, this difference was not statistically significant. AL/CR was significantly ($p<0.0001$) higher in the myopic group (3.2 ± 0.2) than in the hyperopic group (2.8 ± 0.1). The correlation between AL/CR and SE was also highly significant ($p<0.0001$, $r=-0.93$, slope=$–0.058D^{-1}$, intercept at 0 D=3.02) including both groups, as well as for myopes ($p<0.0001$, $r=0.87$, slope= $-0.07D^{-1}$) and hyperopes ($p<0.0001$, $r=0.72$, slope= $-0.04D^{-1}$) alone. Q (Figure 6.1 C) was less negative for the hyperopic (–0.10 ± 0.23) than for the myopic group (–0.20 ± 0.17), indicating a more spherical shape of the hyperopic corneas versus a more prolate shape of the myopic ones. This difference was marginally significant ($p=0.054$).

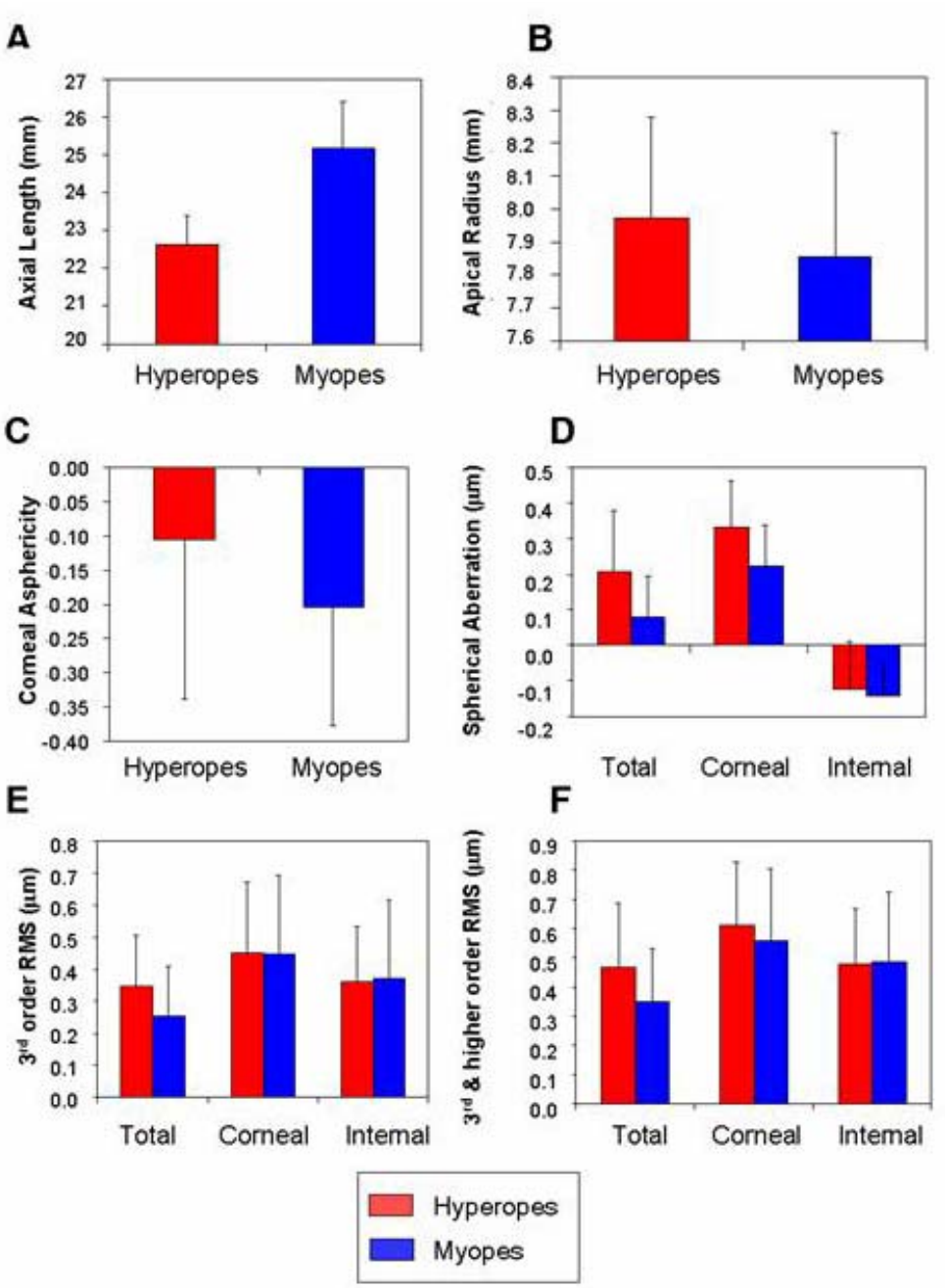

Figure 6.1. Axial length (A), corneal apical radius of curvature (B), corneal Q (C), total, corneal, and internal spherical aberration (D), third-order RMS (E), and third and higher order RMS (F), averaged across hyperopes (red) and myopes (blue). Error bars represent corresponding standard deviation.

6.4.2.- *OPTICAL ABERRATIONS*

Figure 6.2 shows ocular, corneal, and internal wave aberration maps for myopic (#M2, #M8, and #M6) and three of the hyperopic eyes (#H10, #H17, and #H16). Only HOA are represented (i.e., piston, tilts, defocus, and astigmatism are excluded). A common characteristic shown in six of the eyes is that the corneal map is dominated by the positive SA pattern. Myopic eyes #M4, #M7, and #M5 are representative of the general behaviour in the group of myopes. Internal SA is negative, and partly balances the positive SA, resulting in a less positive ocular SA. Occasionally it may happen that the internal SA overcompensates for the corneal SA, resulting in a slightly negative ocular SA (eye #M4). The examples for hyperopic eyes show the case (eye #H10) of an internal map dominated by negative SA that partly compensates for the positive SA of the cornea, and the case (eyes #H17 and #H11) where ocular and corneal maps are quite similar, indicating a small role of the ocular internal aberrations (i.e., ocular aberration pattern dominated by the positive corneal SA).

Figure 6.1 D shows the average ocular (0.22 ± 0.17 μm and 0.10 ± 0.13 μm), corneal (0.34 ± 0.13 μm and 0.24 ±0.13 μm), and internal (-0.12 ± 0.14 μm and -0.14 ± 0.09 μm) SA for the hyperopic and the myopic groups, respectively, included in this study. Ocular and corneal SAs were significantly higher in the hyperopic group than in the myopic one ($p=0.005$ and $p=0.004$, respectively). However, internal SA was not significantly different ($p=0.62$) between hyperopic and myopic eyes.

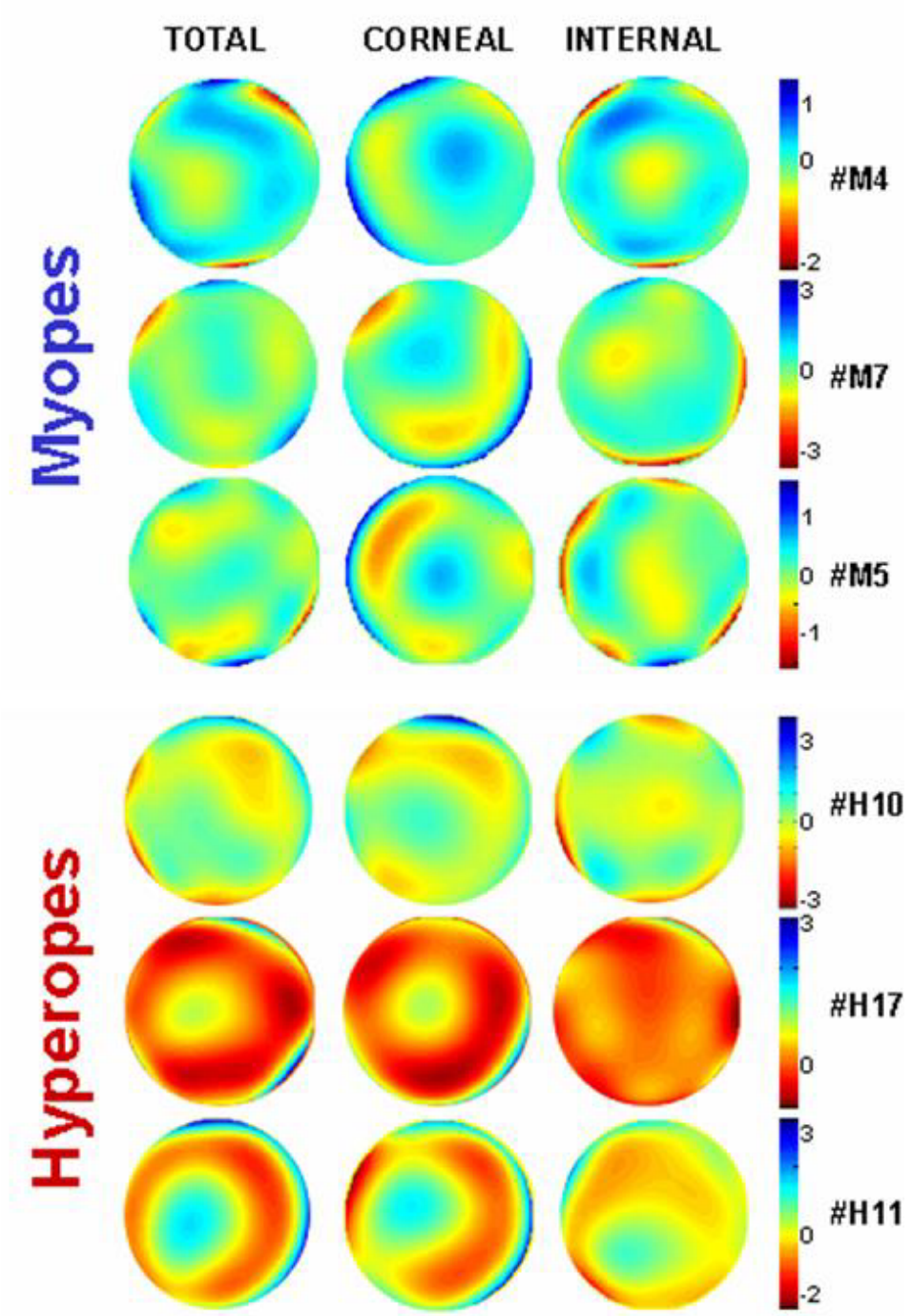

Figure 6.2 Total, corneal, and internal wave aberration maps for three of the hyperopic and three of the myopic eyes. Only HOA are represented. The pupil size was 6 mm.

Although only eyes ≤40 years were recruited for this study, and both groups were age-matched, age-related trends were found in the hyperopic group. Figure 6.3 shows the ocular (green), corneal (red), and internal (blue) SA for each eye sorted by age for the myopic (Figure 6.3 A) and the hyperopic (Figure 6.3 B) group. For the myopic group, there is no particular tendency with age: In most of the eyes, as previously shown, the internal SA is negative and compensates for the positive SA of the cornea. In the hyperopic group, however, this behaviour is followed only by younger eyes (<30 years, n=11), whereas the older eyes (≥30 years, n=11) showed an internal SA significantly (p=0.002) less negative than the internal SA in the younger eyes (–0.04 ± 0.07 µm versus –0.20 ± 0.14 µm). This results in a loss of compensation of corneal and internal aberration in older hyperopes. When the same comparison was carried out between young (<30 years, n=10) and old myopes (≥30, n=14), statistically significant differences were not found in the internal SA of these groups. When comparing similar age groups, significantly higher (more positive) internal (p=0.004) and ocular (p=0.002) SAs were found in the hyperopic than in the myopic older group. In the hyperopic young group, internal SA (-0.20±0.14 µm) tended to be more negative than in the myopic young group (-0.17±0.10 µm), although it did not reach significant levels (p=0.06).

The relationship between age and compensation was statistically significant (p<0.001) whereas the relationship between age and the combination of compensation and refractive group did not reach the limit of significance (p=0.08) (two-way ANOVA, see section 6.3.6.-). The mean age for the hyperopic group with compensation equal or greater than 0.5 was 26.00±1.41 years compared to 29.53±3.50 years for the myopic group. In the case of eyes with less compensation than 50%, the mean age for the hyperopes was 29.67±2.94years, compared to 32.00±3.56 years for the myopes. This confirmed that age had an influence on the compensation of SA, and that there seem to be a displacement in the age of disruption of the compensation of SA between our myopic and hyperopic eyes. The

compensation was significantly related to internal SA ($p<0.0001$), as it was the combination of compensation and refractive group ($p<0.05$) (three-way ANOVA, see section 6.3.6.-). The three-way ANOVA also discarded any influence of the LRT device used on the internal SA (and therefore ocular SA) obtained.

Figure 6.1 E shows the average ocular (0.35±0.16 μm and 0.25±0.16 μm), corneal (0.45±0.22 μm and 0.45±0.25 μm), and internal (0.36±0.17 μm and 0.37±0.25 μm) third-order RMS for the hyperopic and the myopic groups, respectively. Ocular third-order RMS was slightly higher in hyperopes than in myopes ($p=0.02$), due to the contribution of the comatic terms. The RMS of horizontal and vertical coma was also significantly higher in hyperopes ($p=0.004$), although when analyzed independently Z_3^1 and Z_3^{-1} were not significantly different across both groups of eyes. Average third and higher order RMSs for our hyperopic and myopic groups are shown in Figure 6.1 F: ocular (0.47±0.22 μm and 0.35±0.18 μm), corneal (0.61±0.22 μm and 0.56±0.25 μm), and internal (0.48±0.19 μm and 0.48±0.24 μm), respectively. Ocular third and higher order RMS was significantly higher ($p=0.03$) for the hyperopic group. Fifth and higher order RMS was not significantly different between both groups.

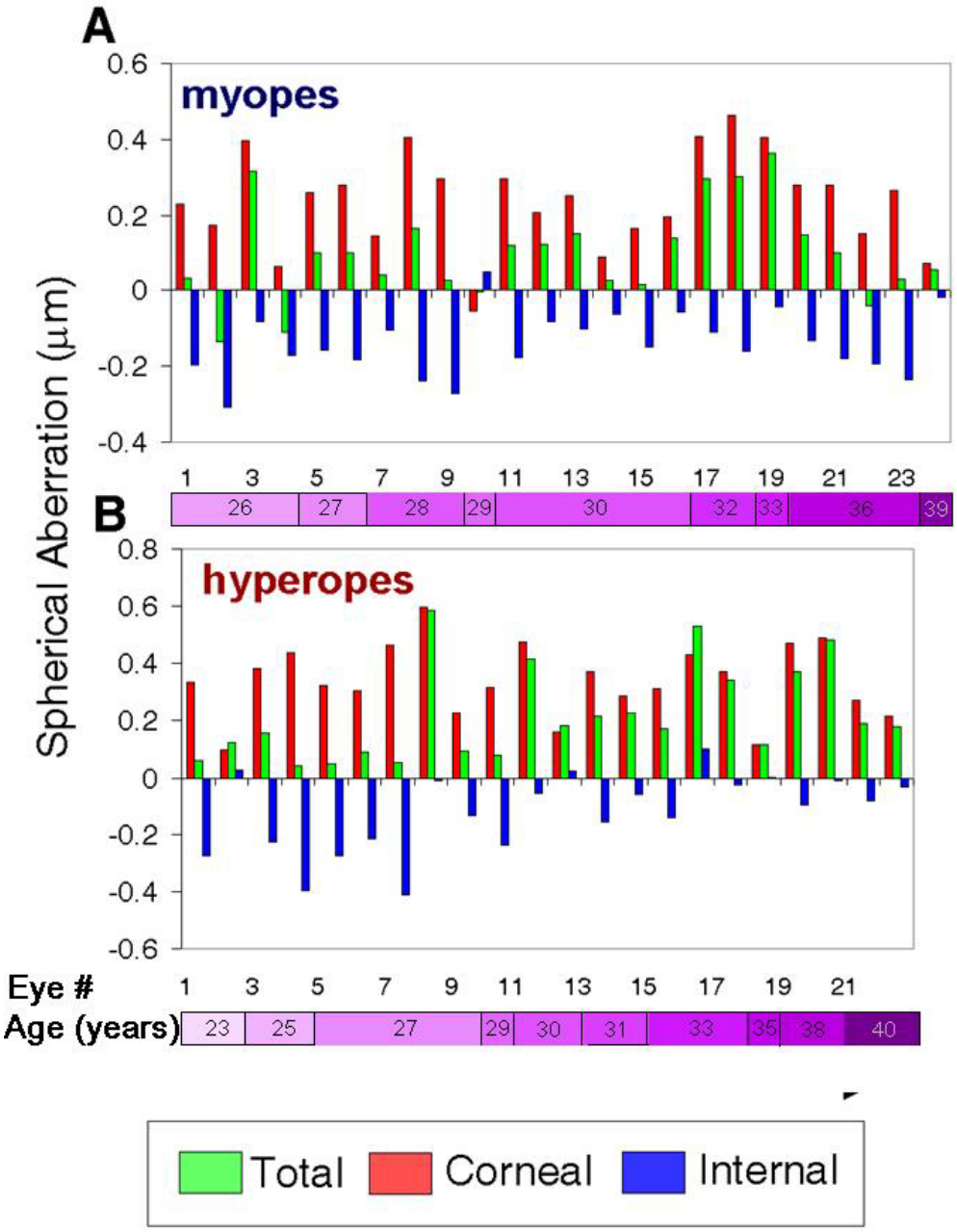

Figure 6.3. Corneal (red), total (green), and Internal (blue) spherical aberration for myopes (A) and hyperopes (B). Eyes are sorted by increasing age, ages ranging from 26 through 39 years in the myopic group and 23 through 40 years in the hyperopic group.

6.5.- DISCUSSION

In this study, geometrical parameters as well as optical aberrations of a group of myopic and hyperopic eyes were measured. Our study showed that differences were not limited to the well-known fact that hyperopic eyes are shorter than myopic eyes. The differences in corneal shape between groups, which are in agreement with some previous studies, resulted in differences in corneal and ocular SA. In addition, Age-related changes were found in the hyperopic internal aberrations, even in the studied small range of ages.

6.5.1.- CORNEAL SHAPE IN MYOPES AND HYPEROPES

As in previous studies (Strang et al., 1998, Carney et al., 1997, Sheridan and Douthwaite, 1989), the hyperopic eyes measured tended to be flatter than myopic eyes, although the variability was large in both groups and no a statistically significant differences were found. A trend towards increased Q in hyperopic eyes, compared with myopic eyes of similar absolute SE, is consistent with the increased corneal SA found in hyperopic eyes of this study. To our knowledge, only three studies (Mainstone et al., 1998, Sheridan and Douthwaite, 1989, Budak et al., 1999) have reported Q in hyperopic eyes, in comparison with myopic and emmetropic eyes. Sheridan and Douthwaite (Sheridan and Douthwaite, 1989) (12 hyperopes and 23 emmetropes) and Mainstone et al. (1998) (25 hyperopes and 10 emmetropes) did not find differences in Q across groups. Budak et al. (1999) did not find a correlation between Q and refractive error. In their group analysis, however, they found more positive Q-values in moderate myopia (-2 to –6 D) than in hyperopia, although this trend was not seen in high myopia or emmetropia. Previous studies (Horner et al., 2000, Carney et al., 1997), including ours (Marcos et al., 2002), found larger amounts of positive corneal SA and Q in high myopia. The present study shows larger amounts of SA in hyperopic than

in moderately myopic eyes. The reasons for the corneal geometrical properties (CR and Q) leading to significant differences in SAs across groups may be associated to ocular growth (moderate hyperopic eyes being smaller (Cheng et al., 1992) and more spherical, whereas moderate myopic eyes may flatten more in the periphery than in the central cornea). As a result of increased corneal SA in hyperopic eyes, ocular SA is significantly higher in our group of hyperopes than in a group of myopes with similar absolute refractive error and age.

6.5.2.- AGE RELATED ABERRATION DIFFERENCES IN MYOPES AND HYPEROPES

As opposed to ocular and corneal SA, no significant differences in the internal (i.e., primarily the crystalline lens) SA were found between our groups of myopes and hyperopes. However, despite the fact that inclusion criteria was to be younger than 40 years, age-related differences were found in the hyperopic group, which are not present in the myopic group, as shown in Figure 4B. It seems fairly established that the positive SA of the cornea is balanced by the negative SA of the crystalline (Artal and Guirao, 1998). Artal et al. (2002) showed that this balance is disrupted with age. Several groups have reported changes of ocular SA as a function of age. Figure 6.4 represents data from different cross-sectional studies (Mclellan et al., 2001, Artal et al., 2002, Smith et al., 2001, Calver et al., 1999) showing the increase of SA with age resulting from a shift of the internal SA of the crystalline lens towards positive or less negative values. The myopic (blue) and hyperopic (red) eyes of our study have been superimposed. Ocular SA in myopic eyes does not correlate with age in the small range of ages of our study ($p=0.49$). However, there is a marginally significant dependence of ocular SA with age in the hyperopic group ($p=0.06$), with a slope higher than the average data from literature.

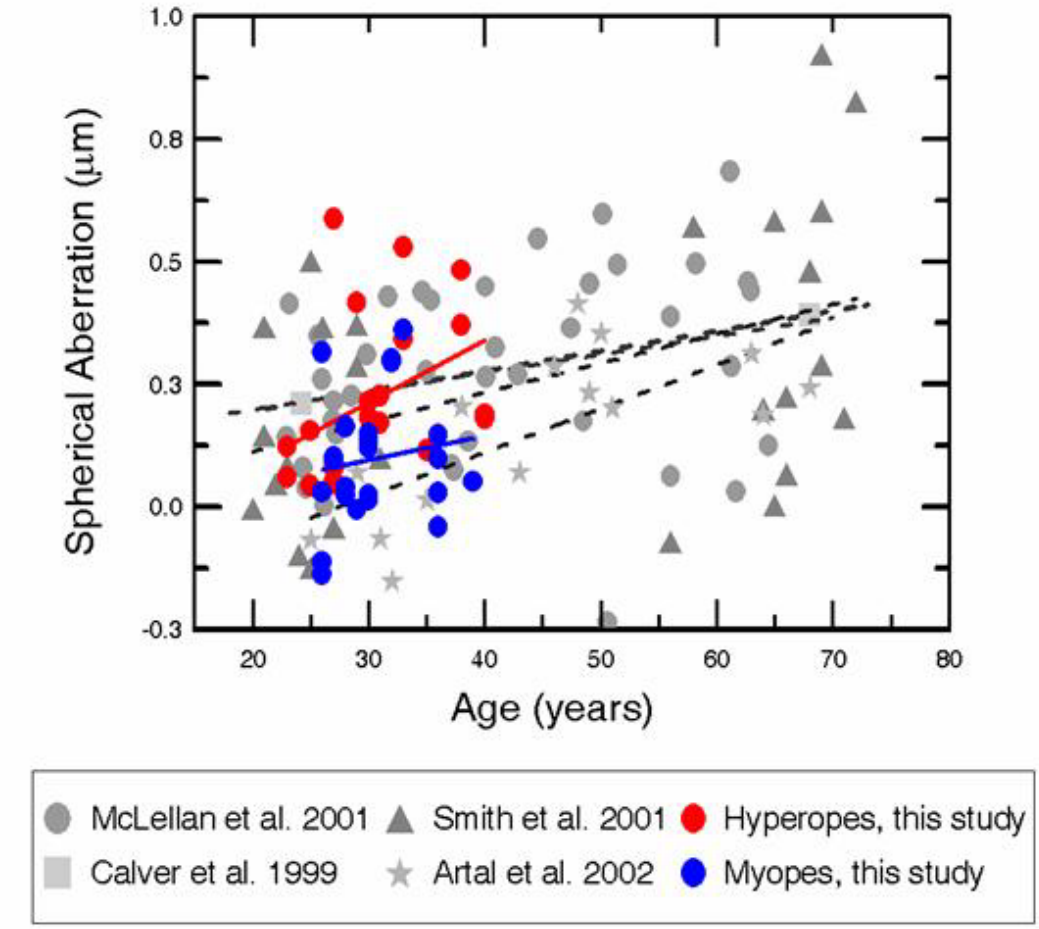

Figure 6.4. Spherical aberration of the hyperopic (red) and myopic (blue) eyes included in this study (6.5-mm pupil) as a function of age in comparison with spherical aberration of eyes from aging studies [circles are data from Mclellan et al. (2001) for 7.32 mm pupil; triangles are estimates from Smith et al. (2001) for a 7.32-mm pupil; squares are averages across two different age groups from Calver et al. (1999) for a 6-mm pupil; and stars are data from Artal et al. (2002), for a 5.9-mm pupil]. Solid lines are the corresponding linear regression to the data.

Our group of myopes shows in general a good compensation of corneal by internal SA. Marcos et al. (2002) showed that the SA balance was in fact well preserved in young myopes across a wide refractive error range. Both younger and older myopic groups show good average corneal by internal compensations (76% and 48%, respectively). The young hyperopes in our study also show a good balance of corneal and internal SA (56% on average), but the average compensation decreases to 14% in older hyperopes. In fact, because corneal SA is higher in hyperopes than in myopes, a more negative internal SA is required to achieve similar proportions of balance.

The negative SA of the crystalline lens is likely due to the aspheric shapes of the crystalline lens surface, with contributions of the radii of curvature and the refractive index distribution. Lack of knowledge of the crystalline lens geometrical and optical properties in hyperopes and myopes prevents assessment of the reasons for the differences in the SA of the crystalline lens in myopes and hyperopes. Reports of changes of SA with accommodation have shown a shift towards less positive (or even negative) ocular SA with increasing accommodative effort (He et al., 2000). Changes in crystalline lens properties that accompany accommodation (increased power, but more likely changes in Q, and perhaps the distribution of refractive index) result in negative SA of the crystalline lens. It is well known that achieving a totally unaccommodated state can be problematic in the hyperopic young eye that tends to accommodate continuously to self-correct for distance vision. Our measurements were performed under tropicamide instillation, which may not be fully paralyzing accommodation or paralyzes it in a resting state that differs between myopes and hyperopes. Our data showed that autorefraction measurements after tropicamide instillation were more positive (0.66 D on average for eight of our hyperopic eyes) than under normal viewing, indicating that tropicamide relaxed accommodation at least partially. It is interesting however that, regardless of whether or not the slight increased negative internal SA is a result of latent accommodation in young hyperopes, the balance is well preserved in both young hyperopes and myopes. A potentially interesting future study would be to investigate internal SA under natural viewing conditions. If the eye has a feedback system that enables balancing of the corneal and internal aberrations, then this balancing would perhaps be most prominent in the accommodative state that the eye is most often in.

Determining the reasons why the SA shifts significantly towards less negative values in hyperopes at an early age requires further investigation. It might indicate that some changes related to age just occur

earlier in hyperopes (as shown in Figure 6.3). Most previous studies on the changes of aberrations with age do not report the refractive state of the subjects (to our knowledge only Smith et al. 2001 did explicitly, and only 6 of 27 eyes were hyperopes, all of them older than 58 years). Subjects in the McLellan et al. (2001) study were primarily myopes. Hyperopia has been identified to predispose to early development of presbyopia. Significantly lower amplitudes of accommodation have been found in hyperopes compared to emmetropes aged 20 years, the former requiring reading glasses at an earlier age (Spierer and Shalev, 2003). Hyperopes of an older group (35-39 years) were also found to have significant lower amplitude of accommodation when compared to myopes of the same age range (Abraham, 2005). A question remains whether the physical properties of the crystalline lens that lead to the development of presbyopia occur along with changes in the SA of the crystalline lens. In fact, the properties of the crystalline lens that produce the reported shift with age have never been fully explored. Several studies in vivo using Scheimpflug imaging (Koretz et al., 1997, Dubbelman and van der Heijde, 2001) showed that the posterior and anterior surface of the crystalline lens become steeper with age. Dubbelman and van der Heijde (2001) also reported changes of Q with age. Although those changes were not significant, computer simulations have shown that the combination of reported radii of curvature and asphericities predict the expected trend towards more positive SA with age, even without considering changes in the index of refraction (Marcos et al., 2004). Changes in the index of refraction are, however, expected to play a major role in the aging of the crystalline lens. They have been invoked to explain the so-called lens paradox (Koretz and Handelman, 1986): the apparent contradiction between age-related changes of the lens radii and the refractive error shift. It is likely that changes in the gradient index distribution with age contribute also to the reported changes in SA.

6.5.3.- ABERRATIONS AND DEVELOPMENT OF MYOPIA AND HYPEROPIA

The increased interest in measuring aberrations as a function of refractive error is in part motivated by the study of potential factors involved in the development of refractive errors. It seems fairly established, particularly from experimental myopia studies, that emmetropisation is visually guided (Rabin et al., 1981) and that an active growth mechanism uses feedback from the blur of retina image to adjust the focal length of the eye to the power of the ocular components. When the retinal image is degraded by diffusers, the eye becomes myopic (Bartmann and Schaeffel, 1994) and the induced refractive error correlates to the decrease in contrast and deprivation of spatial frequencies of the retinal image. Because aberrations cause a degradation of the retinal image, it has been argued that increased aberrations may play a role in the development of myopia. Higher amounts of aberrations in high myopes (Collins et al., 1995, Paquin et al., 2002) are consistent with that argument. However, the relationship between aberrations and refractive error may be just a result of the geometrical properties of the ocular components of the ametropic eye, somehow related to the axial elongation, rather than the cause of the ametropia. In this fashion, Garcia de la Cera et al. studied longitudinally the change in optical aberrations and refractive error in chicks subject to form deprivation (de la Cera et al., 2006), and concluded that their experiment supported the hypothesis that the aberrations were a consequence of the geometrical structure of the elongated myopic eye.

In this sense, it is interesting to study the ocular aberrations in both myopic and hyperopic eyes. The defects in an active growth feedback mechanism may be responsible for myopia, but this active growth mechanism does not adequately explain hyperopic error. If similar or larger amounts of aberrations are found in hyperopic than in myopic eyes, then the associations of retinal blur imposed by aberrations and myopia

development are not evident. The present study shows that SA is higher in hyperopic eyes than in myopic eyes, and a previous study showed that ocular SA is close to zero even in high myopes (Marcos et al., 2002). Also, the present study shows that third-order aberrations are in fact slightly higher in hyperopes than in myopes of similar absolute refractive errors (up to 7.6 D). If increased HOA occur in myopic eyes, these seem to be more prominent in high myopia (Marcos et al., 2002). It is interesting that even if the emmetropisation mechanism is disrupted, the corneal and internal aberrations are well balanced in young myopes and hyperopes.

Our study is limited to young adults, and data are cross-sectional. Certainly, a possible involvement of the aberrations in the development of refractive errors cannot be fully ruled out unless longitudinal measurements are made at an earlier age. Longitudinal studies would also be useful to assess the reported rapid changes around 30 years of age observed in the cross-sectional data in hyperopic eyes.

6.5.4.- CONCLUSIONS

Some differences of structure and optical properties in hyperopic and myopic eyes have been shown. Myopic eyes, as previously reported, show a significantly higher AL than hyperopic eyes. The AL/CR ratio is also higher in myopic eyes, although no significant difference in CR has been found between both groups. Q tends to be less negative in hyperopic eyes (i.e., more spherical corneal shape), and as a consequence, the corneal SA is also higher in hyperopic than in myopic eyes. Ocular SA is also significantly higher in hyperopic eyes, although internal SA is not significantly different between both groups. HOA were also slightly higher for the hyperopic group, due to the contribution of the comatic terms. A tendency of ocular SA to increase with age at a faster rate in hyperopic than in myopic eyes was also found. Therefore, hyperopic eyes may show an earlier loss of the compensation of the corneal SA by the internal SA.

Chapter 7

CHANGE IN OPTICAL ABERRATIONS OF THE EYE WITH LASIK FOR MYOPIA AND LASIK FOR HYPEROPIA.

This chapter is based on the articles "Optical response to LASIK surgery for myopia from total and corneal aberration measurements" by Marcos et al. (2001), and "Total and corneal optical aberrations induced by Laser in situ Keratomileusis for hyperopia" by Llorente et al. (2004c). The coauthors of these studies were Sergio Barbero, and Jesús Merayo-Lloves.

The contribution of the author of this thesis to the study includes participation in data collection and processing of ocular aberrations in both, myopic and hyperopic LASIK. In the case of hyperopic LASIK study the author also contributed in data analysis, and writing of the corresponding article.

7.1.- ABSTRACT

PURPOSE: To evaluate the changes induced by myopic and hyperopic LASIK on ocular (total) and (anterior) corneal optical quality.

METHODS: Ocular and corneal aberrations were measured before and after myopic and hyperopic LASIK surgery in a group of 14

(preoperative myopia ranging from -2.50 to -13.00 D; mean ± std, -6.8±2.9) and a group of 13 (pre-operative hyperopia ranging from +2.50 to +5.50D; mean ± std, +3.60±1.06 D) eyes, respectively. Ocular aberrations were measured using a LRT and corneal aberrations were estimated from a videokeratoscope. RMS for both ocular and corneal aberrations was used as a global optical quality metric.

RESULTS: Ocular and corneal aberrations (HOA) showed a statistically significant increase after both, myopic and hyperopic LASIK. SA (SA) changed towards positive and negative values after myopic and hyperopic LASIK, respectively. However, the anterior corneal SA increased more than the ocular SA, suggesting also a change in the SA of the posterior corneal surface. Changes in internal SA were of opposite sign to those induced on the corneal anterior surface. Hyperopic LASIK induced larger changes than myopic LASIK. Induced ocular SA was, in absolute value, 3.3 times larger, and induced corneal SA was 6 times larger after hyperopic LASIK, for a similar range of correction, and of opposite sign.

CONCLUSIONS: Because LASIK surgery induces changes in the anterior corneal surface, most changes in the ocular aberration pattern can be attributed to changes in the anterior corneal aberrations. The largest increase occurred in SA, which showed a shift towards positive values in the case of myopic LASIK and towards negative values in the case of hyperopic LASIK, the increase being greater for hyperopic than for myopic LASIK. However, due to individual interactions of the aberrations in the ocular components, a combination of corneal and ocular aberration measurements is critical to understand individual outcomes, and by extension, to design custom ablation algorithms.

7.2.- INTRODUCTION

Laser in situ keratomileusis (LASIK) (Pallikaris et al., 1990, Farah et al., 1998) is nowadays a popular surgical alternative for the correction of myopia. A description of this technique can be found in the Chapter 1, section 1.4.- of this thesis. LASIK clinical outcomes have been widely studied in terms of predictability and accuracy of the achieved correction and visual performance (visual acuity or contrast sensitivity) (Knorz et al., 1998, Lindstrom et al., 1999, Nakamura et al., 2001, Mutyala et al., 2000), or from a biological point of view (Vesaluoma et al., 2000). The implementation of techniques for ocular wave aberration measurement (Charman, 1991a, He et al., 1998, Liang et al., 1994, Navarro and Losada, 1997, Liang and Williams, 1997, Mierdel et al., 1997, Howland and Howland, 1977, Webb et al., 1992, Seiler et al., 2000, Moreno-Barriuso et al., 2001a) and estimation of the wave aberration of the anterior corneal surface from corneal topography (Guirao and Artal, 2000, Barbero et al., 2001, Schwiegerling and Greivenkamp, 1997) have allowed objective assessment of the effect of corneal refractive surgery on the optical quality of the eye (Seiler et al., 2000, Moreno-Barriuso et al., 2001b) and the anterior cornea (Oshika et al., 1999b, Applegate and al, 1998, Dausch et al., 2000).

Oliver et al. (1997) assessed the outcomes of PRK (a -6D attempted correction) before and 1 year after surgery for 50 myopic eyes using anterior corneal aberrations for 5 and 7 mm pupils. They reported a significant increase of corneal SA and coma-like aberrations, the former increasing less for the larger of the ablation zones they tested. This increase in aberrations affected the corneal MTF. Oshika et al. (1999a) studied the corneal aberrations for 3 and 7mm pupils before and up to 1 year after LASIK and PRK surgery bilaterally on 22 subjects. Both surgical procedures significantly increased high order aberrations for both studied pupil sizes, and the effect remained even 12 months after the surgery.

Although no changes were found for 3 mm pupils when comparing both surgical procedures, aberrations after LASIK were significantly higher for 7 mm pupils, specifically for spherical-like aberrations, which they attributed to the smaller transition zone in this procedure. Whereas for 3 mm pupils the proportion of coma-like aberration increased after both procedures, for 7 mm pupils, SA became dominant. Schwiegerling and Snyder (2000) computed corneal SA induced by PRK on 16 eyes and found that the magnitude of induced SA was correlated with the attempted correction. Kohnen et al., (Kohnen et al., 2004) compared the change in corneal aberrations in 50 eyes after LASIK for myopia and 50 eyes after LASIK for hyperopia. In the myopic eyes they found an increase in HOA, SA, coma and 5th order aberrations.

In terms of corneal Q, Holladay et al. (1999a) found that Q turned more positive (more oblate corneal shape- see Chapter 1, section 1.1.1.-) after myopic LASIK, reducing corneal optical quality, and some years later, Holladay and Janes (2002) found that Q increased more with increasing attempted correction. Hersh et al. (2003) confirmed the previous findings regarding an increase in Q after three different laser refractive surgical procedures (LASIK, LASEK and PRK), and they found that the corresponding change in SA was well predicted by a mathematical model that considered the ablation rate drop off in the periphery due to the change of the angle of incidence.

In terms of ocular aberrations, Seiler et al. (2000) and Yamane et al. (2004) reported a significant increase in HOA after (3 months and 1 month, respectively) PRK and LASIK, respectively, particularly in coma-like terms and spherical-like terms. SA changed towards positive values, as reported by previous studies for corneal aberrations. These optical changes were related with a decrease in the ocular visual performance.

Previous studies of hyperopic correction with excimer laser also suggest an increase of optical aberrations with the procedure. Oliver et al.

(2001) studied anterior corneal aberrations induced by photorefractive keratectomy (PRK) for hyperopia in nine eyes. They reported a change in corneal SA, which was positive in all eyes prior to surgery, towards negative values for 5.5-mm and 7-mm pupil diameters. A significant increase in coma RMS was also reported. Comparing the results of this study with those obtained in a previous study on myopic PRK (Oliver et al., 1997) they found that the change of anterior corneal aberrations following PRK for hyperopia was greater than those after myopic PRK. In their study previously described, Kohnen et al. (2004) also measured 50 hyperopic eyes (SE ranging from +0.25 to +5.00D) and found a significant increment of HOA and coma RMSs for a 6 mm pupil. Fifth order RMS also increased. When comparing these results with those for the myopic group in their study, they found, in agreement with Oliver et al. (2001), that hyperopic LASIK induced more 3rd and 5th order coma-like aberrations than the myopic procedure. Wang et al. (2003a) also studied the effect of hyperopic LASIK on corneal aberrations for a 6mm pupil in 40 eyes, finding the significant decrease in corneal SA previously reported, and that this decrease was significantly correlated with the attempted correction. They also found a significant increase in HOA after surgery when SA term was excluded.

Chen et al. (2002) studied corneal Q in a corneal radius of 4.5mm for 33 eyes before and after hyperopic LASIK. They found a significant change in corneal Q towards more negative values, which resulted in a shift of SA in the same direction. Ma et al. (2004) compared wave aberrations for a 6 mm pupil in 29 control eyes with 59 eyes after LASIK and lensectomy corrections (with intraocular lens implantation) for hyperopia. The LASIK group had the highest RMS aberration, and the most negative corneal and ocular SA. In addition, they found significant differences in the internal SA in the LASIK group.

In this chapter, corneal and ocular aberrations in the same eyes before and after LASIK for myopia and before and after LASIK for hyperopia are presented. It is shown that the combination of these two pieces of information is important for understanding individual surgical outcomes (which becomes critical in customizing ablation algorithms). It also provides insights into the biomechanical response of the cornea (both the anterior and posterior surfaces) to laser refractive surgery. In addition, a comparison of the outcomes of the myopic and hyperopic LASIK is presented.

7.3.- METHODS

7.3.1.- SUBJECTS

The group of myopic eyes consisted of fourteen eyes of eight patients (six women and two men; mean age, 28.9± 5.4 years; age range 23 to 39 years), which were measured before (28± 35 days) and after (59±23 days) myopic LASIK surgery. The preoperative spherical refractive error ranged from -2.50 to -13.00 D (mean, -6.79±2.90 D) in these eyes. The hyperopic group consisted on thirteen eyes from seven patients (three women and four men; mean±std age, 37 ± 11 years; age range 24 to 54 years), which were measured before (15 ± 17 days) and after (68 ± 43 days) LASIK for hyperopia. The preoperative spherical refractive error ranged from +2.50 to +5.50 diopters (D) (mean±std +3.60 ± 1.06 D) in this group of eyes. Postoperative recovery was uneventful and none of the patients was retreated.

7.3.2.- LASIK SURGERY

The standard LASIK procedure was applied in all eyes by the same surgeon, using the same laser system (a narrow beam, flying spot excimer laser, Chiron Technolas 217-C, equipped with the PlanoScan software; Bausch & Lomb Surgical, Munich, Germany). The laser had an emission

wavelength of 193 nm, a fixed pulse repetition rate of 50 Hz, and a radiant exposure of 400 mJ. The flap diameter (created using a Hansatome microkeratome; Bausch & Lomb Surgical, Munich, Germany) was 8.5 mm with an intended depth of 180 µm for all myopic eyes, and 9.5 mm with an intended depth of 160 µm for all hyperopic eyes except three (H5, H12 and H13), in which the intended depth was 180 µm. The treatment zone diameter was 9 mm with an optical zone diameter of 6 mm for the myopic eyes. For the hyperopic eyes, the treatment and optical zones varied across eyes as shown in Table 7.1. The hinge was always superior, and the procedure was assisted by an eye-tracker. All the LASIK procedures were conducted at the Instituto de Oftalmobiología Aplicada (IOBA), Universidad de Valladolid, Spain, except for three hyperopic patients (eyes H5, H6, H7, H8 and H10) whose surgery took place at Centro Oftalmológico de Madrid (COM), Madrid, Spain, using identical equipment.

Eye #	Optical zone diameter (mm)	Treatment Zone Diameter (mm)	Attempted spherical equivalent (D)	Attempted spherical correction (D)
H1	5	8.5	1.375	0.25
H2	5	8.5	1.5	0.5
H3	5	8.5	2.125	1.5
H4	5	8.5	2.375	2
H5	6	12.8*9.4	2.375	2.75
H6	6.5	10	3.5	3
H7	6	9.7	3.5	3.5
H8	6	9.7	3.5	3.5
H9	5	8.6	4	4
H10	6.5	10	4	3.75
H11	5	8.7	4.25	4.25
H12	5	8.5	4.25	3.5
H13	5	8.5	4.5	4

Table 7.1 Refractive surgery data for hyperopic eyes. Asterisk (*) indicates that the treatment area for this eye was elliptical; numbers indicate the length in millimetres of the main axes of the elliptical treatment area.

7.3.3.- *MEASUREMENTS AND STATISTICAL ANALYSIS*

Ocular aberrations were measured using LRT1 (see Chapter 2). The illumination wavelength used was 543 nm for the myopic LASIK study and 786 nm for the hyperopic LASIK study. (See Chapter 4 for a verification of the results using both wavelengths). Corneal aberrations were estimated from corneal topography as previously discussed in Chapter 6, section 6.3.4.- of this thesis. CR and Q were obtained by fitting the anterior corneal height data to a conicoid (see Chapter 1, section 1.1.1.-) using custom software written in Matlab.

A paired Student t-test was applied when the comparisons were performed in the same refractive group, and an unpaired Student t-test was applied when the different refractive groups were compared. A Pearson's correlation test was applied to find the strength of linear correlations, followed by a t-test to test its significability.

7.4.- **RESULTS**

7.4.1.- *OCULAR AND CORNEAL WAVE ABERRATION PATTERNS*

Figure 7.1 and Figure 7.2 show ocular (left) and corneal (right) wave aberration maps for six significant myopic and six significant hyperopic eyes before (upper row) and after (lower row) LASIK surgery. Piston tilts, defocus, and astigmatism have been excluded in all cases, so that these maps represent simulated best refraction corrected optical quality. Pupil diameter is 6.5 mm for all eyes, and the same scale has been used for the four diagrams corresponding to each eye. Contour lines are plotted every 1 μm for each eye, with thicker and thinner lines indicating positive and negative values of the wave aberration, respectively. The number below each map indicates the corresponding RMS for HOA.

The pre-operative maps reflect the behaviours described in Chapter 6, section 6.4.2.-: in most eyes the ocular map shows less positive SA than

the corneal map, indicating compensation by the internal optics (crystalline lens); in some of the eyes, however, no compensation exists, and ocular and corneal aberration maps show similar patterns of SA. Most of these eyes are hyperopic and belong to subjects over thirty years old (internal SA < ± 0.1 μm in 8 out of the 13 hyperopic eyes, or 62%, mean age 41±9 years old), as described in Chapter 6, section 6.5.2.-. The pre-operative mean (± std) HOA RMS (i.e. excluding tilts, defocus and astigmatism) was 0.72±0.40 μm for ocular and 0.60±0.29 μm for corneal aberrations for the myopic eyes, and 0.63 ± 0.22 μm for ocular and 0.68 ± 0.13 μm for corneal aberrations across the hyperopic eyes included in this study.

Regarding post-operative maps, ocular and corneal wave aberration patterns were very similar one to another in both, myopic and hyperopic eyes, showing the dominance of the corneal aberrations after the procedure. The mean (± std) post-operative HOA RMS was 1.33±0.76 μm for ocular and 1.60±0.79 μm for corneal aberrations in the myopic group, and 1.23±0.45 μm for ocular and 1.18±0.51 μm for corneal aberrations in the hyperopic group. There was a significant increase of aberrations after both types of surgery, indicated by the increase in the number of contour lines of both, corneal and ocular diagrams, and by the increase in the corresponding RMS wavefront error. In the case of myopic correction, LASIK induced a round central area (with various amounts of decentration, depending on the eye) of positive aberration, surrounded by an area of negative aberration. In the case of hyperopic LASIK, the pattern is the opposite, with a central area of negative aberration surrounded by an area of positive aberration. This indicates that positive and negative SA is induced by standard myopic and hyperopic LASIK procedures, respectively, as will be shown later. These changes in SA are consistent with a change in corneal Q towards more positive and negative values, respectively (see Chapter 1, section 1.1.1.-)

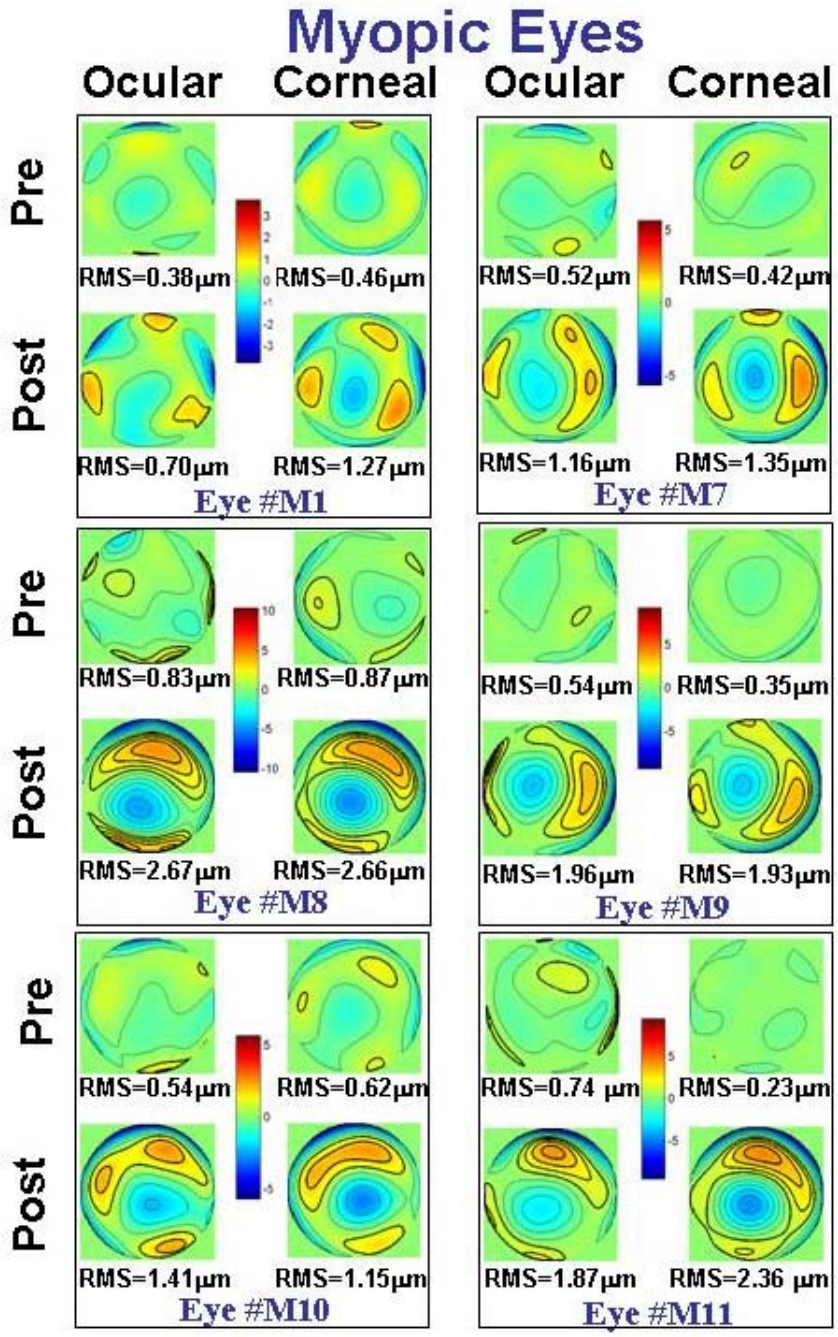

Figure 7.1. A.- Wave aberration maps for HOA, before and after LASIK surgery for myopic correction. For each eye, the maps on the upper row show the wave aberrations before surgery, and the maps on the lower row show the aberrations after LASIK surgery. The maps on the right correspond to corneal (anterior surface) aberrations and on the left to ocular (whole eye) aberrations. All four maps corresponding to the same subject are plotted in the same scale. The number below each map indicates RMS values for HOA in microns. Contour lines are plotted every 1 µm. Pupil size is 6.5 mm.

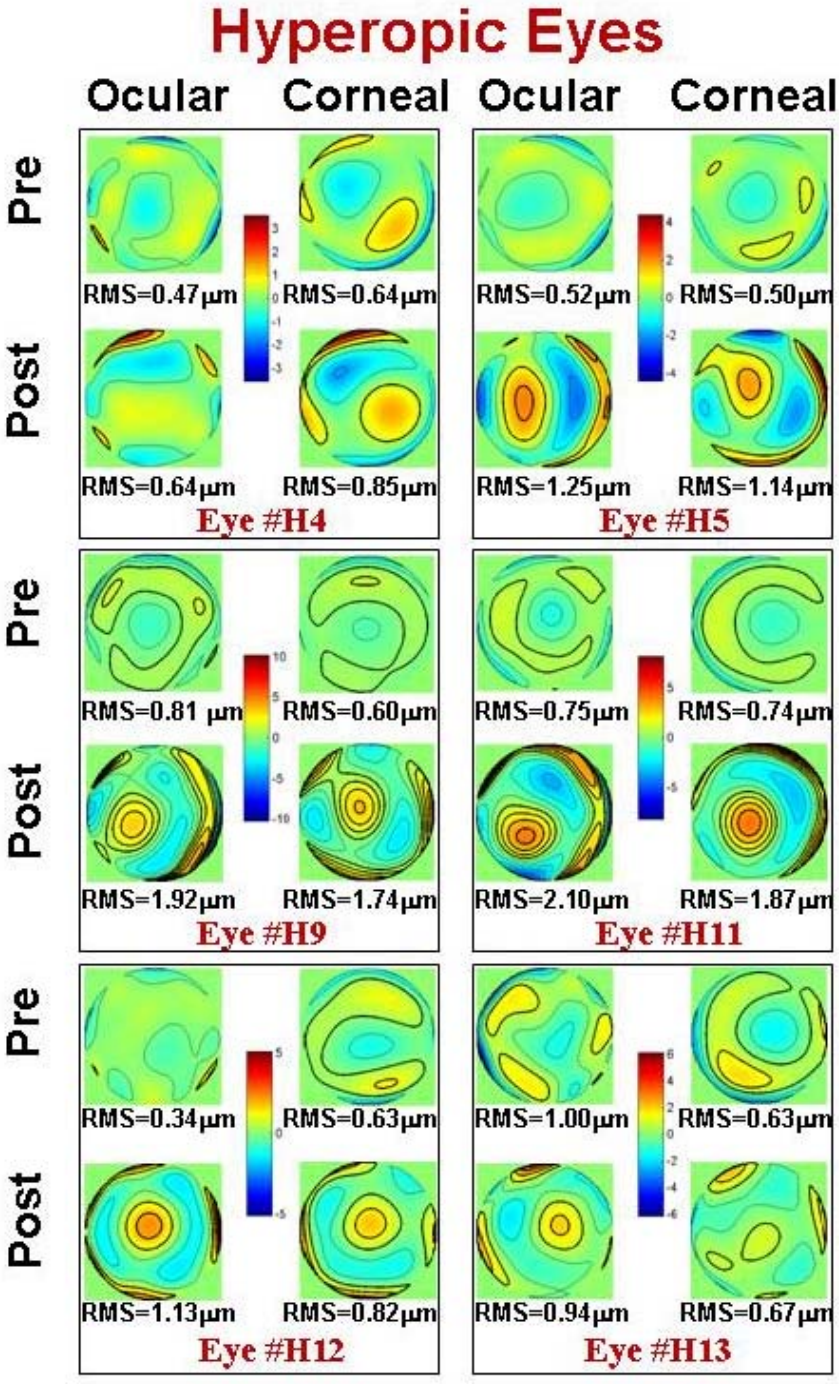

Figure 7.2. B.- Wave aberration maps for HOA, before and after LASIK surgery for hyperopic correction. For each eye, the maps on the upper row show the wave aberrations before surgery, and the maps on the lower row show the aberrations after LASIK surgery. The maps on the right correspond to corneal (anterior surface) aberrations and on the left to ocular (whole eye) aberrations. All four maps corresponding to the same subject are plotted in the same scale. The number below each map indicates RMS values for HOA in microns. Contour lines are plotted every 1 µm. Pupil size is 6.5 mm.

7.4.2.- CHANGE IN OCULAR AND CORNEAL ABERRATIONS WITH MYOPIC LASIK

Figure 7.3 A shows ocular (left panel) and corneal (right panel) RMS for HOA —that is, best corrected for defocus and astigmatism— before (lighter bars) and after (darker bars) LASIK for myopia. Eyes were sorted by increasing preoperative spherical refractive error. Before surgery, ocular aberrations tended to increase with absolute value of refractive error, although this tendency was not evident in corneal aberrations. Both ocular and corneal aberrations increased after LASIK, except for eye M6 for ocular aberrations, and eye M4 for corneal aberrations. For both ocular and corneal aberrations the post-operative increase was much more pronounced in the most myopic eyes, i.e., in those eyes undergoing higher refractive corrections.

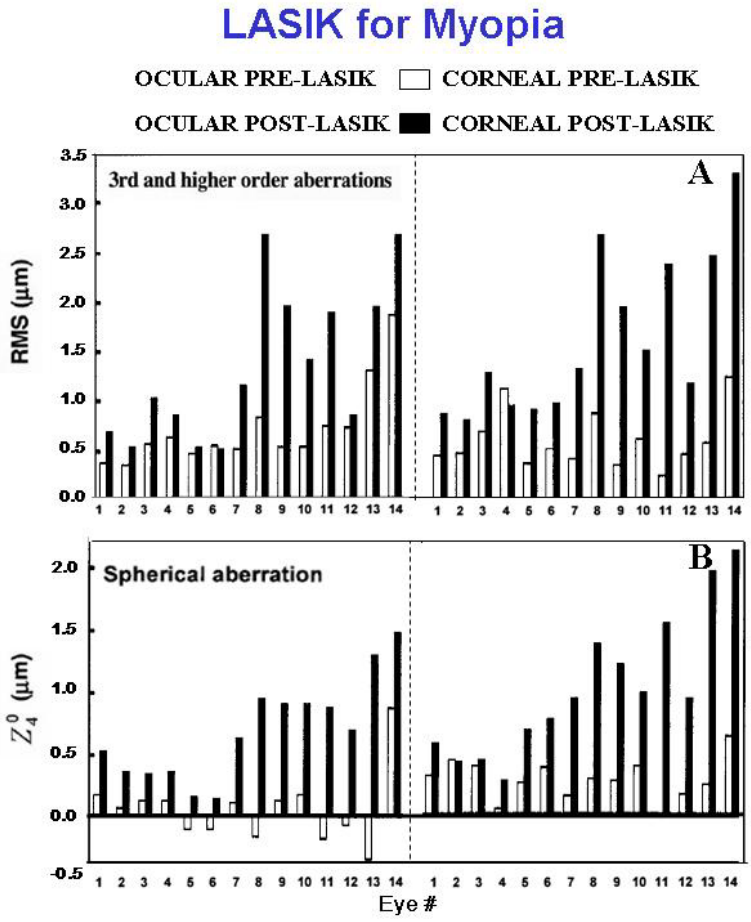

Figure 7.3. Ocular (left) and Corneal (right) HOA RMS values (A) and SA (B) before (light bars) and after (dark bars) LASIK surgery for myopia. Eyes are sorted by increasing preoperative spherical refraction. Pupil size=6.5 mm.

Ocular aberrations increased on average by a factor of 1.92±0.82 (range: 0.90 to 3.64) and corneal aberrations by a factor of 3.72 ±2.34 (range: 0.85 to 10.29) in this group. Ocular and corneal RMS differences (post- minus pre-surgical values) ranged from -0.05 to 0.80 μm, and from -0.16 to 2.04 μm, respectively. Part of this increase is accounted for by an increase in third- (increasing by an average factor of 1.98 for ocular and 2.73 for corneal aberrations), and fourth-order aberrations (increasing by an average factor of 2.54 for ocular and 3.94 for corneal aberrations). Figure 7.4 represents the pre- and post-operative RMS values for different orders averaged across the eyes of the myopic with error bars indicating std values across the eyes. Significant differences ($p<0.05$) between pre- and post-surgical values exist for third, fourth and third and higher orders.

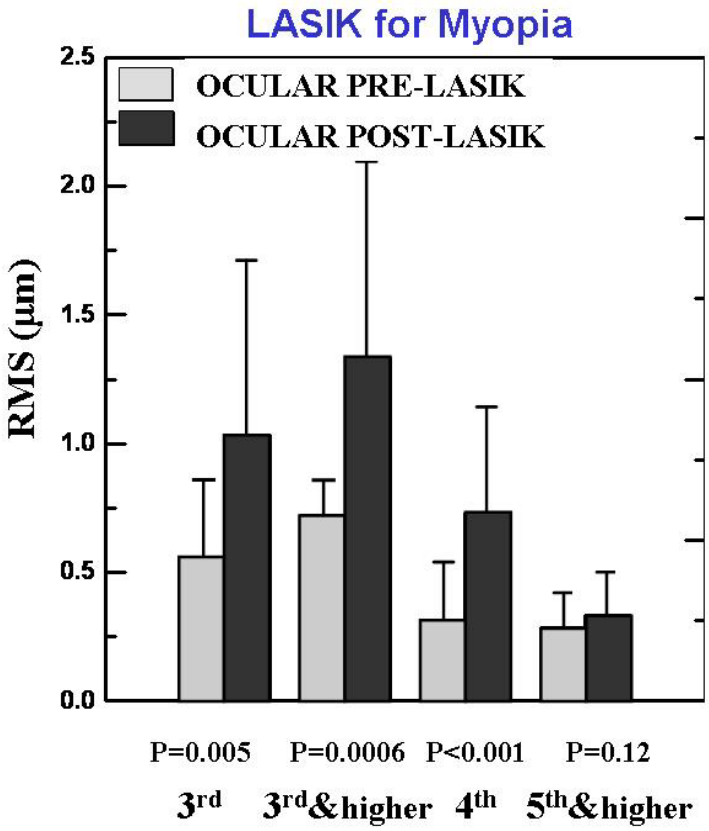

Figure 7.4. Pre- (light bars) and post-operative (dark bars) RMS wavefront error, averaged across all myopic eyes, for 3rd and higher order aberrations, 3rd order aberrations, 4th order aberrations and 5th and higher order aberrations, for a 6.5-mm pupil. Statistical significability of differences between pre and postoperative values is indicated by p.

Since the SA pattern was dominant in the wave aberration maps, the the trends followed by SA in this group were verified. Figure 7.3 B shows ocular (left) and corneal (right) fourth order SA (Z_4^0) before and after LASIK for myopia. The preoperative ocular SA coefficient was close to zero in most eyes, whereas preoperative corneal SA was positive in all eyes. Ocular and corneal SA increased significantly after LASIK: from 0.06±0.28 μm to 0.66±0.43 μm; $p<0.00001$, and from 0.28±0.17 μm to 1.02±0.57 μm; $p<0.00001$). The most dramatic increase occurred in patients with the highest preoperative myopia, both for ocular and corneal aberrations. As expected from the changes found in SA, corneal Q (computed from our videokeratographic data) shifted significantly ($p=0.001$) towards more positive values (from -0.14 to 1.09) after myopic LASIK.

Time after surgery ranged from about 1 month to three months in our group of subjects. Within this sample of eyes, no correlation between post-operative SA ($p=0.66$ for the cornea, $p=0.82$ for the ocular eye) and time after surgery was found.

7.4.3.- CHANGE IN OCULAR AND CORNEAL ABERRATIONS WITH HYPEROPIC LASIK

Figure 7.5 A shows ocular (left panel) and corneal (right panel) RMS for HOA, before (lighter bars) and after (darker bars) LASIK for hyperopia, with eyes sorted by increasing preoperative spherical refractive error. Both ocular and corneal aberrations increased after LASIK, except for eyes H1 and H13 for ocular aberrations, and eyes H1 and H13 for corneal aberrations. For both ocular and corneal aberrations the post-operative increase was much more pronounced in those eyes undergoing higher refractive corrections.

For this group, the average increase factor was 2.15±1.02 (range: 0.91 to 4.03) for ocular aberrations and 1.77±0.75 (range: 0.76 to 3.03) for corneal

aberrations. Ocular and corneal RMS differences (post- minus pre-surgical values) ranged from -0.08 to 1.35 μm, and from -0.27 to 1.53 μm, respectively across the eyes in this group. Third- (2.16 μm for ocular and 2.06 μm for corneal) and fourth-order (2.52 μm for ocular and 1.49 μm for corneal increase average factor**)** aberrations account for most of this increase.

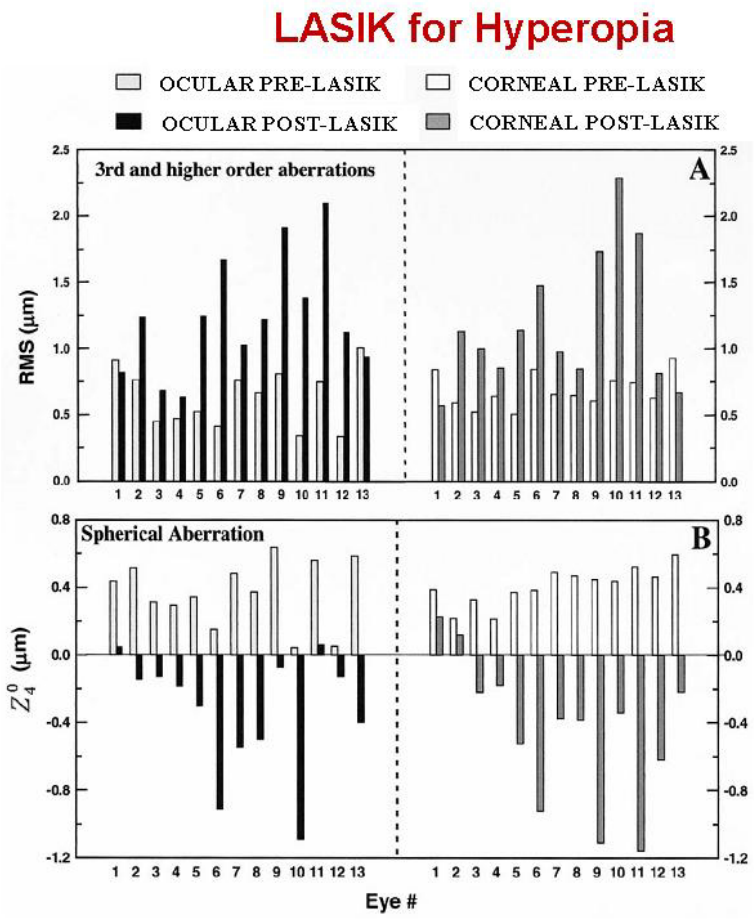

Figure 7.5. Ocular (left) and Corneal (right) HOA RMS wavefront error (A) and SA (B) before (light bars) and after (dark bars) LASIK surgery for hyperopia.

Eyes are sorted by increasing preoperative spherical refraction. Pupil size=6.5 mm.

Figure 7.6 represents the pre- and post-operative average RMS values for different orders. Error bars indicate std values across the eyes. Significability (p) less than 0.05 indicates that differences are statistically significant. Significant differences between pre- and post-surgical values exist for third, fourth and third and higher orders, as happened after LASIK for myopia. However, for these eyes significant differences are also found for fifth and higher order aberrations.

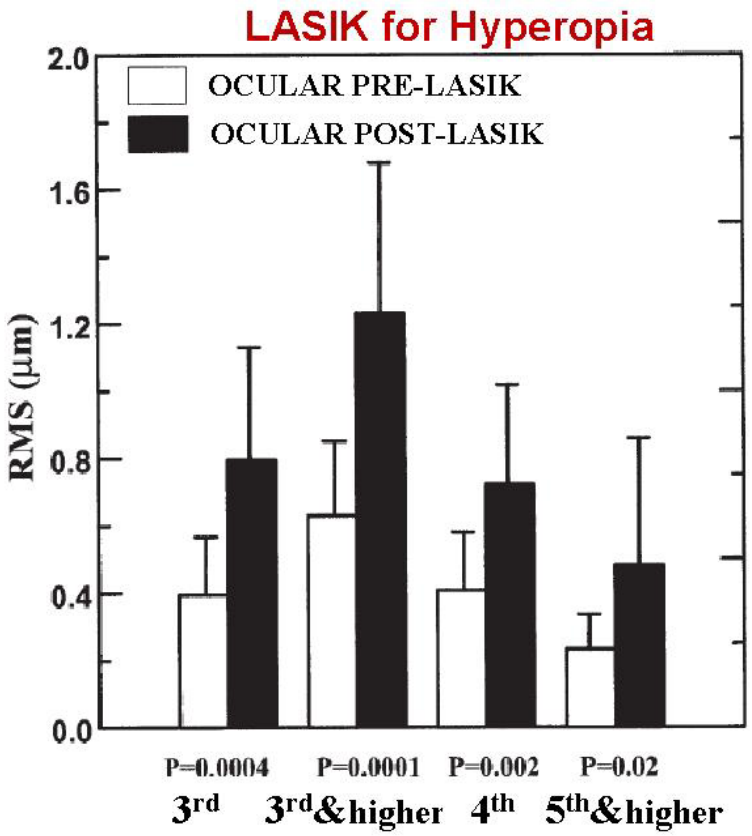

Figure 7.6. Pre- (light bars) and post-operative (dark bars) RMS wavefront error, averaged across all hyperopic eyes, for HOA, 3rd order aberrations, 4th order aberrations and 5th and higher order aberrations, for a 6.5-mm pupil. Statistical significability of differences between pre and postoperative values is indicated by p.

Figure 7.5 B shows ocular (left) and corneal (right) fourth order SA (Z_4^0) before (light bars) and after (dark bars) hyperopic LASIK. Preoperative ocular and corneal SA coefficient was positive for all eyes (0.37±0.19 μm and 0.41±0.11 μm, respectively). SA changed significantly ($p<0.00001$ for both, ocular and corneal) towards more negative values (-0.33±0.35 μm and -0.44± 0.43 μm, respectively) after surgery, turning into

negative in most cases (11 out of 13 eyes). Ocular SA decreased on average by -0.70 ± 0.30 μm, and corneal SA decreased on average by –0.85± 0.48 μm. Consistently, corneal Q changed significantly ($p<0.00001$) towards more negative values (from -0.21 to -0.54) for these eyes.

It should be noted that, although different optical zones were programmed for different eyes, aberrations in eyes with smaller optical zones (5 mm as opposed to 6 or 6.5 mm) did not increase more than in those with the largest optical zone. The aberrations of all subjects were calculated for a 5-mm pupil and similar increase factors were obtained: 2.1 for 3rd order aberrations and higher, and 2.2 for 3rd order aberrations alone. In addition, SA in eyes with smaller optical zones (5 mm) was not found to be greater than in eyes with larger optical zones (6 or 6.5 mm), for either the cornea ($p=0.99$) or the ocular eye ($p=0.67$). Time after surgery ranged from about 1 month to five months in our group of subjects. Within this sample of eyes, no correlation between post-operative SA ($p=0.54$ for the cornea, $p=0.58$ for the ocular eye) and time after surgery was found.

7.4.4.- COMPARISON BETWEEN THE CHANGES IN OPTICAL ABERRATIONS AFTER MYOPIC AND AFTER HYPEROPIC LASIK

Figure 7.7 A and B show ocular and corneal SA, respectively, induced by myopic (black circles) and hyperopic (white circles) LASIK as a function of absolute attempted spherical correction. As previously described, ocular and corneal induced SAs were always positive in myopes and negative in hyperopes. Induced ocular SA (post minus pre-operative values for Z_4^0) ranged from 0.22 to 1.64 μm (0.63±0.45μm, on average), and induced corneal SA ranged from -0.02 to 1.72 μm (0.74±0.57 μm on average) for myopic eyes. For the hyperopic eyes, induced SA ranged from -0.39 to -1.13 μm (-0.76±0.26 μm) for the whole eye and from -0.1 to -1.68 μm (-0.85±0.48 μm) for the cornea. The induced corneal and

ocular SA were correlated with attempted spherical correction for both myopic ($r=-0.87$, $p<0.0001$ and $r=-0.81$, $p<0.0005$, respectively) and hyperopic eyes ($r=-0.81$, $p<0.0005$ and $r=-0.85$, $p<0.05$, respectively). The rate of ocular SA increment per dioptre of attempted spherical correction tended to be higher for the myopic procedure (+0.13 µm/D of myopic error and -0.07 µm/D of hyperopic error). For the purpose of comparison between groups, a subgroup of myopic (n=4) and a subgroup of hyperopic (n=4) eyes of similar absolute attempted correction (1.5 to 3.00 D) were selected. For these subgroups, ocular and corneal HOA increased a factor of 1.62 and 1.58 in myopes, respectively, compared to 2.33 and 1.81 in hyperopes. The average induced ocular SA was, in absolute value, 3.3 times higher for the hyperopic than for the myopic eyes (-0.66 ± 0.28 µm and 0.20 ± 0.06 µm, respectively). The average induced corneal SA for the previous subgroups was -0.78 ± 0.40 µm for hyperopes and 0.13 ± 0.14 µm for myopes (i.e., six times more for hyperopic than for myopic LASIK). The rate for the corneal spherical error increments was higher for the hyperopic procedure (-0.28 µm/D) than for the myopic procedure (0.17 µm/D). The amount of absolute SA after surgery (both myopic and hyperopic) was lower in the ocular eye (-0.38 ± 0.36 µm and 0.40 ± 0.09 µm for the previous hyperopic and myopic subgroups, respectively) than on the cornea alone (-0.46 ± 0.34 µm and 0.43 ± 0.12 µm for the previous hyperopic and myopic subgroups, respectively).

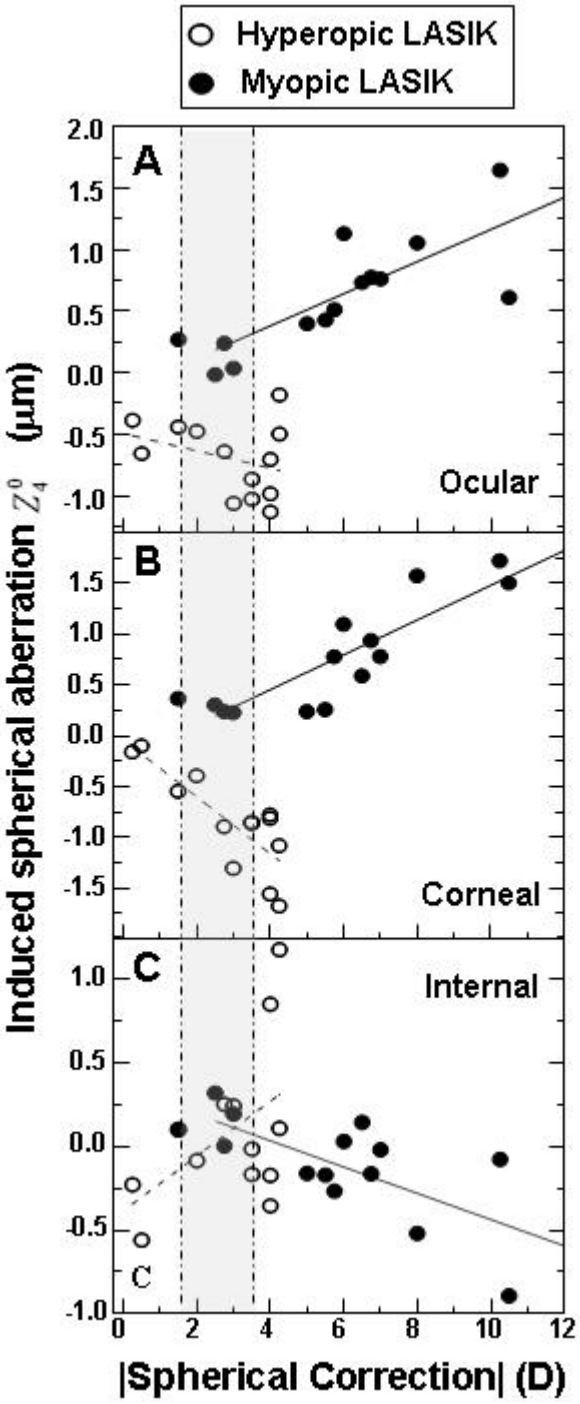

Figure 7.7. Total (A), corneal (B) and internal (C) SA induced by myopic (black circles) and hyperopic (open circles) LASIK as a function of absolute spherical correction, for a 6.5-mm pupil. Shaded areas indicate eyes included in the averages reported in the text comparing the results from both hyperopic and myopic techniques.

7.4.5.- CHANGE OF INTERNAL ABERRATIONS WITH LASIK

Figure 7.7 C shows the internal SA (Z_4^0) induced by hyperopic (white circles) and myopic (black circles) LASIK as a function of absolute attempted spherical correction. As seen in Figure 7.7 A and B, induced ocular SA is generally smaller in absolute value than the induced corneal SA (average SA induced was 0.74 μm and -0.85 μm for the cornea versus 0.61 μm and -0.76μm for the whole eye across myopic and hyperopic subjects, respectively; ocular slope was -0.13 and -0.11 versus -0.19 and -0.30 for the whole eye, for myopic and hyperopic eyes, respectively). In the myopic group, induced internal SA tended to decrease towards negative values with spherical correction (r=0.57, p=0.04). In the hyperopic group the trend was for induced internal SA to increase towards positive values with spherical correction (r=0.52, p=0.06). This indicates that internal SA, of opposite sign than induced corneal SA is reducing the impact of the corneal changes and its magnitude increases with attempted correction as does the induced corneal SA. Since the LASIK surgery is a corneal procedure (i.e. no change is happening on the crystalline lens) changes in internal aberrations must account for changes on the posterior surface of the cornea in this case. No similar behaviour was found for induced third-order aberrations, indicating that third-order aberrations do not seem to be induced in the posterior corneal surface.

Experiments in control subjects (who had not undergone a surgical procedure) performed in two different experimental sessions (separated by at least one month, as in the surgical eyes) did not reveal statistically significant changes in the internal aberrations across sessions. This indicates that possible changes across sessions in the accommodative state or decentrations of corneal topography data (which otherwise are compensated by the recentration algorithm) cannot account for the observed differences in the internal optics found between pre- and post-LASIK results. Therefore these changes must be attributable to surgery.

7.5.- DISCUSSION

Ocular and corneal aberrations increased after LASIK surgery for myopia and after LASIK surgery for hyperopia. The higher the preoperative ametropia (and therefore, the surgical correction to be applied), the higher the increase. In general, although the trends are similar when looking at ocular and corneal HOA, the induced SA in the anterior corneal surface was greater than that of the entire eye in absolute value, for both groups. In the following sections, several other factors that indicate that anterior corneal aberrations alone are not sufficient to explain surgical outcomes will be discussed. In addition, our findings will be related to those in current biomechanical models of corneal response to surgery and previous observations. Finally, the implications of these results in the evaluation of refractive surgery outcomes and aberration-free ablation procedures will be discussed.

7.5.1.- CHANGE IN ABERRATIONS WITH MYOPIC AND HYPEROPIC LASIK

Corneal aberrations were expected to change with the procedure, and this change was expected to implie a change in ocular aberrations. However, the fact that the amount of absolute SA after surgery (both myopic and hyperopic) was lower in the ocular eye than on the cornea alone (-0.38 ± 0.36 µm and 0.40 ± 0.09 µm for ocular versus -0.46 ± 0.34 µm and 0.43 ± 0.12 µm for corneal SA for the previous hyperopic and myopic subgroups, respectively) suggests a compensation by internal aberrations (see section 7.4.5.-). Part of this compensation was due to aberration of the crystalline lens. The role of the preoperative internal SA (primarily aberrations of the crystalline lens) in hyperopes, compared to myopic eyes, will be discussed in the next section. The posterior surface of the cornea seems to play also a compensatory role, which will also be discussed.

As expected, major changes occurred on the anterior corneal surface for both myopic and hyperopic LASIK. The causes of a change in corneal Q leading to important changes in SA found clinically are not well understood (Gatinel et al., 2001, Anera et al., 2003). It has been shown analytically (Gatinel et al., 2001), computationally (Marcos et al., 2003) and experimentally (Dorronsoro et al., 2006) that those changes are not inherent to the Munnerlyn ablation algorithm, or at least to the exact application of it. Radial changes of laser efficiency across the cornea, due to angular changes of reflectivity and laser fluence, have been shown to be responsible for at least part of the discrepancies of postoperative asphericities with respect to predictions (Anera et al., 2003, Mrochen and Seiler, 2001). These effects are expected to be much more relevant in hyperopic LASIK than in myopic LASIK, since in the hyperopic procedure corneal tissue is removed primarily in the periphery where the effects of laser efficiency losses are more important (Berret et al., 2003).

The biomechanical response, presumably responsible for some of the Q changes found with LASIK (Roberts and Dupps, 2001), is probably also higher in hyperopic LASIK. In the myopic LASIK profile, there is only one inflection zone per hemimeridian (located at the border between the treated and the untreated peripheral cornea) for purely spherical corrections, or at the steepest meridian for astigmatic myopic correction, as shown in Figure 7.8 A (see arrows), and two inflection zones in the flattest hemimeridian (located at the junctions between the ablation optical zone and the transition zone (1), and between the transition zone and the untreated peripheral cornea (2), respectively) for myopic astigmatic correction, as shown in Figure 7.8 B (MacRae, 1999). However, the hyperopic profile shows three inflection zones per hemimeridian, as represented in Figure 7.8 C: (1) located at the centre of the ablation (some high hyperopic treatment plans treat the central cornea optical zone); (2) at the deepest portion of the ablation, which is at the boundary border between the ablation optical zone and the transition zone; and (3) at the

boundary between the transition zone and the untreated peripheral cornea. The increased number of inflection zones may result in a larger biomechanical response than occurs for myopic LASIK, although the actual mechanisms still need to be worked out. This has also been considered to reduce the maximum amount of treated hyperopic refractive error to about one-third of the treated myopic error (MacRae, 1999). In addition, ocular third order aberrations were found to increase slightly more in hyperopic than in myopic LASIK eyes (factor of 2.2 and 1.7, respectively), in agreement with the report by Oliver et al. (2001) and Kohnen et al. (2004). However, no correlation was found between induced third order aberrations and attempted spherical correction. This result suggests that coma was primarily associated with decentration of the ablation pattern, and the amounts of decentration were rather variable

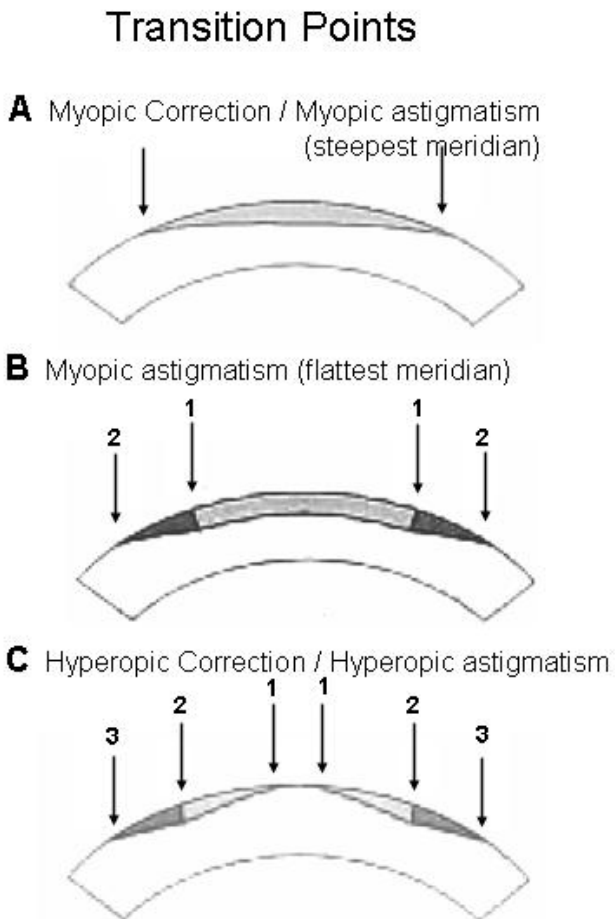

Figure 7.8. Diagrams showing corneal transition points after ablation for correction of myopia or myopic astigmatism on the steepest meridian (A), myopic astigmatism on the flattest meridian (B), hyperopia or hyperopic astigmatism (C). Modified from (MacRae, 1999)

across eyes, both myopic and hyperopic.

7.5.2.- ROLE OF PREOPERATIVE INTERNAL OPTICS

Ocular aberrations result from the combination of corneal and internal aberrations and their inter-relationships. According to the study described in Chapter 6 of this thesis, this combination may be different for myopic and hyperopic eyes. Therefore, different outcomes between both groups of eyes after surgery may be expected due to different combinations of ocular, corneal and internal aberrations, in addition to differences attributable to the LASIK procedures.

In general, before myopic surgery, both components contributed to the whole aberration with comparable amounts of aberrations—in some cases even balancing each other. Figure 7.1 A and Figure 7.3 A (white bars) show that whereas before surgery the cornea dominated the ocular wave aberration pattern in some eyes (eye M1 or M7 for example), in some others there was little similarity between ocular and corneal patterns, indicating an important contribution of the internal optics. Although the relative contribution of the internal optics is expected to be much lower after refractive surgery, interactions between corneal and internal optics may still play some role in determining the surgical outcomes. A high degree of balance between corneal and internal aberrations in normal young eyes has been reported in previous studies (Artal et al., 2002, Marcos et al., 2002). A discussion on the percentage of balance for hyperopic and myopic eyes depending on the age group can be found in Chapter 6 , section 6.5.2.- of this thesis. Before surgery, a term-by-term balance of at least 50% of the aberration was found in 28% of the 14 myopic eyes of this study. For SA, this balance increased to 57% of the eyes. In 78% of the eyes, the SA of the anterior corneal surface and the internal optics had a different sign, resulting in less positive ocular SA (Figure 7.3 B, white bars). Furthermore, it is not uncommon (35%) that the amount of negative internal SA - likely from the crystalline lens (Artal and

Guirao, 1998, Elhage and Berny, 1973) - exceeds the amount of positive SA of the anterior corneal surface.

Figure 7.9 illustrates one of these cases (eye M6), with a corneal preoperative SA (Z_4^0) of 0.38 μm and internal preoperative aberration of -0.48 μm. The upper row shows the pre-operative measured ocular and corneal and the computed internal aberration patterns. The negative internal aberration dominates the central area ocular aberration pattern. After LASIK (lower row), positive SA is induced on the anterior corneal surface, which cancels (actually overcompensates) the preoperative negative SA of the internal optics. For this reason, the post-LASIK ocular aberration pattern for this eye is much better than predicted from corneal aberrations alone. Unlike other subjects with similar preoperative myopia and similar corneal topography after LASIK, this subject did not show any loss of contrast sensitivity (actually improved at two spatial frequencies) (Marcos, 2001). An individual comparison of pre and post-surgical ocular and corneal aberration can be invoked to explain the surprisingly good surgical outcomes in this patient.

In general, the possible balance between corneal and internal aberration gets disrupted with refractive surgery. In this group, compensation of more than 50% of the corneal SA by the preoperative internal aberrations decreased from eight eyes before surgery to four eyes after surgery and only happened in eyes with the lowest preoperative spherical errors (eyes M2, M3, M5, and M6). However, at least in these eyes, these interactions are relevant in determining the ocular wave aberration pattern. The counteracting effects of the crystalline lens may be accounted for by adding the induced corneal SA and internal preoperative SA (which accounts mainly for crystalline lens SA), and then dividing this number by the induced corneal aberration to provide a relative value. A value between 0 and 1 will be indicative of compensation by the crystalline lens, a value close to 1 indicative of no compensation, and a

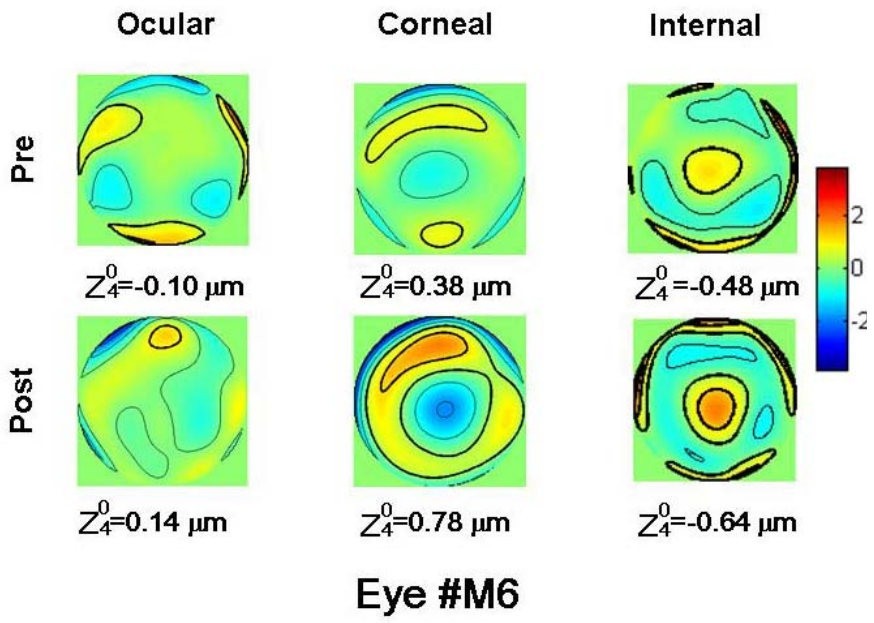

Figure 7.9. Ocular (left), corneal (middle) and internal (right) HOA maps before (top) and after (bottom) myopic LASIK for eye M6 (with a particularly good surgical outcome). Before surgery, the negative internal aberration dominates the total pattern. After surgery, the positive SA induced on the anterior corneal surface partially cancels the preoperative negative SA of the internal optics. Contour lines were plotted every 1 µm, and pupil diameter was 6.5 mm.

value higher than 1 indicative of additional contribution of the crystalline lens to the degradation. In the myopes from our study, where attempted spherical error correction ranged up to -10.50 D, a counteracting value of 0.375 was found.

In our hyperopic group, a dominance of preoperative corneal aberrations (particularly SA) in the preoperative ocular aberration pattern in several of the eyes (see Figure 7.1 B and Figure 7.5) was found. When the eyes of this study were sorted by age, younger eyes (H6, H10 and H12; 24 through 25 years old) showed negative internal SA, while older eyes, showed less negative SA (eyes H13, H5, H7, H8, H3, 25 through 43 years old), which turned into positive for the oldest eyes (H4, H1, H2, H9, H11, 43 through 54 years old), disrupting the balance of the positive SA of the cornea by the crystalline lens. This balance between internal and corneal aberrations observed in our younger hyperopic eyes has been reported in previous studies in normal young eyes (Artal et al., 2002) and myopic eyes

(Marcos et al., 2002), as well as the loss of this compensation with age (from 45 years) in normal eyes (Marcos et al., 2002). In the age and absolute refractive error matched comparison of hyperopic and myopic eyes reported in Chapter 6 of this thesis, an early loss (at approximately 30 years of age) of corneal to internal balance in hyperopic eyes was found. This loss was not present in the myopic group of the same study, which did not show a significant trend of balance at this age.

These findings may be relevant to understanding the outcomes of hyperopic LASIK and to predicting possible changes in performance with age. Given that corneal SA shifts to negative values after a hyperopic procedure (Figure 7.5 B), the fact that the crystalline lens contributes with additional negative SA is disadvantageous in young hyperopic eyes, whereas for myopic eyes the negative SA of the crystalline lens subtracts from the induced positive corneal SA (Figure 7.9). However, since SA of the crystalline lens becomes more positive with age, patients who undergo hyperopic LASIK will experience an absolute decrease of SA with age (and potentially an increase in optical quality), whereas for myopic eyes, SA will increase with aging (Marcos, 2002). Aberrations of the crystalline lens therefore play a significant role in the evaluation of the individual surgical outcomes and in the prediction of long-term optical performance. In this group, compensation of more than 50% of the corneal SA by the preoperative internal aberrations was present in 3 of the 13 hyperopic eyes, which were the youngest eyes (H6, H10 and H12; 24, 24 and 25 years old). After the surgery, compensation of more than 50% was found in four eyes, which were the oldest eyes of the group (H1, H2, H9 and H11; 48, 48, 54 and 54 years old). For this group a counteracting value of 1.04 was found.

Possible effects of preoperative corneal aberrations on postoperative outcomes were also studied. For myopic eyes, no correlation between preoperative and postoperative SA was found. Although a slight

correlation for hyperopic eyes (r=-0.42) was found, this was not significant (p=0.16), and could be driven by the correlation between spherical error and corneal SA in preoperative hyperopic eyes (r=0.76, p=0.002), which was not found for preoperative myopic eyes (see Chapter 6).

7.5.3.- CHANGES IN INTERNAL ABERRATIONS AND BIOMECHANICAL RESPONSE

Absolute value of induced ocular SA (Figure 7.7 A) was generally smaller than induced corneal SA (Figure 7.7 B) in absolute value for both, myopic and hyperopic groups. This indicates that induced internal SA (Figure 7.7 C), of opposite sign to induced corneal SA, reduces the impact of corneal changes. The effect was larger as the preoperative spherical refractive error (and therefore attempted correction) increased and did not depend on the preoperative internal aberrations. There was a significant correlation between induced internal SA and spherical attempted correction (r=0.57, p=0.04) in the myopic group. In the hyperopic group the correlation (r=0.52) is on the limit of significability (p=0.06), probably due to higher variability and a limited refractive range. The effect is only present for SA, but not for other terms.

Since LASIK surgery is not likely to induce changes in the crystalline lens, one might think that the changes occur in the posterior corneal surface. This hypothesis is consistent with some studies using scanning slit-lamp corneal topography in myopic subjects that reported a forward shift of the posterior corneal surface after PRK for myopia (Naroo and Charman, 2000) and LASIK (Seitz et al., 2001, Baek et al., 2001, Bruno et al., 2001). They suggested that the thinner, ablated cornea may bulge forward slightly, steepening the posterior corneal curvature. This effect has been thought to account for the regression towards myopia that is sometimes found after treatment, particularly in the patients with highest preoperative myopia (Naroo and Charman, 2000).

Using a simple corneal model with aspherical surfaces developed by Sergio Barbero (Barbero, 2004), the observed mean changes of internal SA were found to be consistent with the changes in power (from -6.28 to -6.39 D) and Q (from 0.98 to 1.14) of the posterior corneal surface reported by Seitz et al. for a group of eyes undergoing LASIK with preoperative spherical refractive error similar to those in our study (range: -1.00 to -15.50 D, mean, -5.07±2.81 D) (Seitz et al., 2001). The induced SA of the posterior corneal surface computed using the model (-0.103 μm) was very similar to the change in internal SA measured experimentally in this study (-0.110 μm, on average).

To our knowledge, equivalent changes in posterior corneal curvatures and asphericities after hyperopic LASIK have not been studied. Ma et al. (2004) compared internal aberrations after hyperopic LASIK eyes with a control group of eyes and found more positive internal SA in the operated eyes, consistent with a shift of the posterior corneal surface towards more positive values. In both myopic and hyperopic eyes, the shift of internal SA resulted in slight compensation of the aberration induced on the anterior surface of the cornea. On the other hand, recent studies using Scheimpflug imaging report that no changes are found in the topography of the posterior cornea after LASIK for myopia (Ciolino and Belin, 2006, Ciolino et al., 2007). Early studies reporting disagreement in pachymetry measured with slit-lamp corneal topography and ultrasound (Yaylali et al., 1996, Chakrabarti et al., 2001, Modis et al., 2001) have lead to the application of correction factors (acoustic factor) to slit-lamp topography to minimise this discrepancy. Although with the correction factor this discrepancy decreased for measurements in normal corneas, slit-lamp topography has been reported to underestimate central corneal thickness for post-LASIK eyes (Prisant et al., 2001, Iskander et al., 1999). Studies comparing Scheimpflug imaging and slit-lamp topography find differences between both techniques (Quisling et al., 2006), specially in post surgery eyes (Matsuda et al., 2008). Therefore, the question of the

changes on the posterior corneal surface induced by LASIK remains unclear.

In summary, using a combination of aberrometry and anterior corneal topography, the change in the posterior corneal shape was found to produce a decrease of ocular SA in comparison with that predicted from anterior corneal aberrations alone, and the effect is rather variable across eyes. Our results confirm that this effect is correlated with the amount of preoperative refractive error (or, equivalently, with the depth of corneal ablation).

7.5.4.- COMPARISON WITH OTHER STUDIES

Direct comparison among studies is usually hampered by differences in surgical technique (type of surgery, optical and transition zone diameters, type of laser, use of an eye-tracker) and the characteristics of the study population (age range, preoperative correction, preoperative HOA, etc). In this section our results are compared with those in literature.

The change of corneal aberrations with LASIK for myopia found in this study - increase of coma, SA and HOA (by a factor of 2.73, 3.94 and 3.72, respectively) - agrees with results reported by Oshika (1999b) (increment factor of 2.48, 5.11 and 3.24, for coma, SA and HOA, respectively) and Oliver et al. (1997) (increment factor of 2.11 and 2.38, for coma and SA respectively). The correlation between induced corneal SA and attempted correction found in this study ($r=-0.81$, $p<0.0005$) agrees with the results reported by Schwiegerling and Snyder (2000) for PRK patients ($r=-0.84$).

As expected from the results for corneal SA, and in agreement with published studies on LASIK for myopia (Hersh et al., 2003, Holladay et al., 1999b), anterior corneal Q increased (more oblate corneas) with the surgery (from -0.14 to 1.09, compared to from -0.17 to 0.92 by Hersh et al. (2003), and from -0.16 to 0.47 by Holladay et al. (1999b)). Holladay et al.'s

post-surgical mean value was smaller than Hersh et al.'s and ours, maybe due to differences in the pre-surgical refraction, and therefore the attempted correction (-2.50D through -13D for this work, -3.75D through -10.75D for Hersh et al., -2.25D through -10.12D for Holladay et al.) used, or the specific laser platform.

The significant increase in ocular aberrations found in this work after myopic LASIK agrees with those reported by other studies (Seiler et al., 2000, Yamane et al., 2004). However, the values reported by Seiler et al. are greater than ours: RMS_{post}/RMS_{pre} ratios (Moreno-Barriuso et al., 2001) for 3rd order, 4th order, and HOA (3rd through 6th order) were 4.7, 4.11 and 4.20 compared to our 1.98 μm, 2.54 μm and 1.92 μm). This could be attributed to the different surgical techniques (PRK vs LASIK, broad beam vs flying spot), and the slightly greater pupil they use (7 mm vs 6.5mm in diameter). The ratio values from Yamane et al. were slightly smaller than ours, probably because the pupil diameter they used was smaller (4 mm): 1.46 for 3rd, 1.63 for 4th and 1.70 for 3rd through 5th RMSs.

Recent studies report a decrease in the aberrations induced by LASIK procedures that use modified laser algorithms such as wavefront-guided or wavefront-optimised compared to standard algorithms. For example, Kim et al. (2004) reported post surgery RMS values of 0.34 μm, 0.23 μm and 0.47 μm for 3rd order, 4th order and HOA RMSs (increase factors 1.93, 2.00 and 2.16), respectively, for the standard procedure, compared to 0.29 μm, 0.22 μm, and 0.38 μm (increase factors 1.65, 2.32 and 1.84), respectively for the wavefront-guided procedure for corrections ranging from -2.75 to -8D. However, differences were not statistically significant.

Our findings on the increase of corneal aberrations with hyperopic surgery, and particularly the change in corneal SA towards negative values, are in general agreement with the findings previously reported (Oliver et al., 2001, Wang, 2003, Ma et al., 2004) Changes reported by Oliver et al. were greater (postoperative mean corneal SA of -0.44 ± 0.43

μm and third-order corneal RMS of 0.91 ± 0.39 μm) than those found in the present study in spite of using a slightly smaller pupil probably due to inclusion of higher hyperopes (+2.50 to +7.50 D) and differences between surgical procedures (PRK versus LASIK). They also found a statistically significant increase in coma RMS (from 0.64 ± 0.24 μm to 1.76 ± 1.39 μm after 12 weeks). Also, our values were greater than Wang et al.'s pre- and postoperative values for corneal SA (0.27 ± 0.08 μm and -0.058 ± 0.16 μm, respectively) and RMS for HOA (0.49 ± 0.09 μm and 0.56 ± 0.20 μm, respectively).

Regarding corneal Q, the relative changes that found in this study were similar to those (-0.32 versus average of -0.39) in Chen et al.'s (2002) study, even though our pre (-0.21 ± 0.12) and postoperative (-0.54 ± 0.19) mean Q were less negative. In agreement with Chen et al, correlation between the postoperative Q and the attempted spherical correction was found, although it was not statistically significant (r=-0.47, p=0.1), as well as some correlation between pre and postoperative corneal Q (r=-0.40, which was statistically significant; r=-0.76, p=.005, without eye #H5). Unlike reported by Chen et al, a good correlation between the preoperative corneal radius of curvature and the postoperative Q (r=-0.68, p=.008) was found in the current study.

Ocular aberration postoperative values reported by Ma et al. on LASIK for hyperopia were comparable to those found in this study (1.18 μm and 0.86 μm for ocular and corneal HOA RMS for a 6-mm diameter pupil, as opposed to our 1.23 and 1.18 μm for a 6.5-mm-diameter pupil; and -0.41 and -0.24 μm for ocular and corneal SA for 6-mm, as opposed to our -0.44 μm and -0.33 μm for 6.5-mm), in spite of the differences between preoperative spherical error ranges in both studies (+0.75 to +7.25 D in Ma et al versus +2.50 to +5.50 D in our study). However, their study reported larger changes in internal SA, which they attributed partly to reshaping of

the posterior surface of the cornea and partly to possible errors in their techniques.

7.5.5.- IMPLICATIONS

Our results have important implications for the evaluation of the outcomes in standard LASIK surgery as well as for the design of wavefront-guided ablation procedures (designed to individual cancelling preoperative aberrations). It has been shown that the combination of corneal and ocular aberrations is necessary to understand individual surgical outcomes and their impact on visual performance. In general, both corneal and ocular aberrations increased with surgery, but the particular increment depended on the individual subject. This is particularly critical in any aberration-free procedure, which cannot rely on the mean population response, but must be adapted to the individual patient. Moreover, ocular wavefront aberration measurements complement corneal topography information to gain insight into the biomechanical corneal response. Although the ablation is applied on the anterior corneal surface, our analysis revealed changes in the shape of the posterior corneal surface, assessed by the modification of its SA.

In the last years, the induction of aberrations with surgery, specifically SA, has driven the advance of corneal refractive surgery due to its impact on postsurgical visual quality. Different approaches have been followed to avoid the induction of aberrations (Kohnen, 2006, Mrochen, 2006). Technological advances and experience in wavefront-guided procedures have resulted in an improvement of the outcomes of this surgery reported by more recent studies (Kim et al., 2004, Zhang et al., 2008). Some studies report less aberrations induced during the wavefront-guided procedure compared to standard procedures (Schallhorn et al., 2008, Kim et al., 2004). However, the differences reported in terms of optical aberrations or impact on visual functions are not always statistically significant (Chisholm et al., 2004, Netto et al., 2006, Kim et al.,

2004). Wavefront-optimised laser profiles aim at not altering pre-surgical ocular aberrations, and specifically at avoiding the induction of SA reported for the standard procedure (Mrochen et al., 2004), whereas aspheric ablation patterns have been designed to optimise the corneal Q (Schwiegerling and Snyder, 2000, Manns et al., 2002). Nevertheless, the results reported for these techniques are not better than those reported for wavefront-guided procedures (Padmanabhan et al., 2008, Koller et al., 2006). Different studies (Jimenez, 2004b, Jimenez, 2004a, Dorronsoro et al., 2006, Kwon et al., 2008, Arba-Mosquera and de Ortueta, 2008, Dupps and Wilson, 2006, Hersh et al., 2003) have been carried out with the purpose of identifying the different factors that contribute to the induction of the aberrations during the surgery. All these different works reflect the influence of the findings of the work presented in this chapter.

7.5.6.- CONCLUSIONS

1) High order aberrations (3rd through 7th order) increase with standard LASIK treatment, particularly SA, which changes towards positive values with myopic LASIK and towards negative values with hyperopic LASIK.

2) However, the increase in the anterior corneal SA is slightly counteracted by the posterior corneal SA, resulting in an increase of the whole eye SA smaller than that of the anterior cornea. This indicates that corneal biomechanics play a role in the surgery outcomes.

3) Preoperative aberrations play also an important role in the outcomes of the surgery, due to the disruption of the balance existing between the corneal and the lens aberrations resulting from aberrations induced by LASIK. The fact that aberrations change with time, should also be considered.

4) The combined use of ocular and anterior corneal aberrations is essential to asses the outcomes of refractive surgery as well as to select the

individuals suitable for the surgery. In the first case, the combined use of both devices allowed us to gain insight into the biomechanical corneal response. In the second case, the study of the relationship between anterior corneal and internal aberrations before surgery may allow to predict the outcomes of the procedure.

5) These results have important implications for wavefront-guided procedures. Ocular wavefront aberration measurements complement corneal topography information to gain insight into the biomechanical corneal response. Although the ablation is applied on the anterior corneal surface, our analysis revealed changes in the shape of the posterior corneal surface, assessed by the modification of its SA.

Chapter 8

CONCLUSIONS

This thesis contributes to both methodological advances in wavefront sensing (Laser Ray Tracing and Hartmann Shack techniques) and advance in the assessment of ocular aberration in ametropia, and the optical changes after corneal refractive surgery.

The main conclusions regarding the aberrometry technology implemented in this thesis are:

1.- High order aberrations (third and higher order terms) can be reliably measured in infrared, both with Laser Ray Tracing (LRT) and Hartmann Shack (HS) techniques. There are no statistically significant differences in high order aberrations measured with visible (543 nm) and near infrared (787 nm) light.

2.- Differences in defocus from aberrometry using green (532 nm) and near infrared (787 nm) are consistent with longitudinal chromatic aberration, with an average chromatic difference of focus of 0.78 ± 0.29 D.

3.- Despite large differences in the intensity distribution of retinal spot patterns (both with LRT and HS) as a function of the polarisation state of the illumination and recording channels, the estimated aberrations are independent of polarisation.

4.- The metrics refined to compare estimates of ocular aberrations using different sampling pattern configurations (RMS of the difference , RMS_diff, and percentage of differences between wave aberration maps, W%), the hierarchical cluster analysis and Student's t-test have proved adequate to assess the performance of different sampling patterns.

5.- The variability of the wave aberration is generally larger than the effects due to the sampling. In healthy human eyes the sampling pattern does not seem to play a major role on the accuracy of the aberrations estimated, as long as the number of samples is sufficient for the number of Zernike terms to estimate. The spatial distribution of the sampling can be more important than the number of samples. Moderate density sampling patterns based on the zeroes of Albrecht's cubature (49 samples) or hexagonal sampling (37 samples) performed relatively well.

The main conclusions on ocular aberrations of ametropic eyes and following LASIK correction are:

1.- Hyperopic and myopic eyes (23-40 years and 26-39 years; +0.5-+7.4 D and –0.8 - –7.6 D, respectively) differ both geometrically and optically. Hyperopic eyes are statistically significantly shorter than myopic eyes and have less prolate corneas. Hyperopic eyes also show larger corneal spherical aberration and less negative internal spherical aberration than myopic eyes.

2.- Hyperopic eyes show an earlier loss of the balance between corneal and internal spherical aberration, perhaps associated to an earlier onset of presbyopia.

3.- Standard LASIK for myopia and hyperopia produce a change of ocular (total) and corneal spherical aberration towards positive and negative values, respectively. This change in spherical aberration is correlated with the attempted correction.

4.- Slightly higher changes in the anterior cornea compared to the total ocular changes suggest a slight counteracting effect from the posterior cornea.

5.- The fact that changes are relatively higher after LASIK for hyperopia than after LASIK for myopia are suggested of a larger influence of geometrically-related laser efficiency losses and of biomechanical effects in hyperopic LASIK.

In brief, this thesis has contributed to the understanding and improvement of ocular wavefront sensors by indentifying optimal configuration parameters (wavelength, polarisation and sampling). This technology has been used to expand the knowledge and understanding of ametropic eyes, and to assess the optical changes induced by LASIK surgery for myopia and hyperopia. This research has implications in the identification of best candidates for surgery and interpretation of the surgical outcomes through the combination of total and corneal aberration measurements. These findings are important to understand the limitation of standard LASIK ablation algorithms, and the optimisation of the state-of-the-art wavefront customised procedures.

Trying to look into the future, it looks like aberrometry has arrived to stay. In the last years, aberrometry has earned a place in the clinical environment thanks to refractive surgery. However, it has also been proven valuable at identifying ocular conditions affecting the optics of the eye (keratocous, pellucid marginal corneal degeneration, dry eye, lenticonus, cataracts) and as an objective assessing tool for different correction methods (contact lenses, intraocular lenses, orthokeratology, apart from refractive surgery) (see review by Maeda, 2009). There is no reason to think that in the future aberrometry will be not applied to early identification of new ocular conditions, perhaps in combination with new imaging techniques which might also benefit of the correction of aberrations. Additionally, the power of aberrometry as an objective

evaluation tool will surely be useful to assess *in vivo* new correction methods and to understand better the psychophysical and psychometric outcomes of these corrections when combined with the optics of the eye.

Additionally, aberrometry has helped to advance in the knowledge of the optical mechanisms of the eye, such as the balance between corneal and internal aberrations, or the change in aberrations with accommodation. There are still some questions to be clarified where aberrometry could contribute maybe in combination with biometric or imaging techniques. Specifically, some issues related to the crystalline lens are still unknown, given its inaccessibility *in vivo*, and the complications of reproducing the *in vivo* conditions *ex vivo*. These issues include the exact structure of the GRIN, the changes taking place in the lens, including GRIN distribution, during the process of accommodation or the structural changes taking place in the lens with age leading to presbyopia onset. For this last issue a comparison between different refractive groups around pre-presbyopia age range might help to identify early gradual changes on the aberration pattern that might give an insight in the optical changes involved.

Regarding methodology, there are still issues to tackle, such as which is the adequate sampling pattern for general population, or for screening of particular conditions. Although it seems quite clear that the sampling pattern should be adapted to the aberrations to measure, this implies to predict in advance what is to be found. A future study in a wider population would be desirable, as well as having a gold standard such an interferometric aberration pattern for comparison across patterns. Population subgroups with similar optimum sampling might be then determined and therefore the characteristics making a sampling pattern more suitable for specific eyes could be identified.

Finally, will ocular (and corneal, internal, etc) aberrations still be represented using Zernike polynomials?. Although for some particular

applications Zernike polynomials might not be accurate enough, they have been doing the job quite well all these years, becoming a standard. Aberrometry has brought together such different disciplines as physicists and physicians. Many physicians have made an effort to update and complement their training in order to be able to understand and apply aberrometry in their practice. This effort included understanding the Zernike expansion. If a more adequate mathematical tool is found, it should be used for those specific cases where Zernike polynomials fail. However, before changing the standard, it is important to make sure that the new tool is really bringing a general benefit, and to make available a way to convert to and from Zernike into the new base.

APPENDIX A

JACOBI, LEGENDRE AND ALBRECHT SAMPLING COORDENATES.

The position of the samples in the sampling patterns J49, L49 and A49 is given by the zeroes of Jacobi, Legendre and Albrecht functions, respectively. The zeroes of Albrecht function have been obtained from the book *Numerical quadrature and cubature (*Engels, 1980), pages 44-46. The zeroes of Legendre and Jacobi functions have been obtained using Matlab. The programs that generate the sampling program were written in Matlab by Susana Marcos. The coordinates corresponding to each pattern is represented on table A.1.

Ray label	Albretch 49		Legendre49		Jacobi 49	
	X	Y	X	Y	X	Y
1	0.180704	0.180704	0	0	0	0
2	0.000000	0.255554	0	0.255899	0	0.230056
3	-0.180704	0.180704	0	0.709138	0	0.659429
4	-0.255554	0.000000	0	1	0	1
5	-0.180704	-0.180704	0.097928	0.236420	0.088039	0.212544
6	0.000000	-0.255554	0.271375	0.655158	0.252353	0.609233
7	0.180704	-0.180704	0.382683	0.923880	0.382683	0.923880
8	0.255554	0.000000	0.180948	0.180948	0.162674	0.162674
9	0.391891	0.391891	0.501436	0.501436	0.466287	0.466287
10	0.000000	0.554218	0.707107	0.707107	0.707107	0.707107
11	-0.391891	0.391891	0.236420	0.097928	0.212544	0.088039
12	-0.554218	0.000000	0.655158	0.271375	0.609233	0.252353
13	-0.391891	-0.391891	0.923880	0.382683	0.923880	0.382683
14	0.000000	-0.554218	0.255899	0	0.230056	0
15	0.391891	-0.391891	0.709138	0	0.659429	0
16	0.554218	0.000000	1	0	1	0
17	0.606775	0.606775	0.236420	-0.097928	0.212544	-0.088039
18	0.000000	0.858110	0.655158	-0.271375	0.609233	-0.252353
19	-0.606775	0.606775	0.923880	-0.382683	0.923880	-0.382683
20	-0.858110	0.000000	0.180948	-0.180948	0.162674	-0.162674
21	-0.606775	-0.606775	0.501436	-0.501436	0.466287	-0.466287
22	0.000000	-0.858110	0.707107	-0.707107	0.707107	-0.707107
23	0.606775	-0.606775	0.097928	-0.236420	0.088039	-0.212544
24	0.858110	0.000000	0.271375	-0.655158	0.252353	-0.609233
25	0.693252	0.693252	0.382683	-0.923880	0.382683	-0.923880

26	0.000000	0.980406	0	-0.255899	0	-0.230056
27	-0.693252	0.693252	0	-0.709138	0	-0.659429
28	-0.980406	0.000000	0	-1	0	-1
29	-0.693252	-0.693252	-0.097928	-0.236420	-0.088039	-0.212544
30	0.000000	-0.980406	-0.271375	-0.655158	-0.252353	-0.609233
31	0.693252	-0.693252	-0.382683	-0.923880	-0.382683	-0.923880
32	0.980406	0.000000	-0.180948	-0.180948	-0.162674	-0.162674
33	0.707439	0.293031	-0.501436	-0.501436	-0.466287	-0.466287
34	0.293031	0.707439	-0.707107	-0.707107	-0.707107	-0.707107
35	-0.293031	0.707439	-0.236420	-0.097928	-0.212544	-0.088039
36	-0.707439	0.293031	-0.655158	-0.271375	-0.609233	-0.252353
37	-0.707439	-0.293031	-0.923880	-0.382683	-0.923880	-0.382683
38	-0.293031	-0.707439	-0.255899	0	-0.230056	0
39	0.293031	-0.707439	-0.709138	0	-0.659429	0
40	0.707439	-0.293031	-1	0	-1	0
41	0.883097	0.365791	-0.236420	0.097928	-0.212544	0.088039
42	0.365791	0.883097	-0.655158	0.271375	-0.609233	0.252353
43	-0.365791	0.883097	-0.923880	0.382683	-0.923880	0.382683
44	-0.883097	0.365791	-0.180948	0.180948	-0.162674	0.162674
45	-0.883097	-0.365791	-0.501436	0.501436	-0.466287	0.466287
46	-0.365791	-0.883097	-0.707107	0.707107	-0.707107	0.707107
47	0.365791	-0.883097	-0.097928	0.236420	-0.088039	0.212544
48	0.883097	-0.365791	-0.271375	0.655158	-0.252353	0.609233
49	0	0	-0.382683	0.923880	-0.382683	0.923880

Table A.1. Coordinates of the 49 samples of the Albrecht, Jacobi and Legendre patterns.

REFERENCES AND BIBLIOGRAPHY

ABRAHAM, L. (2005) Amplitude of accommodation and its relation to refractive errors. Indian Journal of Ophthalmology. *Indian journal of ophthalmology,* 53**,** 105-108.

ANSI (2000) *American National Standard for the safe use of lasers, ANSI 136.1-2000,* Orlando, FL, The Laser Institute of America.

ANERA, R., JIMENEZ, J., JIMENEZ DEL BARCO, L. & HITA, E. (2003) Changes in corneal asphericity after laser refractive surgery, including reflection losses and nonnormal incidence upon the anterior cornea. *Optics Letters,* 28**,** 417-419.

APPLEGATE, R. A., HOWLAND, H. C., SHARP, R. P., COTTINGHAM, A. J. & YEE, R. W. (1998) Corneal aberrations and visual performance after radial keratotomy. *Journal of Refractive Surgery*, 14, 397-407.

APPLEGATE, R., HILMANTE, L. G., HOWLAND, H., TU, E., STARCK, T. & ZAYAC, E. (2000) Corneal first surface optical aberrations and visual performance. *Journal of Refractive Surgery,* 16**,** 507-514.

APPLEGATE, R. A., DONNELLY, W. J., MARSACK, J. D., KOENIG, D. E. & PESUDOVS, K. (2007) Three-dimensional relationship between high-order root-mean-square wavefront error, pupil diameter, and aging. *Journal of the Optical Society of America A,* 24**,** 578-587.

APPLEGATE, R. A., HILMANTEL, G. & HOWLAND, H. C. (1996) Corneal aberrations increase with the magnitude of radial keratotomy refractive correction. *Optometry and Vision Science,* 73**,** 585-9.

APPLEGATE, R. A., SARVER, E. J. & KHEMSARA, V. (2002) Are all aberrations equal? *Journal of Refractive Surgery,* 18**,** S556-S562.

ARBA-MOSQUERA, S. & DE ORTUETA, D. (2008) Geometrical analysis of the loss of ablation efficiency at non-normal incidence. *Optics Express,* 16**,** 3877-3895.

ARTAL, P., BENITO, A. & TABERNERO, J. (2006) The human eye is an example of robust optical design. *Journal of Vision,* 6**,** 1-7.

ARTAL, P., BERRIO, E., GUIRAO, A. & PIERS, P. (2002) Contribution of the cornea and internal surfaces to the change of ocular aberrations with age. *Journal of the Optical Society of America A,* 19**,** 137-143.

ARTAL, P. & GUIRAO, A. (1998) Contributions of the cornea and the lens to the aberrations of the human eye. *Optics Letters,* 23**,** 1713-1715.

ARTAL, P., GUIRAO, A., BERRIO, E. & WILLIAMS, D. R. (2001) Compensation of corneal aberrations by the internal optics in the human eye. *Journal of Vision.,* 1**,** 1-8. http://journalofvision.org/1/1/1, DOI 10.1167/1.1.1.

ARTAL, P., MARCOS, S., NAVARRO, R. & WILLIAMS, D. R. (1995) Odd aberrations and double-pass measurements of retinal image quality. *Journal of the Optical Society of America A.,* 12**,** 195-201.

ATCHISON, D., COLLINS, M., WILDSOET, C., CHRISTENSEN, J. & WATERWORTH, M. (1995) Measurement of monochromatic ocular aberrations of human eyes as a function of accommodation by the Howland aberroscope technique. *Vision Research,* 35**,** 313-323.

ATCHISON, D. A., JONES, C. E., SCHMID, K. L., PRITCHARD, N., POPE, J. M., STRUGNELL, W. E. & RILEY, R. A. (2004) Eye shape in emmetropia and myopia. *Investigative Ophthalmology & Visual Science,* 45**,** 3380-3386.

ATCHISON, D. A., MARKWELL, E. L., KASTHURIRANGAN, S., POPE, J. M., SMITH, G. & SWANN, P. G. (2008) Age-related changes in optical and biometric characteristics of emmetropic eyes. *Journal of Vision*, 8, 1-20.

ATCHISON, D. A. & SMITH, G. (2000) *Optics of the Human Eye,* Oxford, Butterworth-Heinemann.

ATCHISON, D. A. & SMITH, G. (2005) Chromatic dispersions of the ocular media of human eyes. *Journal of the Optical Society of America A,* 22**,** 29-37.

BAEK, T., LEE, K., KAGAYA, F., TOMIDOKORO, A., AMANO, S. & OSHIKA, T. (2001) Factors affecting the forward shift of posterior corneal surface after laser in situ keratomileusis. *Ophthalmology,* 108**,** 317-320.

BARÁ, S., RÍOS, S. & ACOSTA, E. (1996) Integral evaluation of the modal phase coefficients in curvature sensing: Albrecht's cubatures. *Journal of the Optical Society of America A,* 13**,** 1467-1474.

BARBERO, S. (2004) Optical quality of the cornea and the cristalline lens: Implementation of objective techniques and clinical applications. PhD Thesis, Valladolid, University of Valladolid.

BARBERO, S. (2006) Refractive power of a multilayer rotationally symmetric model of the human cornea and tear film. *Journal of the Optical Society of America A,* 23**,** 1578-1585.

BARBERO, S., MARCOS, S., MARTÍN, R., LLORENTE, L., MORENO-BARRIUSO, E. & MERAYO-LLOVES, J. M. (2001) Validating the calculation of corneal aberrations from corneal topography: a test on keratoconus and aphakic eyes. *Investigative Opthalmology and Visual Science,* 42 (Suppl.)**,** 894.

BARBERO, S., MARCOS, S. & MERAYO-LLOVES, J. (2002a) Corneal and total optical in a unilateral aphakic aberrations patient. *Journal of Cataract and Refractive Surgery,* 28**,** 1594-1600.

BARBERO, S., MARCOS, S., MERAYO-LLOVES, J. & MORENO-BARRIUSO, E. (2002b) Validation of the estimation of corneal aberrations from videokeratography in keratoconus. *Journal of Refractive Surgery,* 18**,** 263-270.

BARBERO, S., MARCOS, S., & JIMENEZ-ALFARO, I (2003) Optical aberrations of intraocular lenses measured in vivo and in vitro. *Journal of the Optical Society of America A.,* 20**,** 1841-1851.

BARRAQUER, J. I. (1964) Keratomileusis for the correction of myopia. *Archivos de la Sociedad Americana de Oftalmología y Optometría,* 5**,** 27–48.

BARRAQUER, J. I. (1967) Keratomileusis. *International Surgery,* 48**,** 103-17.

BARTMANN, M. & SCHAEFFEL, F. (1994) A simple mechanism for emmetropization without cues from accommodation or colour. *Vision Research,* 34**,** 873-876.

BEDGGOOD, P., DAABOUL, M., ASHMAN, R., SMITH, G. & METHA, A. (2008) Characteristics of the human isoplanatic patch and implications for adaptive optics retinal imaging. *Journal of Biomedical Optics,* 13**,** 024008.

BENNETT, E. (2008) Contact lens correction of presbyopia. *Clinical & experimental optometry,* 91**,** 265-278.

BERRET, R., KEMMNER, D., OLTRUP, T., BENDE, T. & JEAN, B. (2003) Influence of the reflection on the ablation rate during excimer laser ablation and its compensation. *Annual Meeting of the Association-for-Research-in-Vision-and-Ophthalmology.* Ft Lauderdale, Florida, Assoc Research Vision Ophthalmology Inc.

BETTELHEIM, F. A. (1975) On the optical anisotropy of lens fiber cells. *Experimental Eye Research,* 21**,** 231-234.

BIEDERMANN, K. (2002) The Eye, Hartmann, Shack, and Scheiner. IN CAULFIELD, H. J. (Ed.) *Optical Information Processing: A Tribute to Adolf Lohmann.* Bellingham, Washington, USA., SPIE PRESS.

BORN, M. & WOLF, E. (1993) *Principles of Optics,* Oxford, U.K., Pergamon Press.

BOUR, L. J. (1991) Polarised Light and the Eye. IN CHARMAN, W. N. (Ed.) *Visual Optics and Instrumentation.* CRC Press.

BRINKMANN, R., RADT, B., FLAMM, C., KAMPMEIER, J., KOOP, N. & BIRNGRUBER, R. (2000) Influence of temperature and time on thermally induced forces in corneal collagen and the effect on laser thermokeratoplasty. *Journal of Cataract & Refractive Surgery,* 26**,** 744-754.

BROWN, N. (1972) Advanced slit-image camera. *British journal of ophthalmology,* 56**,** 624-631.

BRUNO, C. R., ROBERTS, C. J., CASTELLANO, D., MAHMOUD, A. & BIRNBAUM, L. (2001) Posterior Corneal Surface Changes After Laser In Situ Keratomileusis. *Investigative Ophthalmology and Visual Science (Suppl),* 42. Abstract nr. 3252.

BUDAK, K., KHATER, T., FRIEDMAN, N., HOLLADAY, J. & KOCH, D. (1999) Evaluation of relationships among refractive and topographic parameters. *Journal of Cataract and Refractive Surgery,* 25**,** 814-820.

BUENO, J. M. (1999) Estudio de las propiedades de polarización del ojo humano. PhD Thesis, Murcia, Universidad de Murcia.

BUENO, J. M. & ARTAL, P. (1999) Double-pass imaging polarimetry in the human eye. *Optics Letters,* 24**,** 64-66.

BUENO, J. M., BERRIO, E. & ARTAL, P. (2006) Corneal polarimetry after LASIK refractive surgery. *Journal of Biomedical Optics,* 11,014001 .

BUENO, J. M. & CAMPBELL, M. C. W. (2001) Polarization properties for in vivo human lenses. *Investigative Ophthalmology and Vision Science (Suppl),* 42**,** S161.

BUENO, J. M. & JARONSKI, J. (2001) Spatially resolved polarization properties for in vitro corneas. *Ophthalmic and Physiological Optics,* 21**,** 384-392.

BULLIMORE, M. A., GILMARTIN, B. & ROYSTON, J. M. (1992) Steady-State Accommodation and Ocular Biometry in Late-Onset Myopia. *Documenta Ophthalmologica,* 80**,** 143-155.

BURNS, S. A., HE, J. C. & DELORI, F. C. (1997) Do the cones see light scattered from the deep retinal layers. *Vision Science and its Applications.* Washington, D.C., OSA Technical Digest Series (Optical Society of America).

BURNS, S. A. & MARCOS, S. (2001) Measurement of the image quality of the eye with the spatially resolved refractometer. IN MACRAE, S., KRUEGER, R. & APPLEGATE, R. (Eds.) *Customized Corneal Ablations.* Thorofare, NJ, Slack Publishing.

BURNS, S. A., MARCOS, S., ELSNER, A. E. & BARÁ, S. (2002) Contrast improvement for confocal retinal imaging using phase correcting plates. *Optics Letters,* 27**,** 400-402.

BURNS, S. A., MCLELLAN, J. S. & MARCOS, S. (2003) Sampling effects on measurements of wavefront aberrations of the eye. *Investigative Ophthalmology & Visual Science,* 44**,** U463-U463.

BURNS, S. A., WU, S., DELORI, F. & ELSNER, A. E. (1995) Direct measurement of human-cone-photoreceptor alignment. *Journal of the Optical Society of America A,* 12**,** 2329-2338.

CALVER, R., COX, M. & ELLIOTT, D. (1999) Effect of aging on the monochromatic aberrations of the human eye. *Journal of the Optical Society of America A,* 16**,** 2069-2078.

CAMPBELL, C. E. (2005) A test eye for wavefront eye refractors. *Journal of Refractive Surgery,* 21**,** 127-140.

CAMPBELL, M. W., HAMAN, H., SIMONET, P. & BRUNETTE, I. (1999) Dependence of optical image quality on refractive error: eyes after excimer laser photorefractive keratectomy (PRK) versus controls. *Investigative Ophthalmology and Visual Science,* 40 (Suppl.)**,** 7.

CARKEET, A., LUO, H., TONG, L., SAW, S. & TAN, D. (2002) Refractive error and monochromatic aberrations in Singaporean children. *Vision Research.,* 42**,** 1809-24.

CARNEY, L., MAINSTONE, J. & HENDERSON, B. (1997) Corneal topography and myopia. A cross-sectional study. *Investigative Ophthalmology & Visual Science,* 38(2)**,** 311-20.

CASTEJON-MOCHON, F. J., LOPEZ-GIL, N., BENITO, A. & ARTAL, P. (2002) Ocular wave-front aberration statistics in a normal young population. *Vision Research,* 42**,** 1611-1617.

CHAKRABARTI, H. S., CRAIG, J. P., BRAHMA, A., MALIK, T. Y. & MCGHEE, C. N. J. (2001) Comparison of corneal thickness measurements using ultrasound and Orbscan slit-scanning topography in normal and post-LASIK eyes. *Journal of Cataract and Refractive Surgery,* 27**,** 1823-1828.

CHARMAN, W. (1991a) Wave-front aberration of the eye - A review. *Optometry and Vision Science,* 68**,** 574-583.

CHARMAN, W. N. (1976) Some sources of discrepancy between static retinoscopy and subjective refraction. *British Journal of Physiological Optics,* 30**,** 108-118.

CHARMAN, W. N. (1991b) Optics of the Human Eye. IN CHARMAN, W. N. (Ed.) *Visual Optics and Instrumentation.* CRC Press.

CHARMAN, W. N. (2005) Aberrations and myopia. *Ophthalmic and Physiological Optics,* 25**,** 285-301.

CHARMAN, W. N. & JENNINGS, J. A. M. (1976) Objective measurements of the longitudinal chromatic aberration of the human eye. *Vision Research,* 16**,** 999-1005.

CHEN, C., IZADSHENAS, A., RANA, M. & AZAR, D. (2002) Corneal asphericity after hyperopic laser in situ keratomileusis. *Journal of Cataract and Refractive Surgery,* 28**,** 1539-1545.

CHENG, H., BARNETT, J. K., VILUPURU, A. S., MARSACK, J. D., KASTHURIRANGAN, S., APPLEGATE, R. A. & ROORDA, A. (2004) A population study on changes in wave aberrations with accommodation. *Journal of Vision,* 4**,** 272-280.

CHENG, H., SINGH, O., KWONG, K., XIONG, J., WOODS, B. & BRADY, T. (1992) Shape of the myopic eye as seen with High-Resolution Magnetic Resonance Imaging. *Optometry and Vision Science,* 69**,** 698-70.

CHENG, X., BRADLEY, A., HONG, X. & THIBOS, L. (2003) Relationship between refractive error and monochromatic aberrations of the eye. *Optometry and Vision Science,* 80**,** 43-49.

CHISHOLM, C. M., ANDERSON, D. F., KVANSAKUL, J., KHAN, A., GARTRY, D. S. & BARBUR, J. L. (2004) Prospective, randomised, double-masked study of conventional versus wavefront-guided LASIK: Visual performance outcomes. *Investigative Ophthalmology and Visual Science,* 45**,** E-Abstract 1101.

CIOLINO, J. B. & BELIN, M. W. (2006) Changes in the posterior cornea after laser in situ keratomileusis and photorefractive keratectomy. *Journal of Cataract & Refractive Surgery,* 32**,** 1426-1431.

CIOLINO, J. B., KHACHIKIAN, S. S., CORTESE, M. J. & BELIN, M. W. (2007) Long-term stability of the posterior cornea after laser in situ keratomileusis. *Journal of Cataract & Refractive Surgery,* 33**,** 1366-1370.

COLLINS, M. J., WILDSOET, C. F. & ATCHISON, D. A. (1995) Monochromatic Aberrations and Myopia. *Vision Research,* 35**,** 1157-1163.

COPE, W. T., WOLBARSHT, M. L. & YAMANASHI, B. S. (1978) The corneal polarization cross. *Journal of the Optical Society of America A,* 68**,** 1139-1141.

CORBETT, M. C., OBRART, D. P. S. & MARSHALL, J. (1995) Do topical corticosteroids have a role following excimer laser photorefractive keratectomy?. *Journal of Refractive Surgery,* 11**,** 380-387.

CUBALCHINI, R. (1979) Modal wave-front estimation from phase derivate measurements. *Journal of the Optical Society of America,* 69**,** 972-977.

DARWIN, C. (1859) *On the Origin of the Species by means of natural selection.*

DAUSCH, D., SCHRODER, E. & DAUSCH, S. (2000) Topography-controlled excimer laser photorefractive keratectomy. *Journal of Refractive Surgery,* 16**,** 13-22.

DAVIES, N., DIAZ-SANTANA, L. & LARA-SAUCEDO, D. (2003) Repeatability of ocular wavefront measurement. *Optometry and Vision Science,* 80**,** 142-150.

DE LA CERA, E. G., RODRIGUEZ, G. & MARCOS, S. (2006) Longitudinal changes of optical aberrations in normal and form-deprived myopic chick eyes. *Vision Research,* 46**,** 579-589.

DE VALOIS, R. L. & DE VALOIS, K. K. (1988) *Spatial Vision,* (page 46), New York, Oxford University Press.

DELORI, F. & BURNS, S. (1996) Fundus reflectance and the measurement of crystalline lens density. *Journal of the Optical Society of America A.,* 13**,** 215-226.

DELORI, F., DOREY, C. K., STAURENGHI, G., AREND, O., GOGER, D. G. & WEITER, J. J. (1995) In vivo fluorescence of the ocular fundus exhibits retinal pigment epithelium lipofuscin characteristics. *Investigative Ophthalmology and Visual Science,* 36**,** 718-729.

DELORI, F. C. & PFIBSEN, K. P. (1989) Spectral reflectance of the human ocular fundus. *Applied Optics,* 28**,** 1061-1077.

DELORI, F. C., WEBB, R. H. & SLINEY, D. H. (2007) Maximum permissible exposures for ocular safety (ANSI 2000), with emphasis on ophthalmic devices. Journal of the Optical Society of America A, 24, 1250-1265.

DIAZ-SANTANA HARO, L. (2000) Wavefront sensing in the human eye with a Shack-Hartmann sensor. PhD Thesis, London, U.K., Imperial College of Science Technology and Medicine.

DIAZ-SANTANA, H. L. & DAINTY , J. C. (1999) Single-pass measurements of the wave-front aberrations of the human eye by use of retinal lipofuscin autofluorescence. *Optics Letters,* 24**,** 61-63.

DIAZ-SANTANA, L., WALKER, G. & BARA, S. X. (2005) Sampling geometries for ocular aberrometry: A model for evaluation of performance. *Optics Express,* 13**,** 8801-8818.

DIERICK, H. & MISSOTTEN, L. (1996) Corneal ablation profiles for correction of hyperopia with the excimer laser. *Journal of Refractive Surgery,* 12**,** 767-73.

DORRONSORO, C., BARBERO, S., LLORENTE, L. & MARCOS, S. (2003a) On-eye measurement of optical performance of Rigid Gas Permeable contact lenses based on ocular and corneal aberrometry. *Optometry and Vision Science.,* 80**,** 115-125.

DORRONSORO, C., CANO, D., MERAYO-LLOVES, J. & MARCOS, S. (2006) Experiments on PMMA models to predict the impact of corneal refractive surgery on corneal shape. *Optics Express,* 14**,** 6142-6156.

DORRONSORO, C., GARCÍA DE LA CERA, E., LLORENTE, L., BARBERO, S. & MARCOS, S. (2003b) Implementación de dos aberrrómetros para aplicaciones biomédicas. *VII Reunión Nacional de Óptica.* Santander, Spain.

DUBBELMAN, M. & HEIJDE, V. (2001) The shape of the aging human lens: curvature, equivalent refractive index and the lens paradox. *Vision Research,* 41**,** 1867-1877.

DUBBELMAN, M., SICAM, V. & VAN DER HEIJDE, R. G. L. (2007) The contribution of the posterior surface to the coma aberration of the human cornea. *Journal of Vision,* 7,1-8.

DUBBELMAN, M., SICAM, V. & VAN DER HEIJDE, G. L. (2006) The shape of the anterior and posterior surface of the aging human cornea. *Vision Research,* 46**,** 993-1001.

DUPPS, J. W. J. & WILSON, S. E. (2006) Biomechanics and wound healing in the cornea. *Experimental Eye Research,* 83**,** 709-720.

EL HAGE, S. G. & BERNY, F. (1973) Contribution of the crystalline lens to the spherical aberration of the eye. *Journal of the Optical Society of America A,* 63**,** 205-211.

ELHAGE, S. G. & BERNY, F. (1973) CONTRIBUTION OF CRYSTALLINE LENS TO SPHERICAL ABERRATION OF EYE. *Journal of the Optical Society of America,* 63**,** 205-211.

ELSNER, A. E., BURNS, S. A., HUGHES, G. W. & WEBB, R. H. (1992) Reflectometry with a scanning laser ophthalmoscope. *Applied Optics,* 31**,** 3697-3710.

ELSNER, A. E., BURNS, S. A., WEITER, J. J. & DELORI, F. C. (1996) Infrared imaging of sub-retinal structures in the human ocular fundus. *Vision Research,* 36**,** 191-205.

ENOCH, J. M. & LAKSHMINARAYANAN, V. (1991) Retinal Fibre Optics. IN CHARMAN, W. N. (Ed.) *Visual Optics and Instrumentation.* 1 ed. London, UK, CRC Press.

FAN-PAUL, N. I., LI, J., MILLER, J. S. & FLORAKIS, G. J. (2002) Night Vision Disturbances After Corneal Refractive Surgery. *Survey of Ophthalmology,* 47**,** 533-546.

FARAH, S., AZAR, D., GURDAL, C. & WONG, J. (1998) Laser in situ keratomileusis: literature review of a developing technique. *Journal of Cataract and Refractive Surgery,* 24**,** 989-1006.

FARRELL, R. A., WHARAM, J. F., KIM, D. & MCCALLY, R. L. (1999) Polarized light propagation in corneal lamellae. *Journal of Refractive Surgery,* 15**,** 700-705.

FERNANDEZ, E. J. & ARTAL, P. (2008) Ocular aberrations up to the infrared range: from 632.8 to 1070 nm. *Optics Express,* 16**,** 21199-21208.

FERNANDEZ, E. J., IGLESIAS, I. & ARTAL , P. (2001) Closed-loop adaptive optics in the human eye. *Optics Letters,* 26**,** 746-748.

FERNANDEZ, E. J., UNTERHUBER, A., PRIETO, P. M., HERMANN, B., DREXLER, W. & ARTAL, P. (2005) Ocular aberrations as a function of wavelength in the near infrared measured with a femtosecond laser. *Optics Express,* 13**,** 400-409.

FISCHER, R. E., TADIC-GALEB, B. & YODER, P. R. (2007) The concept of Optical Path Difference. Optical System Design. 2nd ed. New York, McGraw Hill (page 53).

FRIED, D. L. (1977) Least-Square Fitting a Wavefront Distortion Estimate to an Array of Phase-Difference Measurements. *Journal of the Optical Society of America,* 67**,** 370-375.

FYODOROV, S. N. & DURNEV, V. V. (1979) OPERATION OF DOSAGED DISSECTION OF CORNEAL CIRCULAR LIGAMENT IN CASES OF MYOPIA OF MILD DEGREE. *Annals of Ophthalmology,* 11**,** 1885-1889.

GARCÍA DE LA CERA, E. (2008) Optical Quality and Role of the Ocular Aberrations in animal models of myopia., PhD Thesis, Vallaolid, Universidad de Valladolid.

GARNER, L., YAP, M. & SCOTT, R. (1992) Crystalline lens power in myopia. *Optometry and Vision Science.,* 69**,** 863-865.

GATINEL, D., HOANG-XUAN, T. & AZAR, D. (2001) Determination of corneal asphericity after myopia surgery with the excimer laser: a mathematical model. *Investigative Ophthalmology & Visual Science,* 42**,** 1736-1742.

GEE, S. & TABBARA, K. (1988) Increase of ocular axial length in patients with corneal opacification. *Ophthalmology,* 1988**,** 1276-1278.

GILMARTIN, B. (2004) Myopia: precedents for research in the twenty-first century. *Clinical and Experimental Ophthalmology,* 32**,** 305-324.

GLASSER, A. & CAMPBELL, M. (1998) Presbyopia and the optical changes in the human crystalline lens with age. *Vision Research,* 38**,** 209-229.

GLICKSTEIN, M. & MILLODOT, M. (1970) Retinoscopy and eye size. *Science,* 168**,** 605-606.

GORRAND, J. M. (1979) Diffusion of the human retina and quality of the optics of the eye on the fovea and the peripheral retina. *Vision Research,* 19**,** 907-912.

GORRAND, J. M., ALFIERI, R. & BOIRE, J. Y. (1984) Diffusion of the retinal layers of the living human eye. *Vision Research,* 24**,** 1097-1106.

GOSS, D. A., VANVEEN, H. G., RAINEY, B. B. & FENG, B. (1997) Ocular components measured by keratometry, phakometry, and ultrasonography in emmetropic and myopic optometry students. *Optometry and Vision Science,* 74**,** 489-495.

GOTZINGER, E., PIRCHER, M., STICKER, M., FERCHER, A. F. & HITZENBERGER, C. K. (2004) Measurement and imaging of birefringent properties of the human cornea with phase-resolved, polarization-sensitive optical coherence tomography. *Journal of Biomedical Optics,* 9**,** 94-102.

GROSVENOR, T. & GOSS, D.A. (1998) Role of the cornea in emmetropia and myopia. *Optometry and Vision Science,* 75**,** 132-45.

GROSVENOR, T. & GOSS, D. A. (1999) *Clinical Management of Myopia*, Butterworth-Heinemann.

GROSVENOR, T. & SCOTT, R. (1991) Comparison of refractive components in youth-onset and early adult-onset myopia. *Optometry and Vision Science.,* 68**,** 204-209.

GROSVENOR, T. & SCOTT, R. (1994) Role of the axial length/corneal radius ratio in determining the refractive state of the eye. *Optometry and Vision Science,* 71**,** 573-9.

GUIRAO, A. & ARTAL, P. (2000) Corneal wave aberration from videokeratography: accuracy and limitations of the procedure. *Journal of the Optical Society of America A,* 17**,** 955-965.

GUIRAO, A., REDONDO, M. & ARTAL, P. (2000) Optical aberrations of the human cornea as a function of age. *Journal of the Optical Society of America A,* 17**,** 1697-1702.

GUIRAO, A., REDONDO, M., GERAGHTY, E., PIERS, P., NORRBY, S. & ARTAL, P. (2002) Corneal optical aberrations and retinal image quality in patients in whom monofocal intraocular lenses were implanted. *Archives of Ophthalmology,* 120**,** 1143-1151.

GUPTA, P. D., K., J. & A., V. (2004) Causative and preventive action of calcium in cataractogenesis. *Acta Pharmacologica Sinica,* 25**,** 1250-1256.

HARTMANN, J. (1900) Bemerkungen Uber den Bau und die Justirung von Spektrographen. *Zeitschrift fuer instrumentenkunde,* 20**,** 47-58.

HE, J. C., BURNS, S. A. & MARCOS, S. (2000) Monochromatic aberrations in the accommodated human eye. *Vision Research,* 40**,** 41-48.

HE, J. C., GWIAZDA, J., THORN, F. & HELD, R. (2003) Wave-front aberrations in the anterior corneal surface and the whole eye. *Journal of the Optical Society of America A,* 20**,** 1155-1163.

HE, J. C., MARCOS, S., WEBB, R. H. & BURNS, S. A. (1998) Measurement of the wave-front aberration of the eye by a fast psychophysical procedure. *Journal of the Optical Society of America A,* 15**,** 2449-2456.

HE, J. C., SUN, P., HELD, R., THORN, F., SUN, X. R. & GWIAZDA, J. E. (2002) Wavefront aberrations in eyes of emmetropic and moderately myopic school children and young adults. *Vision Research,* 42**,** 1063-1070.

HELMHOLTZ, H. V. (1885) *Popular lectures on scientific subjects,* New York, Appleton.

HERRMANN, J. (1981) Cross Coupling and Aliasing in Modal Wave-Front Estimation. *Journal of the Optical Society of America,* 71**,** 989-992.

HERSH, P. S., FRY, K. & BLAKER, J. W. (2003) Spherical aberration after laser in situ keratomileusis and photorefractive keratectomy, : Clinical results and theoretical models of etiology. *Journal of Cataract & Refractive Surgery,* 29**,** 2096-2104.

HOCHEIMER, B. F. & KUES, H. A. (1982) Retinal polarization effects. *Applied Optics,* 21**,** 3811-3818.

HOFER, H., ARTAL, P., SINGER, B., ARAGON, J. & WILLIAMS, D. (2001a) Dynamics of the eye´s wave aberration. *Journal Optical Society of America A,* 18**,** 497-506.

HOFER, H., CHEN, L., YOON, G., SINGER, B., YAMAUCHI, Y. & WILLIAMS, D. (2001b) Improvement in retinal image quality with dynamic correction of the eye's aberrations. *Opics. Express.,* 8**,** 631-643.

HOLLADAY, J., DUDEJA, D. & CHANG, J. (1999a) Functional vision and corneal changes after laser in situ keratomileusis determined by contrast sensitivity, glare, testing, and corneal topography. *Journal of Cataract and Refractive Surgery,* 25**,** 663-669.

HOLLADAY, J. & JANES, J. A. (2002) Topographic changes in corneal asphericity and effective optical zone after laser in situ keratomileusis. *Journal of Cataract and Refractive Surgery,* 28**,** 942-947.

HOLLADAY, J. T., DUDEJA, D. R. & CHANG, J. (1999b) Functional vision and corneal changes after laser in situ keratomileusis determined by contrast sensitivity, glare testing and corneal topography. *Journal of Cataract and Refractive Surgery,* 25**,** 663-669.

HONG, X., HIMEBAUGH, N. & THIBOS, L. (2001) On-eye evaluation of optical performance of rigid and soft contact lenses. *Optometry and Vision Science,* 78**,** 872-80.

HORNER, D. G., SONI, P. S., VYAS, N. & HIMEBAUGH, N. L. (2000) Longitudinal changes in corneal asphericity in myopia. *Optometry and Vision Science,* 77**,** 198-203.

HOWARTH, P. A., ZHANG, X. X., BRADLEY, A., STILL, D. L. & THIBOS, L. N. (1988) Does the chromatic aberration of the eye vary with age? *Journal of the Optical Society of America A,* 5**,** 2087-2092.

HOWLAND, B. (1968) Use of Crossed Cylinder Lens in Photographic Lens Evaluation. *Applied Optics,* 7**,** 1587-1599.

HOWLAND, B. & HOWLAND, H. C. (1976) Subjective Measurement of High-Order Aberrations of the Eye. *Science,* 193**,** 580-582.

HOWLAND, H. C. (1991) Determination of Ocular Refraction. IN CHARMAN, W. N. (Ed.) *Visual Optics and Instrumentation.* CRC Press.

HOWLAND, H. C. (2000) The history and methods of ophthalmic wavefront sensing. *Journal of Refractive Surgery,* 16**,** S552-S553.

HOWLAND, H. C. (2002) High order wave aberration of eyes. *Ophthalmic and Physiological Optics,* 22**,** 434-439.

HOWLAND, H. C. & HOWLAND, B. (1977) A subjective method for the measurement of the monochromatic aberrations of the eye. *Journal of the Optical Society of America A,* 67**,** 1508-1518.

IP, J. M., ROSE, K. A., MORGAN, I. G., BURLUTSKY, G. & MITCHELL, P. (2008) Myopia and the urban environment: Findings in a sample of 12-year-old Australian school children. *Investigative Ophthalmology & Visual Science,* 49**,** 3858-3863.

ISKANDER, N. G., PENNO, E. A., PETERS, N. T., GIMBEL, H. V. & FERENSOWICZ, M. (1999) Accuracy of Orbscan pachymetry measurements and DHG ultrasound pachymetry in primary laser in situ keratomileusis and LASIK enhancement procedures. *Annual Meeting of the United-Kingdom-and-Ireland-Society-of-Cataract-and-Refractive-Surgeons.* Chester, England, Elsevier Science Inc.

IVANOFF, A. (1953) *Les aberrations de l'oeil. Leur role dans l'accommodation,* Paris, Éditions de la Revue d'Optique Théorique et Instrumentale.

JARONSKI, J. W. & KASPRZAK, H. T. (2003) Linear birefringence measurements of the in vitro human cornea. *Ophthalmic and Physiological Optics,* 23**,** 361-369.

JENKINS, T. C. A. (1963) Aberrations of the eye and their effects on vision - Part II. *British Journal of Physiological Optics,* 20**,** 161-201.

JIMENEZ, J. (2004a) Corneal asphericity after refractive surgery when the Munnerlyn formula is applied. *Journal of the Optical Society of America,* 21**,** 98-103.

JIMENEZ, J. (2004b) Influence of laser polarization on ocular refractive parameters after refractive surgery. *Optics Letters,* 29**,** 962-964.

KELLY, J. E., MIHASHI, T. & HOWLAND, H. C. (2004) Compensation of corneal horizontal/vertical astigmatism, lateral coma, and spherical aberration by internal optics of the eye. *Journal of Vision,* 4**,** 262-271.

KIELY, P. M., SMITH, G. & CARNEY, L. G. (1982) The mean shape of the human corneal. *Optica Acta,* 29**,** 1027-1040.

KIM, A. & CHUCK, R. S. (2008) Wavefront-guided customized corneal ablation. *Current opinion in ophthalmology,* 19**,** 314-320.

KIM, T.I.., YANG, S.J., HAH, H (2004) Bilateral comparison of wavefront-guided versus conventional laser in situ keratomileusis with bausch and lomb zyoptix. *Journal of refractive surgery,* 20**,** 432-438.

KISILAK, M. L., CAMPBELL, M. C. W., IRVING, E. L. & HUNTER, J. J. (2002) Hartmann-Shack measurement of the monochromatic image quality in the chick eye during emmetropization. *Investigative Ophthalmology & Visual Science,* 43**,** U825-U825.

KNORZ, M. C., WIESINGER, B., LIERMANN, A., SEIBERTH, V. & LIESENHOFF, H. (1998) Laser in situ keratomileusis for moderate and high myopia and myopic astigmatism. *Ophthalmology,* 105**,** 932-940.

KOHNEN, T. (2006) Classification of excimer laser profiles. *Journal of Cataract & Refractive Surgery,* 32**,** 543-544.

KOHNEN, T., MAHMOUD, K. & BUHREN, J. (2004) Comparison of corneal higher-order aberrations induced by myopic and hyperopic LASIK. *108th Annual Meeting of the American-Academy-of-Ophthalmology.* New Orleans, LA, Elsevier Science Inc.

KOLLER, T., ISELI, H. P., HAFEZI, F., MROCHEN, M. & SEILER, T. (2006) Q-factor customized ablation profile for the correction of myopic astigmatism. *Journal of Cataract & Refractive Surgery,* 32**,** 584-589.

KOMAI, Y. & USHIKI, T. (1991) The three-dimensional organization of collagen fibrils in the human cornea and sclera. *Investigative Ophthalmology & and Visual Science,* 32**,** 2244-2258.

KORETZ, J., COOK, C. & KAUFMAN, P. (1997) Accommodation and presbyopia in the human eye. Changes in the anterior segment and crystalline lens with focus. *Investigative Ophthalmology & and Visual Science,* 38**,** 569-578.

KORETZ, J. & HANDELMAN, G. (1986) The lens paradox and image formation in accommodating human lenses. *Topics in Aging Research in Europe,* 6**,** 57-64.

KWON, Y., CHOI, M. & BOTT, S. (2008) Impact of ablation efficiency reduction on post-surgery corneal asphericity: simulation of the laser refractive surgery with a flying spot laser beam. *Optics Express,* 16**,** 11808-11821.

LAND, M. F. & NILSSON, D.-E. (2002) *Animal eyes,* Oxford, Oxford University Press.

LE GRAND, Y. & EL HAGE, S. G. (1980) *Physiological Optics (Vol. 1),* Berlin-Heidelberg, Springer Verlag.

LIANG, J. & WILLIAMS, D. R. (1997) Aberrations and retinal image quality of the normal human eye. *Journal of the Optical Society of America A,* 14**,** 2873-2883.

LIANG, J., WILLIAMS, D. R. & MILLER, D. T. (1997) Supernormal vision and high resolution retinal imaging through adaptive optics. *Journal of the Optical Society of America A,* 14**,** 2884-2892.

LIANG, J. Z., GRIMM, B., GOELZ, S. & BILLE, J. F. (1994) Objective Measurement of Wave Aberrations of the Human Eye with the Use of a

Hartmann-Shack Wave-Front Sensor. *Journal of the Optical Society of America A,* 11**,** 1949-1957.

LINDSTROM, R. L., HARDTEN, D. R., HOUTMAN, D. M., WITTE, B., PRESCHEL, N., CHU, Y. R., SAMUELSON, T. W. & LINEBARGER, E. J. (1999) Six-month results of hyperopic and astigmatic LASIK in eyes with primary and secondary hyperopia. *Transactions of the American Ophthalmoogical Society,* 97**,** 241-55; discussion 255-60.

LOMBARDO, M., LOMBARDO, G. & SERRAO, S. (2006) Interocular high-order corneal wavefront aberration symmetry. *Journal of the Optical Society of America A,* 23**,** 777-787.

LOPEZ-GIL, N. & HOWLAND, H. (1999) Measurement of the eye's near infrared wave-front aberration using the objective crossed- cylinder aberroscope technique. *Vision Research,* 39**,** 2031-2037.

LOPEZ-GIL, N. & ARTAL, P. (1997) Comparison of double-pass estimates of the retinal-image quality obtained with green and near-infrared light. *Journal of the Optical Society of America A,* 14**,** 961-971.

LLORENTE, L., BARBERO, S., CANO, D., DORRONSORO, C. & MARCOS, S. (2004a) Myopic versus hyperopic eyes: axial length, corneal shape and optical aberrations. *Journal of Vision,* 4**,** 288-298.

LLORENTE, L., BARBERO, B., MERAYO, J. & MARCOS, S. (2004) Changes in corneal and total aberrations induced by LASIK surgery for hyperopia. *Journal of Refractive Surgery,* 20**,** 203-216.

LLORENTE, L., DIAZ-SANTANA, L., LARA-SAUCEDO, D. & MARCOS, S. (2003) Aberrations of the human eye in visible and near infrared illumination. *Optometry and Vision Science,* 80**,** 26-35.

LLORENTE, L., DORRONSORO, C., BURNS, S. A. & MARCOS, S. (2004b) Influence of pupil sampling and density on ocular wave aberration measurements (Oral Communication). *II International topical meeting on Physiological Optics (European Optical Society).* Granada (Spain).

MA, L. X., ATCHISON, D. A., ALBIETZ, J. M., LENTON, L. M. & MCLENNAN, S. G. (2004) Wavefront aberrations following laser in situ keratomileusis and refractive lens exchange for hypermetropia. *Journal of Refractive Surgery,* 20**,** 307-316.

MACRAE, S. (1999) Excimer ablation design and elliptical transition zones. *Journal of Cataract & Refractive Surgery,* 25**,** 1191-1197.

MAEDA, N. (2009) Clinical applications of wavefront aberrometry – a review. *Clinical and Experimental Ophthalmology,* 37**,** 118-129.

MAINSTONE, J., CARNEY, L., ANDERSON, C., CLEM, P., STEPHENSEN, A. & WILSON, M. (1998) Corneal shape in hyperopia. *Clinical and Experimental Optometry,* 81**,** 131-137.

MALACARA, D. (1992) *Optical Shop Testing,* New York, John Wiley & Sons, Inc.

MANNS, F., HO, A., PAREL, J. & CULBERTSON, W. (2002) Ablation profiles for wavefront-guided correction of myopia and primary spherical aberration. *Journal of Cataract & Refractive Surgery,* 28**,** 766-774.

MANZANERA, S., CANOVAS, C., PRIETO, P. M. & ARTAL, P. (2008) A wavelength tunable wavefront sensor for the human eye. *Optics Express,* 16**,** 7748-7755.

MARCOS, S. (2001) Aberrations and Visual Performance following standard laser vision correction. *Journal of Refractive Surgery,* 17**,** 596-601.

MARCOS, S. (2002) Are changes in ocular aberrations with age a significant problem for refractive surgery? *Journal of Refractive Surgery,* 18**,** 572-578.

MARCOS, S., BARBERO, B., LLORENTE, L. & MERAYO-LLOVES, J. (2001) Optical response to LASIK for myopia from total and corneal aberrations. *Investigative Ophthalmology and Visual Science.,* 42**,** 3349-3356.

MARCOS, S., BARBERO, S. & LLORENTE, L. (2002a) The sources of optical aberrations in myopic eyes. *2002 Annual Meeting Abstract and Program Planner accessed at www.arvo.org. Association for Research in Vision and Ophthalmology. Abstract 1510.*

MARCOS, S., BARBERO, B., MCLELLAN, J. S. & BURNS, S. (2004) Optical quality of the aging eye. IN KRUEGER R.R., A. R. A., MCRAE S.M., (Ed.) *Wavefront Customized Visual Corrections: The Quest for Super Vision II.* Slack.

MARCOS, S., BARBERO, S., MORENO-BARRIUSO, E., LLORENTE, L., MERAYO-LLOVES, J. & MARTÍN, R. (2001) Total and corneal aberrations before and after standard LASIK refractive surgery. *Investigative Ophthalmology and Visual Science,* 42 (Suppl.)**,** 529.

MARCOS, S. & BURNS, S. A. (1999) Cone spacing and waveguide properties from cone directionality measurements. *Journal of the Optical Society of America A,* 16**,** 995-1004.

MARCOS, S. & BURNS, S. A. (2000) On the symmetry between eyes of wavefront aberration and cone directionality. *Vision Research,* 40**,** 2437-2447.

MARCOS, S., BURNS, S. A., MORENO-BARRIUSO, E. & NAVARRO, R. (1999) A new approach to the study of ocular chromatic aberrations. *Vision Research,* 39**,** 4309-4323.

MARCOS, S., CANO, D. & BARBERO, S. (2003) The increase of corneal asphericity after standard myopic LASIK surgery is not inherent to the Munnerlyn algorithm. *Journal of Refractive Surgery,* 19**,** 592-596.

MARCOS, S., DÍAZ-SANTANA, L., LLORENTE, L. & Dainty, C. (2002b) Ocular aberrations with ray tracing and Shack-Hartmann wavefront sensors: does polarization play a role? *Journal of the Optical Society of America A.,* 19**,** 1063-1072.

MARCOS, S., MORENO-BARRIUSO, E., NAVARRO, R. & LLORENTE, L. (2000) Retinal reflectivity in laser ray tracing measurements: What can we learn apart from ocular aberrations? *Technical Digest Optical Society of America Annual Meeting.*

MARCOS, S., ROSALES, P., LLORENTE, L., BARBERO, S. & JIMENEZ-ALFARO, I. (2008) Balance of corneal horizontal coma by internal optics in eyes with intraocular artificial lenses: Evidence of a passive mechanism. *Vision Research,* 48**,** 70-79.

MARSACK, J. D., PESUDOVS, K., SARVER, E. J. & APPLEGATE, R. A. (2006) Impact of Zernike-fit error on simulated high- and low-contrast acuity in keratoconus: implications for using Zernike-based corrections. *Journal of the Optical Society of America A,* 23**,** 769-776.

MARTIN, J. A. & ROORDA, A. (2003) Predicting and assessing visual performance with multizone bifocal contact lenses. *Optometry and Vision Science,* 80**,** 812-819.

MARTINEZ, C., APPLEGATE, R., KLYCE, S. & PEPE (1998) Effects of pupillary dilation on corneal optical aberrations after photorefractive keratectomy. *Archives of Ophthalmology,* 116**,** 1053-1062.

MATSUDA, J., HIEDA, O. & KINOSHITA, S. (2008) Comparison of central corneal thickness measurements by Orbscan II and Pentacam after corneal refractive surgery. *Japanese Journal of Ophthalmology,* 52**,** 245-249.

MCBRIEN, N. & ADAMS, D. (1997) A longitudinal investigation of adult-onset and adult-progression of myopia in an occupational group. Refractive and biometric findings. *Investigative Ophthalmology and Visual Science,* 38**,** 321-333.

MCDONALD, M. B., KAUFMAN, H. E., FRANTZ, J. M., SHOFNER, S., SALMERON, B. & KLYCE, S. D. (1989) Excimer laser ablation in a human eye. *Archives of Ophthalmology,* 107**,** 641-642.

MCLELLAN, J., MARCOS, S. & BURNS, S. (2001) Age-related changes in monochromatic wave aberrations in the human eye. *Investigative Ophthalmology and Visual Science***,** 42, 1390-1395.

MCLELLAN, J. S., PRIETO, P. M., MARCOS, S. & BURNS, S. A. (2006) Effects of interactions among wave aberrations on optical image quality. *Vision Research,* 46**,** 3009-3016.

MEEK, K. M. & NEWTON, R. H. (1999) Organization of collagen fibrils in the corneal stroma in relation to mechanical properties and surgical practice. *Journal of Refractive Surgery,* 15**,** 695-699.

MIERDEL, P., KRINKE, H. E., WIEGAND, W., KAEMMERER, M. & SEILER, T. (1997) Measuring device for determining monochromatic aberration of the human eye. *Ophthalmologe,* 94**,** 441-5.

MILLER, D. T., WILLIAMS, D. R., MORRIS, G. M. & LIANG, J. (1996) Images of the cone photoreceptors in the living human eye. *Vision Research,* 36**,** 1067-1079.

MILLODOT, M. (1976) The influence of age on the chromatic aberration of the eye. *Albrecht Von Graefes Arch Klin Exp Ophthalmol,* 198**,** 235-243.

MILLODOT, M. & O'LEARY, D. (1980) On the artifact of retinoscopy and chromatic aberration. *Am J Optom Physiol Opt.,* 57**,** 822-824.

MILLODOT, M. & SIVAK, J. (1979) Contribution of the cornea and lens to the spherical aberration of the eye. *Vision Research,* 19**,** 685-687.

MODIS, L., LANGENBUCHER, A. & SEITZ, B. (2001) Scanning-slit and specular microscopic pachymetry in comparison with ultrasonic determination of corneal thickness. *Cornea,* 20**,** 711-714.

MOLEBNY, V. V., PALLIKARIS, I. G., NAOUMIDIS, L. P., CHYZH, I. H., MOLEBNY, S. V. & SOKURENKO, V. M. (1997) Retina Ray-Tracing technique for eye-refraction mapping. *Proceedings of the SPIE,* 2971**,** 175-183.

MOLEBNY, V. V., PANAGOPOULOU, S. I., MOLEBNY, S. V., WAKIL, Y. S. & PALLIKARIS, I. G. (2000) Principles of Ray tracing aberrometry. *Journal of Refractive Surgery,* 16**,** S572-S575.

MONTES-MICO, R. & CHARMAN, W. N. (2002) Mesopic contrast sensitivity function after excimer laser photorefractive keratectomy. *Journal of Refractive Surgery,* 18**,** 9-13.

MORDI, J. & ADRIAN, W. (1985) Influence of age on chromatic aberration of the human eye. *American Journal of Optometry and Physiological Optics,* 62**,** 864-869.

MORENO-BARRIUSO, E. (2000) Laser Ray Tracing in the human eye: measurement and correction of the aberrations by means of phase plates. PhD Thesis. Santander, University of Cantabria.

MORENO-BARRIUSO, E., MARCOS, S., NAVARRO, R. & BURNS, S. A. (2001a) Comparing Laser Ray Tracing, Spatially Resolved Refractometer and Hartmann-Shack sensor to measure the ocular wavefront aberration. *Optometry and Vision Science,* 78**,** 152 - 156.

MORENO-BARRIUSO, E., MERAYO-LLOVES, J., MARCOS, S., NAVARRO, R., LLORENTE, L. & BARBERO, S. (2001b) Ocular aberrations before and after myopic corneal refractive surgery: LASIK-induced changes measured with Laser Ray Tracing. *Investigative Ophthalmology and Visual Science,* 42**,** 1396-1403.

MORENO-BARRIUSO, E. & NAVARRO, R. (2000) Laser Ray Tracing versus Hartmann-Shack Sensor for Measuring Optical Aberrations in the Human Eye. *Journal of the Optical Society of America A,* 17**,** 974-985.

MORRELL, A., WHITEFOOT, H. & CHARMAN, W. (1991) Ocular chromatic aberration and age. *Ophthalmic and Physiological Optics,* 11**,** 385-390.

MROCHEN, M. (2001) Improvement in photorefractive corneal laser surgery results using an active eye-tracking system. *Journal of Cataract and Refractive Surgery,* 27**,** 1000-1006.

MROCHEN, M. (2006) Ablation profiles in corneal laser surgery. *Der Ophthalmologe***,** 103, 175-183.

MROCHEN, M., DONITZKY, C., WÜLLNER, C. & LÖFFLER, J. (2004) Wavefront-optimized ablation profiles, : Theoretical background. *Journal of Cataract & Refractive Surgery,* 30**,** 775-785.

MROCHEN, M. & SEILER, T. (2001) Influence of corneal curvature on calculation of ablation patterns used in photorefractive laser surgery. *Journal of Refractive Surgery,* 17**,** S584-S587.

MUNNERLYN, C. R., KOONS, S. J. & MARSHALL, J. (1988) Photorefractive Keratectomy - a Technique for Laser Refractive Surgery. *Journal of Cataract and Refractive Surgery,* 14**,** 46-52.

MUTYALA, S., MCDONALD, M., SCHEINBLUM, K., OSTRICK, M., BRINT, S. & THOMPSON, H. (2000) Contrast sensitivity evaluation after laser in situ keratomileusis. *Ophthalmology,* 107**,** 1864-1867.

NAKAMURA, K., BISSEN-MIYAJIMA, H., TODA, I., HORI, Y. & TSUBOTA, K. (2001) Effect of laser in situ keratomileusis correction on contrast visual acuity. *Journal of Cataract and Refractive Surgery,* 27**,** 357-361.

NAROO, S. & CHARMAN, W. (2000) Changes in posterior corneal curvature after photorefractive keratectomy. *Journal of catarat and refractive surgery,* 26**,** 872-878.

NAVARRO, R. & LOSADA, M. A. (1995) Phase transfer and point-spread function of the human eye determined by a new asymmetric double-pass method. *Journal of the Optical Society of America A,* 12**,** 2385-2392.

NAVARRO, R. & LOSADA, M. A. (1997) Aberrations and relative efficiency of light pencils in the living human eye. *Optometry and Vision Science,* 74**,** 540-547.

NAVARRO, R. & MORENO-BARRIUSO, E. (1999) Laser ray-tracing method for optical testing. *Optics Letters,* 24**,** 1-3.

NAVARRO, R., MORENO-BARRIUSO, E., BARÁ, S. & MANCEBO, T. (2000) Phase-plates for wave-aberration compensation in the human eye. *Optics Letters,* 25**,** 236 - 238.

NAYLOR, E. J. & STANWORTH, A. (1954) Retinal pigment and the Haidinger effect. *Journal of Physiology,* 124**,** 543-552.

NEGISHI, K., OHNUMA, K., HIRAYAMA, N., NODA, T. & FOR THE POLICY-BASED MEDICAL SERVICES NETWORK STUDY GROUP FOR INTRAOCULAR LENS AND REFRACTIVE, S. (2001) Effect of Chromatic Aberration on Contrast Sensitivity in Pseudophakic Eyes. *Archives of Ophthalmology,* 119**,** 1154-1158.

NETTO, M. V., DUPPS, J. W. & WILSON, S. E. (2006) Wavefront-Guided Ablation: Evidence for Efficacy Compared to Traditional Ablation. *American Journal of Ophthalmology,* 141**,** 360-360.

NILSSON, D. E. & ARENDT, D. (2008) Eye Evolution: The Blurry Beginning. *Current Biology,* 18**,** R1096-R1098.

OLIVER, K., HEMENGER, R., CORBETT, M., O'BRART, D., VERMA, S., MARSHALL, J. & TOMLINSON, A. (1997) Corneal optical aberrations induced by photorefractive keratectomy. *Journal of Refractive Surgery,* 13**,** 246-254.

OLIVER, K., O'BRART, D., STEPHENSON, C., HEMENGER, R., APPLEGATE, R., TOMLINSON, A. & MARSHALL, J. (2001) Anterior corneal optical aberrations induced by photorefractive keratectomy for hyperopia. *Journal of Refractive Surgery,* 17**,** 406-413.

OSHIKA, T., KLYCE, S. D., APPLEGATE, R. A. & HOWLAND, H. C. (1999a) Changes in corneal wavefront aberrations with aging. *Investigative Ophthalmology and Visual Science,* 40**,** 1351-1355.

OSHIKA, T., KLYCE, S. D., APPLEGATE, R. A., HOWLAND, H. C. & EL DANASOURY, M. A. (1999b) Comparison of corneal wavefront aberrations after photorefractive keratectomy and laser in situ keratomileusis. *American Journal of Ophthalmology,* 127**,** 1-7.

PADMANABHAN, P., MROCHEN, M., BASUTHKAR, S., VISWANATHAN, D. & JOSEPH, R. (2008) Wavefront-guided versus wavefront-optimized laser in situ keratomileusis: Contralateral comparative study. *Journal of Cataract & Refractive Surgery,* 34**,** 389-397.

PALLIKARIS, I., PAPATZANAKI, M., STATHI, E., FRENSCHOCK, O. & GEORGIADIS, A. (1990) Laser in situ keratomileusis. *Lasers in Surgery and Medicine,* 10**,** 463-468.

PAQUIN, M. P., HAMAM, H. & SIMONET, P. (2002) Objective measurement of optical aberrations in myopic eyes. *Optometry and Vision Science,* 79**,** 285-291.

PHILIPSON, B. T., HANNINEN, L. & BALAZS, E. A. (1975) Cell contacts in human and bovine lenses. *Experimental Eye Research,* 21**,** 205-219.

PLAINIS, S., GINIS, H. S. & PALLIKARIS, A. (2005) The effect of ocular aberrations on steady-state errors of accommodative response. *Journal of Vision,* 5**,** 466-477.

PLAINIS, S. & PALLIKARIS, I. G. (2006) Ocular monochromatic aberration statistics in a large emmetropic population. *3rd European Meeting in Physiological Optics.* London, ENGLAND, Taylor & Francis Ltd.

PORTER, J., GUIRAO , A., COX , I. & WILLIAMS, D. (2001) Monochromatic aberrations of the human eye in a large population. *Journal of the Optical Society of America A,* 18**,** 1793-803.

PRIETO, P., VARGAS-MARTÍN, F., MCLELLAN, J. & BURNS, S. (2002) The effect of the polarization on ocular wave aberration measurements. *Journal of the Optical Society of America A., 18, 809-814.*

PRISANT, O., CALDERON, N., CHASTANG, P., GATINEL, D. & HOANG-XUAN, T. (2001) Reliability of pachymetric measurements using Orbscan after excimer refractive surgery. *105th Annual Meeting of the American-Academy-of-Ophthalmology.* New Orleans, Louisiana, Elsevier Science Inc.

QUISLING, S., SJOBERG, S., ZIMMERMAN, B., GOINS, K. & SUTPHIN, J. (2006) Comparison of Pentacam and Orbscan IIz on Posterior Curvature Topography Measurements in Keratoconus Eyes. *Ophthalmology,* 113**,** 1629-1632.

RABIN, J., VAN SLUYTERS, R. C. & MALACH, R. (1981) Emmetropization: a vision-dependent phenomenon. *Investigative Ophthalmology and Visual Science*, 561-564.

RADHAKRISHNAN, H. & CHARMAN, W. N. (2007) Refractive changes associated with oblique viewing and reading in myopes and emmetropes. *Journal of Vision,* 7, 1-15.

RASOOLY, R. & BENEZRA, D. (1988) Congenital and traumatic cataract- the effect on ocular axial length. *Archives of Ophthalmology.,* 106, 1066-1068.

RIMMER, M. P. (1974) Method for Evaluating Lateral Shearing Interferograms. *Applied Optics,* 13, 623-629.

RIOS, S., ACOSTA, E. & BARA, S. (1997) Hartmann sensing with Albrecht grids. *Optics Communications,* 133, 443-453.

ROBERTS, C. & DUPPS, W. (2001) Corneal biomechanics and their role in corneal ablative procedures. IN MCRAE, S., KRUEGER, R. & APPLEGATE, R. (Eds.) *Customized corneal ablation: The quest for super vision.* Stack publising.(pages 110-131)

ROORDA, A., ROMERO-BORJA, F., DONNELLY, I., W. J. , QUEENER, H., HEBERT, T. J. & CAMPBELL, M. C. W. (2002) Adaptive optics scanning laser ophthalmoscopy. *Opt. Express. http://www.opticsexpress.org/abstract.cfm?URI=OPEX-10-9-405,* 10, 405-412.

RYNDERS, M. C., NAVARRO, R. & LOSADA, M. A. (1998) Objective measurement of the off-axis longitudinal chromatic aberration in the human eye. *Vision Research,* 38, 513-522.

SAFIR, A., HYAMS, L. & PHILPOT, J. (1971) The retinal directional effect: A model based on the Gaussian distribution of cone orientations. *Vision Research,* 11, 819-831.

SAKIMOTO, T., ROSENBLATT, M. I. & AZAR, D. T. (2006) Laser eye surgery for refractive errors. *Lancet,* 367, 1432-1447.

SALMON, T. O. & DE POL, C. V. (2006) Normal-eye Zernike coefficients and root-mean-square wavefront errors. *Annual Meeting of the American-Academy-of-Optometry.* San Diego, CA, Elsevier Science Inc.

SANTAMARÍA, J., ARTAL, P. & BESCÓS, J. (1987) Determination of the point-spread function of human eyes using a hybrid optical-digital method. *Journal of the Optical Society of America A,* 4, 1109-1114.

SATO, T. (1942) Crosswise incisions of Descemet's membrane for the treatment of advanced keratoconus. *Acta Soc Ophthalmol (Jpn),* 46, 469-470.

SAW, S.-M. (2003) A synopsis of the prevalence rates and environmental risk factors for myopia. *Clinical and Experimental Optometry,* 86, 289-94.

SCHAEFFEL, F. & DIETHER, S. (1999) The growing eye: an autofocus system that works on very poor images. *Vision Research,* 39, 1585-1589.

SCHAEFFEL, F., SIMON, P., FELDKAEMPER, M., OHNGEMACH, S. & WILLIAMS, R. W. (2003) Molecular biology of myopia. *Clinical and Experimental Optometry,* 86**,** 295-307.

SCHALLHORN, S. C., FARJO, A. A., HUANG, D., BOXER WACHLER, B. S., TRATTLER, W. B., TANZER, D. J., MAJMUDAR, P. A. & SUGAR, A. (2008) Wavefront-Guided LASIK for the Correction of Primary Myopia and Astigmatism: A Report by the American Academy of Ophthalmology. *Ophthalmology,* 115**,** 1249-1261.

SCHEINER, C. (1619) *Oculus, sive fundamentum opticum,* Innspruk, Austria.

SCHMID, K. L. & WILDSOET, C. F. (1997) The sensitivity of the chick eye to refractive defocus. *Ophthalmic and Physiological Optics,* 17**,** 61-67.

SCHWIEGERLING, J. & GREIVENKAMP, J. E. (1997) Using corneal height maps and polynomial decomposition to determine corneal aberrations. *Optometry and Vision Science,* 74**,** 906-16.

SCHWIEGERLING, J. & SNYDER, R. W. (2000) Corneal ablation patters to correct for spherical aberration in photorefractive keratectomy. *Journal of Cataract and Refractive Surgery,* 26**,** 214-221.

SEIDEL, L. (1856) Zur Dioptrik. Uber die Entwicklung der Glieder 3ter Ordnung. *Astronomische Nachrichten,* 43**,** 289.

SEILER, T., KAEMMERER, M., MIERDEL, P. & KRINKE, H.-E. (2000) Ocular optical aberrations after photorefractive keratectomy for myopia and myopic astigmatism. *Archive of Ophthalmology,* 118**,** 17-21.

SEILER, T. & WOLLENSAK, J. (1986) In vivo exeriments with the excimer laser - technica parameters and healing processes. *Ophthalmologica,* 192**,** 65-70.

SEITZ, B., TORRES, F., LANGENBUCHER, A., BEHRENS, A. & SUAREZ, E. (2001) Posterior corneal curvature changes after myopic laser in situ keratomileusis. *Ophthalmology,* 108**,** 666-673.

SHACK, R. V. & PLATT, B. C. (1971) Production and Use of a Lenticular Hartmann Screen. *Journal of the Optical Society of America,* 61**,** 656.

SHERIDAN, M. & DOUTHWAITE, W. (1989) Corneal asphericity and refractive error. *Ophthalmic and Physiological Optics,* 9**,** 235-238.

SICAM, V., DUBBELMAN, M. & VAN DER HEIJDE, R. G. L. (2006) Spherical aberration of the anterior and posterior surface of the human cornea. *Journal of the Optical Society of America A,* 23**,** 544-549.

SMIRNOV, M. S. (1961) Measurement of the wave aberration of the human eye. *Biofizika,* 6**,** 687-703.

SMITH & AL, E. (2001) The spherical aberration of the crystalline lens of the human eye. *Vision Research.* 15;41**,** 235-43.

SMITH, E., III (1998) Environmentally induced refractive errors in animals. *Myopia and Nearwork. Butterworth Heinemann Oxford.***,** 57-90.

SMITH, E. L. & HUNG, L. F. (1999) The role of optical defocus in regulating refractive development in infant monkeys. *Vision Research,* 39**,** 1415-1435.

SMITH, G. & ATCHISON, D. A. (1997) *The Eye and Visual Optical Instruments,* Cambridge University Press.

SMITH, G., COX, M. J., CALVER, R. & GARNER, L. F. (2001) The spherical aberration of the crystalline lens of the human eye. *Vision Research,* 41**,** 235-243.

SMOLEK, M. K. & KLYCE, S. D. (2003) Zernike polynomial fitting fails to represent all visually significant corneal aberrations. *Investigative Ophthalmology & Visual Science,* 44**,** 4676-4681.

SOKAL, R. R. & ROHLF, F. J. (1995) *Biometry: the principles and practice of statistics in biological research,* New York, W.H. Freeman and Company.

SOLOVIEV, O. & VDOVIN, G. (2005) Hartmann-Shack test with random masks for modal wavefront reconstruction. *Optics Express,* 13**,** 9570-9584.

SORSBY, A., BENJAMIN, B. & A.G., B. (1981) Steiger on refraction: a reappraisal. *British Journal of Ophthalmology,* 65**,** 805-811.

SORSBY, A., BENJAMIN, B., DAVEY, J. B., SHERIDAN, M. & TANNER, J. M. (1957) Emmetropia and Its Aberrations. A Study in the Correlation of the Optical Components of the Eye. *Medical Research Council Special Report Series.*

SORSBY, A., BENJAMIN, B. & SHERIDAN, M. (1961) Refraction and its Components During the Growth of the Eye from the Age of Three. *Medical Research Council Special Report Series.* London: HMSO.

SOUTHWELL, W. H. (1980) Wave-front estimation from wave-front slope measurements. *Journal of the Optical Society of America A,* 70**,** 998-1006.

SPIERER, A. & SHALEV, B. (2003) Presbyopia among normal individuals. *Graefe's Archive of Clinical and Experimental Ophthalmology.,* 241**,** 101-105.

STANWORTH, A. & NAYLOR, E. J. (1950) The polarization optics of the isolated cornea. *British Journal of Ophthalmology,* 34**,** 201-211.

STENSTRÖM, S. (1946) Untersuchungen über die Variation und Kovariation der optischen Elemente des menschlichen Auges. *Acta Ophthalmologica (Kbh)., (Suppl.)* 26.

STRANG, N., SCHMID, K. & CARNEY, L. (1998) Hyperopia is predominantly axial in nature. *Current Eye Research,* 17**,** 380-383.

STRAUB, M. (1909) Uber die Aetilogie der Brechungsanomalien des Auges und den. *Ursprung der Emmetropie*. 70**,** 130-199.

THIBOS, L. N., APPLEGATE, R. A., SCHWIEGERLING, J. T., WEBB, R. H. & MEMBERS, V. S. T. (2000) Standards for reporting the optical aberrations of eyes. *Vision Science and its Applications, OSA Trends in Optics & Photonics,* 35**,** 110-130.

THIBOS, L. N., FAAO, P. & XIN HONG, M. (1999) Clinical applications of the Shack-Hartmann aberrometer. *Optometry and Vision Science,* 76**,** 817-825.

THIBOS, L. N., HONG, X., BRADLEY, A. & CHENG, X. (2002) Statistical variation of aberration structure and image quality in a normal population of healthy eyes. *Journal of the Optical Society of America A,* 19**,** 2329-2348.

THIBOS, L. N., YE, M., ZHANG, X. X. & BRADLEY, A. B. (1992) The chromatic eye: a new reduced-eye model of ocular chromatic aberration in humans. *Applied Optics,* 31**,** 3594-3600.

THORN, F., HELD, R., GWIAZDA, J. E. & HE, J. C. (2003) Method for preventing myopia progression through identification and correction of optical aberrations. (Patent). USA, New England College of Optometry.

TOMLINSON, A., HEMENGER, R. P. & GARRIOTT, R. (1993) Method for Estimating the Spheric Aberration of the Human Crystalline Lens in Vivo. *Investigative Ophthalmology and Visual Science,* 34**,** 621-629.

TROKEL, S. L., SRINIVASAN, R. & BRAREN, B. (1983) Excimer Laser-Surgery of the Cornea. *American Journal of Ophthalmology,* 96**,** 710-715.

TSCHERNING, M. (1894) Die monochromatishen Aberrationen des menschlichen Auges. *Z. Psychol. Physiol. Sinn.,* 6**,** 456-471.

VAN ALPHEN, G. (1961) On emmetropia and ametropia. *Optica Acta (Lond),* 142(Suppl)**,** 1-92.

VAN BLOKLAND, G. J. (1985) Ellipsometry of the human retina in vivo: preservation of polarization. *Journal of the Optical Society of America A,* 2**,** 72-75.

VAN BLOKLAND, G. J. (1986) The optics of the human eye with respect to polarized light.,PhD Thesis, Utrech, University of Utrecht.

VAN BLOKLAND, G. J. & VERHELST, S. C. (1987) Corneal polarization in the living human eye explained with a biaxial model. *Journal of the Optical Society of America A,* 4**,** 82-90.

VAN DEN BERG, T. J. (1997) Light scattering by donor lenses as a function of depth and wavelength. *Investigative Ophthalmology and Visual Science,* 38**,** 1321-1332.

VAN DER BRINK, G. (1962) Measurements of the geometrical aberrations of the eye. *Vision Research,* 2**,** 233-244.

VAN HEEL, A. C. S. (1946) Correcting the Spherical and Chromatic Aberrations of the Eye. *Journal of the Optical Society of America A,* 36**,** 237-239.

VERDON, W., BULLIMORE, M. & MALONEY, R. K. (1996) Visual performance after photorefractive keratectomy. A prospective study. *Archives of Ophthalmology,* 114**,** 1465-1472.

VESALUOMA, M., PEREZ-SANTONJA, J., PETROLL, W., LINNA, T., ALIO, J. & TERVO, T. (2000) Corneal stromal changes induced by myopic LASIK. *Investigative Ophthalmology and Visual Science***,** 41, 369-376.

VON BAHR, G. (1945) Investigations into the spherical and chomatic aberrations of the eye and their influence on its refraction. *Acta Ophthalmologica,* 23,1-47.

WALLMAN, J. (1993) Retinal Control of Eye Growth and Refraction. *Progress in Retinal Research,* 12**,** 133-153.

WALLMAN, J. & WINAWER, J. (2004) Homeostasis of eye growth and the question of myopia. *Neuron,* 43**,** 447-468.

WALSH, G., CHARMAN, W. N. & HOWLAND, H. C. (1984) Objective technique for the determination of monochromatic aberrations of the human eye. *Journal of the Optical Society of America A,* 1**,** 987-992.

WANG, J. Y. & SILVA, D. E. (1980) Wave-front interpretation with Zernike polynomials. *Applied Optics,* 19**,** 1510-1518.

WANG, L., D., D. & KOCH, M. (2003a) Anterior corneal optical aberrations induced by laser in situ keratomileusis for hyperopia. *Journal of Cataract and Refractive Surgery,* 29**,** 1702-1708.

WANG, L., DAI, E., KOCH, D. D. & NATHOO, A. (2003b) Optical aberrations of the human anterior cornea. *Journal of Cataract and Refractive Surgery,* 29**,** 1514-1521.

WEALE, R. A. (2003) Epidemiology of refractive errors and presbyopia. *Survey of Ophthalmology,* 48**,** 515-543.

WEBB, R. H., PENNEY, C. M. & THOMPSON, K. P. (1992) Measurement of ocular wavefront distortion with a spatially resolved refractometer. *Applied Optics,* 31**,** 3678-3686.

WESTHEIMER, G. & CAMPBELL, F. W. (1962) Light distribution in the image formed by the living human eye. *Journal of the Optical Society of America,* 52**,** 1040-1044.

WESTHEIMER, G. & LIANG, J. (1995) Influence of ocular light scatter on the eye's optical performance. *Journal of the Optical Society of America A***,** 12**,** 1417-1424.

WILDSOET, C. F. (1997) Active emmetropization - Evidence for its existence and ramifications for clinical practice. *Ophthalmic and Physiological Optics,* 17**,** 279-290.

WILLIAMS, D. R., BRAINARD, D. H., MCMAHON, M. J. & NAVARRO, R. (1994) Double-pass and interferometric measures of the optical quality of the eye. *Journal of the Optical Society of America A,* 11**,** 3123-3135.

WYSZECKI, G. & STILES, W. S. (1982) *Color Science- Concepts and Methods, Quantitative Data and Formulae,* New York, John Wiley & Sons.

YAMANE, N., MIYATA, K., SAMEJIMA, T., HIRAOKA, T., KIUCHI, T., OKAMOTO, F., HIROBARA, Y., MIHASHI, T. & OSHIKA, T. (2004) Ocular higher-order aberrations and contrast sensitivity after conventional laser in situ keratomileusis. *Investigative Ophthalmology & Visual Science,* 45**,** 3986-3990.

YAYLALI, V., KAUFMAN, S. C. & THOMPSON, H. W. (1996) Corneal thickness measurements with the Orbscan Topography System and ultrasonic pachymetry. *Pre-AAO Conference of the International-Society-of-Refractive-Surgery.* Chicago, Il, Amer Soc Cataract Refractive Surgery.

YOUNG, F. A. & LEARY, G. A. (1991) Refractive Error in Relation to the Development of the Eye. IN CHARMAN, W. N. (Ed.) *Visual Optics and Instrumentation.* CRC Press. (Pages 29-44).

YU, K., SWARTZ, T., BOERMAN, H. & WANG, M. (2006) Anatomy and physiology of the cornea. IN WANG, M. (Ed.) *Corneal topography in the wavefront era.* Slack incorporated.

ZHANG, J., ZHOU, Y. H., WANG, N. L. & LI, R. (2008) Comparison of visual performance between conventional LASIK and wavefront-guided LASIK with iris-registration. *Chinese Medical Journal,* 121**,** 137-142.

ZHU, M., COLLINS, M. J. & ISKANDER, D. R. (2004) Microfluctuations of wavefront aberrations of the eye. *Ophthalmic and Physiological Optics,* 24**,** 562-571.